Iowa Research Online
The University of Iowa's Institutional Repository

University of Iowa
Iowa Research Online

Theses and Dissertations

Fall 2013

Applications of near-infrared spectroscopy in temperature modeling of aqueous-based samples and polymer characterization

Chamathca Priyanwada Kuda-Malwathumullage
University of Iowa

Copyright 2013 Chamathca Priyanwada Kuda-Malwathumullage

This dissertation is available at Iowa Research Online: http://ir.uiowa.edu/etd/5007

Recommended Citation
Kuda-Malwathumullage, Chamathca Priyanwada. "Applications of near-infrared spectroscopy in temperature modeling of aqueous-based samples and polymer characterization." PhD (Doctor of Philosophy) thesis, University of Iowa, 2013.
http://ir.uiowa.edu/etd/5007.

Follow this and additional works at: http://ir.uiowa.edu/etd


Part of the Chemistry Commons

APPLICATIONS OF NEAR-INFRARED SPECTROSCOPY IN TEMPERATURE MODELING OF AQUEOUS-BASED SAMPLES AND POLYMER CHARACTERIZATION

by

Chamathca Priyanwada Kuda Malwathumullage

A thesis submitted in partial fulfillment of the
requirements for the Doctor of
Philosophy degree in Chemistry in
the Graduate College of
The University of Iowa

December 2013

Thesis Supervisor: Professor Gary W. Small

Copyright by

CHAMATHCA PRIYANWADA KUDA MALWATHUMULLAGE

2013

All Rights Reserved

Graduate College
The University of Iowa
Iowa City, Iowa

CERTIFICATE OF APPROVAL

_____

PH.D. THESIS

_____

This is to certify that the Ph.D. thesis of

Chamathca Priyanwada Kuda Malwathumullage

has been approved by the Examining Committee
for the thesis requirement for the Doctor of
Philosophy degree in Chemistry
at the December 2013 graduation.

Thesis Committee: _____
Gary. W. Small, Thesis Supervisor

_____
Mark A. Arnold

_____
M. Lei Geng

_____
Alexei V. Tivanski

_____
Paul D. Kleiber

To my parents, my brother and Suranga

ACKNOWLEDGMENTS

I would like to acknowledge several people for their support and guidance throughout this study without which this work would not have been possible. First of all I would like to express my sincere gratitude to my advisor Prof. Gary W. Small for his guidance, support and encouragement over the last five years which helped me to perform quality research and develop a professional career.

I would also like to gratefully acknowledge my Comprehensive and PhD committee members Prof. Mark Arnold, Prof. Lei Geng, Prof. Alexei Tivanski, Prof. Gregory Friestad and Prof. Paul Kleiber for their valuable discussions and suggestions which helped me to successfully continue my research work.

I would like to thank my former and current research group members; Wei Wang, Dr. Qiaohan Guo, Sanjeewa Karunathilake, Hua Yu, Brian Dess and Ziqi Fan for being such wonderful friends. Thank you very much for all your help and suggestions in the lab.

I would like to gratefully acknowledge the following four people in the Department of Chemistry at the University of Iowa for their great insight, helpful suggestions and priceless creativity in building the flow cell and brass heater used in my research: Mike Estenson, the manager of the electronics shop, Frank Turner, the manager of the machine shop and Peter Hatch and Benjamin Revis, former and current managers of the glass shop.

I would also like to thank Janet Kugley (graduate admissions coordinator) and Sharon Robertson (graduate student administrator) for their kindness and help in my adjustment to life in the USA.

I would also like to acknowledge the Mark Arnold research group of the University of Iowa for providing the bovine plasma samples and the Tori Forbes research

group of the University of Iowa for helping me with the thermogravimetric measurements.

I am truly grateful to the National Institutes of Health, Department of Chemistry and the Graduate College of the University of Iowa for the funding support throughout my research work.

Finally I would like to express my deepest thanks to my parents, my brother and my husband, Suranga, for their continuous encouragement and endless love. Thank you very much for being there for me during all my victories as well as my failures.

ABSTRACT

Near-infrared (NIR) spectroscopy is a widely used technique in quantitative analytical applications. Near-infrared spectroscopy is commonly used in clinical, environmental and industrial applications because of its compatibility with aqueous samples and with relatively thick samples. However, NIR spectra typically contain weak and highly overlapped spectral features which require multivariate data analysis techniques (chemometrics) to yield meaningful and chemically relevant information.

This dissertation consists of two main themes which include applications of NIR spectroscopy combined with chemometrics to (1) model temperatures in clinically relevant aqueous-based samples and (2) model temperature and moisture content in nylon-6,6 polymer samples. This research employed overtone and combination bands of C-H, O-H and N-H bonds situated in the 4000 - 5000 cm^{-1} region to develop partial least-squares (PLS) regression models to predict analyte properties such as temperature, concentration and moisture content.

The research described in the first part of this dissertation includes the development of a spectral preprocessing strategy based on the standard variate transform (SNV) and discrete wavelet transform (DWT) to isolate the low-frequency baseline information which carries the spectral features due to temperature fluctuations in aqueous-based samples. This approach was used to develop calibration models to determine the temperature of aqueous-based samples directly from their NIR spectra. This is an important development due to the fact that extreme temperature sensitivity of the underlying water bands can lead to poor quantitative analyte prediction results. These temperature models were developed using pH 7.4 phosphate buffer solutions spanning

the range of 20 to 40.5 °C. Following the temperature models, a temperature-correction strategy based on the systematic pattern of concentration residuals was successfully developed to improve quantitative analyte predictions in aqueous-based samples. These analyte prediction models included glucose solutions and glucose-lactate mixture solutions prepared in pH 7.4 phosphate buffer. The computed temperature models gave excellent long-term prediction results. The temperature correction strategy gave promising results with the glucose solutions as well as the glucose-lactate mixture solutions.

The research presented in the second part of this dissertation includes the development of calibration models to determine the temperature and moisture content of a piece of nylon-6,6 polymer directly from its NIR spectrum combining SNV and DWT procedures followed by PLS regression. Both of these models gave good long-term prediction results and performed well when used to predict temperatures and moisture content across different nylon-6,6 sheets. Computed moisture model provides a reliable and fast method to determine the moisture content of a nylon polymer when compared to existing techniques and it could be easily integrated with on-line analyses. Extended research towards polymer characterization including preliminary investigations of inhomogeneous nature of nylon polymers using Infrared microscopy is documented in the latter part of this dissertation.

TABLE OF CONTENTS

LIST OF TABLES

LIST OF FIGURES

CHAPTER 1
INTRODUCTION

The infrared (IR) region of the electromagnetic spectrum encompasses radiation with wavelengths extending from red light in the visible region towards the microwave region.[1-5] Infrared spectroscopy is based on IR-active molecular vibrations (stretching and bending modes) to obtain chemical information regarding molecules.[1,2] Infrared radiation can be subdivided into three regions: near-IR, mid-IR and far-IR. The near-infrared (NIR) region contains radiation ranging from 0.78 to 2,500 μm or 4,000 to 12,800 cm^{-1}.[1] Vibrational transitions occurring in this region are overtones and combination bands; particularly the overtones and combination bands resulting from N-H, C-H and O-H fundamental vibrations.[1-4] The NIR region was once considered to be less useful when compared to the mid-IR region because of the weak and overlapping nature of the spectral features located there. With the development of better instrumentation and data analysis techniques in the latter part of the 20^{th} century, NIR spectroscopy gained significant attention from the scientific community.[2-4] Present applications of NIR spectroscopy can be found in quantitative determinations of chemical species in agricultural, clinical, food, petroleum, pharmaceutical and chemical industries.[3,24,27-31,45,52] Chapter 2 provides a detailed discussion about the background, development, principles and applications of NIR spectroscopy.

Several different types of instruments are available for use in the NIR region.[1] The introduction of commercial Fourier transform (FT) instruments for the NIR region in the 1980's has given scientists additional instrumentation choices for NIR measurements. Since then, Fourier transform infrared (FTIR) instruments have largely replaced the traditional dispersive instruments in many applications due to their fast data acquisition ability and improved accuracy and reproducibility.[1,2] Fourier transform infrared spectrometry is based on the principle of superposition in which the interference of

radiation between two or more beams yields an interference pattern known as an interferogram.[1-4] Fourier transform spectroscopy is a time-domain spectroscopic technique that records the radiant power as a function of time. The inter-conversion of time- and frequency-domain signals is achieved by a complex mathematical transformation known as the Fourier transform.[1,2] Fourier transform infrared spectroscopy can also be combined with microscopic analysis.[1,12,13] This fairly new technique is known as infrared microscopy (IR microscopy) and is used to obtain chemical information from samples which are very small. Fourier transform IR microscopes has found successful applications in clinical chemistry, polymer, textile and electronics industries.[1,12,13] Chapter 2 discusses the principles of FTIR spectroscopy, IR microscopy, generation of an interferogram, mathematical manipulation of an interferogram (apodization, zero-filling, phase correction etc.) and advantages of FT spectroscopy.

As mentioned above, NIR spectra often produce weak, broad and highly overlapped spectral features which demand the use of data analysis techniques in order to obtain meaningful and chemically relevant information.[17,26] Chemometrics is defined as the chemical discipline that uses mathematical and statistical methods to provide maximum chemical information by analyzing chemical data.[14] Chemometric methods are widely applied in the field of analytical chemistry.[14,15] Chemometric methods for evaluating chemical data are employed in experimental design, signal preprocessing, image processing, calibration model building, and model optimization.[14] Chapter 3 provides a detailed discussion about the background, development and applications of chemometric methods that are employed in this dissertation.

In the analysis of NIR spectra, the presence of noise or other data artifacts is of concern as they can complicate data interpretation, thereby reducing the performance of quantitative calibration models that relate spectral intensities to desired measurement properties (e.g., concentration). One solution to this problem is to preprocess the raw

spectra mathematically to remove undesirable artifacts without altering the information that is pertinent to the problem under study.[3] This is known as signal preprocessing. In the research work described in Chapters 4 through 8, two main signal preprocessing methods; the standard normal variate (SNV) transform and the discrete wavelet transform (DWT), are employed. The SNV transform, also known as autoscaling, is a scaling method which corrects for multiplicative and additive signal drift.[18] The wavelet transform (WT) is a fairly new mathematical technique which was first introduced to chemistry in the 1990's. It has been widely used in many chemical applications since then.[15,20,21] The DWT uses a finite function (wavelet function) to decompose an input signal into hierarchical sets of wavelet coefficients termed approximations and details which carry specific frequency infromation[15]. The decomposition process is iterative so that the original signal can be broken down into many lower-resolution components. The input signal can then be reconstructed using only a selected subset of the approximations and details in order to remove undesired components such as noise and background variation. A detailed discussion of the SNV and DWT transforms is provided in Chapter 3.

Development of a well-performing calibration model is an important application in chemometrics and these calibration models are typically required in NIR spectroscopy due to the overlapped nature of spectral features found in NIR spectra.[3,14,17,19,25] In simplest terms, building a calibration model involves constructing mathematical models to explore relationships between variables (e.g., relationships between spectral intensities at a given wavelengths and the corresponding concentrations of a target analyte). Principal component regression (PCR) is a widely used multivariate technique to develop calibration models in chemometrics.[3,14,17,19] The term, PCR, refers to the combination of principal component analysis (PCA) and multiple linear regression (MLR). Partial least-squares (PLS) is another widely used technique to develop calibration models in chemometrics. When coupled with MLR to build an inverse regression model, PLS is

termed PLS regression (PLSR). [3,14,17,19] Principal component and partial least-squares regression have been widely employed in NIR spectroscopy.[3,14] Chapter 3 discusses the principles of MLR, PCR and PLS in detail along with the development, optimization and validation of calibration models which were employed in the research work described in Chapters 4 through 8.

Near-infrared spectroscopy is widely used in biological and clinical applications in which the samples are primarily aqueous-based.[3] The hydrogen-bonded structure of water and its extreme temperature sensitivity have been extensively studied.[6,37-39,51,52] If precise control of temperature during spectral collection is not ensured, peak shifts in the water spectrum can result in large baseline variations in absorbance spectra computed from spectral ratios. Spectral artifacts due to temperature fluctuations are especially problematic in NIR spectra of samples which are primarily aqueous-based and can complicate the data analysis steps required to perform accurate quantitative analyses.[6,37-39] In the work presented in Chapter 4, a strategy is explored to determine the temperature of an aqueous-based sample directly from the NIR spectrum. In the work presented in Chapter 4, signal preprocessing methods (SNV + DWT) combined with PLS regression are used to develop calibration models to determine the temperature of pH 7.4 phosphate buffer samples directly from their NIR spectra.

This chapter also explores temperature modeling in aqueous samples with increasing complexity such as dissolved proteins, pH and molarity variations, as well as flowing solutions. The work presented in Chapter 5 includes development of a temperature-correction strategy to improve the performance of quantitative analyte prediction models by incorporating the temperature modeling information developed in Chapter 4. The concept of coupling a spectral-based temperature determination with a corresponding calibration correction is motivated by applications in which the accurate measurement of sample temperature with a conventional thermistor or thermocouple probe is difficult. One such application and a long-standing area of interest in our

laboratory is NIR-based noninvasive glucose monitoring in which *in vivo* glucose concentration determinations are made from direct spectral measurements of body tissue.[42,54] In this application, it is difficult to use a conventional temperature probe to obtain an accurate internal temperature of the tissue through which the spectral measurement is made. Although the core temperature of the human body is maintained near 37.0 °C, peripheral tissues and fluids (hands, feet, etc.) can be subject to significant temperature fluctuations. In the work presented in Chapter 5, a signal preprocessing method (DWT) and PLS regression were used to develop calibration models to determine analyte concentrations (glucose, lactate) in pH 7.4 phosphate buffer samples. Chapter 5 also focuses on a simple but effective correction strategy which is based on a second-order polynomial correction to the concentration residuals, followed by an additive correction to the analyte prediction at a given temperature.

Near-infrared spectroscopy is widely used in characterization of polymers.[3,76,79,80] Nylons are a group of polyamide polymers which form *via* condensation polymerization of a diamine with a dicarboxylic acid.[64-67] Nylon-6,6 is a subgroup of nylon polymers which is thermoplastic in nature and provides great rigidity, high mechanical strength and durability, thereby making it one of the most widely used nylons in the world. Nylon polymers are not good heat conductors. Changes in temperature primarily affect the intermolecular hydrogen-bonding network that exists between the nylon polymer chains. However, it is also observed that temperature changes can influence the structure of the hydrocarbon chains.[81,86,87] Research presented in Chapter 6 is an extension from Chapters 4 and 5. The primary motivation for this work was to develop methods to predict the temperature of a given solid material directly from NIR spectra. Such methods could be used for temperature determinations of solid materials in applications where it is inaccurate or inconvenient to determine the temperature with a conventional probe such as a thermocouple thermometer. The methodology used in Chapters 4 and 5 is extended towards common materials which are no longer liquids. Since nylon polymers are a

widely used group of materials, it is interesting to investigate the ability to predict the temperature of a nylon sample directly from its NIR spectrum. In the work presented in Chapter 6, signal preprocessing methods (SNV + DWT) combined with PLS regression are used to develop calibration models to determine the temperature of nylon-6,6 polymers directly from NIR spectra.

Nylon polymers have hygroscopic properties meaning they absorb moisture from the surrounding environment.[71,80,82] The degree of affinity for water depends on the chemical structure of the nylon species considered. Near-infrared spectroscopy has also been used to measure the moisture content of nylon polymers.[79,80,82] In the work presented in Chapter 7, signal preprocessing method (SNV) combined with PLS regression are used to develop calibration models to determine the moisture content of nylon-6,6 polymers directly from NIR spectra. The prediction performance of these moisture models is assessed for robustness with time and the ability to predict moisture uptake across different sheets of nylon-6,6 polymers. This methodology is a non-destructive technique as opposed to commonly used destructive techniques such as thermogravimetric analysis (TGA) or differential scanning calorimetry (DSC). This methodology can also be developed as an on-line analysis for routine investigations or quality control purposes. The reliability of using an analytical balance as an alternative to time-consuming TGA measurements to obtain weight measurements was also demonstrated in this work.

Infrared microscopy is a fairly new technique which combines FTIR spectroscopy with microscopic analysis. This technique has successfully been used in polymer characterization.[1,4,12,13] Observations from Chapter 6 and 7 suggested that the non-homogeneous nature nylon-6,6 polymers in a microscopic scale may influence the macroscopic properties such as moisture uptake and thermal degradation of nylon. In the work presented in Chapter 8, a preliminary investigation is performed on nylon-6,6 samples using IR microscopy to understand the effect of the non-homogeneous nature of

the material on macroscopic properties such as moisture uptake and thermal degradation. In the work described in Chapter 8, a signal preprocessing method (SNV) combined with PCR is used to study the NIR spectra obtained from an IR microscope to generate IR images of nylon-6,6 samples at given sets of conditions (degree of moisture uptake, degree of thermal degradation, etc.).

Finally, a collective summary of the research work performed in Chapters 4 through 8 and conclusions derived from each chapter are presented in Chapter 9 along with suggestions for future work.

CHAPTER 2
NEAR-INFRARED SPECTROSCOPY AND INFRARED MICROSCOPY: THEORY AND INSTRUMENTATION

2.1 Introduction

The Infrared (IR) region of the electromagnetic spectrum encompasses radiation with wavelengths ranging from 0.78 to 1,000 μm or wavenumbers ranging from 12,800 to 10 cm^{-1}. The IR region may also be defined as radiation extending from red light in the visible region towards the microwave region.[1-5] Infrared radiation can be subdivided into three regions; near-IR, mid-IR and far-IR. Specific wavenumber regions associated with these three regions are listed in Table 2-1 along with their fundamental applications.[1]

In 1800, an English astronomer named William Herschel who was examining the color in the visible spectrum responsible for heat from the sun, observed a temperature change caused by the tail end of red light. He then postulated that the temperature change was caused by 'an invisible band beyond red light' and named it *infrared* which meant 'below red' in Latin.[2,3] The IR region remained unexamined for many years mainly due to lack of instrumentation suitable to obtain a spectrum in this region. In the early 20th century, instrumentation suitable to detect IR radiation was invented and since then, IR spectroscopy has been a very useful spectroscopic technique in various disciplines such as astronomy, organic chemistry and analytical chemistry.[2-4]

2.2 Principles of infrared spectroscopy

Chemical bonds in molecules vibrate (stretch or bend) when exposed to IR radiation. According to the selection rules, vibrational transitions that result in a change in dipole moment are IR active.[1,4,5] Infrared spectroscopy is based on these IR-active molecular vibrations to obtain chemical information regarding molecules. Characteristics of vibrational transitions can be approximated using a simple harmonic oscillator model.

According to this model, the fundamental/natural frequency (ν_o) of a given vibration can be calculated using Eq. 2-1. [1,4,5]

$$v_o = \frac{1}{2\pi}\sqrt{k/\mu} \qquad (2\text{-}1)$$

According to Eq. 2-1, the natural frequency (ν_o) of a vibration depends on the force constant (k) of the bond and the reduced mass (μ) of the atoms involved.

By combining the harmonic oscillator model with the quantized nature of vibrational energy levels, the fundamental frequency (ν_o) of a given vibration can be related to the energy (E) associated with the transition.[1-4] Equation 2-2 explains this relationship.

$$E = \left(v + \frac{1}{2}\right)\frac{h}{2\pi}\sqrt{k/\mu} = \left(v + \frac{1}{2}\right)hv_o \qquad (2\text{-}2)$$

According to Eq. 2-2, the energy of a given vibrational level, E, is related to its vibrational quantum number (v), Planck's constant (h) and the natural frequency (ν_o) of the vibration.

In reality, bond vibrations have limitations that restrict the application of the harmonic oscillator model. Since the bonds can break as they reach the dissociation energy, an anharmonic oscillator model (Eq. 2-3) is employed to explain the bond vibrations in real molecules.[2,3]

$$E = \left(v + \frac{1}{2}\right)hv_o + \left(v + \frac{1}{2}\right)^2 v_o X_e + higher\ terms \qquad (2\text{-}3)$$

According to Eq. 2-3, the energy of a given vibrational level, E, is related to its vibrational quantum number (v), Planck's constant (h), an anharmonicity constant (X_e) and the natural frequency (ν_o) of the vibration.

For a given polyatomic molecule containing *N* atoms, the number of fundamental vibrational modes (normal modes) allowed can be calculated by *3N-5* (for linear molecules) or *3N-6* (for non-linear molecules).[1,4] The experimentally observed number of normal modes often differs from the theoretical number of normal modes. This can be due to the symmetry of the molecule, degenerate nature of energy levels, anharmonicity leading to overtones, occurrence of combination bands, Fermi resonance and vibrational coupling.[1,4]

2.3 Near-infrared spectroscopy

The near-infrared (NIR) region contains radiation ranging from 0.78 to 2,500 μm or 4,000 to 12,800 cm^{-1}. Vibrational transitions occurring in this region are overtones and combination bands; particularly the overtones and combination bands resulting from N-H, C-H and O-H fundamental vibrations.[1-4] As described in Section 2.2, anharmonicity leads to weaker transitions called overtones which correspond to $\Delta\nu = \pm 2$ or ± 3. In an anharmonic oscillator model, at higher quantum numbers, energy changes become smaller and the selection rule $\Delta\nu = \pm 1$ is not strictly followed.[1,4] Frequencies of overtones are approximately two or three times that of the fundamental frequency. Combination bands occur when a single photon excites two vibrations simultaneously. The frequency of a combination band is the sum or difference of the two fundamental frequencies. Intensities of overtones and combination bands are lower than those of the corresponding fundamental transitions.[1,4] Wavenumber ranges of overtones and combination bands occurring in water are shown in Table 2-2. The NIR region was once considered to be less useful when compared to the mid-IR region because of the weak and overlapping nature of the spectral features located there. With the development of better instrumentation and data analysis techniques in the latter part of the 20^{th} century, NIR spectroscopy and data analysis techniques in the latter part of the 20^{th} century, NIR spectroscopy gained significant attention from the scientific community. Present applications of NIR spectroscopy can be found in quantitative determinations of chemical

Table 2-1. Wavenumber regions associated with the three IR regions along with their fundamental applications.[1]

Region	Wavelength (μm)	Wavenumber (cm^{-1})	Main applications
Near-IR	0.78 – 2.5	12,800 – 4,000	Quantitative determination of solid, liquid and gaseous samples
Mid-IR	2.5 – 50	4,000 – 200	Qualitative determination of complex solids, liquids and gaseous mixtures (specifically organic molecules)
Far-IR	50 – 1,000	200 – 10	Qualitative determination of inorganic and organometallic species

Table 2-2. Occurrence of overtones and combination bands in water.[6,24,37,39,80]

Vibrational transition	Mode	Wavenumber (cm^{-1})
Symmetric and asymmetric O-H stretching	$\nu_{1,3}$	3,300 - 3,800
H-O-H bending	ν_2	1,595 - 1,650
First overtone of O-H stretching	$2\ \nu_{1,3}$	6,900 - 7,000
Combination of first overtone of O-H stretching and H-O-H bending	$2\ \nu_{1,3}+ \nu_2$	8,330 - 8,500
Combination of O-H stretching and H-O-H bending	$\nu_{1,3}+ \nu_2$	5,150 - 5,200

species in agricultural, clinical, food, petroleum, pharmaceutical and chemical industries. Most of these applications are implemented as routine quantitative determinations and process control procedures. Near-infrared spectroscopic measurements can be obtained in different configurations such as transmittance/absorption and diffuse reflectance modes. Near-infrared spectroscopy is often compatible with samples of varying physical forms such as liquids, solids, powders, films, tissues and gases. [1-4]

2.4 Instrumentation

Several different types of instruments are available for use in the NIR region. Dispersive instruments which consist of diffraction gratings or monochromaters are the traditionally used instruments for the NIR region. In addition, acousto-optic tunable filter (AOTF) or other filter-based instruments are a popular option. The introduction of commercial Fourier transform (FT) instruments for the mid-IR in the 1970s and their expansion into the NIR region in the 1980's have given scientists additional instrumentation choices for NIR measurements. In some applications, FT instruments have largely displaced the traditional dispersive and filter-based instruments due to their fast data acquisition ability and improved signal-to-noise (S/N) ratio.[1-4] A Bruker Vertex 70 FT spectrometer (Bruker Optics, Inc., Billerica, MA) was used in the research work described in Chapters 4 through 7.

Radiation sources used in the NIR region are inert solids which are electrically heated to temperatures in the range of 1500 to 2200 K. Upon heating, these inert solids produce continuum radiation which approximates blackbody emission. Commonly used NIR sources are the Globar (SiC), Nernst glower (ZrO_2 & Y_2O_3), nichrome wires and tungsten-halogen lamps.[1.3] A tungsten-halogen lamp was used in the research work described in Chapters 4 through 7.

Common NIR detectors are photon detectors which are made of semiconducting materials such as indium arsenide (InAs), indium antimonide (InSb), lead sulfide (PbS) and indium gallium arsenide (InGaAs). These detectors are based on the excitation of

electrons in the above-mentioned solid semiconducting materials caused by the interaction with incident NIR radiation.[1,3] A liquid nitrogen cooled InSb detector was used in the research work described in Chapters 4 through 7.

2.5 Fourier transform infrared spectrometry

Fourier transform infrared spectrometry (FTIR) is based on the principle of superposition in which the interference of radiation between two or more beams yields an interference pattern known as an interferogram.[1-4] Figure 2-1 illustrates the principle of superposition using two beams which have slightly different frequencies. In the early 1950's, a group of astronomers used FTIR spectrometry to decode information from distant stars. The first chemical application of FTIR spectrometry was documented in the late 1960's which concerned the far-IR region.[1] Since then, FTIR spectrometers have become popular and are commercially available for the mid-IR, NIR and far-IR regions.

Conventionally, spectra are recorded in the frequency domain (i.e., radiant power is recorded as a function of frequency/wavelength/wavenumber). In contrast, time-domain spectroscopic techniques such as FTIR spectrometry record the radiant power as a function of time. The inter-conversion of time- and frequency-domain signals is achieved by a complex mathematical transformation known as the Fourier transform. Obtaining the time-domain signal requires a signal modulation procedure because of the incompatibility of IR frequencies with the response times of IR detectors and sampling electronics. The most commonly used signal modulation procedure in FTIR spectrometers is the Michelson interferometer.[1,3,4]

2.5.1 Michelson interferometer

A schematic representation of a Michelson interferometer is given in Figure 2-2. It consists of two mirrors of which one is fixed and the other is movable. An infrared transparent material (calcium fluoride, potassium bromide, etc.) coated with germanium or iron oxide is used to bisect the beam. This device is known as the beamsplitter. The Michelson interferometer splits an incident radiation beam into two beams of nearly

equal power and then recombines them in such a way that intensity variations in the combined beam can be measured as a function of differences in the pathlengths of the two beams.[1,3,4] The difference in pathlengths of the two beams in known as the retardation (δ) which is explained in Eq. 2-4.

$$\delta = 2(M - F) \tag{2-4}$$

According to Eq. 2-4 and Figure 2-2, *M* is the distance between the moving mirror and the beamsplitter and *F* is the distance between the fixed mirror and the beamsplitter.

As shown in Figure 2-2, for pathlength differences of λ, the two beams interfere constructively whereas for pathlength differences of ½ λ, the two beams interfere destructively. The resultant interference pattern contains all the spectral information of the incident radiation as a function of retardation and is known as an interferogram.[1] The relationship between the optical frequency of the incident radiation (f_o) and the frequency of the interferogram (f_I) can be obtained using the following equation.

$$f_I = \frac{2v_M f_o}{c} \tag{2-5}$$

According to Eq. 2-5, the frequency of the interferogram (f_I) is directly proportional to the moving mirror velocity (v_M) and the optical frequency of the incident radiation (f_o). The value of *c* is the velocity of light.

Figure 2-3 depicts the formation of interferograms at the output of the Michelson interferometer. Interference patterns resulting from a monochromatic source, dichromatic source and a broadband source are shown in separate panels.

For a continuum source, the cosine wave of the interferogram can be represented as a sum of an infinite number of cosine terms (Eq. 2-6).

$$P(\delta) = \int_{-\infty}^{+\infty} B(\bar{v}) \cos 2\pi\bar{v}\delta \, d\bar{v} \tag{2-6}$$

The Fourier transform of the integral in Eq. 2-6 is shown in Eq. 2-7. These two equations are known as a Fourier transform pair.

$$B(\bar{v}) = \int_{-\infty}^{+\infty} P(\delta) \cos 2\pi\bar{v}\delta \, d\delta \qquad (2\text{-}7)$$

For Eqs. 2-6 and 2-7, FT spectrometry consists of recording the radiant power of the interferogram signal, *P(δ)*, as a function of retardation *(δ)* and then mathematically transforming this relation to one that gives an instrumental response $B(\bar{v})$ as a function of wavenumber (frequency-domain).[1] A complete FT requires both real (cosine) and imaginary (sine) components.

However, Eqs. 2-6 and 2-7 have represented only the cosine part which is sufficient for manipulating real and even functions.[1] Equations 2-6 and 2-7 cannot be used as written because they assume infinite boundaries which requires infinite sampling times and infinite mirror lengths.[1]

The resolution (*R*) of a FTIR spectrum can be described as the extent to which two adjacent wavenumbers ($\bar{v}_2$ and $\bar{v}_1$) can be separated. In order for this to be achieved, the retardation (δ) has to be large enough to allow two waves to complete one cycle (in phase, out of phase and back to in phase). This can be explained by Eq. 2-8. Therefore, the best theoretical resolution of the spectrum is obtained at the maximum retardation.[1]

$$R = \frac{1}{\delta} = \bar{v}_2 - \bar{v}_1 \qquad (2\text{-}8)$$

2.5.2 Processing of the interferogram

As discussed in Section 2.5.1, the mathematical process of the FT assumes infinite boundaries. In reality, the interferogram has to be acquired in a finite time with a finite mirror movement. This is achieved experimentally by restricting the mirror retardation to a limited distance.

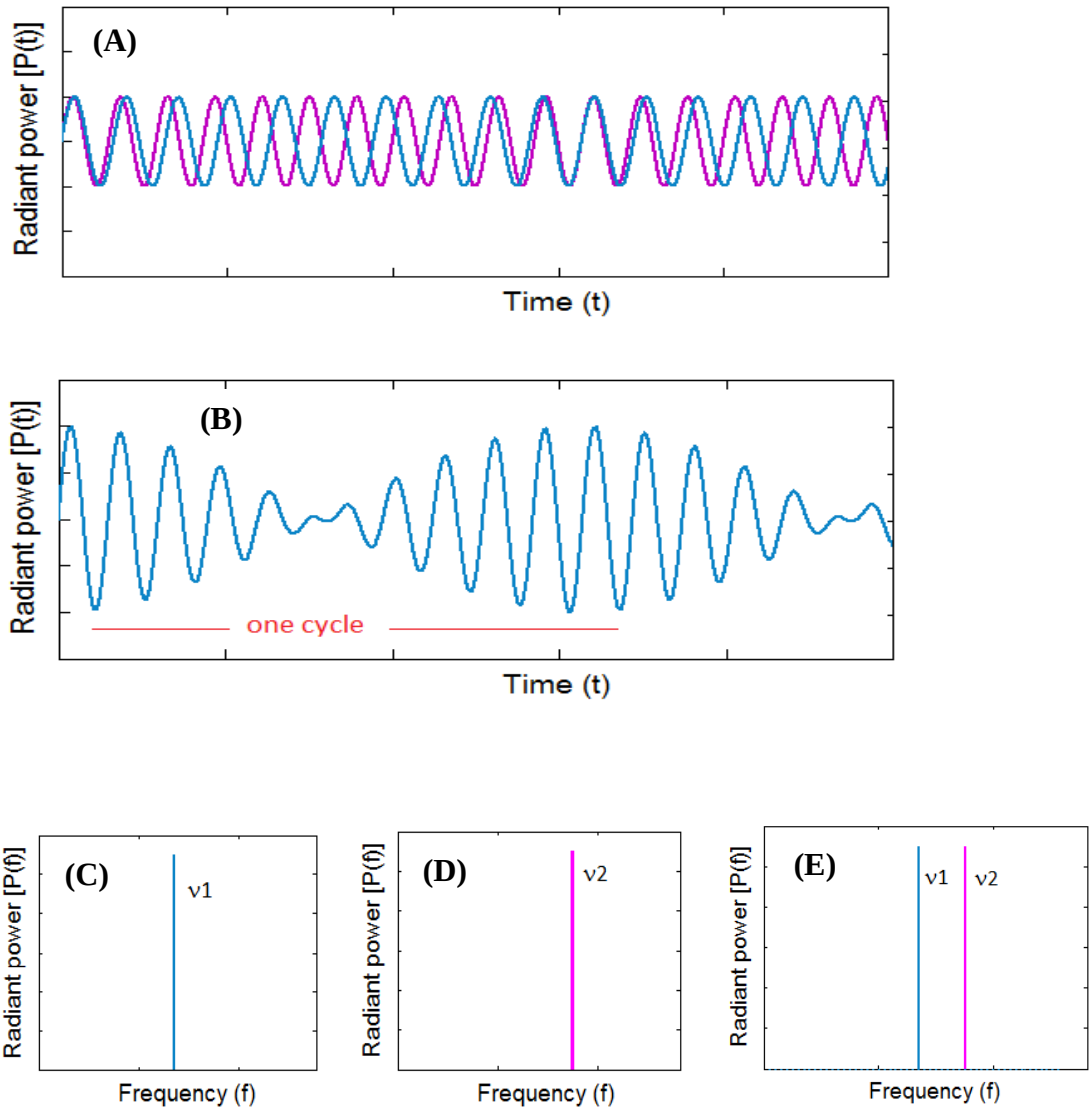

Figure 2-1. Principle of superposition observed in two waves.
(A) Time-domain signal of two slightly different frequencies of the same amplitude.
(B) Time-domain signal of the sum of the two waveforms. Also shown are frequency-domain signals of waveform 1 **(C)** 2 **(D)** and the composite waveform in **B (E).** This figure is based on a similar representation in reference 1.

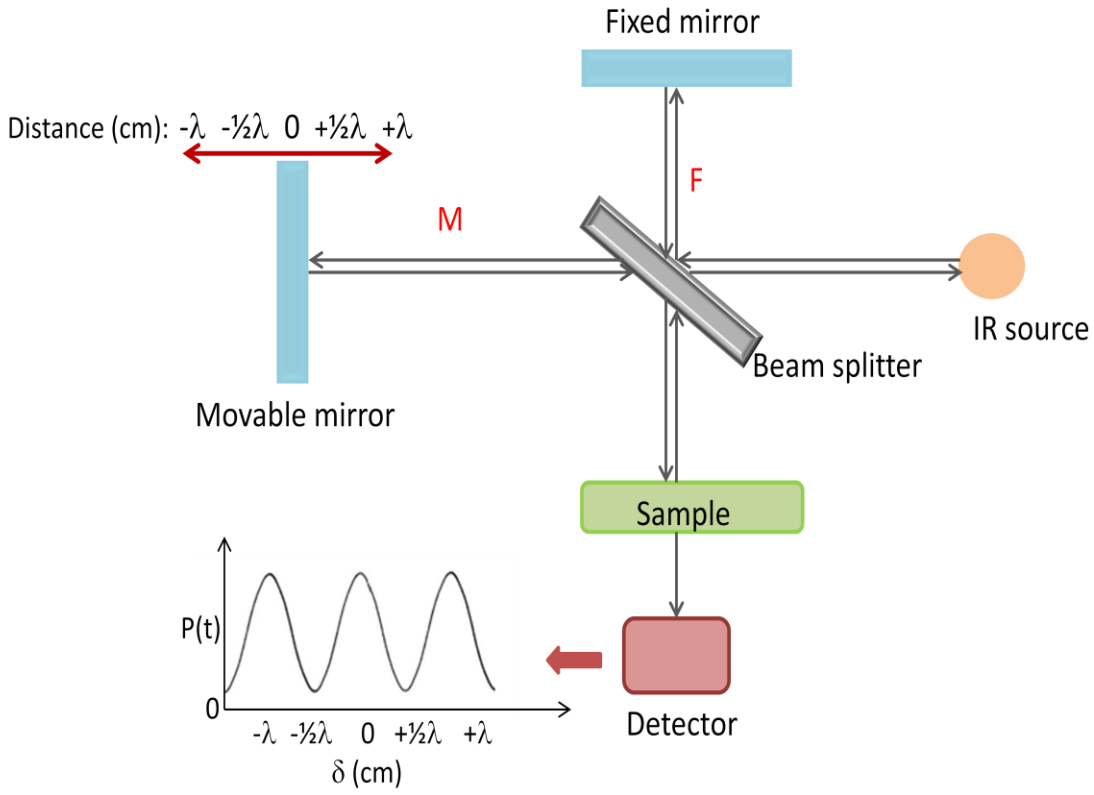

Figure 2-2. Schematic representation of a Michelson interferometer illuminated with a monochromatic source. The resultant interferogram obtained after frequency modulation is shown in the bottom left. This figure is based on a similar representation in reference 1.

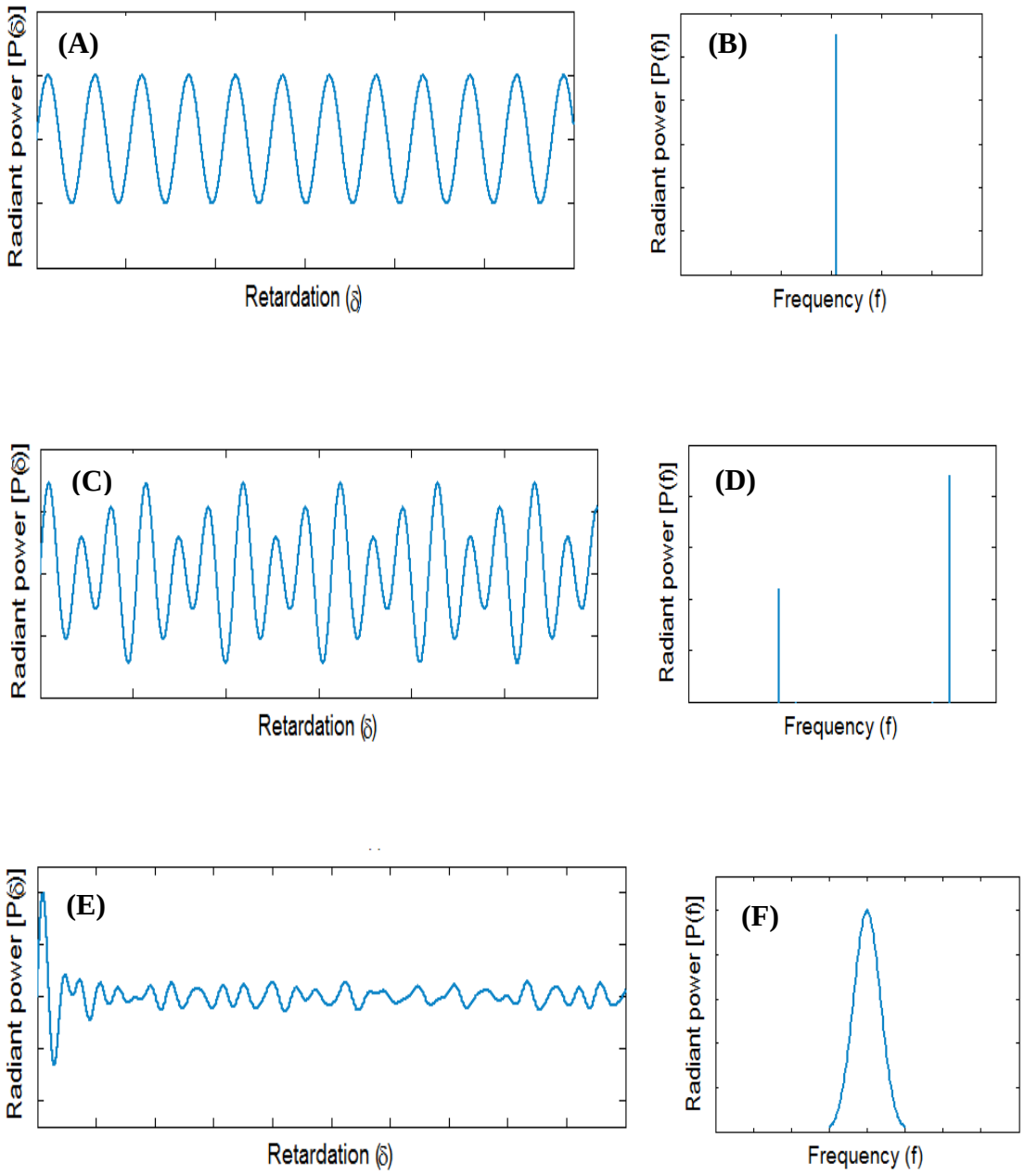

Figure 2-3. Interferogram patterns.
These patterns are formed by a monochromatic source **(A)**, a dichromatic source **(C)** and a broadband source **(E)** at the output of a Michelson interferometer. Frequency-domain spectra obtained by Fourier transformation of the interference patterns in **A**, **B**, and **C** are shown in panels **D**, **E**, and **F,** respectively. This figure is based on a similar representation in reference 1.

Mathematically, this is equivalent to multiplying the infinite interferogram by a boxcar truncation function. This function has a value of one between negative and positive values of the maximum experimental retardation and a value of zero at all the other points. As a consequence of this truncation, a series of side lobes with diminishing amplitudes at either side of the main spectral peak is obtained upon applying the FT.

The process of apodization helps remove these side lobe artifacts by multiplying the interferogram with a suitable function (apodization/windowing function) before the FT is performed. Figure 2-4 illustrates the boxcar truncation and a triangular apodization which is a commonly used apodization function in FT spectrometry.[7-10]

Zero-filling is another technique applied to the interferograms to improve the quality of the output spectral features before the FT is performed. This involves adding zeros (null data) to the tails of the original interferogram. Zero-filling helps smooth the resulting spectrum by adding interpolated data points in between the original non-zero filled data. If the interferogram is zero-filled to contain a total number of points equal to a power of two (i.e., 1024, 2048, 4096, etc.), it becomes compatible with the Fast Fourier Transform (FFT) method, a computationally efficient algorithm to obtain the spectrum.[8,11]

The signal produced from the interferometer has both amplitude and phase characteristics. While the theoretical interferogram has only cosine terms, optical components such as the beamspliter and other electronic components can introduce sine terms into the measured signal. The introduction of sine components into the interferogram causes it to have non-zero phase. This distorts the ideal interferogram symmetry about the point of zero pathlength difference (centerburst). If not corrected, these phase contributions (phase errors) can cause distortions in the shapes of spectral bands in the computed spectrum. A phase correction can be applied to correct for this source of error, thereby making the interferogram symmetric on each side of the centerburst. Several correction methods are available and can be applied directly to the

interferogram to restore its symmetry. Alternately, the FT can be applied to the original measured interferogram and the sine and cosine amplitudes obtained from the FT can be manipulated to apply a spectral correction. The latter approach, termed the Mertz method, was used in the work reported here.[8-10]

There are several acquisition modes available for sampling the interferograms. In a single-sided forward acquisition, data are acquired during the forward movement of the mirror and the retardation range only includes a small section before the centerburst. In a double-sided forward acquisition, data are acquired during the forward movement of the mirror but the retardation range scanned is symmetric about the centerburst. In a forward-backward acquisition, data are acquired during both forward and backward movements of the mirror, thereby resulting in a higher rate of interferogram acquisition (i.e., there is no wait for the mirror to return to the starting position). Both single-sided and double-sided interferograms can be collected in the forward-backward scanning mode. The forward-backward scan mode requires separate applications of the FT to the forward-scanned and backward-scanned interferograms because they are 180° out of phase.[11] This increased computational overhead is rarely significant, however.

The sampling rate of the interferogram (i.e., the rate at which the IR detector is sampled during the scan), determines the spectral range that can be analyzed. Sampling of the interferogram is usually done according to the Nyquist sampling theorem. According to this theorem, a continuous wave can only be sampled correctly when the sampling rate is equal to or higher than twice the maximum spectral frequency.[3]

In the FT spectrometer, a red helium-neon (He-Ne) laser (632.8 nm, ~15,800 cm^{-1}) is directed through the interferometer and onto a photodiode detector. This detector signal serves as a clock for use by the electronics that sample the IR detector. If the IR detector is sampled at a rate of two points per cycle of the He-Ne reference interferogram, the Nyquist criterion is met and the maximum spectral frequency is 15,800 cm^{-1}.

For the research work described in Chapters 4 through 8, a Blackmann-Harris three term apodization function was used with two levels of zero-filling. Mertz phase correction was used to correct for the occurrence of phase errors. A forward-backward data acquisition mode was employed and double-sided interferograms were obtained. Interferograms were sampled at a rate of twice per cycle of the He-Ne reference laser, resulting in a maximum spectral frequency of 15,800 cm^{-1}.

2.5.3 Instrument setup

Fourier transform spectrometers are typically designed as single-beam instruments. A single optical path is present from the light source through the interferometer and onto the detector. The sample is typically placed between the interferometer and detector. Figure 2-5 is a schematic representation of a single-beam FTIR spectrometer. This figure illustrates the typical positioning of the IR source, interferometer, detector, sample compartment, reference laser and other optical components.

2.5.4. Advantages of Fourier transform spectrometry

Fourier transform spectrometry differs from conventional single-channel scanning dispersive spectroscopy in that all of the resolution elements (frequencies/wavelength/wavenumbers) are measured simultaneously, thus reducing the time required to obtain a spectrum at any chosen S/N ratio. Such a measurement is known as a multiplex measurement. This decrease in data acquisition time is often used to enhance the S/N ratio by signal averaging. According to Eq. 2-9, the S/N ratio improves by a factor of $n^{½}$ after averaging n replicate spectra. This inherent advantage of FTIR spectrometry is known as multiplex advantage or Fellgett advantage.[1,3]

$$\left(\frac{S}{N}\right)_n = \sqrt{n}\left(\frac{S}{N}\right)_i \qquad (2\text{-}9)$$

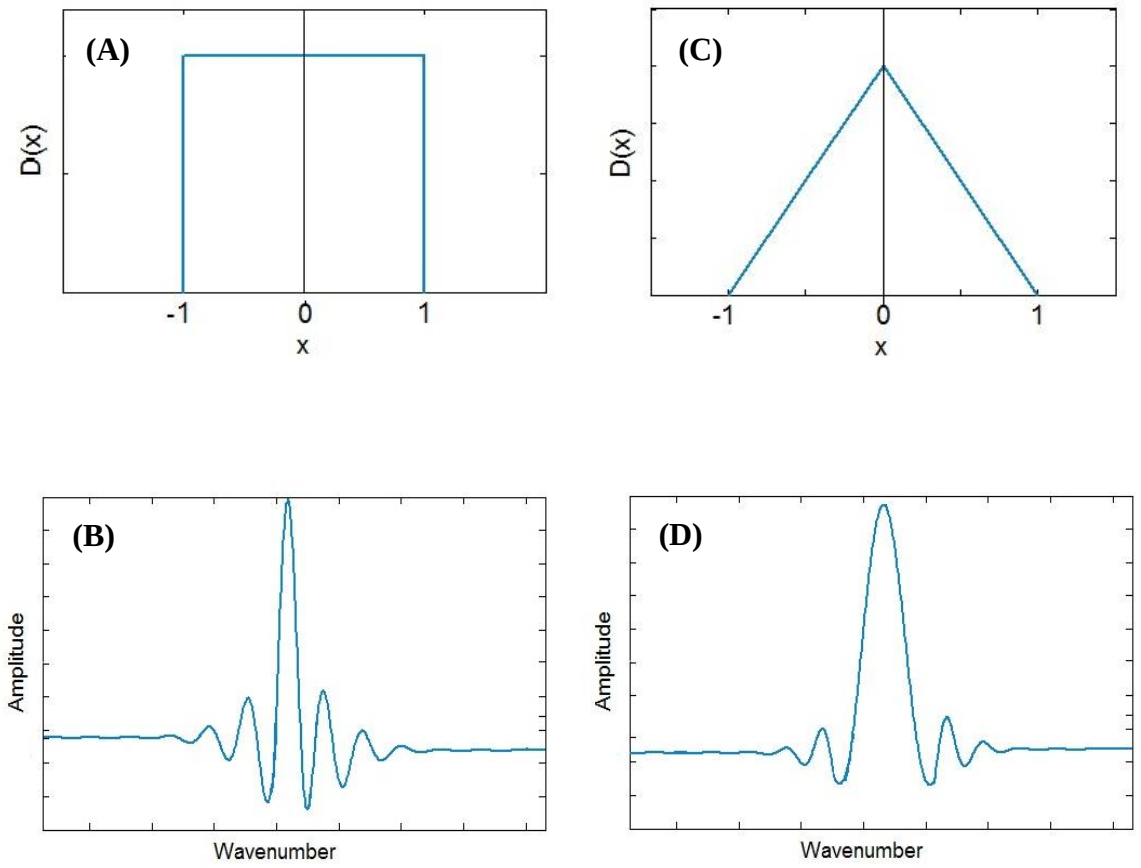

Figure 2-4. Preprocessing of the interferogram.
(A) Boxcar truncation function and the **(B)** resultant spectral features. **(C)** Triangular apodization and the **(D)** resultant spectral features. It can be observed that the side-lobe artifacts from boxcar truncation are reduced after the triangular apodization is applied but the peak is slightly broader. This figure is based on a similar representation in reference 11.

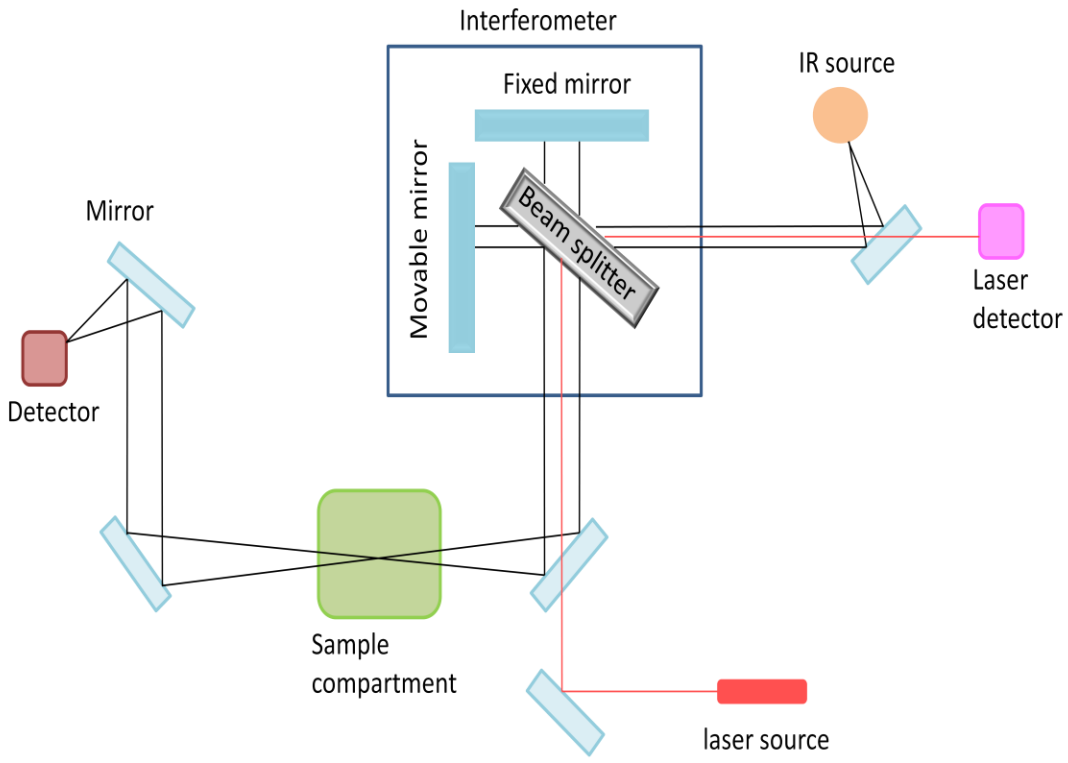

Figure 2-5. Schematic representation of a single-beam FTIR spectrometer. This figure is based on a similar representation in reference 1.

In contrast to conventional dispersive spectroscopy, FTIR spectrometry does not require slits or diffraction gratings that have the undesirable characteristic of attenuating the radiation beam. This result in higher light throughput, hence giving higher signals through strongly absorbing samples. This leads to improved S/N ratios for the case in which the dominant noise source is the intrinsic noise of the detector. This is the typical case in IR measurements. This throughput consideration is known as Jacquinot's advantage.[1,3]

By using the He-Ne laser to control the sampling of the interferogram, the scanned interferograms are sampled with high precision with respect to retardation. This leads to high resolution, high accuracy and reproducibility in frequency determinations.[1,3] High wavenumber reproducibility in the resulting spectra facilitates the use of numerical techniques for spectral processing.

2.6 Fourier transform infrared microscopy

Fourier transform IR microscopy is a technique that combines FTIR spectrometry with microscopic analysis in order to obtain chemical information from samples which are very small (physical dimensions in the range of 10 to 500 μm). Fourier transform IR microscopes were first manufactured in the 1980's and thus the method is fairly new. The technique has found successful applications in clinical chemistry, polymer, textile and electronics industries. A schematic representation of generalized FTIR microscope is illustrated in Figure 2-6. The IR beam from a Michelson interferometer is focused onto a sample mounted on the microscope stage using a reflective Cassegrain condenser. The light transmitted is then collected by a Cassegrain objective and focuses onto either a single-channel or multichannel detector.[1,4,12,13]

2.6.1 Focal plane array detector

Both single-channel and multichannel detectors can be used with IR microscopes. A single-channel detector records the IR intensity for a single location on the sample, while a multichannel detector consists of an array of individual detector elements that can

simultaneously (i.e., at the speed of the sampling electronics) record separate intensities across a grid of locations on the sample. Use of a multichannel detector eliminates the need for translating the sample to acquire an image.[4,12,13]

Multichannel detectors used in IR microspectroscopy are termed focal plane array (FPA) detectors because the two-dimensional detector array is positioned in the focal plane of the microscope.[4,12,13] For the work reported in Chapter 8, an FPA detector was used consisting of 128×128 liquid nitrogen cooled mercury cadmium telluride (MCT) elements. A schematic representation of imaging data collected using an FPA detector is illustrated in Figure 2-7.

Two modes of data acquisition can be used when FPA detectors are coupled to FTIR spectrometers. In step-scan mode, the moving mirror of the interferometer is moved in discrete increments, followed by interrogation of each element of the FPA. After the detector is read, the mirror moves to the next step. In this way, the set of interferograms encompassing the array is assembled point-by-point. In rapid-scan mode, the sampling electronics and computer are fast enough to interrogate the FPA in real-time as the moving mirror operates in a normal manner. In this work, rapid-scan data acquisition was employed.[4,12,13]

Infrared microscopes can operate in both transmittance and reflectance modes depending on the nature of the sample. A visible light beam and associated imaging detector is also used to visually locate the sample to be studied with the IR beam.[4,12] Research work described in Chapter 8 employed a Hyperion 3000 FTIR microscope (Bruker Optics, Inc) interfaced to a Bruker Vertex 70 FTIR spectrometer. For the mid-IR experiments described in Chapter 8, the spectrometer was equipped with a Globar source and potassium bromide (KBr) beamsplitter.

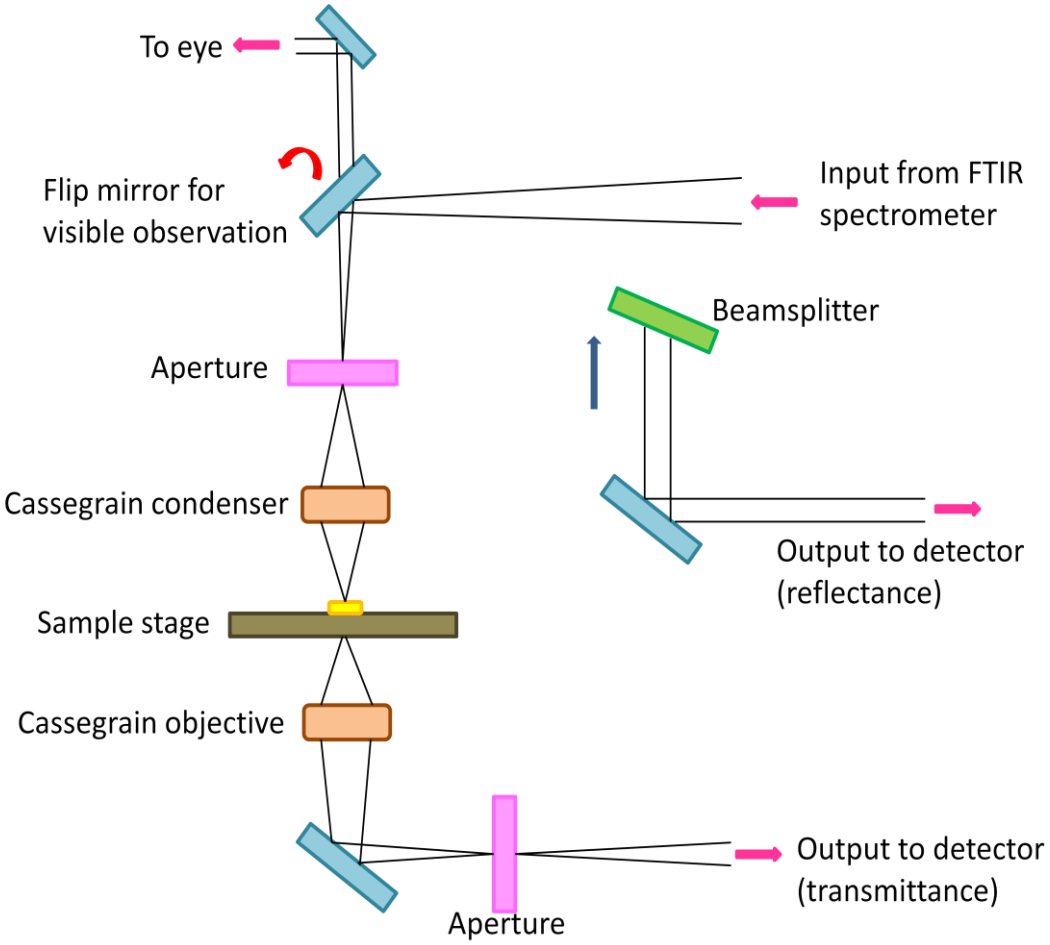

Figure 2-6. Schematic representation of an FTIR microscope. This figure is based on a similar representation in reference 4.

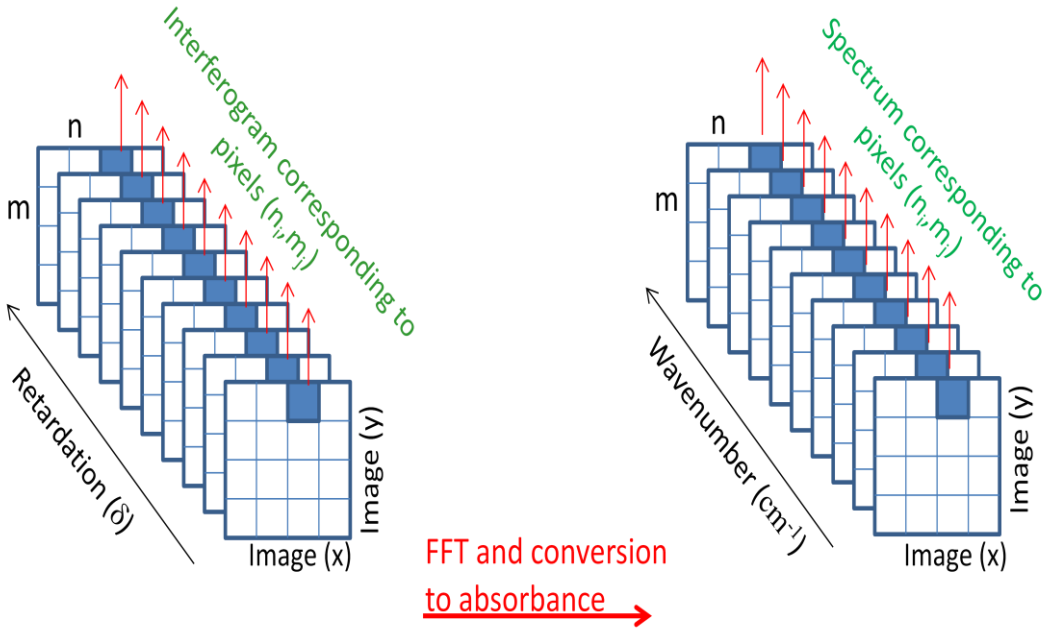

Figure 2-7. Imaging data collected from a FTIR microscope using an FPA detector. This figure is based on a similar representation in reference 4.

CHAPTER 3
DATA ANALYSIS STRATEGIES

3.1 Introduction

In the early 1970's, some analytical chemistry researchers who were using mathematical and statistical methods to analyze and interpret their data gave rise to a new discipline which came to be called chemometrics. The term, chemometrics, was first introduced in 1972 by Svante Wold and Bruce R. Kowalski. Since then, chemometrics has been developing and it is now widely applied to different fields of chemistry, especially analytical chemistry.[14,15] Establishment of The International Chemometrics Society in 1974 and the other devoted organizations and journals further supported the growth of chemometrics to its own discipline.[3,14]

Chemometrics is defined as the chemical discipline that uses mathematical and statistical methods (1) to design or select optimal measurement procedures and experiments and (2) to provide maximum chemical information by analyzing chemical data.[14] Recent advancements in electronics, optical devices, computers and automated chemical systems have led to an explosion of chemical data. In such a situation, the need to acquire meaningful and chemically relevant information from these measured data has demanded the use of chemometric methods.[14-17,26]

Although the origin of chemometrics is in chemistry, it has roots in statistics, applied mathematics and computer science. The major application of chemometrics is in analytical chemistry but it has also found applications in theoretical and physical chemistries, organic chemistry, environmental chemistry, biology, biochemistry and industrial chemistries such as pharmaceutics, food and agriculture.[17] Chemometric methods for evaluating chemical data are versatile. They are employed in experimental design, signal preprocessing, image processing, pattern recognition, calibration model

building, and model optimization.[14] In this chapter, the chemometric methods employed in the research described in this dissertation will be introduced.

3.2 Signal preprocessing methods

The presence of uninformative variances (source intensity drifts, misalignments in optics, temperature fluctuations and other random noise) in measured data can hinder the interpretation of the data and can reduce the performance of quantitative models that are commonly used to relate measured signals to desired properties such an concentration.[3,18]

This issue is especially problematic for the case of weak signals. In the analysis of near-infrared (NIR) spectra, the presence of noise or other data artifacts is of concern as NIR spectra usually contain weak and highly overlapped spectral features. These artifacts can complicate data interpretation, thereby reducing the performance of quantitative calibration models that relate spectral intensities to desired measurement properties (concentration, etc.).

One solution to this problem is to preprocess the raw spectra mathematically to remove undesirable artifacts without altering the informative variances.[3] Signal preprocessing methods can be of several different types. For example, normalization methods or scale corrections help correct for multiplicative and additive drifts. Derivative methods help correct for slow changes such as baseline drifts. Digital filtering and wavelets can model the spectra using basis functions to separate noise/drifts from useful signals. In the sections below, the preprocessing methods used in this research will be described.

3.2.1 Standard normal variate transform

The standard normal variate (SNV) transform is a scaling method which corrects for multiplicative and additive signal drift.[18] This is also known as autoscaling. In an NIR measurement application, each measured spectrum is corrected for additive and multiplicative drift effects by subtracting the mean intensity of the spectrum from each point and then dividing each point by the standard deviation (Eq. 3-1). After applying the

SNV transform, the mean spectral intensity is zero and the standard deviation of the spectral intensities is 1.0. According to Eq. 3-1, $r_{snv,i}$ is the corrected spectral intensity at point *i*, the values of r_i are the intensities in the raw spectrum,, r_{mean} is the mean intensity across the spectrum, and *p* is the number of points in the spectrum. Figure 3-1 illustrates the use of the SNV transform on a data set of NIR spectra.

$$r_{snv,i} = \frac{r_i - r_{mean}}{\sqrt{\frac{\sum_{i=1}^{p}(r_i - r_{mean})^2}{p-1}}} \quad (3\text{-}1)$$

3.2.2 Discrete wavelet transform.[15,20-22]

The wavelet transform (WT) is a fairly new mathematical technique that has been widely used in engineering sciences owing to its localization properties in both the frequency and time domains. The term, wavelet, was first used by Alfred Haar in 1909. Since then wavelets have been developed successfully and found useful applications in many scientific fields such as engineering, medicine, forensic studies, oceanography and earth studies. The WT was first introduced to chemistry in the 1990's and since then it has been widely used in many chemical applications. A wavelet is a waveform of effectively limited duration that has an average value of zero. This is different from the infinite sine waves used in Fourier analysis. Wavelet functions are found in groups called wavelet families. Some examples of wavelet families are Haar, Daubechies, Biothogonal, Meyer, Mexican Hat and Symlet. Within the family, a specific wavelet is defined by its order. For example, Daubechies-5 specifies a fifth-order wavelet from the Daubechies family. Figure 3-2 illustrates selected wavelet functions from commonly used wavelet families.

The WT can be considered a signal modeling or signal decomposition method in which an input signal (e.g., an NIR spectrum) is modeled or decomposed in terms of a set of selected wavelet functions. Just as the Fourier transform models an input signal as a

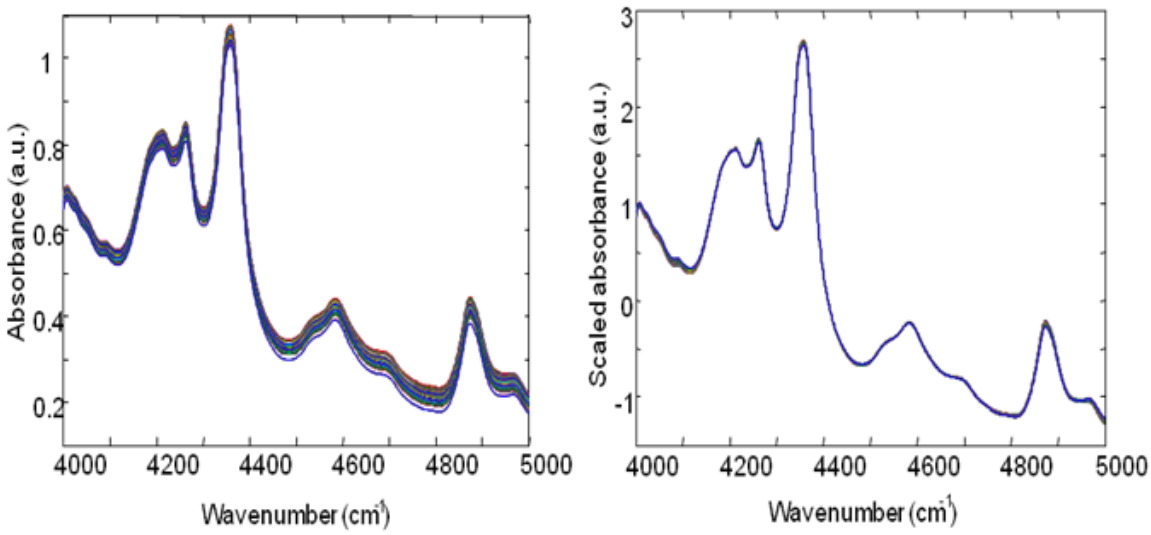

Figure 3-1. Application of SNV transform to correct for additive and multiplicative variances. The two images show a group of 180 NIR spectra before (left) and after (right) preprocessing.

summation of infinite sine and cosine waveforms across a frequency bandwidth, the WT models the signal in terms of the summation of scaled and shifted versions of the selected wavelet function.

Wavelet transforms are mainly of two types: (1) the continuous wavelet transform (CWT) and (2) the discrete wavelet transform (DWT). As shown in Eq. 3-2, the CWT is defined as the sum over all times of the input signal, $f(t)$, multiplied by scaled and shifted versions of the wavelet function (ψ). In this formalism, all input signals are considered to be sampled with respect to time. In practice, the time axis can be considered to coincide with the sampling variable that is appropriate for the specific input data used (e.g., wavenumber or wavelength in the case of an optical spectrum).

$$c(scale, position) = \int_{-\infty}^{+\infty} f(t)\psi\,(scale, position, t)dt \qquad (3\text{–}2)$$

According to Eq. 3-2, the CWT results in many coefficients (c) which are a function of the scale and position of the wavelet. The wavelet coefficients encode information about the input signal in terms of the degree to which it projects onto the scaled and shifted wavelets. Scaling of a wavelet refers to the stretching/compression of the function by a known scaling factor. Scaling is thus related to the signal frequencies that can be represented by the wavelet. For example, a low scaling factor results in a compressed wavelet that can represent high frequencies in the signal, whereas a high scaling factor results in a stretched wavelet that can represent the low frequencies. Shifting of a wavelet refers to the delaying of its onset. By simultaneously shifting and scaling the wavelet function, it is able to model both the frequency content of the signal and the location of that frequency content within the time axis of the signal. Wavelets thus do not require the assumption that all frequencies are present at all times. This provides an added flexibility in modeling the frequency content of a signal. Figure 3-3 illustrates two wavelet functions from the Daubechies family with their scaling factors.

The DWT is conceptually similar to the CWT but is typically more useful in practice because it employs a discrete number of scales and positions. In this technique, scales and positions that are factors of two are chosen to perform the analysis rather than using all possible scales and positions. This results in a more manageable number of wavelet coefficients and requires less computational time.

3.2.3 Wavelet decomposition and reconstruction

The DWT uses a finite function (wavelet function) to decompose an input signal into hierarchical sets of wavelet coefficients termed approximations and details. Approximations encode the high-scale, low-frequency components of the signal whereas details are the low-scale, high-frequency components. The decomposition process is iterative so that the original signal can be broken down into many lower-resolution components. This is known as the wavelet decomposition tree (Figures 3-4 and 3-5). At each level of decomposition, the approximations from the previous decomposition step are submitted to the DWT to obtain a new set of approximations and details. The DWT can also be operated as an inverse transform (IDWT), with the sets of approximations and details being used to reconstruct the original signal.

Depending on the level of decomposition, the coefficients of the approximations and details have different frequency and time resolution information than the original signal. In many practical applications, only certain of the approximations and details contain useful information, while others may be dominated by noise or other data artifacts. The input signal can be reconstructed using only a selected subset of the approximations and details in order to remove undesired components such as noise, background variations, etc. This operation is analogous to a digital filtering application in which the frequency content of an input signal is altered. By optimizing the family and order of the wavelet function along with the level of decomposition and which approximations and details are used in the reconstruction, selected features of the input

signal can be extracted. The resulting reconstructed signal can then be used in a further data analysis step.

In the work described in Chapters 4 to 7, the DWT was employed as a preprocessing tool to remove noise and background variance from NIR spectra before using them to build quantitative models. The DWT was applied to the full spectral range of 4000 to 5000 cm^{-1} in order to maximize the "time" axis available to the transform, In this work, the Daubechies and Symlet wavelet families were employed, and an optimization procedure was used to identify the best function orders, level of decomposition, and which approximations and details to use in reconstructing the spectra.

The optimization of wavelet order, level of decomposition and levels of reconstruction was performed with a grid search. In a typical gird search protocol, a grid space (or a hyperparameter space) is created with pre-specified subsets of key variables needing to be optimized. The grid search is then guided with a performance metric (e.g., the standard error of prediction for a quantitative model) until the optimal combination of the key variables is obtained.

As an example, a typical grid search protocol used in the optimization included scanning the wavelet order from 2 to 10 for a given wavelet family and the decomposition level from 1 to 10. For each wavelet order and decomposition level investigated, the best hierarchical combination of details (2/ 2,3/ 2,3,4/ or 3/ 3,4/ 3,4,5/ etc.) was investigated along with whether or not to include the last level of approximation. The output of the grid search was then combined with a second grid search to optimize the spectral range and number of terms used in constructing the quantitative model. The specific optimization protocols used in each application will be described in the results chapters to follow.

In Chapters 4 and 5, the development of models for determining sample temperatures directly from NIR spectra required information about the aqueous background of the samples. In this work, the last level of approximation which carries the

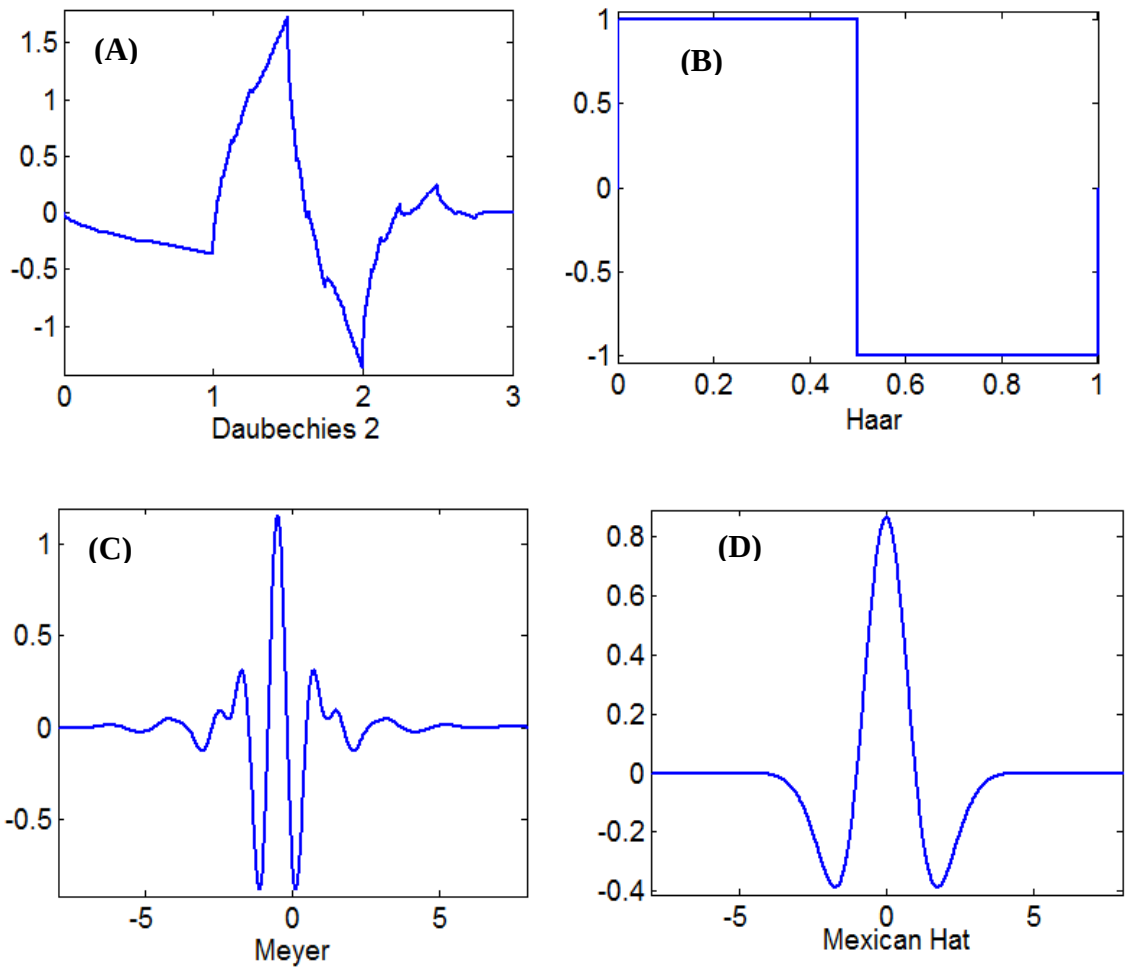

Figure 3-2. Shapes of selected wavelet functions from selected wavelet families. **(A)** Daubechies, **(B)** Haar, **(C)** Meyer and **(D)** Mexican Hat.

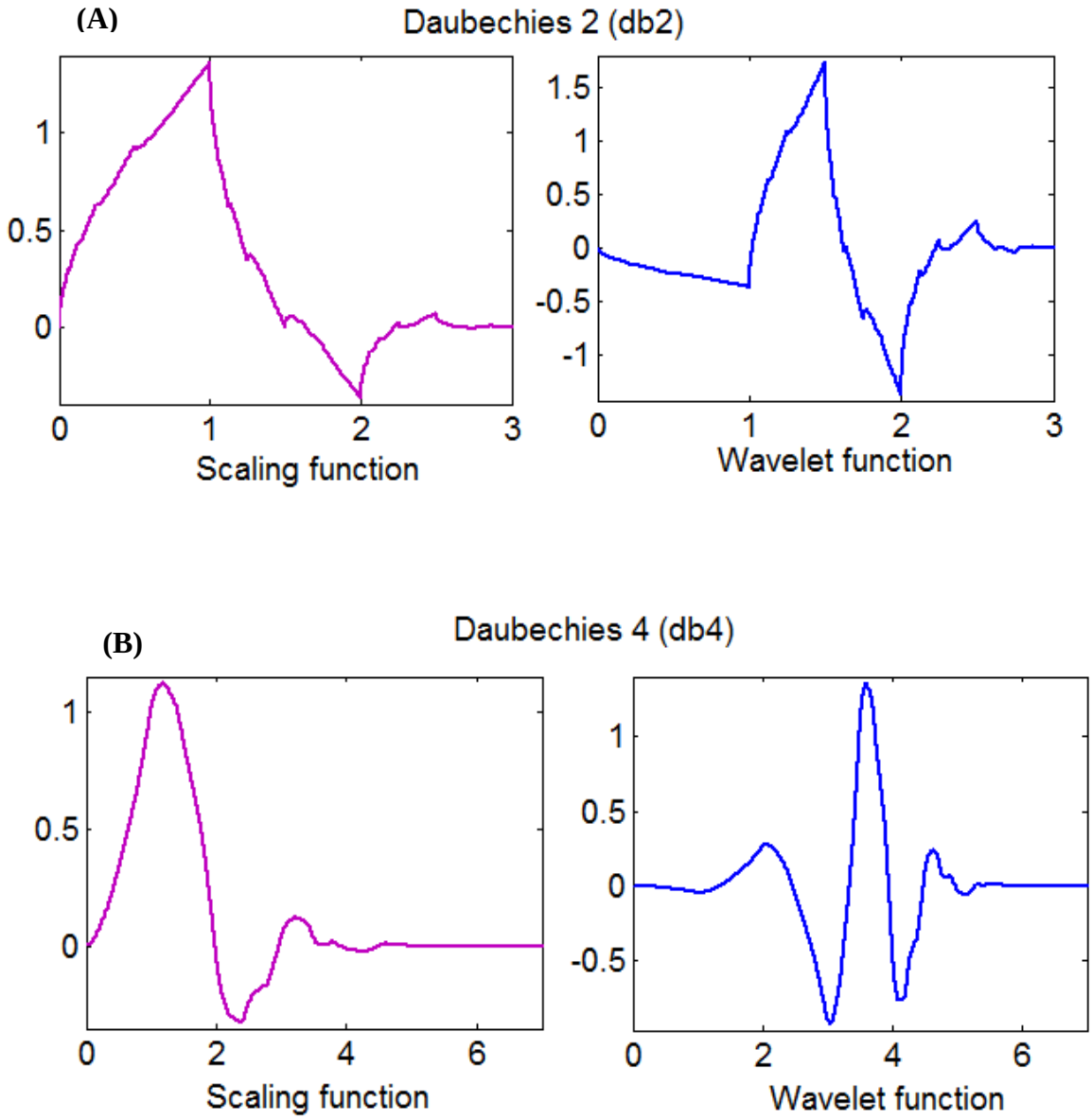

Figure 3-3. Shapes of two wavelet functions in Daubechies family with their respective scaling functions. **(A)** Daubechies 2 and **(B)** Daubechies 4.

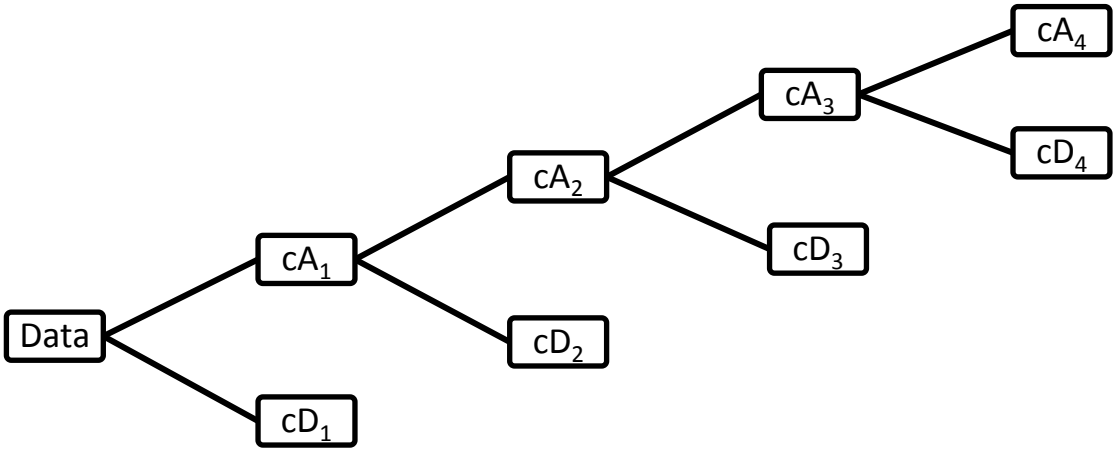

Figure 3-4. Wavelet decomposition tree representing the hierarchical decomposition of an input signal using a given wavelet function. In the schematic, cA_n represents the coefficients of approximations at each decomposition level, while cD_n represents the coefficients of details at each decomposition level.

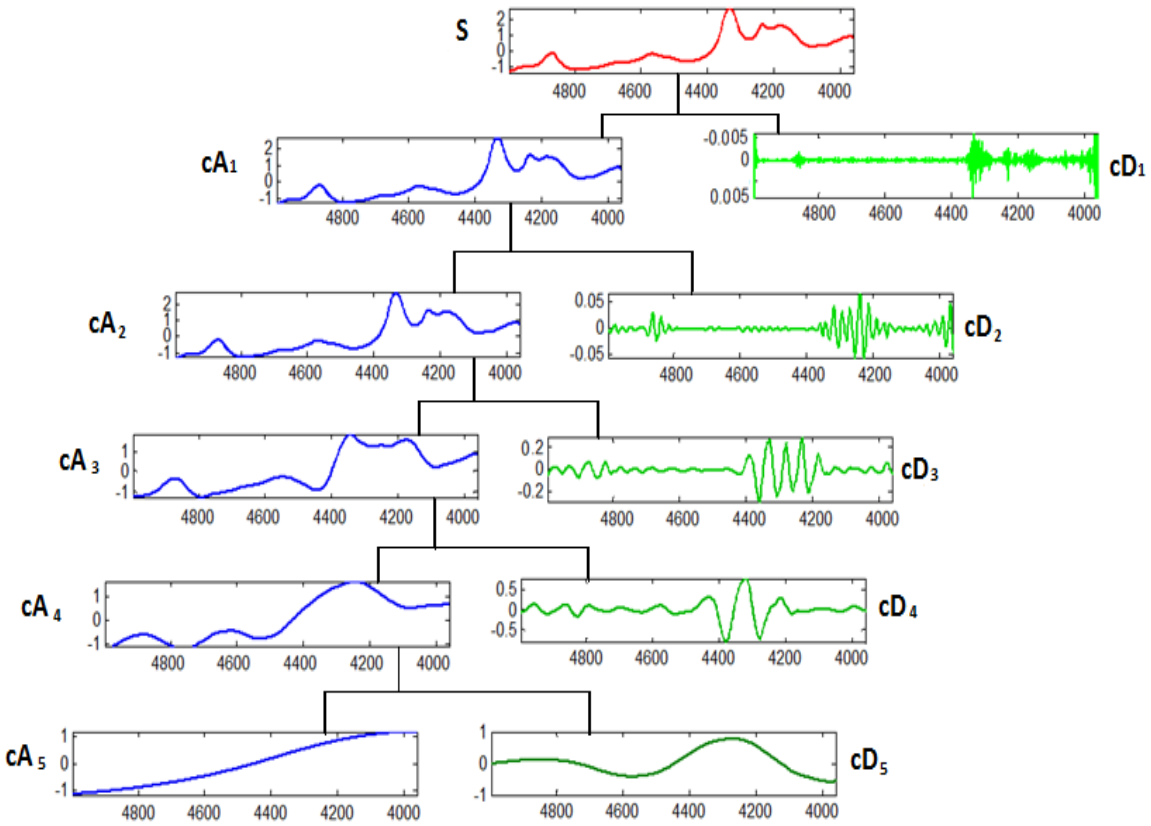

Figure 3-5. Hierarchical decomposition of an NIR absorbance spectrum using the Daubechies-6 (db6) function with five levels of decomposition. In the figure, *s* represents the original spectrum, cA_n represents the coefficients of approximations at each decomposition level, and cD_n represents the coefficients of details at each decomposition level.

lowest frequency information was always included. When quantitative models were built for analyte concentration, however, the last approximation was never found useful because information about the background was not needed (i.e., it was useful to suppress this information). In both applications, the first level of details was never found useful in reconstructing the signal due to the fact that it carries the highest frequency information which is often dominated by noise. These results underscore the need to optimize the wavelet parameters rather than to make *a priori* selections.

3.3 Multiple linear regression models.[3,14,17,19,27]

Multiple linear regression (MLR) is a widely used technique in chemometrics to construct calibration models. The goal of these regression models is to obtain quantitative information regarding analytes of interest in a given sample. The simplest form of a calibration model is a univariate model in which only a single measurement (e.g., spectral intensity at a given wavelength) is used to predict a single variable such as the concentration of an analyte. In more complex situations, multiple measurements (e.g., spectral intensities at multiple wavelengths) are needed to construct an effective model. Multiple linear regression models are typically required in NIR spectroscopy due to the overlapped nature of spectral features found in NIR spectra.[25,28]

Construction of a calibration model depends on the specification of independent (x) and dependent (y) variables for the model. The independent variables are classically defined as those that contain the lowest measurement error and traditionally these were the concentration measurements rather than the instrumental responses. However, this approach becomes problematic as samples become complex and the concentrations of all the sample components that contribute to the measured response cannot be known. In this case, an inverse regression method is used in which the instrumental responses are chosen to be the independent variables and models are sought that explain the variance in measured analyte concentrations across a set of calibration samples.

For an inverse regression model based on a spectral measurement at a single wavelength or wavenumber, the analyte concentration (c) of a given sample can be modeled using a suitable mathematical relationship specified by the instrumental response (x). For sample i, Eq. 3-3 describes the relationship between c and x using a linear offset term (b_o) and a slope term (b_1). The residual about the fit is described by the term, e.

$$c_i = b_1 x_i + e_i \tag{3-3}$$

This relationship can be extended to a multivariate model by using multiple measurements (e.g., instrumental responses obtained at several wavelengths). In such a case, Eq. 3-4 describe the same relationship between c and x as before but now using multiple terms to express the relationship between c and the x values obtained at different wavelengths.

$$c_i = b_1 x_{1,i} + b_2 x_{2,i} + \cdots + b_p x_{p,i} + e_i \tag{3-4}$$

Equation 3-4 describes the relationship between c and x using regression coefficients b_o, b_1, b_2 … b_p which correspond to the instrumental responses (x_1, x_2, …, x_p) obtained at wavelengths 1through p. The residual about the fit is again described by the term, e.

Equation 3-4 can be expanded to h components across n samples and p wavelengths by extending the c, x, and b values to matrices. This can be represented as:

$$\mathbf{C} = \mathbf{XB} \tag{3-5}$$

According to Eq. 3-5, **C** is a ($n \times h$) matrix which contains the concentrations of h components from n samples, **X** represents the $(n \times p)$ matrix with the instrumental responses obtained at p wavelengths, and **B** is a $(p \times h)$ matrix which contains the regression coefficients that establish the relationships between the measured responses and component concentrations. Since the instrumental responses and concentrations are

known for a set of calibration samples, **B** can be estimated using a general inverse method (Eq. 3-6). This is the standard linear regression (least-squares) solution.

$$\mathbf{B} = (\mathbf{X^T X})^{-1}\mathbf{X^T C} \tag{3-6}$$

According to Eq. 3-6, $\mathbf{X}^T$ is the transpose of **X** and $(\mathbf{X}^T\mathbf{X})^{-1}\mathbf{X}^T$ is known as the pseudo-inverse of **X**.

Once **B** has been estimated by use of a set of calibration samples, the model can be applied to obtain concentrations for samples with unknown concentrations by use of Eq. 3-7.

$$\hat{\mathbf{C}} = \mathbf{X_{unk}B} \tag{3-7}$$

In Eq. 3-7, $\hat{\mathbf{C}}$ is the matrix of predicted concentrations and $\mathbf{X}_{unk}$ is the matrix of measured responses for the samples with unknown concentrations. The quality of the regression fit (in units of concentration) for a given analyte (i.e., column of **C**) can be characterized by a standard error of calibration (SEC) calculation for (*n*-*p*-1) degrees of freedom (Eq. 3-8). The values of c_i and $\hat{c}_i$ correspond to the reference and predicted concentrations, respectively. The value of SEC reports a standard error in predicted concentrations for the samples used to build the MLR model.

$$SEC = \sqrt{\frac{\sum_{i=1}^{n}(c_i - \hat{c}_i)^2}{n-p-1}} \tag{3-8}$$

There are two main issues encountered when implementing MLR models with data such as NIR spectra. The first issue is that when developing an MLR model, the American Society for Testing and Materials (ASTM) recommends a minimum *n/p* (number of calibration samples/number of wavelengths) ratio of 6 in order to minimize the possibility of obtaining chance correlations between **X** and **C**.[14,17] If the required

number of wavelengths is large, this may require a prohibitively large number of calibration samples. To address this issue, a large body of work exists in the literature related to wavelength selection methods in which a pool of *p* wavelengths is searched to obtain smaller subsets that can form effective MLR models.[3,14,17] One straightforward approach is to use a stepwise MLR calculation[1,4,3] to screen a large pool of wavelengths to select potentially informative ones.

The second issue in the direct application of MLR to build inverse regression models with spectroscopic data is that $\mathbf{X}^T\mathbf{X}$ must be well-conditioned to matrix inversion. This means the columns of $\mathbf{X}^T\mathbf{X}$ must be linearly independent or nearly so in order to obtain an accurate inversion and thus an accurately computed set of regression coefficients (Eq. 3-6).

Linear dependencies (co-linearity) in the measured responses are commonly observed with spectroscopic or other instrumental data sampled continuously with time, wavelength, etc. For example, if *p* wavelengths are sampled across a spectral band, the intensities corresponding to those wavelengths will have linear dependencies because they all describe aspects of the same band. Stated differently, across a set of measured spectra, the intensity at spectral point *j* will be related to the intensity at point *j*+1. Use of both points *j* and *j*+1 in computing the MLR model can lead to poor conditioning in $\mathbf{X}^T\mathbf{X}$, poorly determined regression coefficients, and ultimately to poor prediction accuracy when the model is applied to samples with unknown concentrations.

A good solution to both of these issues is the latent variable method. The concept of this approach is to compute a new set of independent variables based on linear combinations of the original variables. The new variables are called latent variables and they can be computed using the instrumental response matrix of the calibration samples ($\mathbf{X}$). By projecting the instrumental response vector for sample *i*, $\mathbf{x}_i$, (i.e., the (1×*p*) vector of *p* measured responses for the sample), onto latent variable *j*, $\mathbf{s}_j$ (1×*p*), a scalar

score value, $t_{i,j}$, can be calculated. This is illustrated in Eq. 3-9 for response $\mathbf{x}_1$ and latent variable $\mathbf{s}_1$.

$$t_{i,1} = \frac{\mathbf{x_1}.\mathbf{s_1}}{\|\mathbf{s_1}\|} \tag{3-9}$$

If the latent variable is considered to be a representation of one of the underlying components that add together to generate the response, the score for spectrum *i* along latent variable *j* represents the amount of component *j* contained in the spectrum. In practice, this representation of the contributing component can be completely abstract rather than representing, for example, the pure-component response of a chemical constituent.

By extending Eq. 3-9 to the **X** matrix, a score matrix, **T** (*n*×*l*), and a matrix of *l* latent variables, **S** (*l*×*p*) can be obtained (Eq. 3-10).

$$\mathbf{T} = \mathbf{X}\mathbf{S}^{\mathbf{T}} \tag{3-10}$$

In Eq. 3-10, **T** is the (*n*×*l*) matrix which contains the scores in the columns, **X** is the (*n*×*p*) matrix of instrumental responses, and **S** is the (*l*×*p*) matrix whose rows contain the new spectral components (latent variables) computed from **X**.

A calibration model can then be built with the scores as shown in Eq. 3-11.

$$c_i = b_1 t_{i,1} + b_2 t_{i,2} + \cdots + b_l t_{i,l} + e_i \tag{3-11}$$

Equation 3-11 is similar to Eq. 3-4 with the only difference being the replacement of the original response values by the newly computed scores. Calculation of the regression coefficients is performed by use of Eq. 3-6, with **T** substituting for **X**.

The expectation is that *l* in Eq. 3-11 will be less than *p* in Eq. 3-4, thus reducing the number of calibration samples required (i.e., to meet the criterion of $n/l \geq 6$).

Furthermore, we expect that $\mathbf{T}^T\mathbf{T}$ will be better conditioned to inversion than $\mathbf{X}^T\mathbf{X}$, thus leading to more precisely defined regression coefficients.

The previous discussion outlines a basic framework for building inverse MLR models with latent variables. The key remaining consideration is how to construct the latent variables such that they will be maximally useful in modeling the variance in **C**. There are a variety of strategies and variants of those strategies that can be employed. In the research described in this dissertation, two such methods were used: (1) principal component analysis (PCA) and (2) partial least-squares (PLS). The PCA method computes **S** and **T** solely from **X**, while the PLS method uses **X** and **C** to derive **S**, **T** and a matrix **W** that links **X** and **C**. In both approaches, once **T** has been computed, Eq. 3-6 (**T** substituting for **X**) is used to compute the inverse MLR model. The PCA and PLS methods will be described separately in the next two sections.

3.3.1 Principal component regression.[3,14,17,19]

Principal component regression (PCR) is a widely used multivariate technique to develop calibration models in chemometrics. The term, PCR, refers to the combination of PCA and MLR. As shown in Eq. 3-12, the PCA step decomposes the matrix of instrumental responses (e.g., spectra) into the previously defined matrices, **S** and **T**. The rows of **S** are called the principal components of **X**. They are also termed spectral loadings or simply loadings. The loadings represent the underlying components that encode the "useful" information in **X**. The ($n \times p$) matrix of spectral residuals, **E**, contains the remaining information in **X** that is not modeled by the l principal components in **S**. If $l = p$, **E** will be a matrix of zeros (i.e., **X** will be completely described by **TS**).

$$\mathbf{X} = \mathbf{TS} + \mathbf{E} \tag{3-12}$$

The columns of **S** obtained from PCA are termed "principal" components because they are computed to maximize the information (data variance) explained in **X**. The

"first" principal component (PC) explains the greatest amount of variance in **X**, the "second" PC explains the next greatest amount of variance, etc. Explaining variance in **X** does not guarantee that **S** encodes the information most useful in modeling **C**, but in order to explain a large amount of variance, the loading must express information that is represented throughout **X** (i.e., across the *n* responses). Because noise is often random (uncorrelated), there is a natural separation of signal and noise in the columns of **S**. Those loadings that account for a large amount of data variance necessarily have been biased toward the extraction of signal features rather than noise.

Numerically, the matrix decomposition represented in Eq. 3-12 is most often accomplished by a method known as singular value decomposition (SVD).[23] The SVD can be described as a method for transforming correlated variables into a set of uncorrelated ones that more efficiently represent the various relationships found in the original input data. Stated differently, unlike **X**, **S** and **T** have orthogonal columns that are uncorrelated (i.e., contain no co-linearity).

While the output rows of **S** are normal vectors, the vector magnitudes before normalization (termed the singular values) can be related to the amount of variance in **X** explained by each loading. The singular values determine the ordering of the loadings into first, second, third PCs, etc.

Assuming that **X** contains some co-linearity, if one considers that the columns of **T** are orthogonal, it follows that one column of **T** will typically account for more data variance than any one column of **X**. Considered in this way, the SVD can be seen as a method for data reduction (i.e., *l* columns of **T** will typically carry much more information than any *l* columns of **X**).[23] This helps achieve an important goal of PCR which is the reduction of the dimensionality of the data.

The calibration data in **X** serves as the input to the SVD, and the resulting **T** matrix is used together with **C** to compute the calibration model by MLR. A key consideration in constructing the calibration model is how many or which scores to

include. For a given number of calibration responses (n), the ASTM guidelines dictate a maximum number of terms to include in the model. Whether this maximum is required or determining which terms out of a pool of l scores to use is an optimization problem that typically must be solved empirically. Because the spectral loadings are mathematical constructs, visual interpretation of them to determine their utility is very difficult.

To predict the concentrations corresponding to the spectra of unknown samples, $\mathbf{X}_{unk}$, the corresponding matrix of measured responses is used together with the previously computed **S** to calculate $\mathbf{T}_{unk}$ as in Eq. 3-10. The corresponding predicted concentrations are obtained in a manner analogous to Eq. 3-7, where $\mathbf{T}_{unk}$ replaces $\mathbf{X}_{unk}$.

3.3.2 Partial least-squares regression.[3,14,17,19]

In PCA, loading vectors are selected on the basis of the amount of variance explained in **X**. If the analyte is a minor component and does not account for a large amount of this variance, its information may not be extracted efficiently by PCA. In order to overcome this limitation, the PLS method is used in which the loading vectors are computed with a bias towards explaining the variance associated with the analyte.

Partial least-squares is another widely used technique to develop calibration models in chemometrics. When coupled with MLR to build an inverse regression model, PLS is termed PLS regression (PLSR). This technique was developed by Herman Wold around 1975 and its early applications were primarily found in econometrics. The first application of PLS to NIR spectra was reported by H. Martens and S.A. Jensen in 1983. Since then PLS regression has been widely employed in NIR spectroscopy.

The technique is a latent variable method similar to PCR but with one exception. In PLS regression, concentration information (i.e., the dependent variable or y-variable in Eq. 3-6) is taken into account in addition to the spectral information in the construction of the latent variables. As described in Eqs. 3-13 and 3-14, the spectral data matrix, **X** ($n \times p$), and the concentration information, **c** ($n \times 1$), are decomposed simultaneously into three matrices termed the spectral loadings (**S** ($l \times p$)), concentration loadings (**q** ($l \times 1$)) and

scores (**T** (*n*×*l*)) in such a way that the covariance between the spectral data and concentration information is maximized. The score matrix, **T**, is common to both equations. The scores are orthogonal to each other, but in the variant of PLS employed here, the spectral loadings are not orthogonal. In terms of dimensionality, information in the matrices, **X** and **c**, is reduced to *l* components which are iteratively computed during the decomposition. The matrices, **E** (*n*×*p*) and **f** (*n*×1)**,** are the residuals after the decomposition of **X** and **c**, respectively. Here, **c** is written as a vector to denote the concentrations corresponding to a single analyte. The variant of PLS employed in the work described here uses the concentrations for a single analyte in computing the *l* latent variables (PLS factors).

$$\mathbf{X} = \mathbf{TS} + \mathbf{E} \tag{3-13}$$

$$\mathbf{c} = \mathbf{T}\boldsymbol{q} + \mathbf{f} \tag{3-14}$$

In order to compute a common set of scores between Eqs. 3-13 and 3-14, a link has to be formed between **X** and **c**. This link takes the form of a (*p*×*l*) weight matrix, **W**. Usually, **X** and **c** are mean-centered before the decomposition. Then the first weight vector ($\mathbf{w}_1$ (*p*×1)) can be computed as:

$$\mathbf{w_1} = \frac{\mathbf{X^T c}}{\|\mathbf{X^T c}\|} \tag{3-15}$$

According to Eq. 3-15, $\mathbf{X^T}$ is the transpose of the **X** matrix and $\|\mathbf{X^T c}\|$ is the vector magnitude. Dividing by the magnitude normalizes the weight vector to unit length. The elements of $\mathbf{w}_1$ encode the covariance of each spectral point (across the *n* samples) and the concentration vector. Thus, large values in $\mathbf{w}_1$ specify that the corresponding spectral point should be given a large weight in extracting information from **X**.

The first score vector, $\mathbf{t}_1$ (n×1), first spectral loading vector ($\mathbf{s}_1$ (1×p)) and first concentration loading (q_1) can be then calculated as follows:

$$\mathbf{t_1} = \mathbf{X w_1} \tag{3-16}$$

$$\mathbf{s_1} = \frac{\mathbf{t_1}^T \mathbf{X}}{\|\mathbf{t_1}^T \mathbf{t_1}\|} \tag{3-17}$$

$$\boldsymbol{q_1} = \frac{\mathbf{t_1}^T \mathbf{c}}{\|\mathbf{t_1}^T \mathbf{t_1}\|} \tag{3-18}$$

After the calculation of scores and loadings for the first latent variable, residuals can be calculated using Eqs. 3-19 and 3-20.

$$\mathbf{E_1} = \mathbf{X} - \mathbf{t_1 s_1} \tag{3-19}$$

$$\mathbf{f_1} = \mathbf{c} - \mathbf{t_1} \boldsymbol{q_1} \tag{3-20}$$

This procedure can be iterated by substituting **E** and **f** for **X** and **c,** respectively, and continuing with Eq. 3-15 to obtain $\mathbf{w}_2$, $\mathbf{t}_2$, $\mathbf{s}_2$, etc. The process continues until the desired l latent variables are computed. This produces the full **W**, **T**, and **S** matrices as defined previously. The calibration model is then constructed from the **T** matrix using MLR as described previously for the PCR technique.

As described previously with the PCR method, determination of the optimal number of latent variables to use in the model is an empirical optimization problem. Because the PLS calculation is biased toward the explanation of variance in the dependent variable, the latent variables will typically be ordered according to their significance in the regression equation relating the y-variable to the PLS scores. Thus, the scores corresponding to the first latent variable will tend to be the most significant, followed by the second, third, etc. One negative characteristic of PLS, however, is that some of the later scores may appear to be significant but in actuality are based on the

extraction of noise components from the calibration spectra that happen to correlate with the dependent variable. If such terms are included in the model, they may have unpredictable behavior when applied to data outside of the calibration set. This makes careful optimization of the number of latent variables extremely important when applying PLSR.

To apply the computed model to new responses to obtain the concentrations corresponding to unknown samples, the **W** and **S** matrices computed with the calibration data are employed along with the regression coefficients obtained from the use of Eq. 3-6. The **W** and **S** matrices are applied in an iterative calculation similar to that described previously to obtain the scores corresponding to the spectra of the unknown samples.

The matrix of measured responses of the unknowns, $\mathbf{X}_{unk}$, is first mean-centered with the mean of the calibration spectra and substituted into Eq. 3-16 along with the previously computed $\mathbf{w}_1$ to obtain the first set of scores, $\mathbf{t}_{unk,1}$. Then, $\mathbf{X}_{unk}$ replaces **X** and $\mathbf{t}_{unk,1}$ replaces $\mathbf{t}_1$ in Eq. 3-19 and the previously computed $\mathbf{s}_1$ is used to obtain the residual spectra, $\mathbf{E}_{unk,1}$. The residuals then replace $\mathbf{X}_{unk}$ in Eq. 3-16 and the second set of scores is produced. This process continues until the required number of scores for the new samples have been obtained. These are used together with the previously calculated regression coefficients (Eq. 3-11) to yield the estimated concentrations for the unknown samples.

3.4 Optimization of a calibration model

Development of a well-performing calibration model is an important application in chemometrics. In simplest terms, building a calibration model involves constructing mathematical models to explore relationships between variables (e.g., relationships between spectral intensities at a given wavelengths and the corresponding concentrations of a target analyte). As discussed above, calibration methods such as PCR and PLSR are widely used in NIR spectral analyses. Once the independent and dependent variables have been established and a suitable experimental design has been developed,

mathematical approaches such as those discussed in Section 3.3 can be applied to develop a calibration model.

As discussed previously, one of the issues in building a good calibration model with PCR and PLS is to determine the optimal number of terms (principal components, PLS factors, etc.) required by the calibration model. This value depends on the characteristics of the input data and is also sensitive to whether the full range of responses is used or a subset of those responses is employed. Improved calibrations can often be obtained by selecting a subset of the responses before submission of the data to PCA or PLS. In a spectroscopy application, this involves selecting a subset of spectral points that is most effective in modeling the dependent variable.

One solution to solving this optimization problem is to employ a grid search in which the responses that are input into PCA or PLS are varied along with the number of latent variables used in the calculation of the calibration model. Section 3.2.3 described the concept of a grid search, and the latter part of Section 3.2.3 explained the development of a grid search for optimizing the wavelet decomposition and reconstruction parameters. For the work described in Chapters 4 to 7, the output of that grid search (preprocessed spectra from 4000 to 5000 cm^{-1} using a given wavelet function, decomposition level and reconstruction) was then combined with a second grid search to optimize the wavenumber range and number of factors employed in a PLS calibration model.

For example, the grid search used in developing models for temperature in Chapter 4 included scanning the wavenumber range from 4150 to 4850 cm^{-1} in steps of 25 cm^{-1} using window sizes from 300 to 700 cm^{-1} in steps of 25 cm^{-1}. For each wavenumber range investigated, calibration models based on 1-10 latent variables (PLS factors) were computed and the corresponding errors in the predicted temperatures were obtained.

In this optimization procedure, a cross-validation method was used to optimize the number of PLS factors in the calibration model. This procedure involved leaving out a fraction of spectra (i.e., 10 % in the work described in Chapters 4-7) with their replicate measurements and generating a calibration model from the remaining spectra. The calibration model developed was then used to predict the withheld spectra. This procedure was iterated such that all observations were withheld and predicted once. The errors in predicted values were pooled to obtain a standard error (Eq. 3-21) termed the cross-validated standard error of prediction (CV-SEP).

$$CVSEP = \sqrt{\frac{\sum_{i=1}^{m}(c_i - \hat{c}_i)^2}{m}} \tag{3-21}$$

According to Eq. 3-21, *CVSEP* is the average root mean square error value in prediction across the *m* samples. In the equation, c_i denotes the reference value (e.g., concentration) for observation *i*, and $\hat{c}_i$ is the value predicted by the model.

Plotting *CV-SEP* vs. the number of latent variables is a useful graphical tool (Figure 3-6) to determine the optimal number of factors needed for the calibration model. The goal is to obtain the minimum statistically significant *CV-SEP*. An *F*-test at a defined confidence level can also be used to assess whether adding an additional term causes a reduction in *CV-SEP* that is significant. Often, the rationale is employed that adding a term with only marginal significance will not be of benefit when the model is subsequently applied to data outside of the calibration set.

3.5 Model validation.[3,14,17]

Calibration models need to be evaluated for their performance (i.e., their ability to predict the desired quantity such as analyte concentration). This can be done in many different ways. An internal prediction can be performed to evaluate the model's prediction ability. In this case, using the same data employed in building the calibration model, the prediction performance of the calibration model is determined by computing

the SEC as described previously in Eq. 3-8. A smaller value of SEC corresponds to an improved fit of the calibration data to the model

An external prediction can also be performed to evaluate the model's prediction ability. In such a case, data that were not employed in building the calibration model are used. Prediction performance is determined by the standard error of prediction (SEP) which is the root mean square error in prediction. This equation takes the same form as Eq. 3-21. A smaller value of SEP corresponds to improved model performance in prediction.

Graphical methods are also useful to evaluate the prediction performance of a calibration model. Use of correlation plots (a plot of predicted values vs. reference values) and residual plots (a plot of residuals vs. predicted values) is helpful in determining any bias or inadequacies in the calibration model. Figure 3-7 illustrates a typical correlation plot and a residual plot. A good correlation (straight line) between predicted and reference values indicates a good model. Randomly displaced small residual values also indicate a good model.

3.6 Assessing quality of the measured spectra.[24]

The usability of a set of NIR spectra in building a successful calibration model is determined by having a significantly lower noise level than the anayte signal. Therefore, a quality assessment of the collected spectra needs to be conducted prior to attempting to develop calibration models. While the sample spectra dictate the usability of spectra in the calibration model, background spectra can be used to evaluate the stability of the instrument itself with time.

To make these assessments, a root-mean-square (RMS) noise calculation was employed to evaluate the noise levels in all the spectra collected for use in the research described in Chapters 4 through 8. In this calculation, ratios were taken between consecutive single-beam spectra (replicate spectra) and the resulting transmittance values

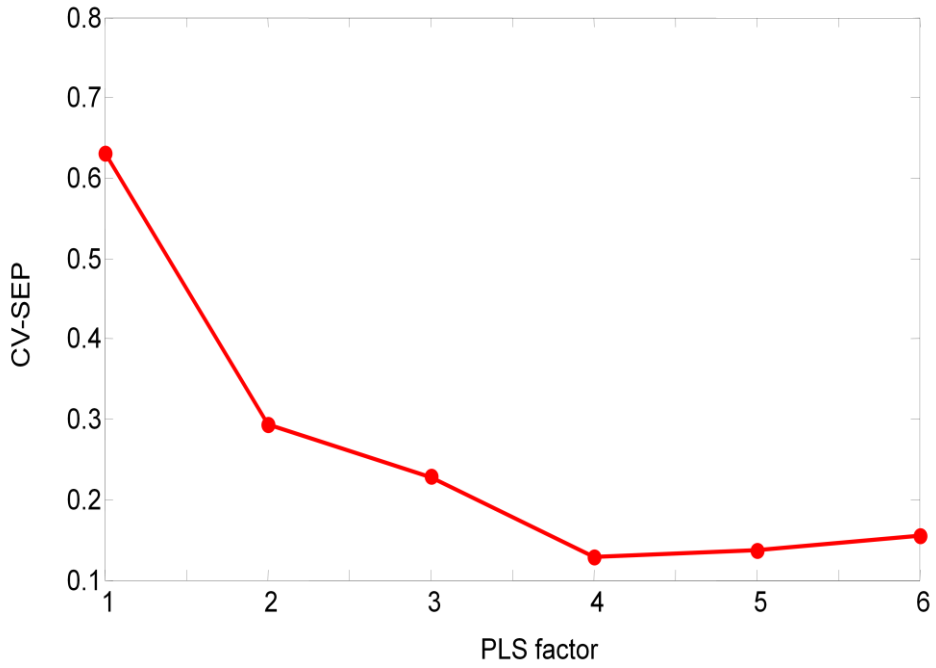

Figure 3-6. Plot of *CV-SEP* vs. the number of latent variables (PLS factors) used in the model. The lower the value of *CV-SEP*, the better the model performs. The units of *CV-SEP* will be the units of the *y*-variable in the calibration model. According to this plot, the model based on four latent variables provides the best performance. An increase in *CV-SEP* after the minimum is a common result, indicating that the added terms are causing degradation in model performance.

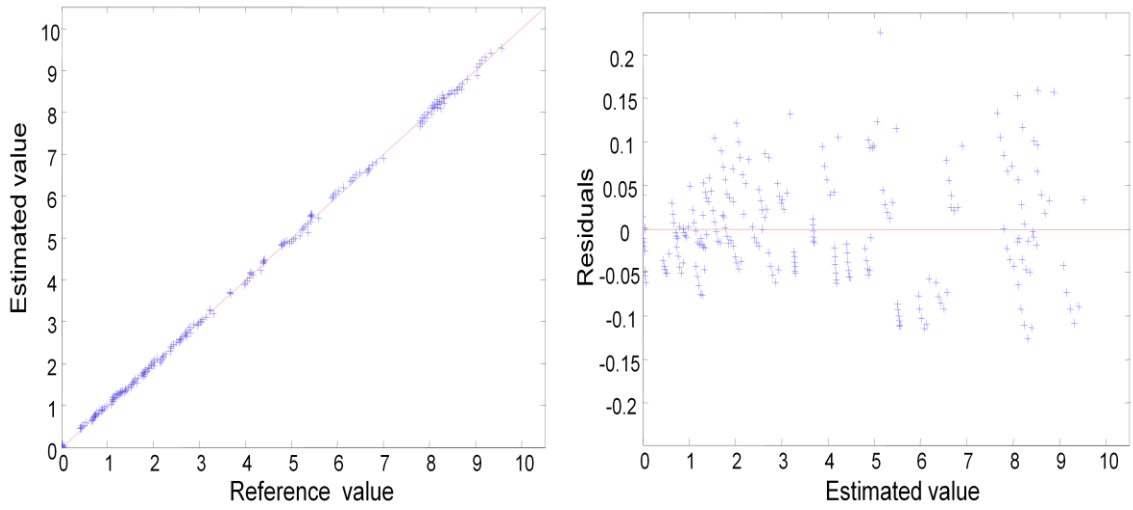

Figure 3-7. Typical correlation plot (left) and residual plot (right) indicating the performance of a calibration model. All values plotted are in the units of the *y*-variable. The red lines indicate perfect correlation in the left panel and zero residuals (i.e., perfect fits) in the right panel. The residual plot shown exhibits no apparent systematic structure. This suggests the model is adequate.

were converted to absorbance. In the absence of noise (random or systematic), the resulting noise spectrum would be a flat line at 0.0 absorbance units (AU).

There are three main sources of noise possible: (1) a simple drift in the light intensity during the spectral collection that introduces a systematic positive or negative offset in the noise spectrum; (2) a drift in temperature that causes a systematic spectral shift that results in baseline curvature in the noise spectrum when the ratio is taken between the shifted spectra; and (3) the intrinsic noise of the instrument that appears as random positive and negative deviations about 0.0 AU. The magnitude of these three noise sources can be characterized by changing the origin in the calculation of the RMS noise (e.g., calculating the RMS noise about the mean absorbance in the noise spectrum can remove the simple additive offset caused by intensity drift).

In the research described here, the random noise component was estimated to characterize the overall quality of the data. To remove systematic effects, the noise spectrum was fitted to a third-order polynomial model to correct for the possible sources of systematic noise. This calculation is shown in Eq. 3-22.

$$RMS = \sqrt{\frac{\sum_{i=1}^{p}(A_i - b_o - b_1\bar{\nu}_i - b_2\bar{\nu}_i^2 - b_3\bar{\nu}_i^3)^2}{p-q}} \qquad (3\text{-}22)$$

In Eq. 3-22, RMS denotes the estimated noise level computed over a given spectral range of interest containing p spectral points corresponding to wavenumber values $\bar{\nu}_i$ and absorbance values A_i. Coefficients b_o through b_3 denote the regression coefficients of the polynomial model that encodes the origin values for the RMS calculation, and q is the number of coefficients b_o through b_3 (i.e., 4). This calculation assumes that the third order polynomial can fit the baseline curvature properly.

3.7 Summary

The preceding sections have described the data analysis methods employed in the research to be described in Chapters 4 to 8. Within each chapter, specific information will

be given regarding the implementation details that are relevant to understanding how each analysis method was utilized in that specific work.

CHAPTER 4
DETERMINATION OF TEMPERATURE OF AQUEOUS-BASED SAMPLES DIRECTLY FROM NEAR-INFRARED SPECTRA

4.1 Introduction

Near-Infrared (NIR) spectroscopy has found successful applications in quantitative determinations of analytes in the pharmaceutical, clinical, chemical, food, and agricultural industries.[3,24,29-36,50,58] As described in Chapter 2, spectral features in the NIR region include combinations and overtones of the fundamental vibrational bands associated with C-H, O-H and N-H bonds.[3,6,24,37] Near-infrared spectroscopy is a non-destructive analysis technique which requires little to no sample preparation. It is also compatible with biological and environmental samples as water exhibits reduced absorption in the NIR region when compared to the mid-IR (MIR). However, the weak and highly overlapped spectral features observed in the NIR preclude the development of simple models that relate spectral intensities and quantitative variables such as concentration. Successful quantitative models require the use of multivariate calibration techniques such as partial least-squares (PLS) regression.[3,24]

Near-infrared spectroscopy is widely used in biological and environmental applications in which the samples are primarily aqueous-based.[3] Water has a fundamental O-H stretching band centered at 3,300 - 3,800 cm^{-1} and the first overtone of this O-H stretching vibration is centered at 6,900 - 7,000 cm^{-1}. A combination band of O-H fundamental stretching and H-O-H bending mode is centered at 5,150 - 5,200 cm^{-1}.[6,24,37,39] These bands are broad in nature as they are influenced by intermolecular features of water such as hydrogen bonding.

The hydrogen-bonded structure of water and its extreme temperature sensitivity have been extensively studied.[6,37-39,46,51-53] If precise control of temperature during spectral collection is not ensured, peak shifts in the water spectrum can result in large

baseline variations in absorbance spectra computed from spectral ratios. These baseline artifacts can negatively affect the performance of quantitative calibration models based on linear additivity (e.g., PLS regression models).[6,37,38]

As discussed in Hazen et al. and Arimoto et al., one approach to address this issue is to develop a temperature-insensitive calibration model by suppressing the effects of temperature variation in the measured spectra.[37,63] However, a drawback with such an approach is the danger of suppressing the analyte information along with the temperature information. In the work presented here, an alternative strategy is explored in which an attempt is first made to determine the temperature of an aqueous-based sample directly from the NIR spectrum, followed by the application of a temperature correction method. This chapter will explore temperature modeling in aqueous samples, while Chapter 5 will present the proposed temperature correction algorithm.

Several studies addressing temperature modeling in aqueous-based solutions have been documented in the literature.[47,48,49,62] Thompson et al. used the thermally induced absorbance changes of the second overtone of the O-H band centered at ~10,416 cm^{-1} to develop a non-invasive temperature monitoring strategy to measure the temperatures of aqueous solutions up to 0.1 M of electrolyte concentration.[47] One drawback of this strategy is that it is based on using only a single peak to model temperature variations, thereby limiting the accuracy of the model. Otal et al. used temperature-induced spectral changes of the second overtone of the O-H band centered at ~10,416 cm^{-1} to develop single linear and multiple linear regression models to evaluate the ability to predict temperatures of aqueous-based samples.[48] One drawback of this study is that the effect of matrix variations on the temperature models was only assessed for a single temperature, thereby limiting the application of these models. Kakuta et al. used temperature-induced spectral changes of ~6944 cm^{-1} water absorption band to develop univariate linear regression and PLS regression models to measure temperatures of turbid intralipid solutions.[49] Lin et al. used the perturbations of NIR water bands in the region of 5,000 to

9,000 cm^{-1} to generate multiple linear regression and principal component regression models that measured the temperatures of aqueous solutions.[62] In the previous three studies, models developed provided good calibration results but no long-term predictive ability was assessed to determine the robustness of the models with time. Although the LED device and fiber optic device developed by Thompson et al. and Lin et al., respectively, offer applications of temperature measurements in many environments, both devices have limited applications in measuring internal temperatures of body fluids and tissues.

The research presented in this chapter addresses these issues by developing PLS regression models for temperature in aqueous-based solutions based on spectral variations in the 4,000 to 5,000 cm^{-1} region. Temperature information is extracted from the same data used to build models for determining analyte concentration. The robustness of the models with time and matrix fluctuations were also assessed to further evaluate the predictive ability of the models.

The concept of coupling a spectral-based temperature determination with a corresponding calibration correction is motivated by applications in which the accurate measurement of sample temperature with a conventional thermistor or thermocouple probe is difficult. One such application and a long-standing area of interest in our laboratory is NIR-based noninvasive glucose monitoring in which *in vivo* glucose concentration determinations are made from direct spectral measurements of body tissue.[42,54] In this application, it is difficult to use a conventional temperature probe to obtain an accurate internal temperature of the tissue through which the spectral measurement is made. Although the core temperature of the human body is maintained near 37.0 °C, peripheral tissues and fluids (hands, feet etc.) can be subject to significant temperature fluctuations.

4.2 Effect of temperature fluctuation on water absorption bands

Water can exhibit two types of O-H bonds: ‘free’ or non-hydrogen-bonded O-H groups and hydrogen-bonded O-H groups. Free O-H groups show narrow absorption features whereas hydrogen-bonded O-H groups show broad absorption features.[6,37,38] As discussed in Section 4.1, absorption features of water that arise due to O-H groups are broad in nature as they are influenced by intermolecular interactions of water such as hydrogen bonding. Moreover, absorption bands arising from hydrogen-bonded O-H groups are found shifted to slightly lower wavenumbers than their free O-H group counterparts.

Water molecules exist as hydrogen-bonded clusters in nature.[6,37,38,40,41,55] The sizes of these clusters are dependent on the temperature. As the temperature increases, intermolecular hydrogen bonds are broken, thereby decreasing the cluster sizes of the water molecules. This results in an increase in the number of free O-H groups in water. The increase of free O-H groups with increasing temperature narrows the width of the water absorption peaks and shifts them to higher wavenumbers.[6,37] This phenomenon is illustrated in Figure 4-1 in which the absorbance spectra of a pH 7.4 phosphate buffer solution obtained at seven different temperatures are displayed. As seen in the figure, when the temperature of the solution is higher than the reference temperature (37 °C), negative baseline variation is observed at higher wavenumbers and positive baseline variation is observed at lower wavenumbers. The opposite behavior is true when the solution temperature is lower than the reference temperature. These deviations are caused by the shift of the water absorption bands toward higher wavenumbers with increasing temperature. These baseline variations are more significant at higher wavenumbers as the temperature sensitivity of the 5,150 - 5,200 cm^{-1} band is greater than that of the peak at 3,300 - 3,800 cm^{-1}.

4.3 Experimental design

4.3.1 Apparatus

The spectral data collections reported here were performed with a Bruker Vertex

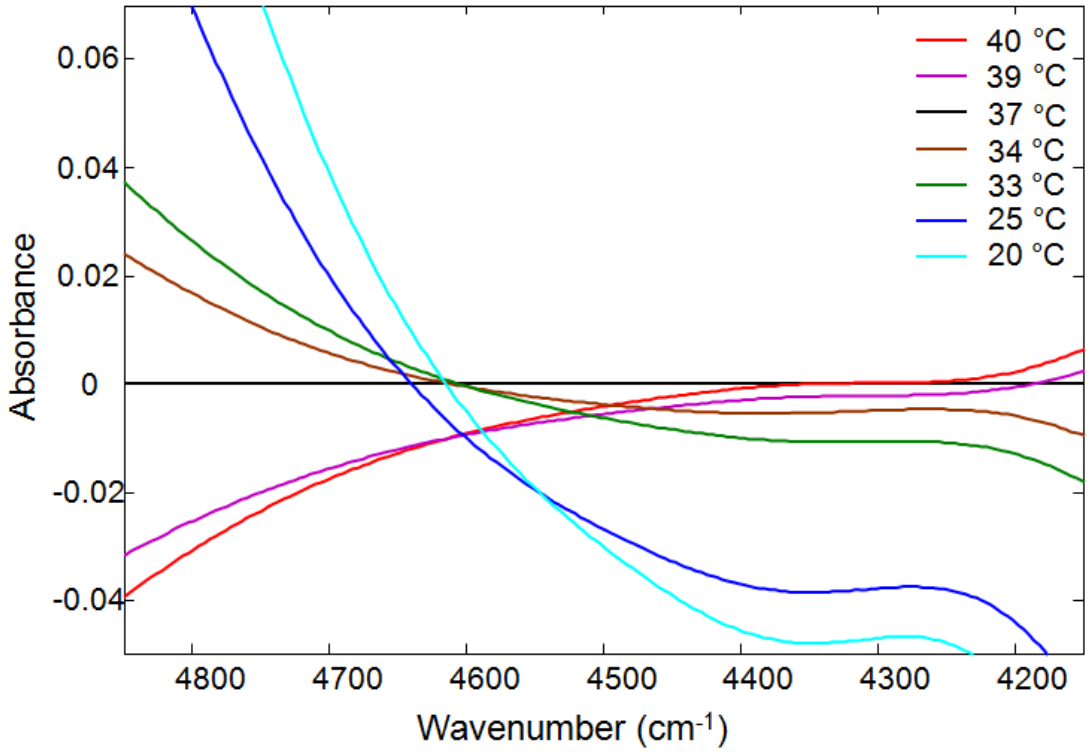

Figure 4-1. Absorbance spectra of pH 7.4 phosphate buffer spectra obtained at different temperatures. These spectra were generated on the basis of the ratio of single-beam spectra of pH 7.4 phosphate buffer collected at 20, 25, 33, 34, 37, 39 and 40 °C to a single-beam background buffer spectrum taken at 37 °C.

70 (Bruker Optics, Inc., Billerica, MA) Fourier transform (FT) spectrometer configured with a tungsten-halogen lamp source, a calcium fluoride (CaF_2) beam splitter and a liquid nitrogen cooled indium antimonide (InSb) detector. A low-pass interference filter (OCLI, Santa Rosa, CA) was used to restrict the light beyond 5,000 cm^{-1} from reaching the detector.

Spectra were collected from both static and flowing samples. For the static samples, a liquid transmission cell with a 20 mm diameter circular aperture (Model 118–3, Wilmad Glass, Inc., Buena, NJ) and sapphire windows (Meller Optics, Inc., Providence, RI) were used to hold the samples. The pathlength of the cell was fixed at 1.5 mm by use of Teflon spacers. Sample temperatures were maintained at the desired value (± 0.1 °C) by placing the transmission cell in an insulating metal jacket in conjunction with a circulatory water bath (Fisher Scientific Isotemp Model 3016D, Thermo Fisher Scientific Inc., Waltham, MA). The temperature of the sample was monitored with a copper-constantan (T-type) thermocouple probe (Model 5TC-GG-T-32-72, Omega Engineering, Inc., Stamford, CT) placed in contact with the inner wall of the metal jacket. A digital thermocouple thermometer (Omega Model 670, Omega Engineering, Inc.) was used to obtain the temperature measurements. A schematic representation of the experimental setup for the measurement of static samples is shown in Figure 4-2.

For the measurement of flowing samples, a custom temperature-controlled flow cell was designed. A schematic of this cell is shown in Figure 4-3. The cell consisted of four modules: (1) a sample reservoir, (2) a brass cube for heating/cooling the flowing solution, (3) the same liquid transmission cell (described previously) used in the measurement of the static samples, and (4) a peristaltic pump for circulating the sample solution through the system. Plastic tubing (TYGON®-R3603, Lowe's, Coralville, IA) of 6 mm and 5 mm internal diameters was used to connect the components. Two T-type thermocouples (5TC-GG-T-32-72, Omega Engineering, Inc.) were used to obtain

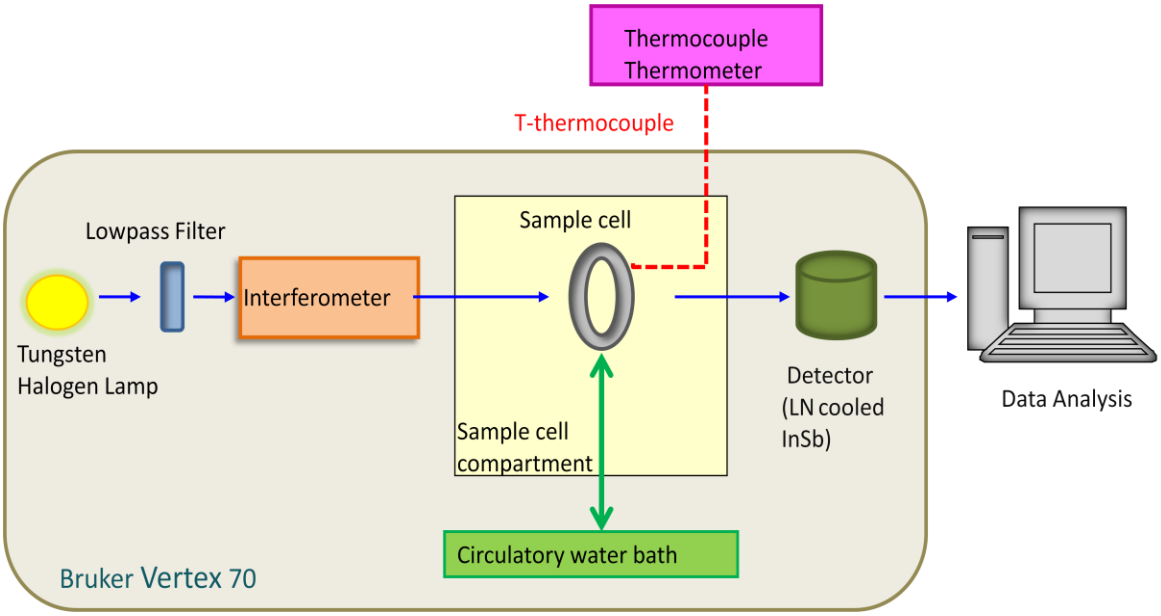

Figure 4-2. Schematic representation of the experimental setup used for collecting NIR spectra of static samples at a given temperature.

reference temperature measurements of the inflow and outflow to/from the transmission cell. These thermocouples are labeled, T_{in} and T_{out} in Figure 4-3. A third thermocouple (T_{cell} in Figure 4-3) monitored the temperature at the edge of the sapphire windows in the transmission cell. The same Omega 670 digital thermocouple thermometer described previously was used to obtain the temperature measurements. Reference temperatures of the measured samples were assigned as the average of T_{in} and T_{out}.

The sample reservoir consisted of a custom-made glass container (maximum volume 100 mL) equipped with an insulating jacket. This outer jacket was connected to a circulatory water bath (Fisher Scientific Isotemp 3016D) and heated to the target temperature of the measurement to help prevent sample cooling.

The brass cube (4.5 cm on each side, ~25 mL volume) was used as the central heating/cooling system for the flow cell. Two thermoelectric coolers (High Performance Peltier Thermoelectric Cooler Modules, HP-127-1.0-0.8, TE Technology, Inc., Traverse City, MI) were mounted on two opposite faces of the brass cube to heat/cool the cube. An Omega CN7500 controller (Omega Engineering, Inc.) was used to set the temperature of the thermoelectric coolers to a desired value.

A peristaltic pump (Model SP200.VO-12V/dc, APT Instruments, Rochester, IL) with variable flow rate capability was used to control the flow of the solution. Pump settings 0 to 10 produced flow rates of 62, 63, 66, 68, 71, 76, 81, 85, 87, 94, and 100 (± 6) mL/min, respectively. It was observed that flow rates in the extremes (63 mL/min ≥ flow rate ≥ 94 mL/min) did not produce a steady flow and that considerable turbulence was introduced at very high flow rates (flow rate ≥ 94 mL/min).

4.3.2 Reagents

Phosphate buffer solutions were prepared by dissolving appropriate amounts of reagent-grade sodium dihydrogen phosphate ($NaH_2PO_4.H_2O$, MW: 137.99 g/mol, Thermo Fisher Scientific, Inc.) in reagent-grade water obtained with a Water Pro PS Station (Model 9000601, Labconco Corporation, Kansas City, MO). Sodium benzoate

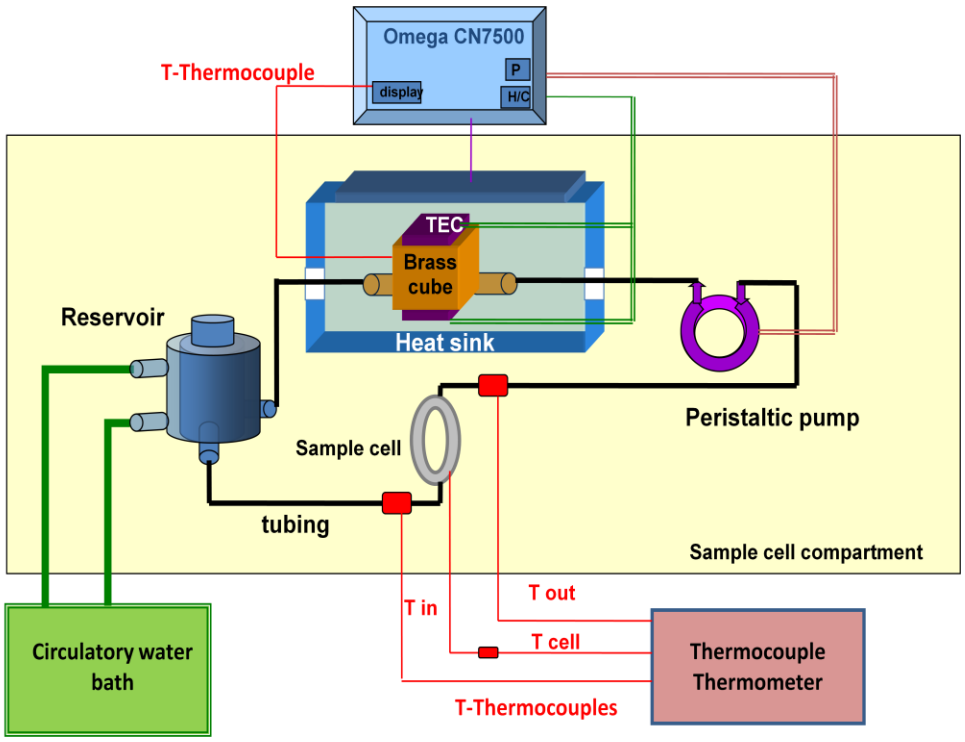

Figure 4-3. Schematic representation of the custom-made flow cell. The sample liquid placed in the reservoir was pumped through the brass cube and then through the transmission cell.

($NaC_7H_5O_2$, MW: 144.11 g/mol, Thermo Fisher Scientific, Inc.) was added as a preservative (5g/L in buffer).

For the majority of the work reported here, the buffer solutions were prepared with an initial $H_2PO_4^-$ concentration of 0.100 M and the pH was adjusted to 7.40 (± 0.01 pH units) by use of a 50 % (w/w) solution of sodium hydroxide (NaOH, Thermo Fisher Scientific, Inc.). All pH measurements were performed with an Orion Model 920A pH meter (Thermo Fisher Scientific, Inc.). Buffer solutions prepared in this way were used in the experiments with both static and flowing samples.

For the separate study of the effects of pH and buffer concentration on the ability to predict temperatures from NIR spectra, 11 pH levels were studied (4.76, 5.20, 5.44, 5.87, 6.23, 6.98, 7.20, 7.41, 7.85, 8.32, and 8.68). Each of these solutions was prepared in 0.100 M phosphate buffer. For the study of buffer concentration, the pH was held constant at 7.40 and seven levels of initial $H_2PO_4^-$ concentration were evaluated (0.050, 0.075, 0.100, 0.125, 0.150, 0.175, and 0.200 M)

To investigate the effects of sample matrixes of increased complexity, glucose, lactate and urea samples were prepared by dissolving appropriate amounts of reagent-grade *D*-glucose (dextrose) anhydrous ($C_6H_6O_6$, MW: 180.16 g/mol, Thermo Fisher Scientific, Inc.), sodium-*L*-lactate ($NaC_3H_5O_3$, MW: 112.06 g/mol, Sigma Aldrich, Inc., St. Louis, MO) and urea (CH_4N_2O, MW: 60.06 g/mol, Thermo Fisher Scientific, Inc.) in pH 7.40 phosphate buffer solution. Stock solutions of glucose, lactate and urea (250. mM) were used to prepare mixture samples of glucose, lactate and urea ranging from 1.4 to 19.6 mM.

Sample matrixes with additional complexity were also studied. A sample of bovine plasma (BVP) obtained from our collaborators in the Arnold research group at the University of Iowa was studied initially in conjunction with the glucose/lactate/urea solutions. On the basis of effects noted in the study of the BVP samples, subsequent measurements were performed with a sample of human serum albumin (HSA). The

measured sample was prepared using a stock solution of HSA (100. g/L, Sigma Aldrich) in pH 7.40 phosphate buffer. The final concentration of dissolved proteins (represented by HSA) in the prepared sample was 4.8 g/dL.

A YSI Model 2300 Stat Plus Glucose/Lactate Analyzer (YSI, Inc., Yellow Springs, OH) and an ACE Alera™ Clinical Chemistry System (Alfa Wassermann, Inc., West Caldwell, NJ) were used as reference methods to verify the component concentrations in the prepared samples.

4.3.3 Procedures

Initial work focused on static solutions of 0.100 M phosphate buffer at pH 7.40. To allow the construction of quantitative models for predicting temperature, 126 buffer calibration spectra were collected over two consecutive days, with sample temperatures ranging from 20.0 to 40.5 °C (± 0.1 °C). In order to assess the long-term predictive ability of the computed temperature model, 13 sets of pH 7.40 buffer spectra were collected over a period of 13 months. A summary of the data collection protocol is given in Table 4-1. The sample temperatures used in each data collection session were randomly assigned from the range noted above, and the order of data collection was randomized with respect to time to minimize the inclusion of correlations between temperature and time in the data. Figure 4-4 shows an example of the randomization of temperatures with time.

In order to assess the predictive ability of the temperature models in increasingly complex matrixes, seven prediction sets of spectra corresponding to laboratory prepared samples of glucose in pH 7.40 buffer, mixture samples of glucose, lactate and urea in pH 7.40 buffer and BVP samples were collected. The temperature range for this study was also from 20.0 to 40.5 °C (± 0.1 °C), and static samples were used. For each chemical sample, a set of randomly chosen temperatures was assigned from this range. The sample temperatures and analyte concentrations were randomized with respect to time during the

Table 4-1. Summary of spectral collection protocol for the long-term temperature prediction of phosphate buffer solutions

Data set	Number of samples/spectra[a]	Time since calibration (months)
Calibration	42/126	n.a.
Prediction set 1 (PS01)	21/63	1
Prediction set 2 (PS02)	21/63	2
Prediction set 3 (PS03)	21/63	3
Prediction set 4 (PS04)	21/63	4
Prediction set 5 (PS05)	21/63	5
Prediction set 6 (PS06)	21/63	6
Prediction set 7 (PS07)	21/63	7
Prediction set 8 (PS08)	21/63	8
Prediction set 9 (PS09)	21/63	9
Prediction set 10 (PS10)	21/63	10
Prediction set 11 (PS11)	21/63	11
Prediction set 12 (PS12)	20/60	12
Prediction set 13 (PS13)	20/60	13

[a]A sample is defined as a specific temperature setting for the solution. Three replicate spectra were collected for each sample.

data collection to minimize temporal correlations. Table 4-2 summarizes the data collection protocol for these samples.

In the follow-on study with static HSA samples, 105 HSA spectra were collected over two consecutive days. The temperature range studied was the same as that described previously. This data set was used to build a model for temperature prediction in samples of HSA. To test the resulting model, two prediction sets (consisting of spectra of HSA and BVP) were collected spanning the same temperature range over a time period of five weeks. Table 4-3 summarizes the data collection protocol for these samples. The sample temperature was again randomized with respect to time during the collection of these data.

To study the effects of buffer concentration and pH, static samples were again employed. To allow the construction of calibration models that incorporated these effects into the temperature prediction, 126 buffer spectra with varying pH levels, molarities, and temperatures were collected. The same temperature range of 20.0 to 40.5 °C (± 0.1 °C) was used as before. To facilitate testing of the resulting calibration model, two prediction sets of buffer spectra with varying pH and molarity values were collected spanning the same temperature range. The spectral collection protocol is summarized in Table 4-4. For these samples, temperature, pH and molarity of the buffer were always randomized to minimize the correlation of these parameters with time. Randomization of pH and molarity values with respect to time is shown in Figure 4-5.

The final set of experiments involved the use of the flowing system to evaluate the effect on temperature predictions of the inherent sample turbulence encountered when a flow system is used. In order to decide the optimal flow rate for the flowing system, calibration models were developed separately for three flow rates (68, 76, 85 mL/min). For calibration purposes, 57 phosphate buffer spectra were collected at each flow rate. The temperature range studied was again from 20.0 to 40.5 °C (± 0.1 °C). Temperature settings were again randomized with respect to time (order of data collection). To test the

computed temperature models, six prediction sets of buffer spectra (two prediction sets at each flow rate) were collected spanning the same temperature range. A summary of the data collection protocol is given in Table 4-5.

Open-beam air spectra were used as the background for all the spectral collections. A 10.0 % transmittance metal thin film neutral density filter (Rolyn Optics, Inc., Covina, CA) was used to attenuate the source intensity during the collection of all of the open-beam air spectra. For a given data collection session, eight warm-up air spectra were collected at the beginning of the day and three intermediate air spectra were acquired after the collection of every fourth sample. Three air spectra were also collected at the end of the day. The average air spectrum for the day was used in the calculation of spectra in absorbance units for all samples collected on that day.

For each sample measured with the static cell, the transmission cell was placed in the spectrometer and the solution was allowed to equilibrate to the specified temperature. Three consecutive spectra were then collected. The temperature value assigned to a given replicate spectrum varied depending on the degree of fluctuation observed in the reference temperature during the time period of the spectral collection.

For measurements performed with the flowing system, the sample to be measured was loaded into the glass reservoir, the flow was started, and the temperature controller was set to the target temperature. After equilibration, three consecutive spectra were collected. Reference temperatures were assigned to each spectrum on the basis of the average of the thermocouple readings taken at the inflow and outflow locations on either side of the transmission cell (T_{in} and T_{out} in Figure 4-3).

Across all the studies, each spectrum collected was based on 256 co-added double-sided interferograms containing 7,110 points acquired at every zero crossing of the helium-neon (He-Ne) reference laser (15,800.45 cm^{-1}). A nominal spectral resolution of 8 cm^{-1} was used, and the source aperture setting was 6 mm. All interferograms were converted to single-beam spectra with a point spacing of 3.8575 cm^{-1} by use of two levels

Table 4-2. Summary of spectral collection protocol for temperature prediction in increasingly complex matrixes.

Data set	Number of samples/ spectra[a]	Time since calibration (months)	Number of chemical samples	Composition of each sample in mM (glucose, lactate and urea respectively)
Calibration	42/126	0	1[b]	0, 0, 0
Prediction set 14 (PS-G)	20/60	1	1	13.3
Prediction set 15 (PS-GLU)	21/63	2	1	11.2, 1.4, 7.7
Prediction set 16 (PS-GLU5)	22/66	3	5	1.4, 7.7, 18.2 5.6, 16.8, 4.9 10.5, 13.3, 9.1 16.1, 17.5, 11.9 19.6, 19.6, 19.6
Prediction set 17 (PS-BVP1)	21/63	4	1	1.5, -, - [c]
Prediction set 18 (PS-GLU10)	24/72	4	10	1.4, 7.7, 18.2 3.5, 15.4, 10.5 5.6, 16.8, 4.9 7.7, 5.6, 16.8 10.5, 13.3, 9.1 12.6, 14.7, 3.5 14.0, 16.1, 15.4 16.1, 17.5, 11.9 18.2, 18.2, 6.3 19.6, 19.6, 19.6
Prediction set 19 (PS-BVP2)	60	5	1	1.4, -, - [c]
Prediction set 20 (PS-BVP3)	21/63	6	1	1.4, -, - [c]

[a]A sample is defined as a given solution at a given temperature.

[b]The calibration spectra were obtained from phosphate buffer only.

[c]Lactate and urea measurements were not available for the BVP samples.

Table 4-3. Summary of spectral collection protocol for temperature modeling in biological samples

Data set	Number of samples/spectra[a]	Time since calibration (weeks)	Type of sample
Calibration	35/105	0	HSA in pH 7.4 buffer
Prediction set 21 (PS-HSA)	19/57	2	HSA in pH 7.4 buffer
Prediction set 22 (PS-BVP4)	20/60	5	BVP

[a]A sample is defined as a given solution at a given temperature.

Table 4-4. Summary of spectral collection protocol for phosphate buffer samples with variation in buffer concentration and pH

Data set	Number of samples/spectra[a]	Time since calibration (weeks)
Calibration	42/126	0
Prediction set 23 (PS23)	22/66	4
Prediction set 24 (PS24)	33/99	8

[a]A sample is defined as a given solution at a given temperature.

Table 4-5. Summary of spectral collection protocol for temperature modeling in flowing solutions

Flow rate (mL/min)	Data sets	Number of samples/spectra[a]	Time since calibration (weeks)
68	Calibration	19/57	0
	Prediction set 25 (PS25)	15/45	1
	Prediction set 26 (PS26)	15/45	2
76	Calibration	19/57	0
	Prediction set 27 (PS27)	15/45	1
	Prediction set 28 (PS28)	15/45	2
85	Calibration	19/57	0
	Prediction set 29 (PS29)	15/45	1
	Prediction set 30 (PS30)	15/45	2

[a]A sample is defined as a given solution at a given temperature.

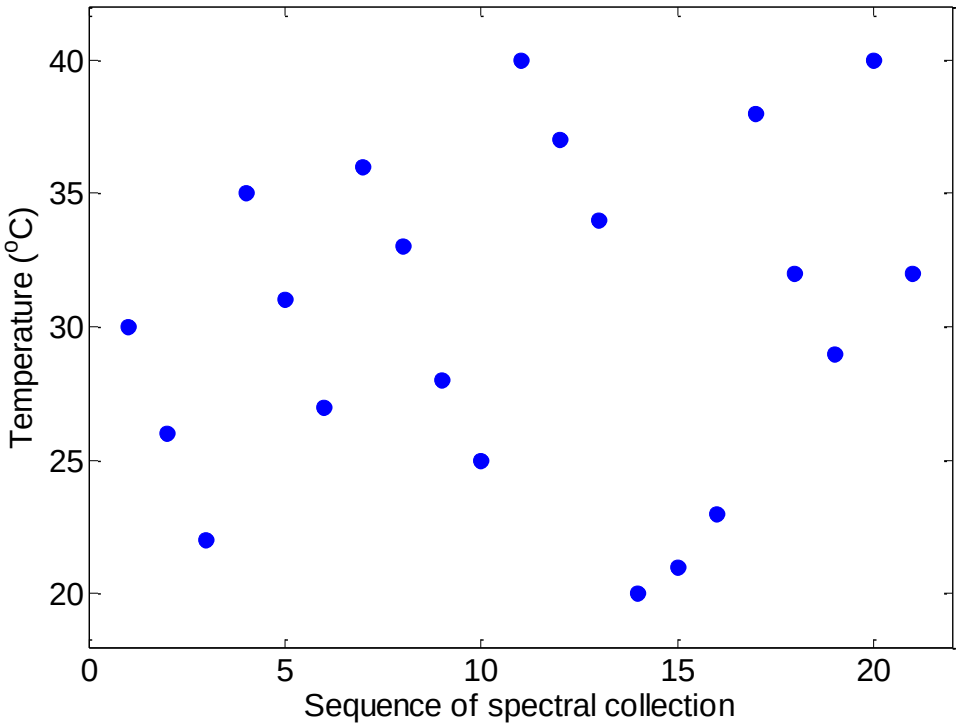

Figure 4-4. Example of randomization of temperature values with respect to the order of data collection to minimize the correlation between temperature and time.

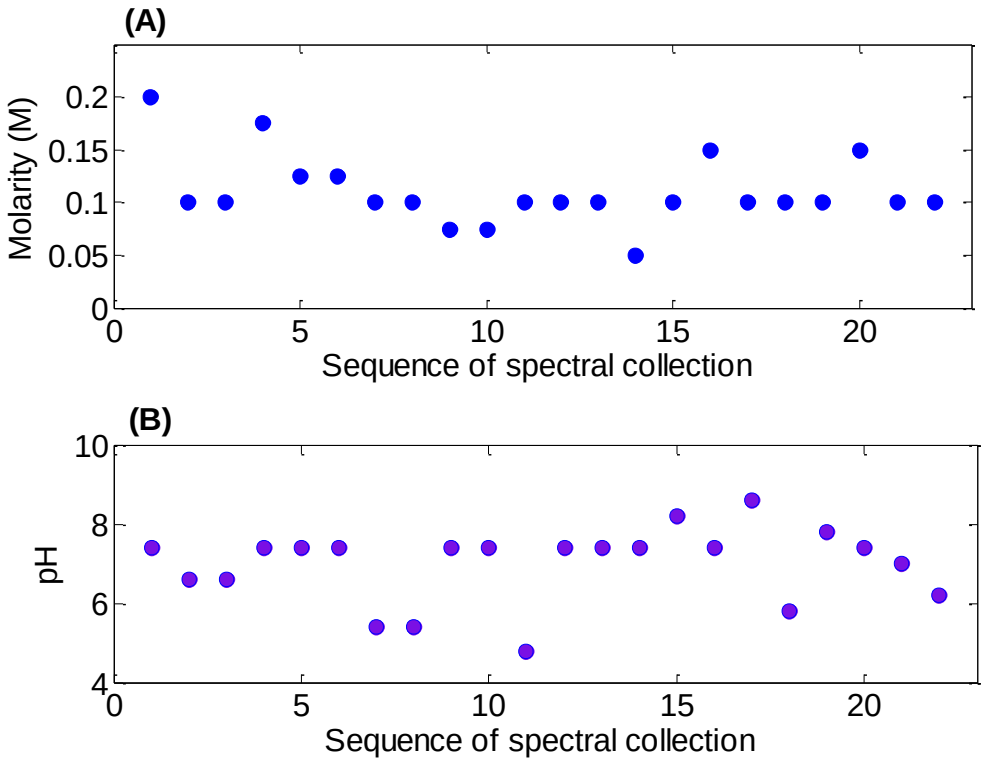

Figure 4-5. Randomization of molarity values and pH values to minimize the correlation between these parameters and time. **(A)** molarity values and **(B)** pH values.

of zero filling, Blackmann-Harris 3-term apodization and Mertz phase correction. The wavenumber range selected for this study was from 4,000 to 5,000 cm^{-1}.

The Fourier processing calculations were performed with the Bruker Opus software (Version 6.5, Bruker Optics, Inc.) controlling the spectrometer. Further calculations were performed with Matlab (Version 7.4, The Mathworks, Inc., Natick, MA) on a Dell Precision 670 workstation (Dell Computer Corp., Round Rock, TX) operating under Red Hat Linux WS (Version 5.2, Red Hat, Inc., Raleigh, NC).

4.4 Results and discussion

4.4.1 Noise evaluation in collected spectra

The quality of the sample spectra in the calibration and prediction sets was assessed by computing the average root-mean-square (RMS) noise of spectra in each data set. This calculation was performed by taking the ratio of each pairwise combination of the three replicate spectra for a given sample and temperature setting. The performance of the instrument itself was determined by the average RMS noise of the air spectra collected on each day. This calculation was performed by taking the ratio of each pairwise combination of the replicate air spectra for a given day. The resulting transmittance spectra were converted to absorbance units before the RMS calculation was performed. In computing the noise value to report, the spectral region from 4500 to 4300 cm^{-1} was fit to a third-order polynomial baseline function to remove systematic components from the noise spectrum. The residuals about this fitted baseline served as the input to the RMS calculation. This calculation is summarized in Chapter 3 (Section 3.6).

For the calibration data collected with static samples of pH 7.4 phosphate buffer, the average RMS noise for the buffer spectra and air spectra were 1.8 ± 0.3 and 1.1 ± 0.3 microabsorbance units (μAU), respectively. Figures 4-6 and 4-7 show the average RMS noise values for air and buffer spectra, respectively, obtained for the corresponding long-term prediction data (prediction sets PS01 to PS13). Figures 4-8 and 4-9 are the

corresponding plots for air and sample spectra obtained for the seven prediction sets collected from sample matrixes with increased complexity. Figures 4-10 and 4-11 are the analogous plots derived from the follow-on study of protein samples, while Figures 4-12 and 4-13 correspond to the investigation of buffer samples with variation in pH and molarity. Figures 4-14 and 4-15 plot the noise values obtained from the spectra collected with the flow system. Inspection of Figures 4-6 through 4-15 confirms the consistency of the spectral noise levels throughout the more than one year of data collection.

4.4.2 Spectra of pH 7.4 buffer at different temperatures

Figure 4-16 displays NIR absorbance spectra of a static pH 7.40 buffer solution obtained in the range of 4,800 to 4,200 cm^{-1}, for the temperature range of 20.0 to 40.5 °C. A total of 126 spectra are plotted in panel A of the figure. Spectra recorded at three different temperatures are plotted in panel B. As discussed in Section 4.1, the primary spectral features are due to the two strong water absorption peaks centered at 5,200 cm^{-1} and 3,800 cm^{-1}.[37] The wavenumber region of interest for this work was from 4,000 to 5,000 cm^{-1} in which the absorption of water is decreased relative to the peak maxima on each side. This region can also be considered as a viewing window for the analyte of interest in an aqueous solution. For example, in the case of glucose, there are three combination bands that are centered at 4,300, 4,400 and 4,750 cm^{-1}.[37] The focus of this study was to evaluate the ability to predict solution temperatures reliably from the 4,000 to 5,000 cm^{-1} region, thereby only requiring the collection of a small spectral region to measure both the analyte concentration and the sample temperature. An inspection of Figure 4-16B reveals that even in this region of reduced absorbance, a clear temperature-dependent effect is observed in the spectra.

4.4.3 Signal preprocessing methods

In this study, the standard normal variate (SNV) transform combined with the discrete wavelet transform (DWT) were investigated for use in preprocessing the pH 7.40 buffer absorbance spectra before attempting to use them to build quantitative models for

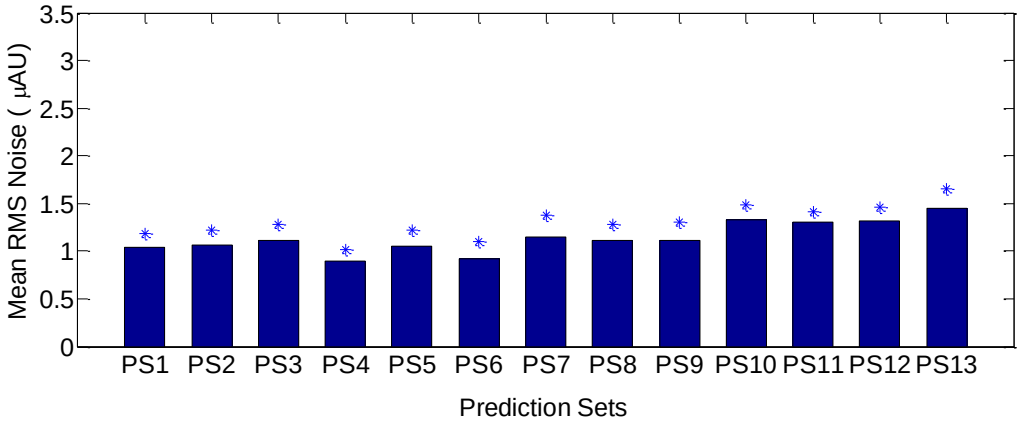

Figure 4-6. Average RMS noise values in units of microabsorbance (μAU) computed from air spectra corresponding to each of the 13 sets of long-term prediction data. The asterisks above the bars indicate one standard deviation from the average.

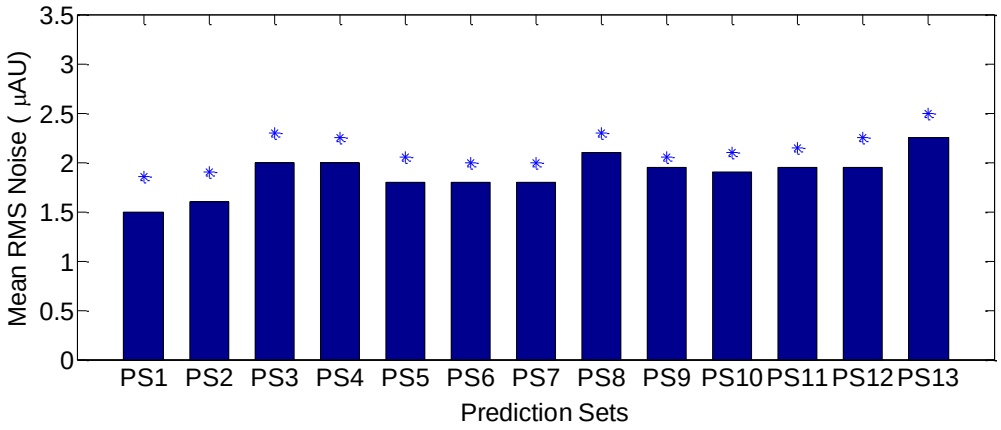

Figure 4-7. Average RMS noise values in units of microabsorbance (μAU) computed from buffer spectra corresponding to each of the 13 sets of long-term prediction data. The asterisks above the bars indicate one standard deviation from the average.

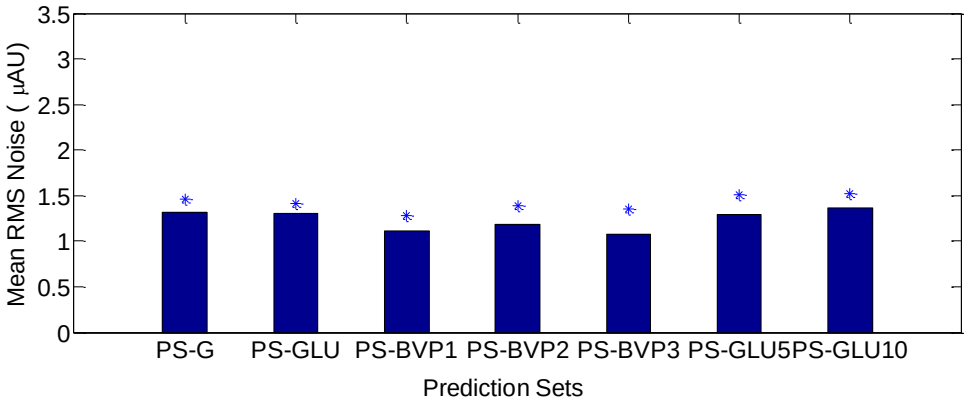

Figure 4-8. Average RMS noise values in units of microabsorbance (μAU) computed from air spectra corresponding to each of the seven sets of prediction data of samples with additional chemical components. The asterisks above the bars indicate one standard deviation from the average.

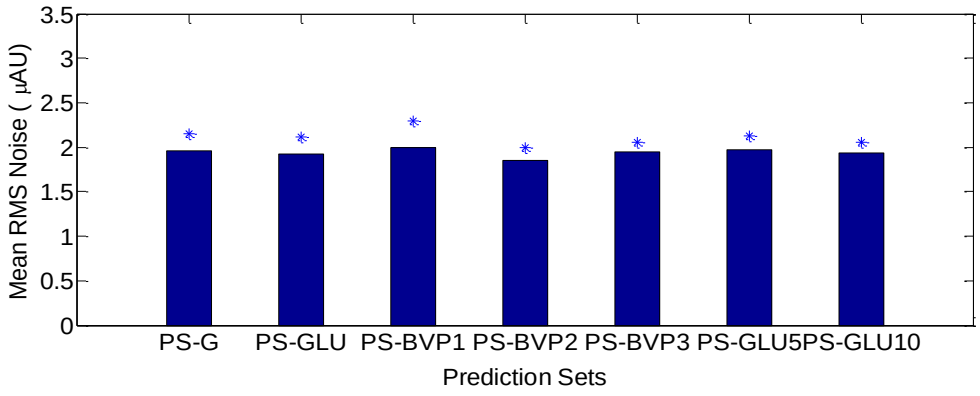

Figure 4-9. Average RMS noise values in units of microabsorbance (μAU) computed from sample spectra corresponding to each of the seven sets of prediction data of samples with additional chemical components. The asterisks above the bars indicate one standard deviation from the average.

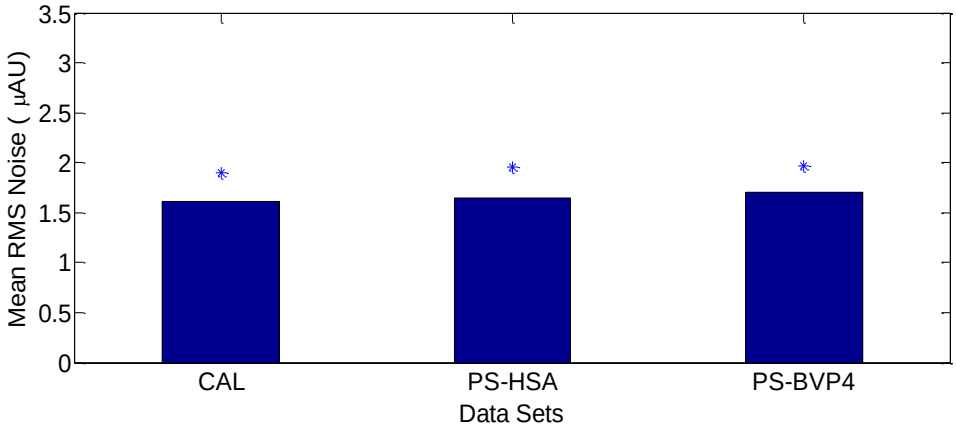

Figure 4-10. Average RMS noise values in units of microabsorbance (µAU) for air spectra corresponding to the study of protein solutions. The asterisks above the bars indicate one standard deviation from the average.

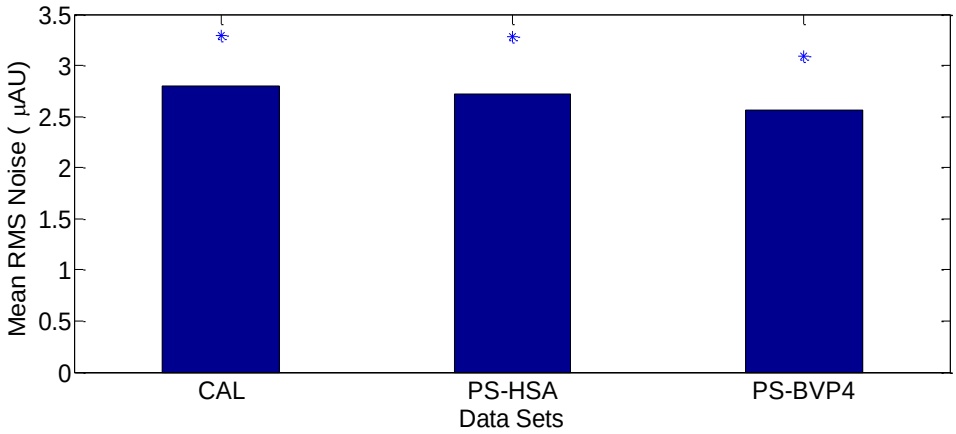

Figure 4-11. Average RMS noise values in units of microabsorbance (µAU) for sample spectra (HSA and BVP) in the study of protein solutions. The asterisks above the bars indicate one standard deviation from the average.

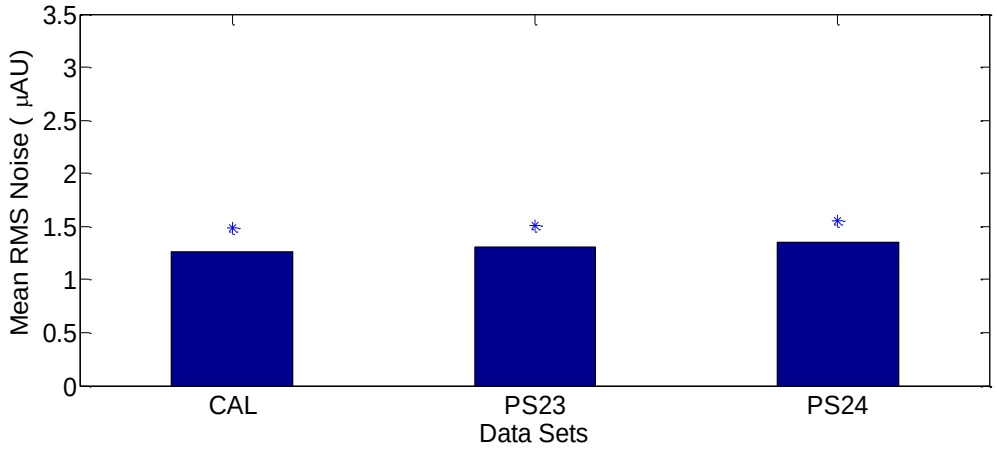

Figure 4-12. Average RMS noise values in units of microabsorbance (μAU) for air spectra associated with the study of variation in pH and buffer molarity. The asterisks above the bars indicate one standard deviation from the average.

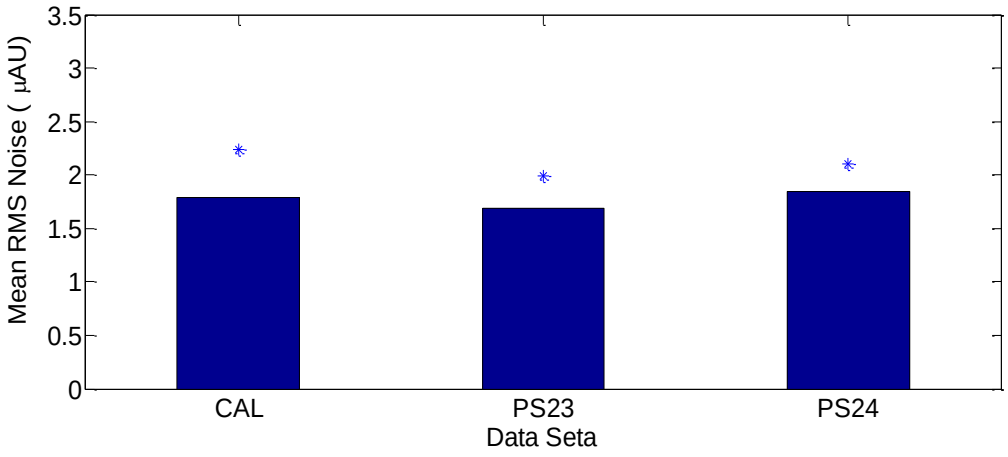

Figure 4-13. Average RMS noise values in units of microabsorbance (μAU) for buffer spectra (including pH and molarity variation) for a given spectral collection. The asterisks above the bars indicate one standard deviation from the average.

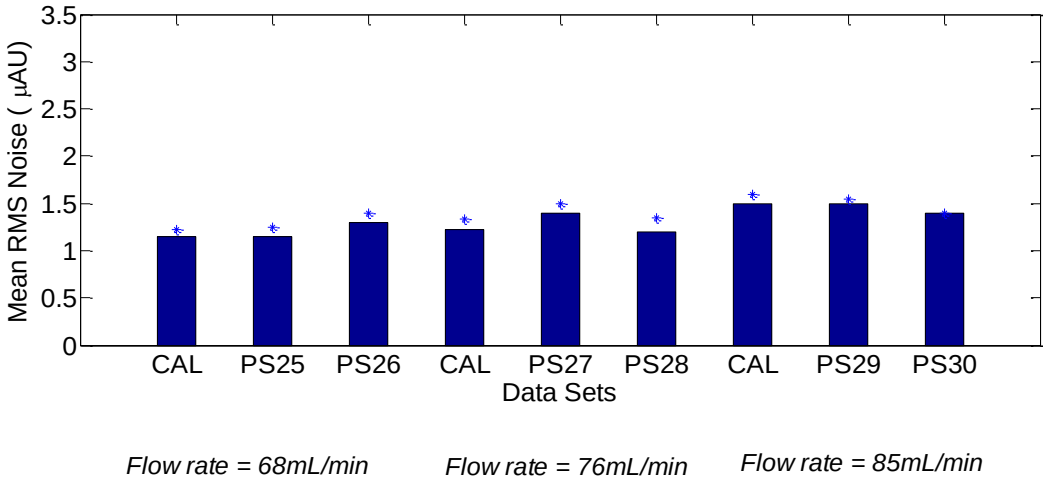

Figure 4-14. Average RMS noise values in units of microabsorbance (µAU) for air spectra acquired during the experiments with the flow system. Data sets were collected at three different flow rates. The asterisks above the bars indicate one standard deviation from the average.

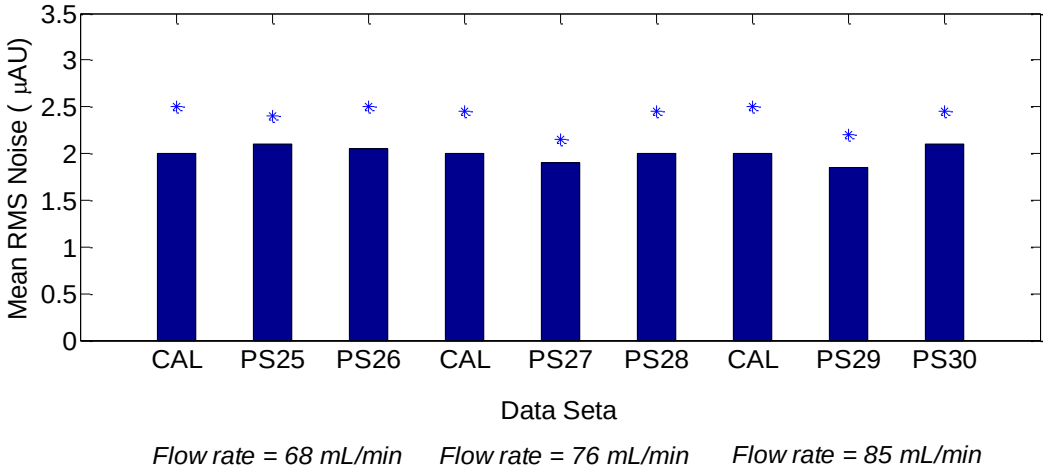

Figure 4-15. Average RMS noise values in units of microabsorbance (µAU) for buffer spectra acquired during the experiments with the flow system. Data sets were collected at three different flow rates. The asterisks above the bars indicate one standard deviation from the average.

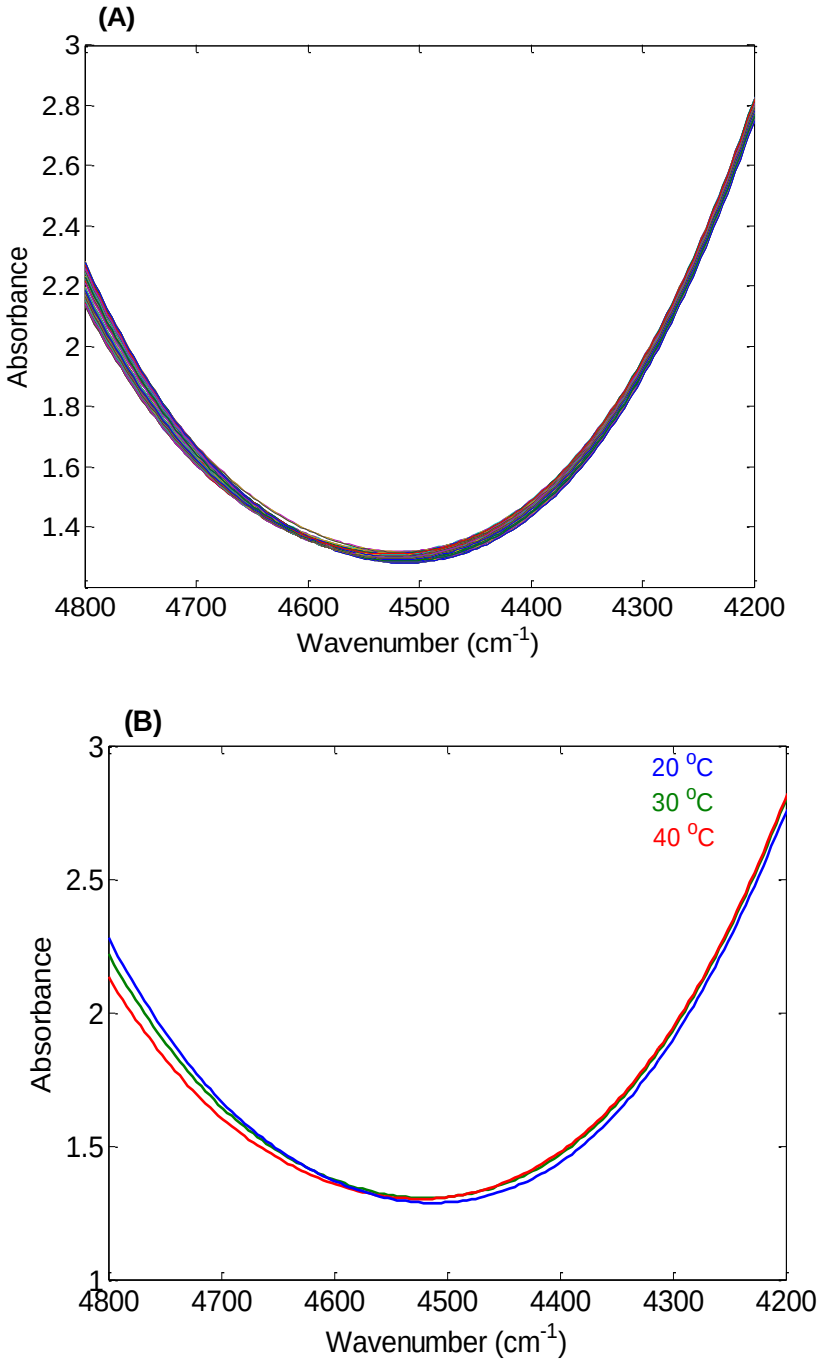

Figure 4-16. Raw NIR absorbance spectra of static pH 7.4 phosphate buffer. An open-beam air spectrum was used as the background in the absorbance calculation. Absorbance spectra of static pH 7.4 phosphate buffer **(A)** collected over the range of 20.0 to 40.5 °C and **(B)** collected at 20.0, 30.0 and 40.0 °C.

temperature. Both of these preprocessing methods were described previously in Chapter 3.

Wavelet functions from the Daubechies (db) and Symlet (sym) families were used with a maximum decomposition level of 10. Parameters optimized included the order of the wavelet function, the level of decomposition employed, and the number of levels used in the reconstruction of the signal. Further details regarding the optimization procedure will be provided in Section 4.4.4.

Figure 4-17 shows the spectral features of buffer absorbance spectra in the range of 4,000 to 5,000 cm^{-1} after preprocessing with the SNV transform. Figure 4-18 shows these spectra after further preprocessing with the DWT. The wavelet function used in this example was Daubechies-5 (db5) with seven levels of decomposition. Only the seventh level of details and approximation were used in the reconstruction of the signal.

The db5 wavelet function is illustrated in Figure 4-19. The wavelet decomposition procedure used in this example with function db5 is illustrated in Figure 4-20. Since the spectral features relevant to temperature fluctuations are primarily found in the background (i.e., low-frequency variations), the last levels of decomposition are expected to contain the useful information regarding temperature fluctuation. Hence, it was found that seven levels of decomposition with only the seventh level of details and approximation used in the reconstruction provided the optimal preprocessing procedure.

4.4.4 Quantitative models for temperature fluctuations in aqueous-based samples

In order to quantify the temperature changes in static pH 7.40 buffer solutions, PLS calibration models (Chapter 3, Section 3.3.2) were generated from buffer absorbance spectra. As noted previously, these absorbance spectra were computed using single-beam pH 7.40 phosphate buffer spectra with respect to an average air spectrum of the day of spectral collection.

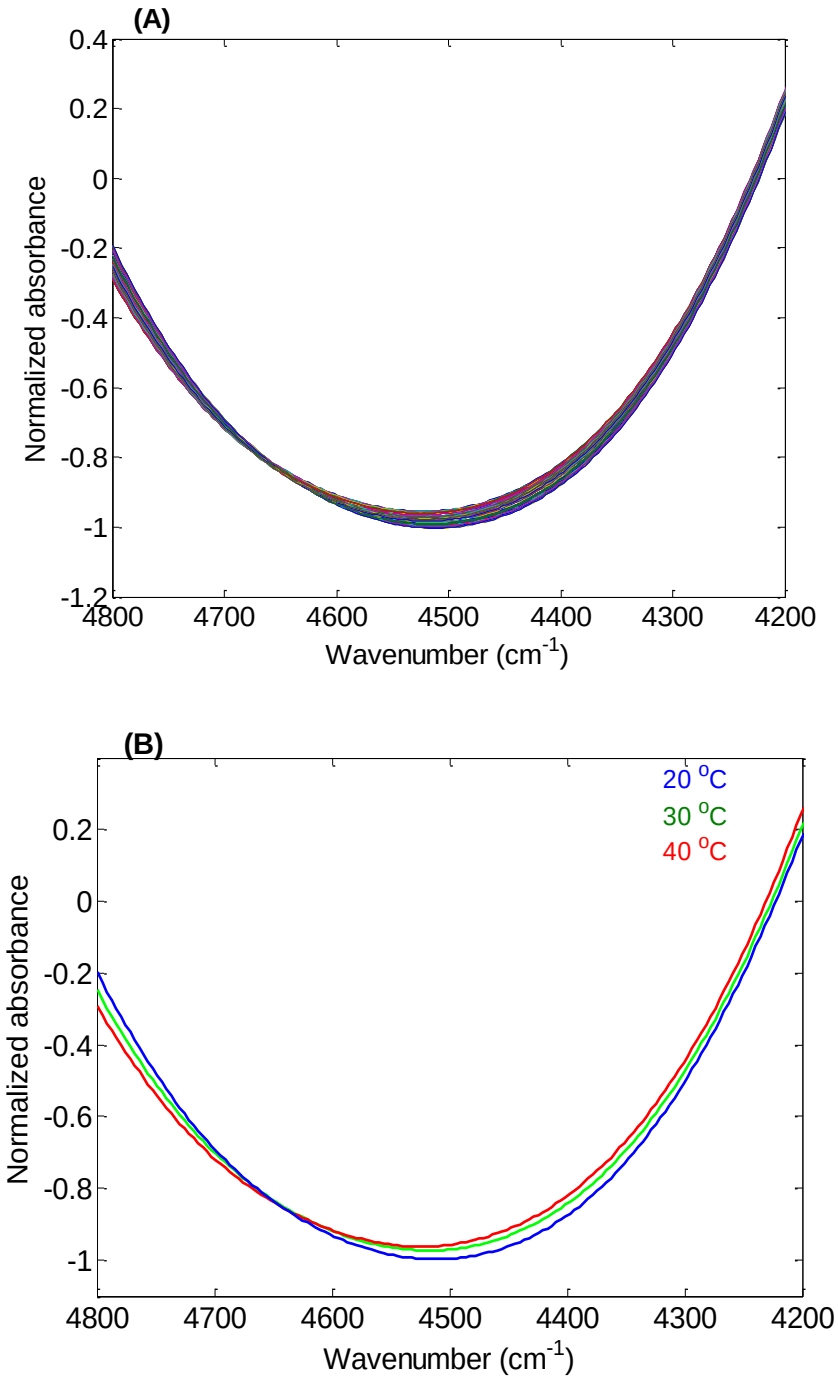

Figure 4-17. Near-infrared spectra of static pH 7.4 phosphate buffer after preprocessing with the SNV transform. Preprocessed NIR spectra of static pH 7.4 phosphate buffer **(A)** collected over the range of 20.0 to 40.5 °C and **(B)** collected at 20.0, 30.0 and 40.0 °C after application of the SNV transform.

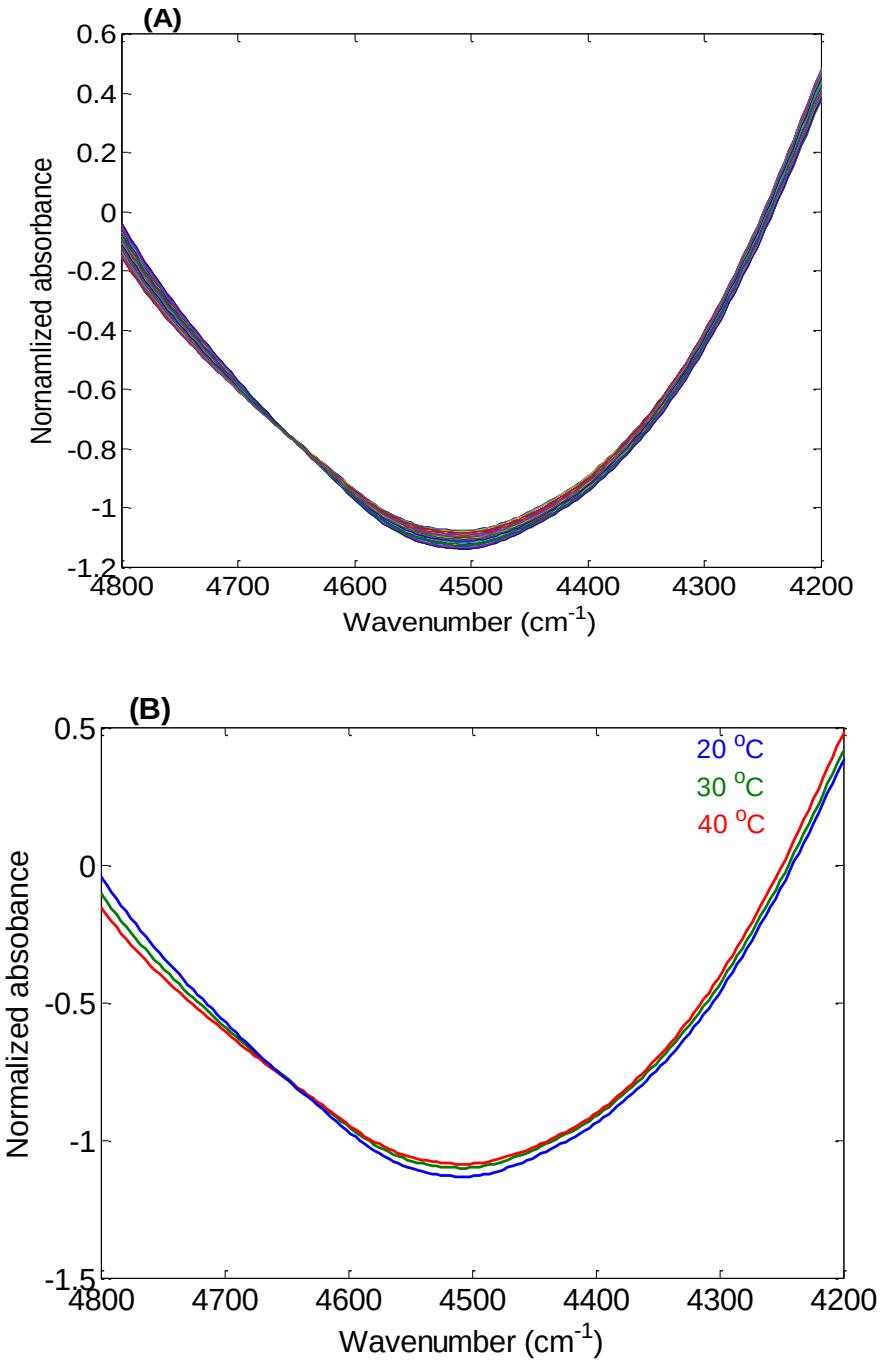

Figure 4-18. Near-infrared spectra of static pH 7.4 phosphate buffer after preprocessing with the SNV and DWT transforms. Preprocessed NIR spectra of static pH 7.4 phosphate buffer **(A)** collected over the range of 20.0 to 40.5 °C **(B)** collected at 20.0, 30.0 and40.0 °C after application of the SNV transform and DWT.

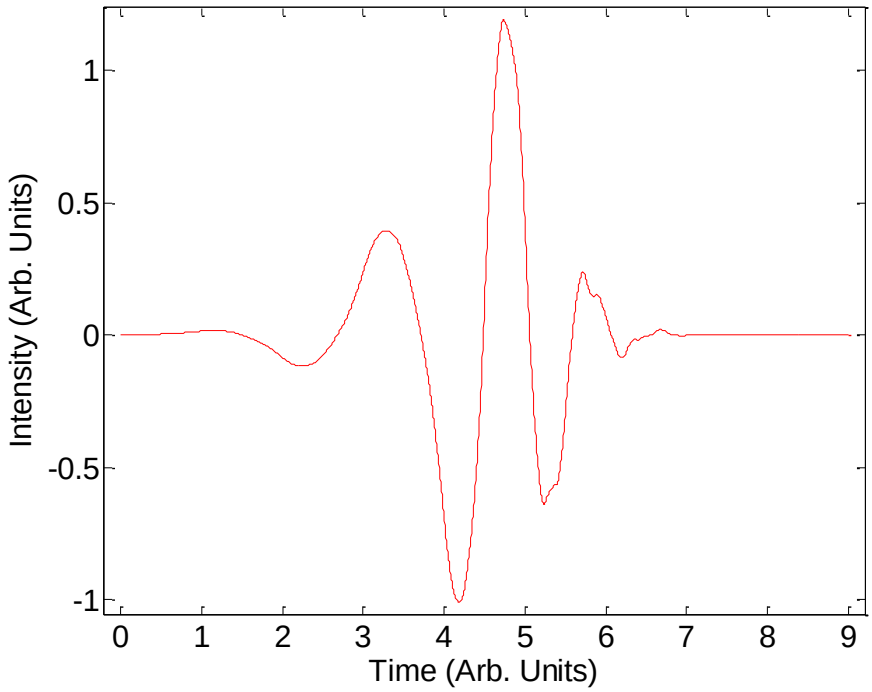

Figure 4-19. Daubechies-5 (db5) wavelet function with arbitrary time and intensity axes.

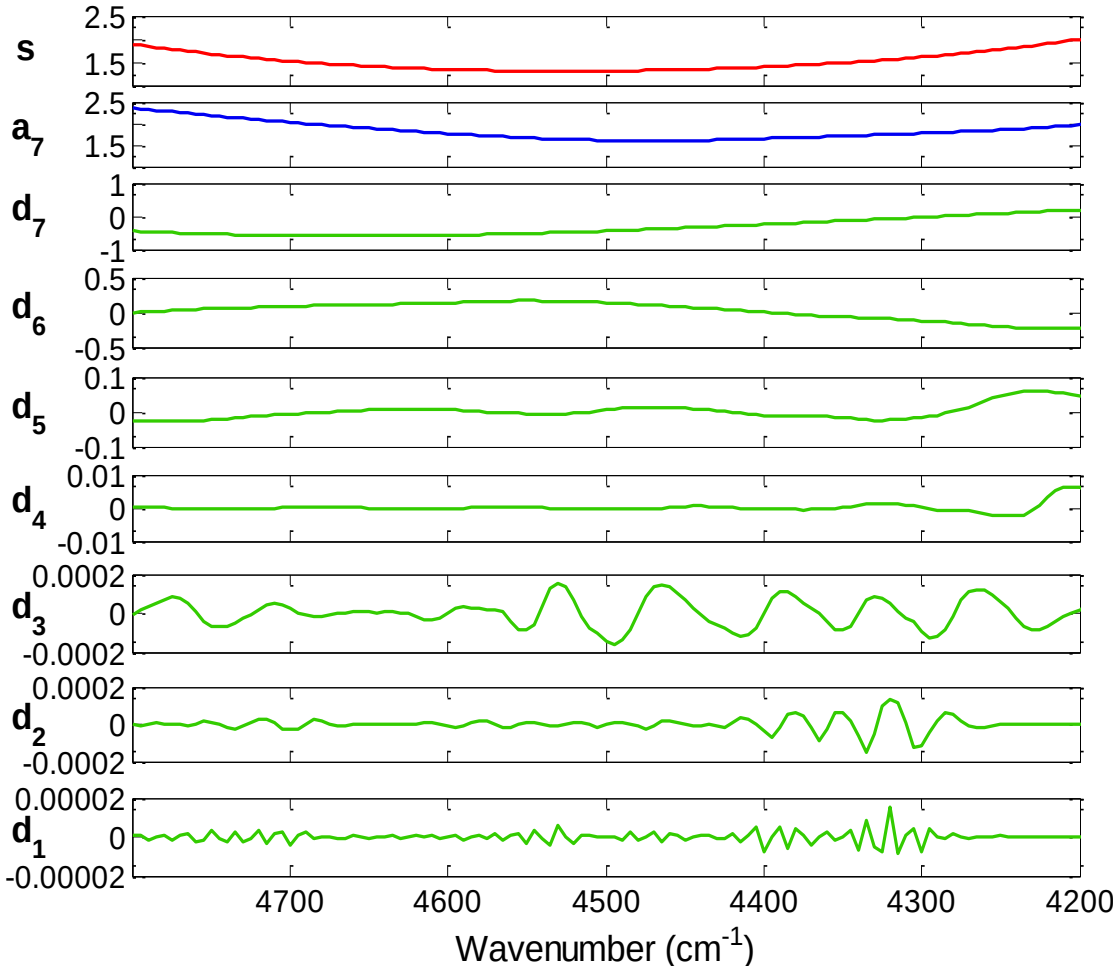

Figure 4-20. Wavelet decomposition for pH 7.40 phosphate buffer spectra using wavelet function Daubechies-5 (db5). The individual panels correspond to (*s*) original buffer spectrum in absorbance units; (d_1-d_7) details coefficients at each of the seven levels of decomposition; (a_7) approximation coefficients at the 7th level of decomposition.

A cross-validation protocol was used to validate the model performance. This procedure involved leaving out 10 % of the spectra with their replicate measurements and generating a calibration model for temperature from the remaining spectra. The calibration model developed was then used to predict the temperatures associated with the withheld spectra. This procedure was iterated 10 times such that all spectra were withheld once. As described in Chapter 3 (Section 3.4), the errors in predicted temperature were pooled to compute a cross-validated standard error of prediction (CV-SEP).

A spectral range study was performed in conjunction with cross-validation to optimize the wavenumber range submitted to the PLS calculation. This procedure was based on a grid search (Chapter 3, Section 3.2.3) and included scanning the wavenumber range from 4,150 to 4,850 cm^{-1} in steps of 25 cm^{-1} using window sizes from 300 to 700 cm^{-1} in steps of 25 cm^{-1}. For each wavenumber range investigated, models based on 1-10 latent variables (PLS factors) were computed and the corresponding CV-SEP values were obtained. The minimum CV-SEP value was used to obtain the optimal wavenumber range and number of PLS factors (latent variables). Once the wavenumber range was selected, an *F*-test at the 95% level was used to determine if the number of latent variables could be reduced without a statistically significant increase in CV-SEP. The final model size corresponded to the number of latent variables that produced a value of CV-SEP that was not statistically different from the minimum CV-SEP.

For models based on preprocessed spectra, the optimization of the wavelet parameters was combined with the selection of the optimal spectral range and number of PLS latent variables. In this work, separate optimizations were run for the Daubechies and Symlet wavelet families. For a given wavelet family, the grid search incorporated the optimization of the wavelet function order, level of decomposition and levels used for reconstructing the spectrum. Spectra preprocessed with the SNV transform were used as

inputs to the grid search, and the DWT was applied to the full spectral range of 5,000 to 4,000 cm^{-1}.

The grid search protocol included scanning the wavelet order from 2 to 8 in steps of 1. For each wavelet order investigated, the degree of decomposition was scanned from levels 3 to 8 in steps of 1. For each wavelet order and decomposition level investigated, starting from the last level, the best hierarchical combination of details was investigated for incorporation with the last approximation. For example, with wavelet function db5 and a decomposition level of 6, approximation 6 was tested with details 6, 5/6, 4/5/6, 3/4/5/6, and 2/3/4/5/6 to evaluate the best reconstruction scheme. This protocol for investigating the details was established by preliminary studies that confirmed the need to include the last approximation, the lack of useful information in detail 1, and the overall greater utility of the higher-level details.

For each parameter combination evaluated, the spectra were preprocessed and submitted to the same wavenumber range/latent variable optimization described above. This produced an overall lowest value of CV-SEP that incorporated the wavelet parameters, spectral range, and number of PLS latent variables. The *F*-test was used as described previously to refine the choice of the optimal number of latent variables.

4.4.5 Best calibration models for temperature fluctuations in aqueous-based samples

Using the procedures described above, PLS calibration models were generated for temperature fluctuations in static pH 7.40 buffer. Three calibration models were developed separately for buffer spectra preprocessed with the Daubechies (db) family wavelets, buffer spectra preprocessed with the Symlet (sym) family wavelets and buffer spectra with no preprocessing. These calibration models are summarized in Table 4-6. Listed in the table are the wavenumber ranges, number of PLS latent variables, and values of the standard error of calibration (SEC) and CV-SEP. As described in Chapter 3

(Section 3.3), the SEC is the standard error in predicted temperature achieved when all calibration spectra are included in the calculation of the model.

The optimal wavenumber range for ‘db’ preprocessed spectra was determined to be from 4,700 to 4,175 cm^{-1} with 1 PLS factor. The optimal preprocessing method was the SNV transform combined with the db5 wavelet function at seven levels of decomposition and using only level 7 (approximation and details) for reconstruction. The best calibration model gave a CV-SEP value of 0.20 °C.

When ‘sym’ preprocessed spectra were used, the optimal wavenumber range was 4,725 to 4,200 cm^{-1} with 1 PLS factor. The optimal preprocessing method was the SNV transform combined with the sym5 wavelet function at seven levels of decomposition and using only level 7 (approximation and details) for reconstruction. The best calibration model gave a CV-SEP value of 0.21 °C.

For spectra without any preprocessing, the optimal wavenumber range was determined to be from 4,700 to 4,275 cm^{-1} with 4 PLS factors. The best calibration model gave a CV-SEP value of 0.20 °C.

Each of the three calibration models produced equivalent values of CV-SEP. The models based on SNV and DWT preprocessing required only a single term vs. four terms for the model based on raw absorbance data. The increased number of terms in this model suggests that additional PLS latent variables are required to account for spectral variation that was removed by the SNV and DWT preprocessing procedures used with the other two models. These models will next be evaluated on the basis of their robustness to long-term prediction.

4.4.6 Long-term prediction performance of the temperature models

The long-term prediction performance of the calibration models was assessed by use of the 13 prediction sets of static pH 7.40 buffer spectra collected over 13 months. The three optimized models computed with the original set of calibration spectra were applied to each prediction set. No attempts were made to update or modify the original

Table 4-6. Best PLS calibration models for temperature fluctuations in phosphate buffer

Model No.	Wavenumber range (cm^{-1})	Preprocessing method	Latent variables	SEC (°C)	CV-SEP (°C)
1	4,700 – 4,275	None	4	0.15	0.20
2	4,725 – 4,200	SNV & DWT sym5, 7 [7][a]	1	0.17	0.21
3	4,700 – 4,175	SNV & DWT db5, 7 [7][a]	1	0.18	0.20

[a]Notation is wavelet family and order of wavelet function, number of levels of decomposition, and the levels used in the reconstruction of the spectrum.

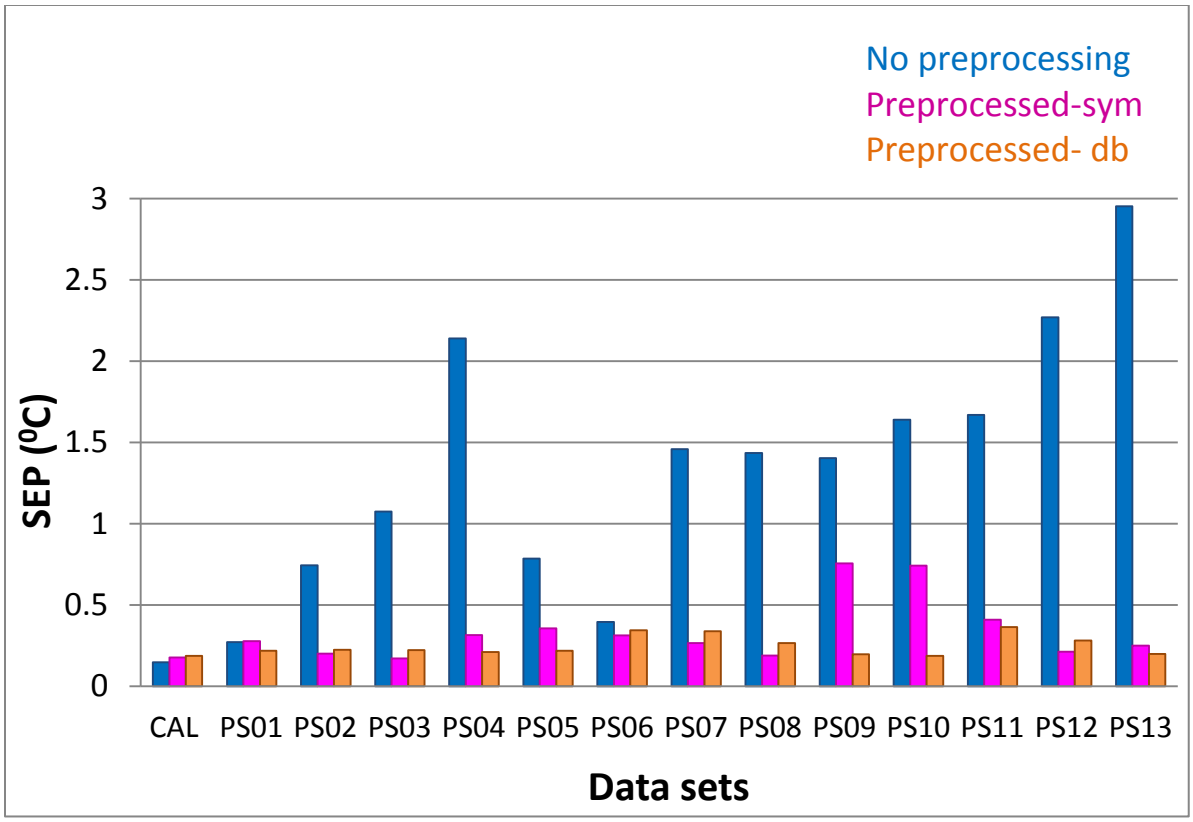

Figure 4-21. Long-term prediction performance of PLS calibration models for temperature fluctuations in phosphate buffer. The values of CV-SEP for the calibration data and SEP for the 13 prediction sets are plotted. The model based on preprocessing with the db5 wavelet produced the best results overall.

Table 4-7. Long-term prediction performance of PLS calibration models for temperature of phosphate buffer solutions

Data set	No preprocessing SEP (°C)	Preprocessed spectra (sym) SEP (°C)	Preprocessed spectra (db) SEP (°C)
Calibration[a]	0.15	0.17	0.18
Prediction set 1 (PS01)	0.27	0.28	0.22
Prediction set 2 (PS02)	0.74	0.20	0.22
Prediction set 3 (PS03)	1.07	0.17	0.22
Prediction set 4 (PS04)	2.14	0.31	0.21
Prediction set 5 (PS05)	0.78	0.35	0.22
Prediction set 6 (PS06)	0.39	0.31	0.34
Prediction set 7 (PS07)	1.46	0.26	0.34
Prediction set 8 (PS08)	1.43	0.19	0.26
Prediction set 9 (PS09)	1.40	0.75	0.19
Prediction set 10 (PS10)	1.64	0.74	0.18
Prediction set 11 (PS11)	1.67	0.41	0.36
Prediction set 12 (PS12)	2.27	0.21	0.28
Prediction set 13 (PS13)	2.95	0.25	0.20

[a]Statistics given for the calibration data are values of CV-SEP.

calibrations. The standard error of prediction (SEP) was computed for each prediction set. As described in Chapter 3 (Section 3.5), this statistic is analogous to CV-SEP in that it provides a standard error in predicted temperatures across the spectra in the prediction set. The model computed from buffer spectra with no preprocessing gave the highest SEP values (> 2 °C) and performed poorly over time. By comparison, the models based on preprocessed spectra gave SEP values ranging from 0.17 to 0.75 °C. It was also observed that 'db' wavelet preprocessing gave the best SEP values (ranging from 0.19 to 0.36 °C) and was robust over the time span of the experiment. The SEP values for the prediction sets are summarized in Table 4-7 and Figure 4-21.

4.4.7 Effects of signal preprocessing

Of the three models evaluated, the prediction performance of the temperature model based on the SNV + 'db' preprocessed buffer spectra was the best with time. Figure 4-22 presents the results of applying principal component analysis (PCA) to the calibration and prediction buffer spectra before (A) and after (B) preprocessing. The PCA calculation is summarized in Chapter 3 (Section 3.3.1). Spectra were mean-centered before submission to PCA and the range of 4,700 to 4,175 cm^{-1} was used in the calculation. In Figure 4-22, the scores along the first and second principal components are plotted, with color coding used to identify the individual data sets.

Improved clustering of the calibration and prediction data sets after preprocessing with the SNV transform and the 'db5' wavelet function can be observed in Figure 4-22. This helps to explain the excellent prediction performance of the calibration model with time. The use of preprocessing to remove spectral variance can also be observed in the % variance explained by the computed principal components. After applying preprocessing, the first principal component computed from the spectral data matrix explains 97% of the data variance compared to 87% before. This is an indication of increased similarity across the spectral data sets.

For the model based on SNV + db5 preprocessing (Model 3 in Table 4-6), Figure 4-23 displays the corresponding correlation and residual plots for the data used to generate the calibration model for temperature fluctuations in buffer spectra. Good correlation is evident between estimated and reference temperatures, although the residual plot exhibits increased variance at higher temperatures. This may suggest lower precision in the reference temperatures as the temperature increases.

Figures 4-24 through 4-26, respectively, represent the analogous correlation and residual plots obtained when this model was applied to prediction sets 3, 5, and 11 (PS03, PS05, PS11). While the overall correlation is still good, bias is evident in the residual plots for PS03 and PS11. Interestingly, the non-constant variance observed for the calibration residuals in Figure 4-23 is not observed in the plots of prediction residuals.

4.4.8 Prediction performance of temperature models in samples with increased complexity

The prediction performance of the temperature models was assessed further by applying them to the seven additional prediction sets described in Table 4-2. These data sets corresponded to sample matrixes with increased complexity. The three optimized calibration models described in Table 4-6 were again used without updating or other modification.

The SEP values obtained for these predictions are summarized in Figure 4-27 and Table 4-8. Also included in Table 4-8 are the bias components of the SEP values. The bias is computed as the numerical average of the errors in the predicted temperatures. It describes the systematic component of the errors.

The model based on phosphate buffer spectra with no preprocessing gave the highest SEP values (> 9 °C) and performed poorly with the increasing complexity of the samples. The models based on spectra preprocessed with the SNV and DWT methods gave SEP values ranging from 0.26 to 1.57 °C. It was also observed that preprocessing with the db5 wavelet gave the best SEP values (ranging from 0.33 to 1.01 °C). This

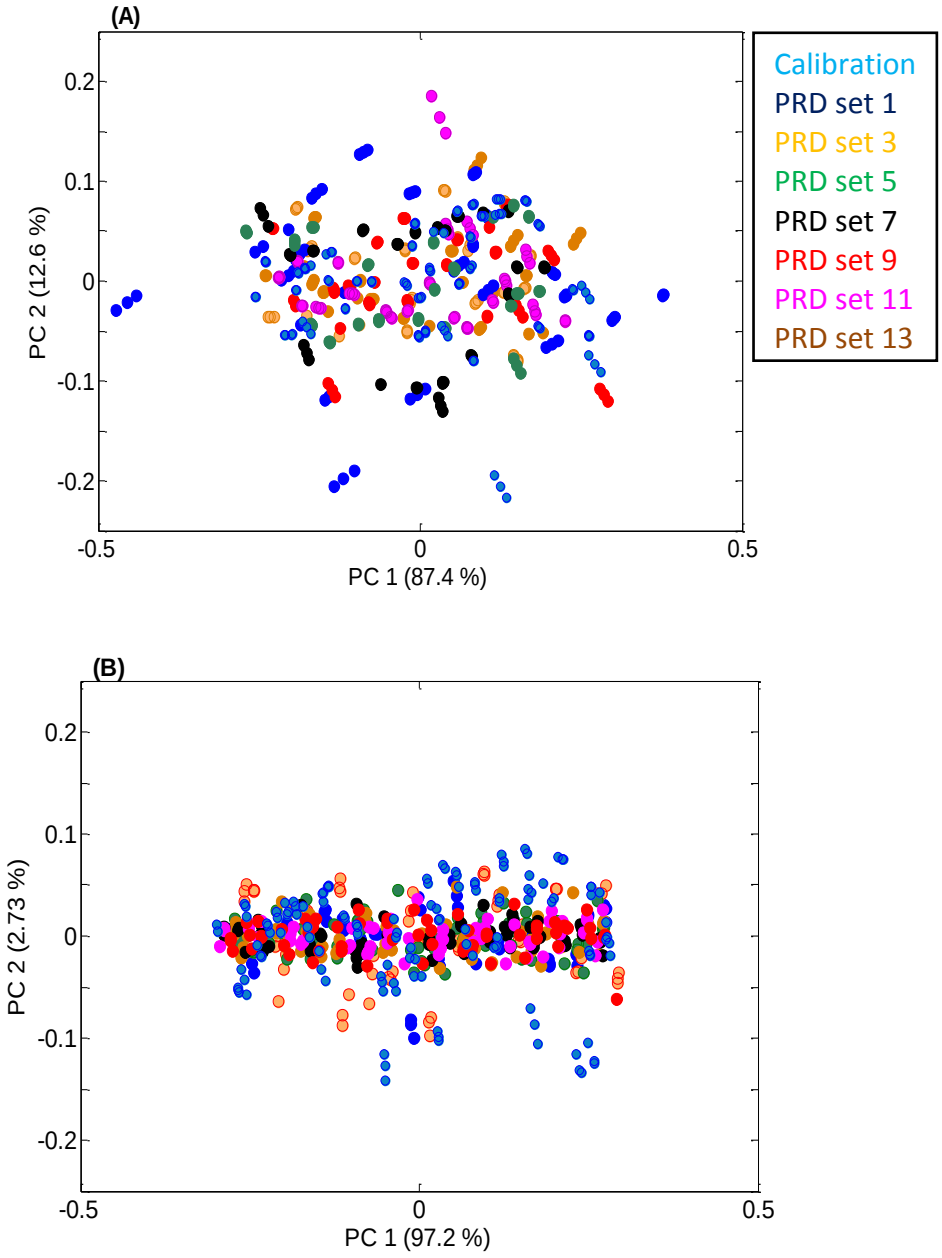

Figure 4-22. Principal component (PC) score plots. These plots correspond to the absorbance spectra of phosphate buffer before **(A)** and after **(B)** preprocessing with the SNV and DWT (db-5 wavelet function) calculations. Only seven sets of prediction spectra are represented in the figure for clarity. The percentage variance explained by each PC is given in the axis label.

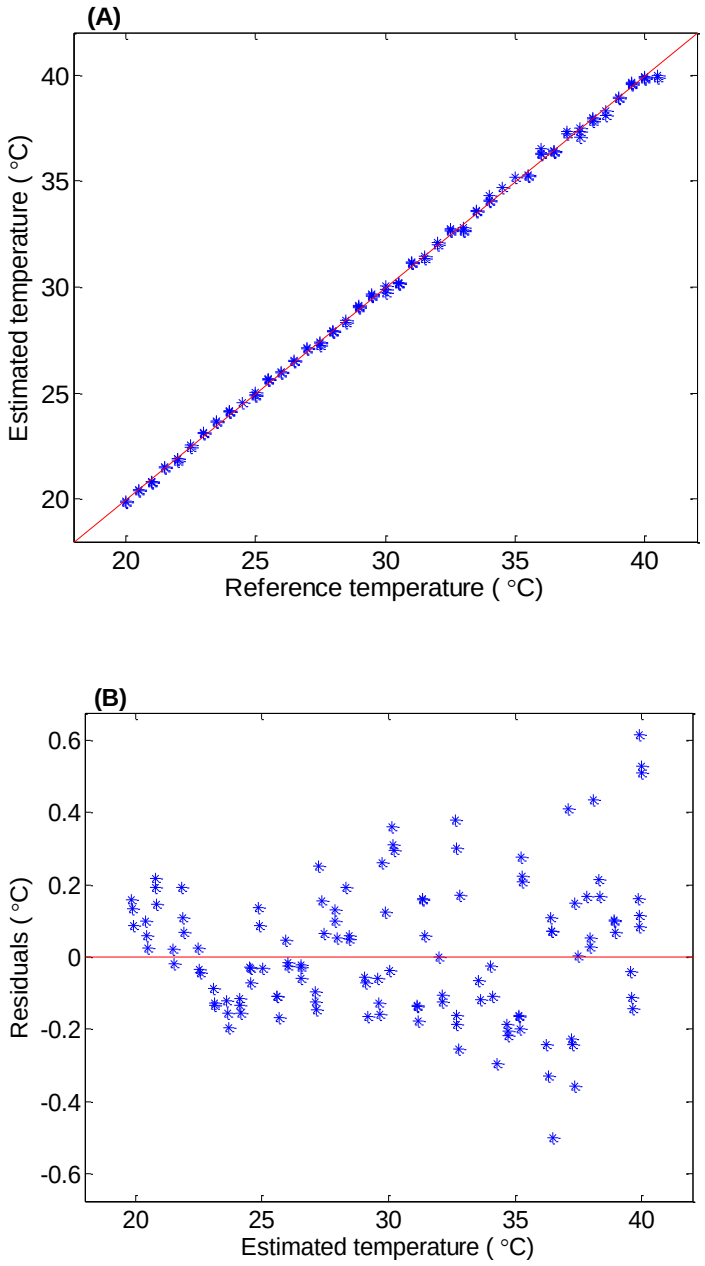

Figure 4-23. Correlations and residual plots for calibration. **(A)** Correlation and **(B)** residual plots corresponding to the calibration spectra used to generate the model for temperature fluctuations in buffer solutions. The model used included spectral preprocessing with the SNV and DWT methods (db5 wavelet). This corresponds to Model 3 in Table 4-6. The red lines in panels A and B, respectively, correspond to 0.0 residuals and perfect correlation between estimated and reference temperatures.

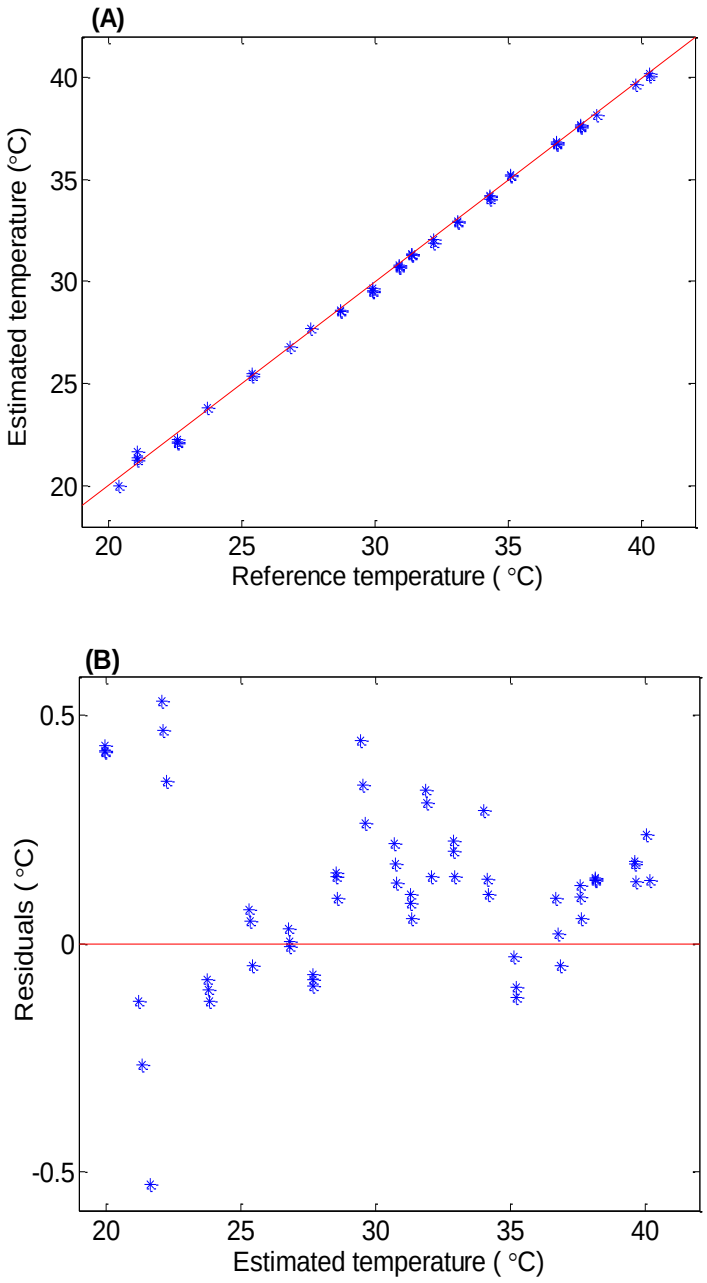

Figure 4-24. Correlation and residual plots. **(A)** Correlation and **(B)** residual plots for prediction set PS03 for temperature fluctuations in phosphate buffer solutions. The model used corresponds to Model 3 in Table 4-6. The red lines in panels A and B, respectively, correspond to 0.0 residuals and perfect correlation between estimated and reference temperatures. This prediction set was collected three months after the collection of the calibration data.

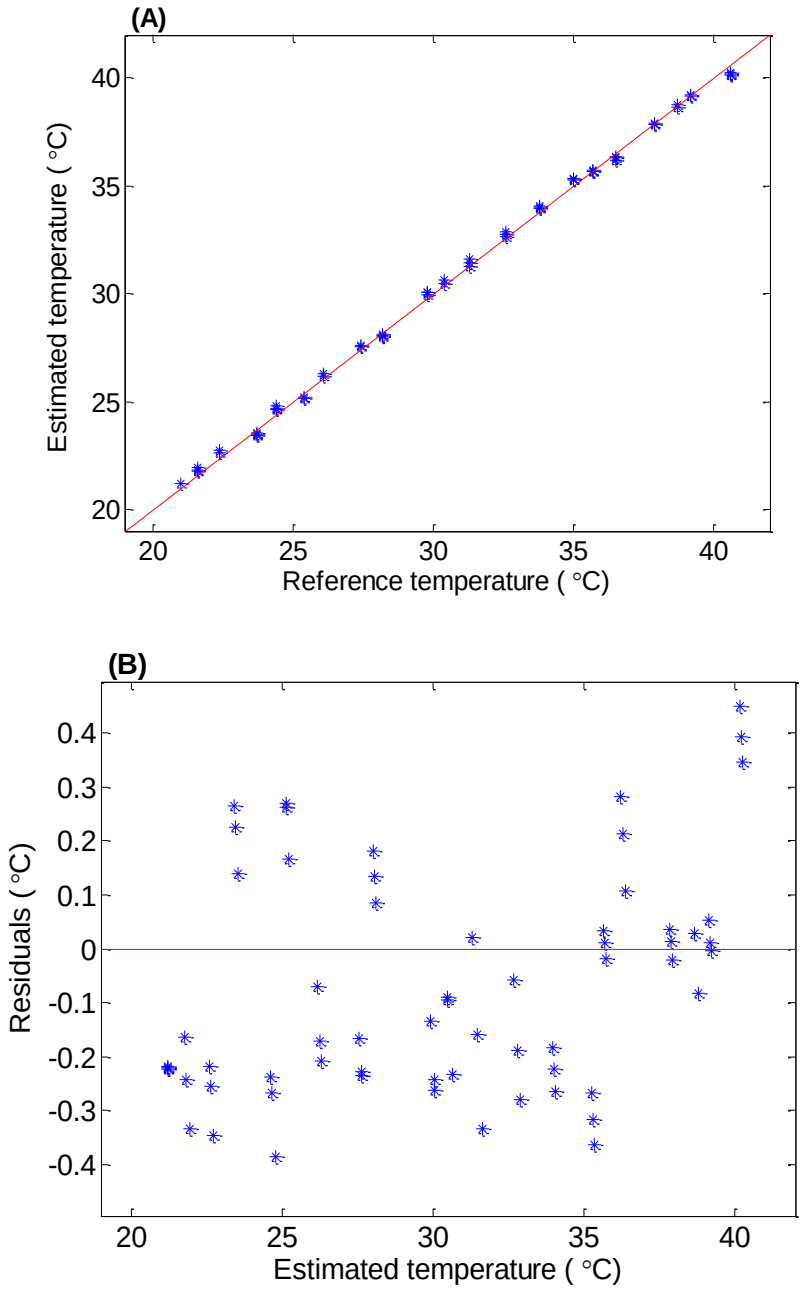

Figure 4-25. Correlations and residual plots. **(A)** Correlation and **(B)** residual plots for prediction set PS05 for temperature fluctuations in phosphate buffer solutions. The model used corresponds to Model 3 in Table 4-6. The red lines in panels A and B, respectively, correspond to 0.0 residuals and perfect correlation between estimated and reference temperatures. This prediction set was collected five months after the collection of the calibration data.

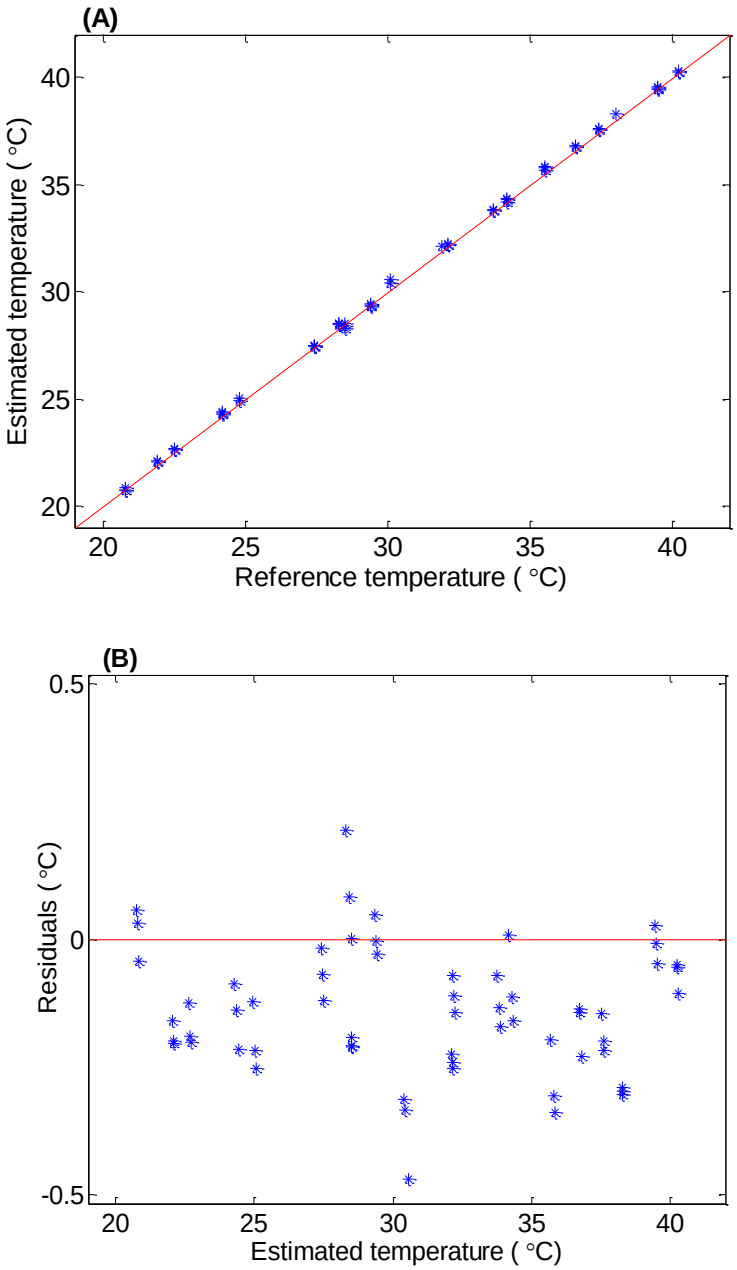

Figure 4-26. Correlations and residual plots. **(A)** Correlation and **(B)** residual plots of prediction set PS10 for temperature fluctuations in phosphate buffer solutions. The model used corresponds to Model 3 in Table 4-6. The red lines in panels A and B, respectively, correspond to 0.0 residuals and perfect correlation between estimated and reference temperatures. This prediction set was collected ten months after the collection of the calibration data

model performed reasonably well with the increasing complexity of the sample matrix.

The SEP values obtained for the BVP samples were the highest regardless of the calibration model used.. This could be due to the presence of dissolved proteins (globulins, albumins etc.) and different ionic species (K^+, Cl^-, Ca^{2+}, etc.) in the plasmasamples.[38,39]. Figures 4-28 through 4-30 represent the correlation and residual plots corresponding to a subset of these prediction sets. All of these figures are based on Model 3 in Table 4-6 (i.e., preprocessed sample spectra based on SNV and the db5 wavelet function).

The correlation plots all show a clear linear response with respect to temperature, although some bias is evident in the predicted temperatures. The residual plots show this bias effect more clearly. The amount and sign (i.e., positive or negative) of the bias appears to be related to the identity of the sample matrix rather than the time since the calibration data were collected.

This is confirmed by an inspection of the bias values reported in Table 4-8. For example, the average ± standard deviation of the bias values for the three data sets based on BVP samples was -0.88 ± 0.18. The corresponding values for the four data sets based on solutions containing glucose or glucose/lactate/urea were 0.32 ± 0.04. This suggests that each sample matrix contributes an approximately constant temperature offset to the calibration model computed from spectra of simple buffer solutions. A matrix-dependent additive correction factor may thus provide a practical solution to reduce this matrix effect.

4.5 Temperature modeling in biological samples

As discussed in Section 4.4.8, temperature models developed based on static measurements of pH 7.40 phosphate buffer gave SEP values in excess of 1.0 °C when applied to spectra of BVP samples. This could be due to the presence of complex biomolecules such as dissolved proteins in the BVP samples. The amount of dissolved proteins present in a plasma sample is approximately 6.0 to 8.0 g/dL. These dissolved

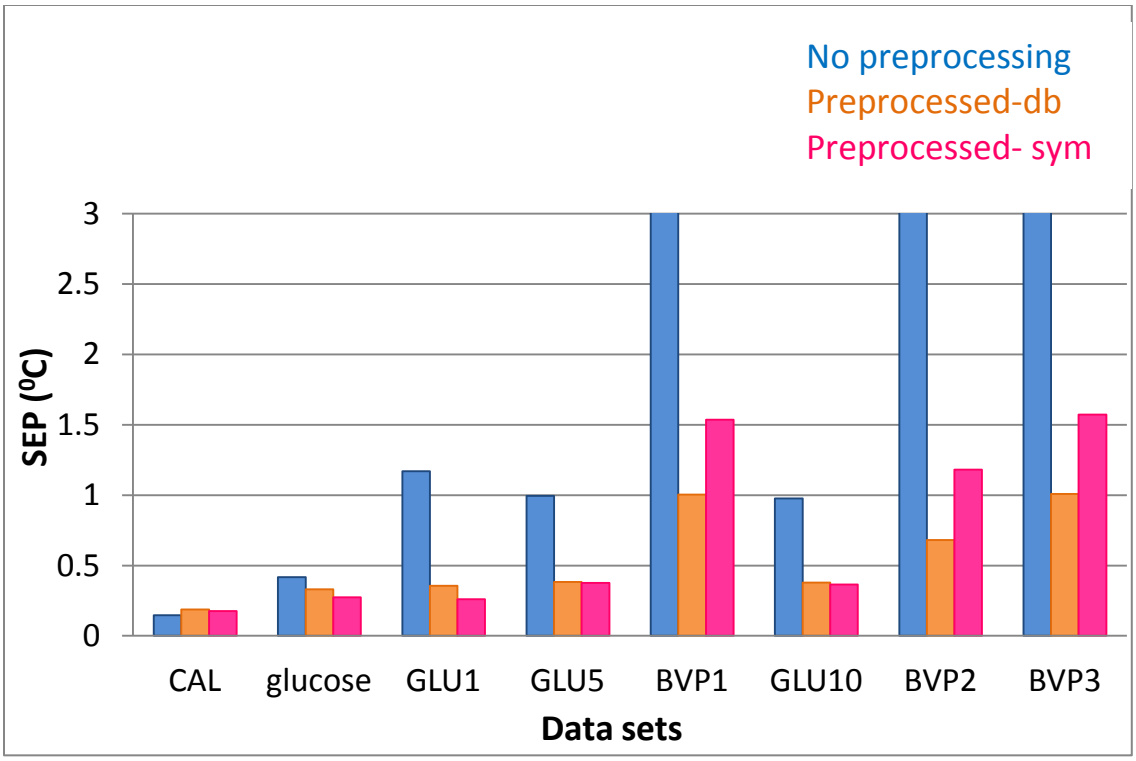

Figure 4-27. Prediction performance of PLS calibration models for temperature fluctuations in aqueous-based samples with increasingly complex matrixes. The values of CV-SEP for the calibration data and SEP for the 7 prediction sets are plotted. The SEP values for the model based on no spectral preprocessing are truncated at 3 °C for clarity. The model based on preprocessing with the db5 wavelet produces the best results overall.

Table 4-8. Prediction performance of PLS calibration models for temperature fluctuations in aqueous-based samples with increasingly complex matrixes.

Data set	No preprocessing		Preprocessed spectra (sym)		Preprocessed spectra (db)	
	SEP (°C)	**Bias (°C)**	**SEP (°C)**	**Bias (°C)**	**SEP (°C)**	**Bias (°C)**
Calibration[a]	0.15	0	0.17	0	0.18	0
Prediction set 14 (PS-G)	0.42	0.52	0.27	0.19	0.33	0.27
Prediction set 15 (PS-GLU1)	1.17	-1.07	0.26	0.20	0.36	0.33
Prediction set 16 (PS-GLU5)	0.99	-0.58	0.38	0.35	0.38	0.36
Prediction set 17 (PS-BVP1)	10.49	10	1.55	-1.52	1.00	-0.99
Prediction set 18 (PS-GLU10)	0.98	-0.29	0.36	0.32	0.38	0.34
Prediction set 19 (PS-BVP2)	9.85	9.6	1.18	-1.21	0.68	-0.67
Prediction set 20 (PS-BVP3)	9.96	9.9	1.57	-1.56	1.01	-0.99

[a]Statistics given for the calibration data are values of CV-SEP.

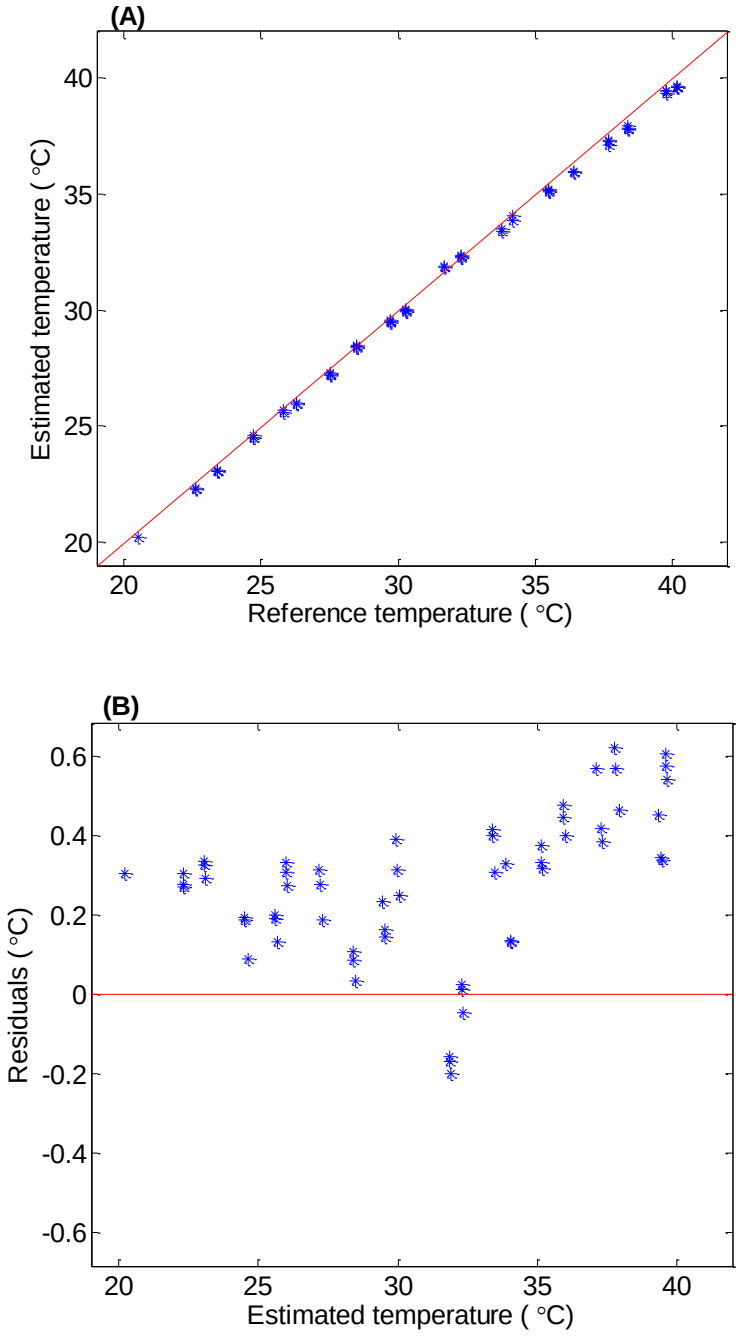

Figure 4-28. Correlations and residual plots. **(A)** Correlation and **(B)** residual plots for prediction set 14 (PS-GLU). The model used corresponds to Model 3 in Table 4-6. The red lines in panels A and B, respectively, correspond to perfect correlation between estimated and reference temperatures and 0.0 residuals.

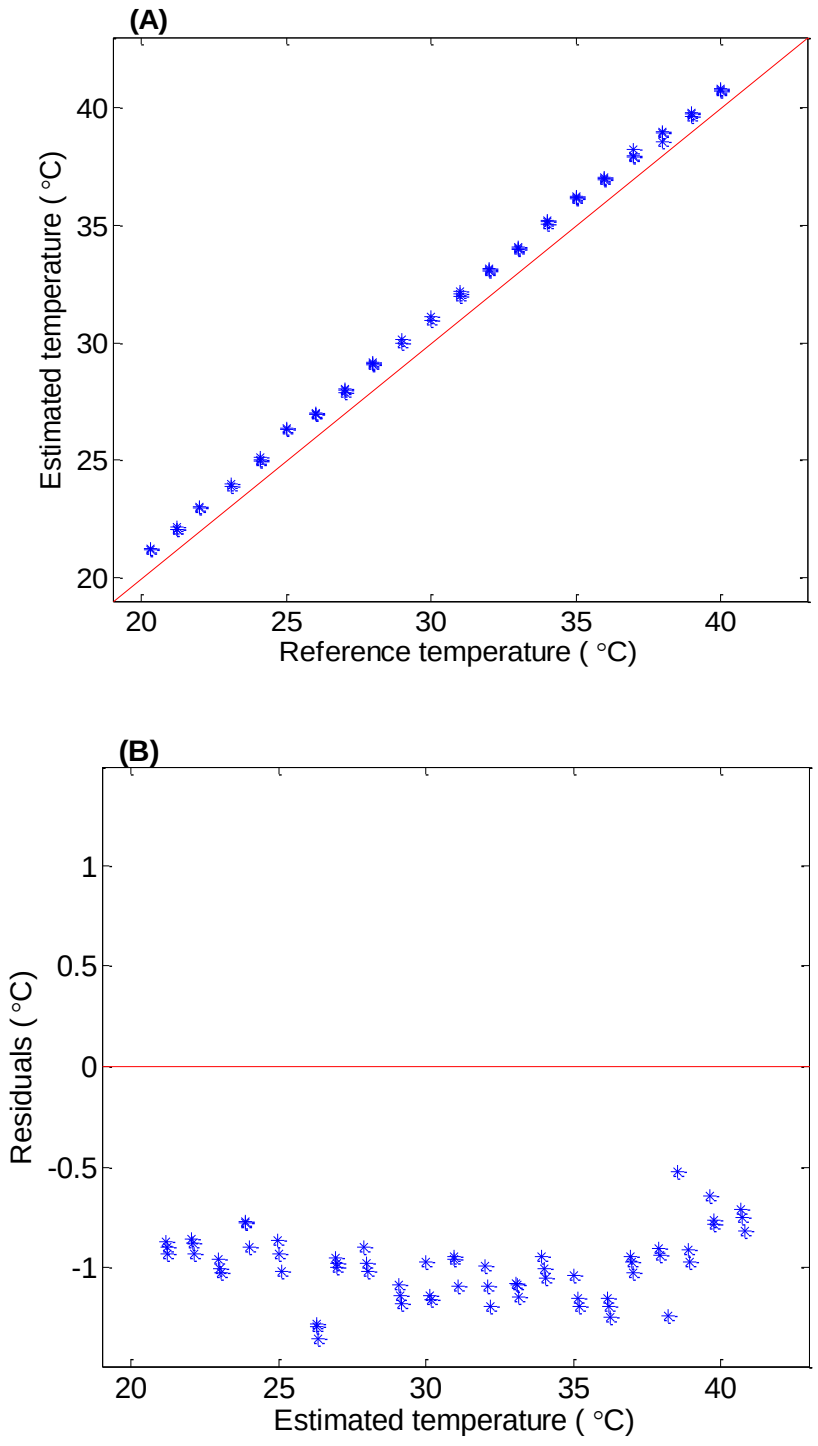

Figure 4-29. Correlations and residual plots for prediction set 17. **(A)** Correlation and **(B)** residual plots for prediction set 17 (PS-BVP1). The model used corresponds to Model 3 in Table 4-6. The red lines in panels A and B, respectively, correspond to perfect correlation between estimated and reference temperatures and 0.0 residuals.

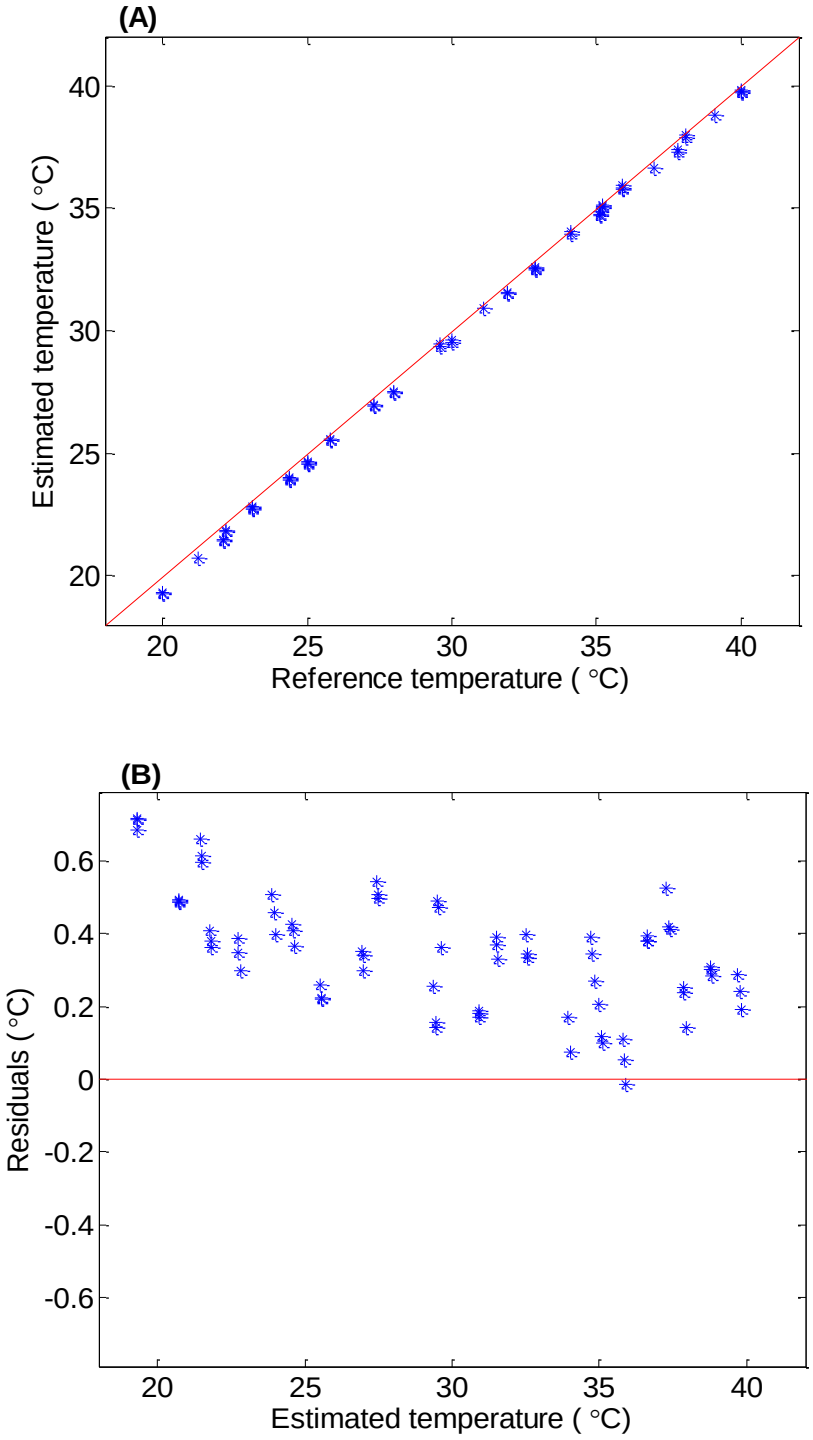

Figure 4-30. Correlations and residual plots for prediction set 18. **(A)** Correlation and **(B)** residual plots for prediction set 18 (PS-GLU10). The model used corresponds to Model 3 in Table 4-6. The red lines in panels A and B, respectively, correspond to perfect correlation between estimated and reference temperatures and 0.0 residuals.

proteins consist of albumins (3.4 to 5.4 g/dL), globulins (1.0 to 1.5 g/dL) and regulatory proteins.[43,44] A simple temperature model based on buffer might not be adequate to model the temperature fluctuations in a biological sample as it does not include the spectral features that arise due to the temperature dependence of dissolved proteins. In this study, the SNV transform combined with the DWT were used to preprocess the HSA absorbance spectra before submitting them to the PLS regression model. On the basis of the work described previously, wavelet functions from the Daubechies family were used. Figure 4-31 shows the spectral features of HSA absorbance spectra in the range of 4,000 to 5,000 cm^{-1} after preprocessing with the SNV and DWT methods.

The same optimization procedure described previously in Section 4.4.4 was employed to identify the optimal order of the wavelet function, level of decomposition and number of levels used in the reconstruction of the signal. As before, the optimization of the wavelet parameters was combined with the selection of the best spectral range and number of PLS latent variables. The minimum CV-SEP value was again used as the criterion for selecting the optimal parameters, and the *F*-test was employed at the 95% level to finalize the choice of the number of latent variables.

4.5.1 Temperature models for protein solutions

The optimized parameters for the best calibration model are summarized in Table 4-9. The optimal wavenumber range was 4,675 to 4,150 cm^{-1} with three PLS factors. The optimal preprocessing method was the SNV transform combined with the db5 wavelet function at six levels of decomposition and using only level 6 for reconstruction. The CV-SEP value for the best model was 0.17 °C, a similar level of performance to that obtained for the simple buffer solutions studied previously (Table 4-6). The presence of proteins did cause the optimal number of terms in the PLS model to increase from 1 to 3, however. This suggests the need to incorporate the increased spectral complexity of the protein spectra into the temperature model.

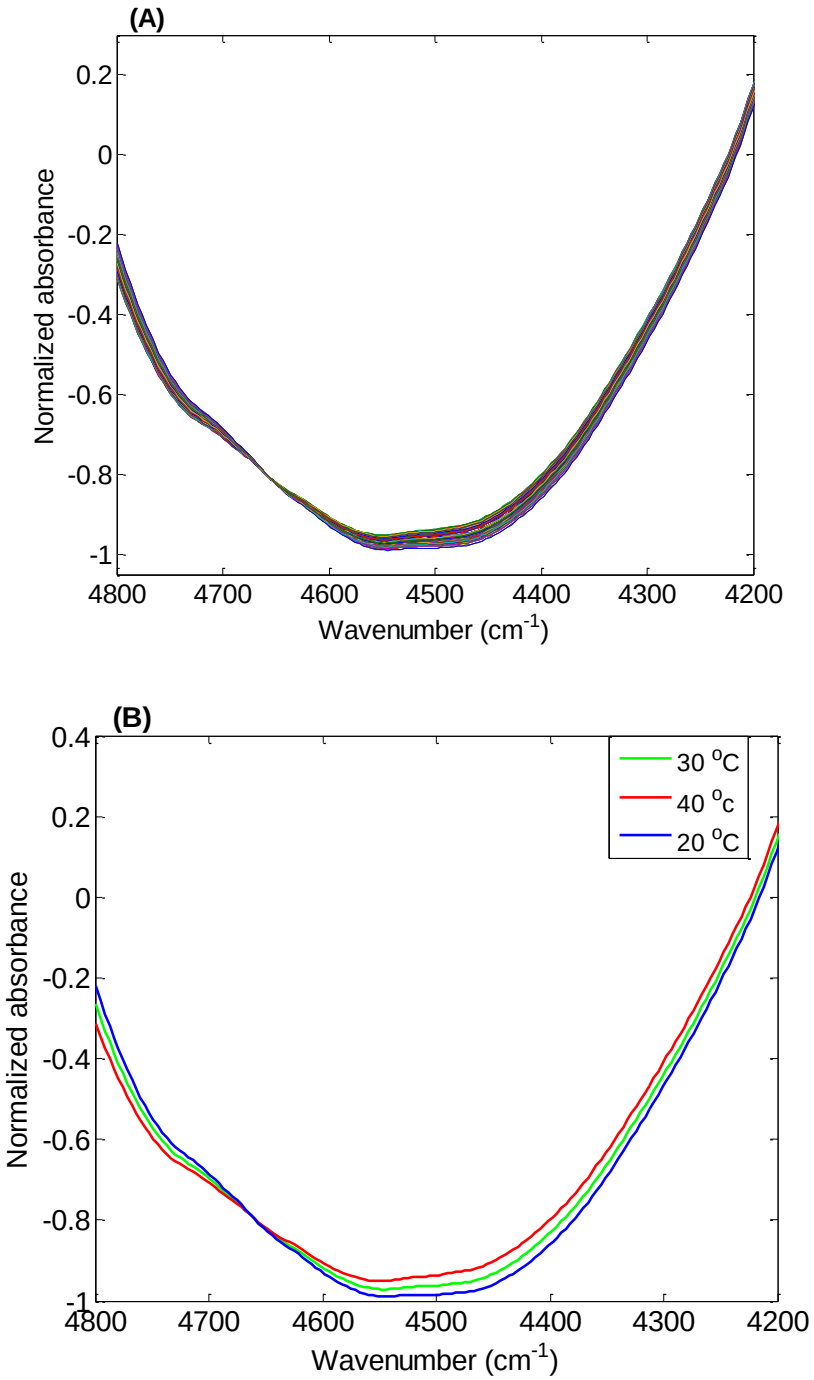

Figure 4-31. Preprocessed NIR spectra of solutions of HSA in phosphate buffer collected over the range of 20.0 to 40.5 °C. Spectral preprocessing was based on application of the SNV and DWT (db5, 6 levels of decomposition, and level 6 only used in reconstruction) methods. The shown spectra are collected **(A)** over the range of 20.0 to 40.5 °C and **(B)** at 20.0, 30.0 and 40.0 °C.

4.5.2 Prediction performance of temperature models for aqueous-based samples in the presence of dissolved proteins

The prediction performance of the calibration model was assessed using two prediction sets consisting of HSA (PS-HSA) and BVP (PS-BVP4) spectra, respectively. The SEP values for the predictions sets are summarized in Table 4-10. For prediction sets PS-HSA and PS-BVP4, the SEP values obtained were 0.29 °C and 0.18 °C, respectively. Figures 4-32 through 4-34 show the correlation and residual plots for the calibration and prediction data sets for the best temperature model. The predictions are very successful, as evidenced by the low SEP values and excellent correlation between estimated and reference temperatures. Some bias in the estimated temperatures of the two prediction sets is noted in the residual plots. The residual plot for PS-HSA also appears to display non-constant variance, with the variance in the residuals increasing toward the higher estimated temperatures. This behavior was also noted in Figure 4-23 but it does not appear in a consistent manner across the prediction sets.

4.6 Effect of pH and concentration variation on temperature predictions

An investigation was conducted to study the impact of pH and buffer concentration on the temperature models. Fluctuations in pH and the molarity of the phosphate buffer can alter the hydrogen-bonding network of water molecules (water clusters) in the solution. As shown in Eqs. 4-1 to 4-3, fluctuations in pH can also change the ratio of phosphate species present in the buffer solution.[40,45]

$$H_3PO_{4\,(aq)} \leftrightarrow H^+_{(aq)} + H_2PO_4^-{}_{(aq)} \qquad pKa_1 = 2.15 \qquad (4\text{-}1)$$

$$H_2PO_4^-{}_{(aq)} \leftrightarrow H^+_{(aq)} + HPO_4^{2-}{}_{(aq)} \qquad pKa_2 = 7.20 \qquad (4\text{-}2)$$

$$HPO_4^{2-}{}_{(aq)} \leftrightarrow H^+_{(aq)} + PO_4^{3-}{}_{(aq)} \qquad pKa_3 = 12.35 \qquad (4\text{-}3)$$

Fluctuations in molarity can change the buffer capacity of the phosphate buffer and can also change the concentration of Na^+ in the solution.

Changes in the ratio of phosphate species present in the solution and buffer capacity can alter the hydrogen bonding between phosphate species and water molecules.

Table 4-9. Best PLS calibration model for temperature fluctuations in aqueous-based samples in the presence of dissolved proteins

Wavenumber range (cm^{-1})	**Preprocessing method**	**Latent variables**	**SEC (°C)**	**CV-SEP (°C)**
4,675-4,150	SNV & DWT (db5, 6 [6])[a]	3	0.14	0.17

[a]Notation is wavelet family and order of wavelet function, number of levels of decomposition, and the levels used in the reconstruction of the spectrum.

Table 4-10. Prediction performance of PLS calibration model for temperature fluctuations in aqueous-based samples in the presence of dissolved proteins.

Data set	**SEP (°C)**
Calibration[a]	0.17
Prediction set 21 (PS-HSA)	0.29
Prediction set 22 (PS-BVP4)	0.18

[a]Statistics given for the calibration data are values of CV-SEP.

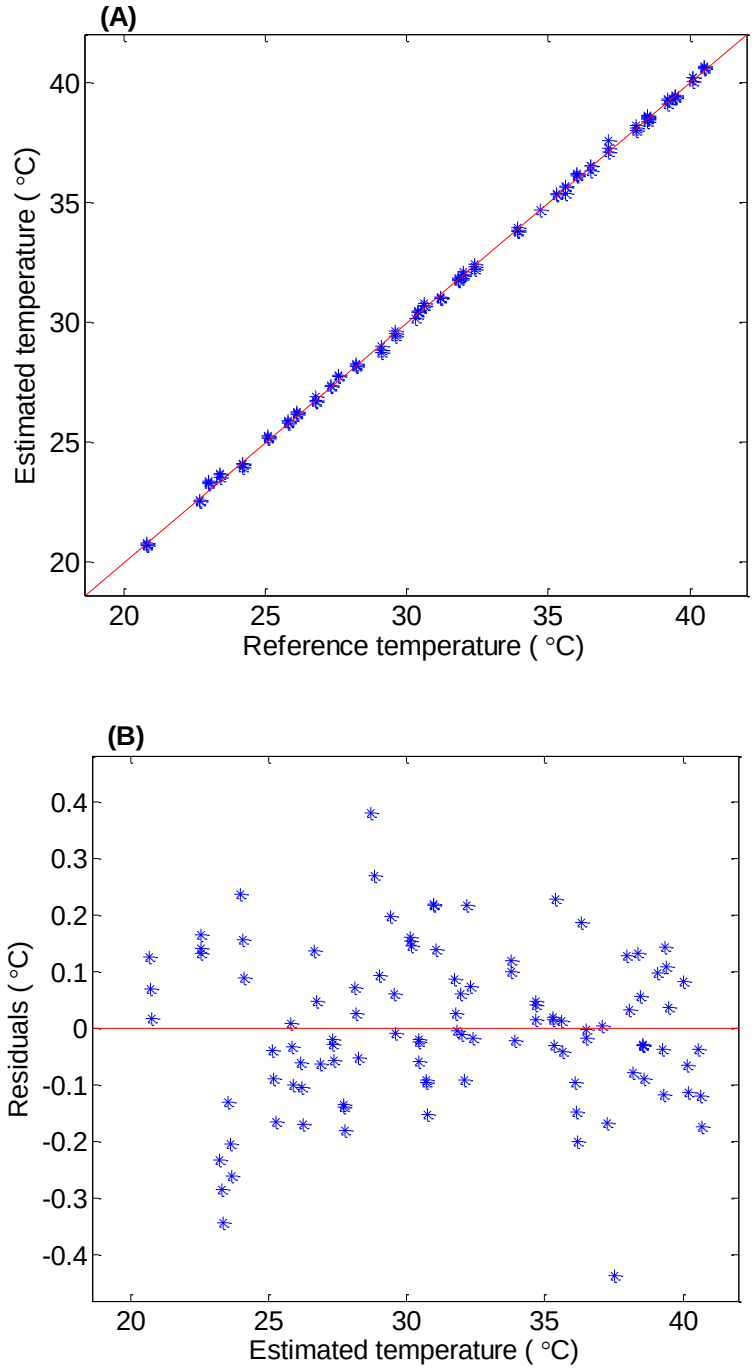

Figure 4-32. Correlation and residual plots for calibration. Correlation (**A**) and residual (**B**) plots for the calibration spectra used to describe temperature fluctuations in buffer solutions in the presence of dissolved proteins. The red lines in panels A and B, respectively, correspond to perfect correlation between estimated and reference temperatures and 0.0 residuals.

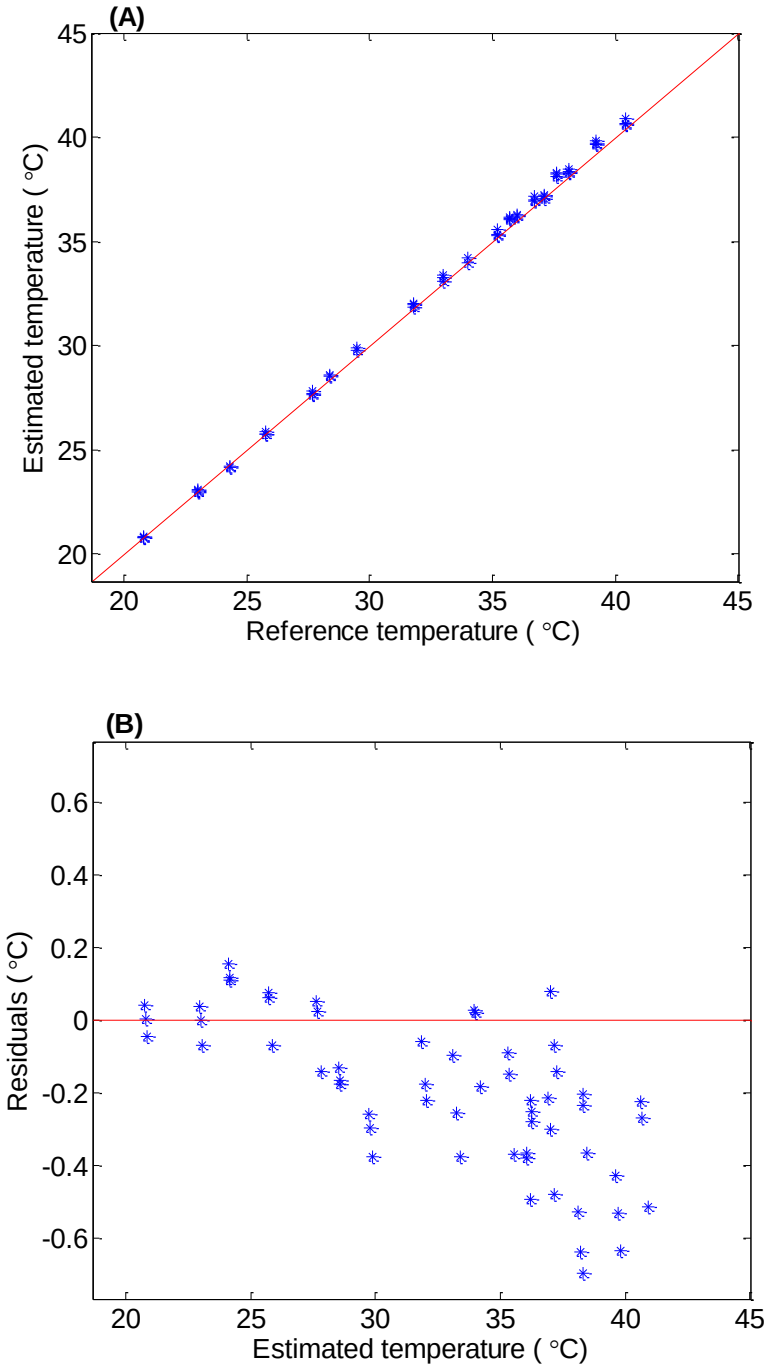

Figure 4-33. Correlation and residual plots. Correlation (**A**) and residual (**B**) plots for prediction set 21 (PS-HSA). The red lines in panels A and B, respectively, correspond to perfect correlation between estimated and reference temperatures and 0.0 residuals.

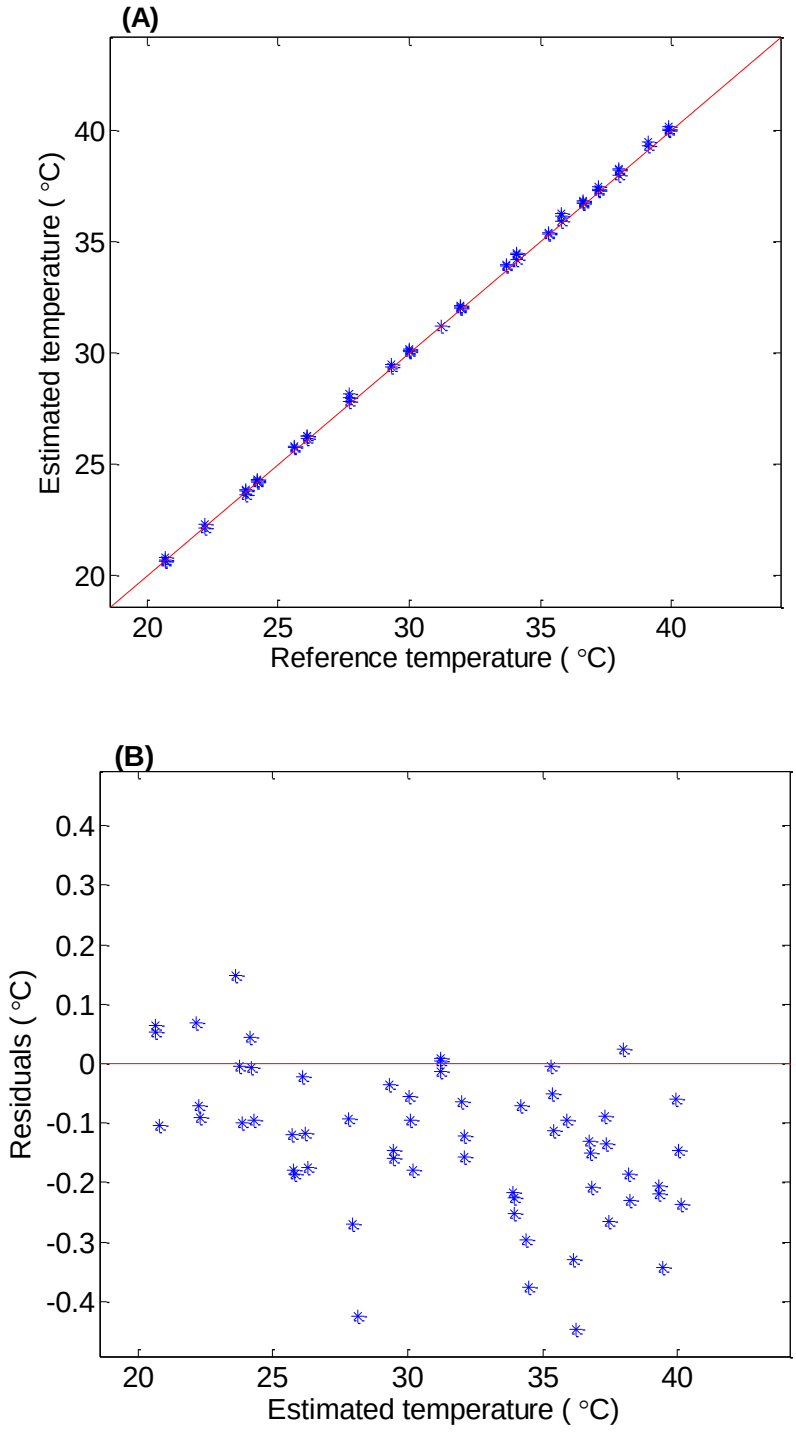

Figure 4-34. Correlations and residual plots. Correlation (**A**) and residual (**B**) plots for prediction set 22 (PS-BVP4). The red lines in panels A and B, respectively, correspond to perfect correlation between estimated and reference temperatures and 0.0 residuals.

Moreover, changes in Na^+ concentration can affect the degree of ion-dipole interactions between Na^+ and water molecules.[40,45] Each of these interactions can ultimately alter the hydrogen-bonding network formed by the water molecules and thereby affect the magnitude of the peak shifts observed in the NIR spectrum as a consequence of temperature fluctuations. Figures 4-35 and 4-36 illustrate absorbance spectra of phosphate buffer obtained at different temperatures with varying molarities and pH values. Clear effects are seen to arise in the spectra from variation in both buffer molarity and pH.

The practical significance of these effects on temperature modeling can be assessed by submitting the spectra collected in the presence of variation in pH and buffer molarity to the previously computed temperature model based on spectra of 0.100 M, pH 7.40 buffer (Model 3 in Table 4-6). In this evaluation, the 291 spectra (calibration and two prediction sets) collected under conditions of varying pH and buffer concentration (Table 4-4) were combined and submitted to the previously computed temperature model. The time span of these prediction data was 14 months relative to the calibration.

The overall SEP for these temperature predictions was 0.59 °C. The SEP for the 126 spectra with varying pH levels and a constant buffer concentration of 0.100 M was 0.53 °C, while the SEP for the 129 spectra with varying buffer concentrations and a constant pH of 7.40 was 0.59 °C. The SEP value for the 36 spectra which were collected at pH 7.40 and buffer concentration of 0.100 M (i.e., the same conditions as the calibration data) was 0.27 °C. When compared to the to the results presented previously in Table 4-7, it is clear that the SEP values obtained under conditions of variation in pH and buffer molarity are higher, even when the time span of the data relative to the calibration is considered. This confirms that variations in pH and molarity complicate the calibration models for temperature prediction.

Figure 4-37 plots the residuals for these temperature predictions as a function of pH (A) and buffer molarity (B). In each panel, points plotted in blue have the same value

of the alternate variable, while points plotted in red have varying values of that variable. For example, in Figure 4-37A, the red points have varying levels of buffer molarity, while the observations plotted in blue all correspond to 0.100 M.

According to Figure 4-37A, the temperature residuals show some dependence on pH, although the exact shape of the functional relationship is not clear. This appears to preclude the use of a simple correction procedure for the predicted temperature on the basis of knowledge of the solution pH.

An inspection of Figure 4-37B reveals no clear relationship between the temperature residuals and the molarity of the buffer, at least over the molarity range studied in this work. This again suggests there is no simple correction for the effects of changes in the molarity of the buffer. It thus appears necessary to incorporate variation in solution pH and molarity into the temperature models.

4.6.1 Models for temperature fluctuations in aqueous-based samples including pH and molarity variation

Given the negative effect on temperature predictions resulting from variation in pH and buffer molarity, new PLS temperature models were computed specifically to account for this variation. Absorbance spectra relative to an air background were used as before and the SNV + DWT preprocessing steps were applied. The Daubechies family of wavelets was again used. The optimization procedures for the wavelet and PLS parameters were the same as described previously in Section 4.4.4. Figure 4-38 illustrates the calibration spectra after preprocessing with the SNV and DWT methods.

The two best calibration models obtained from the optimization procedure are summarized in Table 4-11. The optimal wavenumber range for Model 1 was 4,650 to 4,250 cm^{-1} with 3 PLS factors, while the range for Model 2 was 4,725 to 4,150 cm^{-1} with 3 PLS factors. The optimal preprocessing method for both calibration models was SNV combined with the db5 wavelet function at seven levels of decomposition and using only level 7 for reconstruction. The CV-SEP values for Models 1 and 2 were 0.24 and 0.22 °C

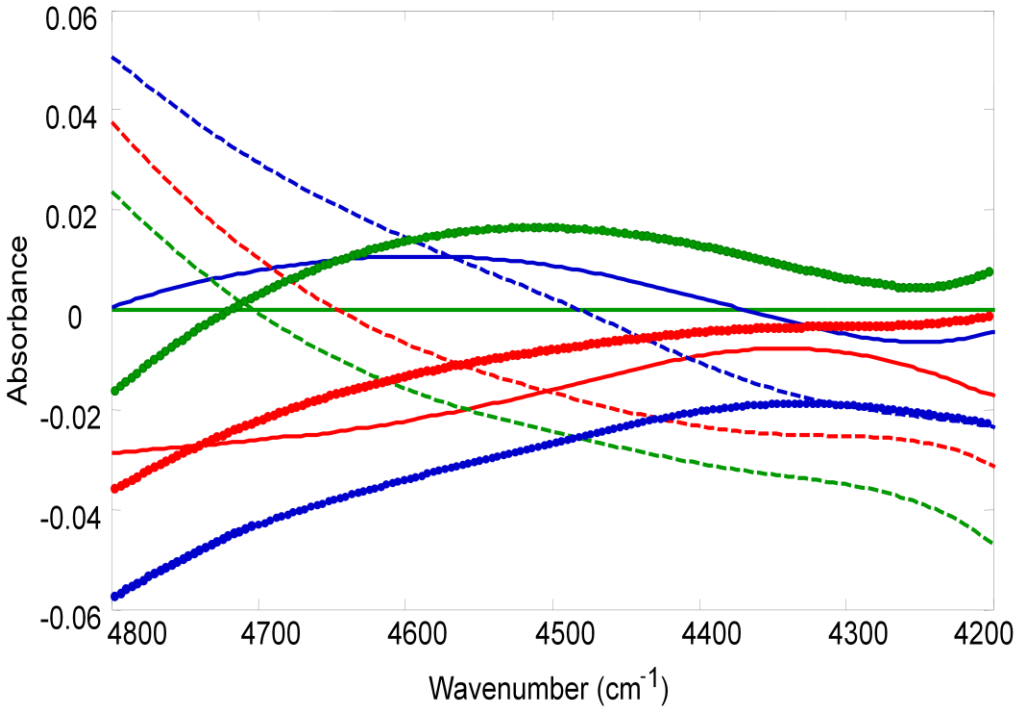

Figure 4-35. Absorbance spectra of pH 7.41 phosphate buffer spectra obtained at different temperatures and molarities. These spectra were generated from the ratio of single-beam spectra of pH 7.41 phosphate buffer collected at combinations of 30, 37 and 40 °C / 0.0500, 0.100 and 0.200 M with respect to a single-beam background buffer spectrum taken at 37 °C, 0.100 M, and pH 7.41. Solid, dashed, and dotted lines represent 37, 30 and 40 °C, respectively. Lines drawn in blue, green and red represent the 0.050, 0.100 and 0.200 M concentrations of buffer, respectively. The green line at a constant absorbance of 0.0 represents an exact match to the conditions of the background spectrum used in the absorbance calculation.

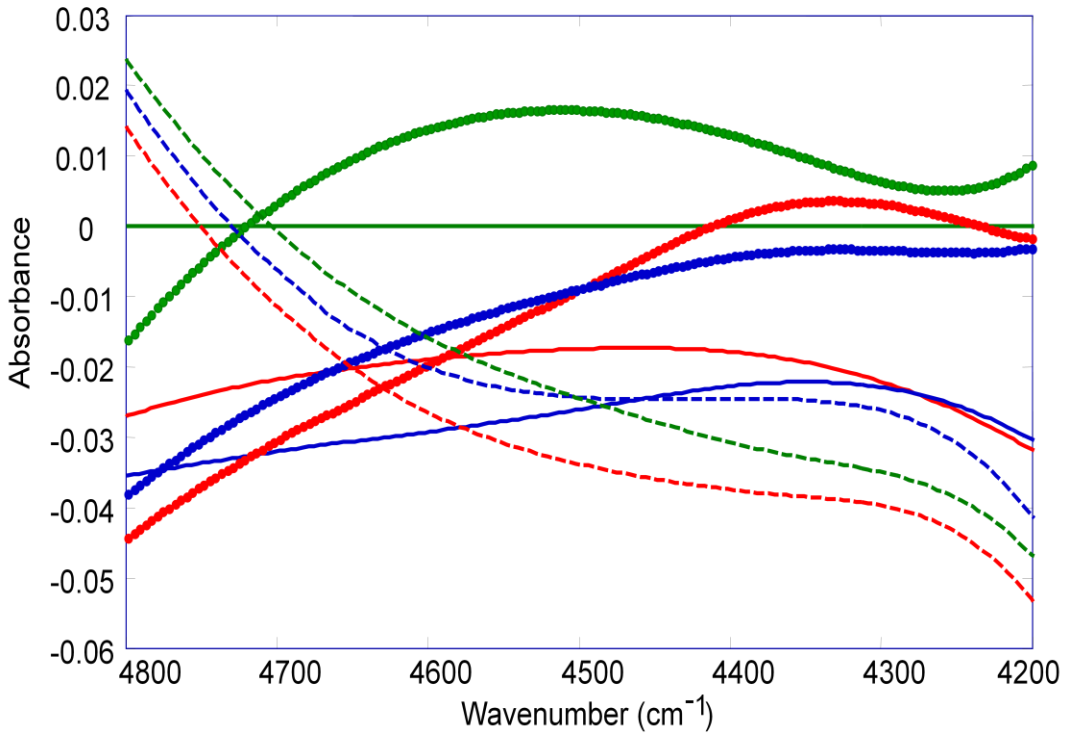

Figure 4-36. Absorbance spectra of 0.100 M phosphate buffer spectra obtained at different temperatures and pH values These spectra were generated from the ratio of single-beam spectra of 0.100 M phosphate buffer collected at combinations of 30, 37 and 40 °C / pH 4.84, 7.41 and 8.68 with respect to a single-beam background buffer spectrum taken at 37 °C, pH 7.41, and 0.100 M. The solid, dashed, and dotted lines represent 37, 30 and 40 °C, respectively. The blue, green and red lines correspond to pH values of 4.76, 7.41 and 8.68, respectively. The green line at a constant absorbance of 0.0 represents an exact match to the conditions of the background spectrum used in the absorbance calculation.

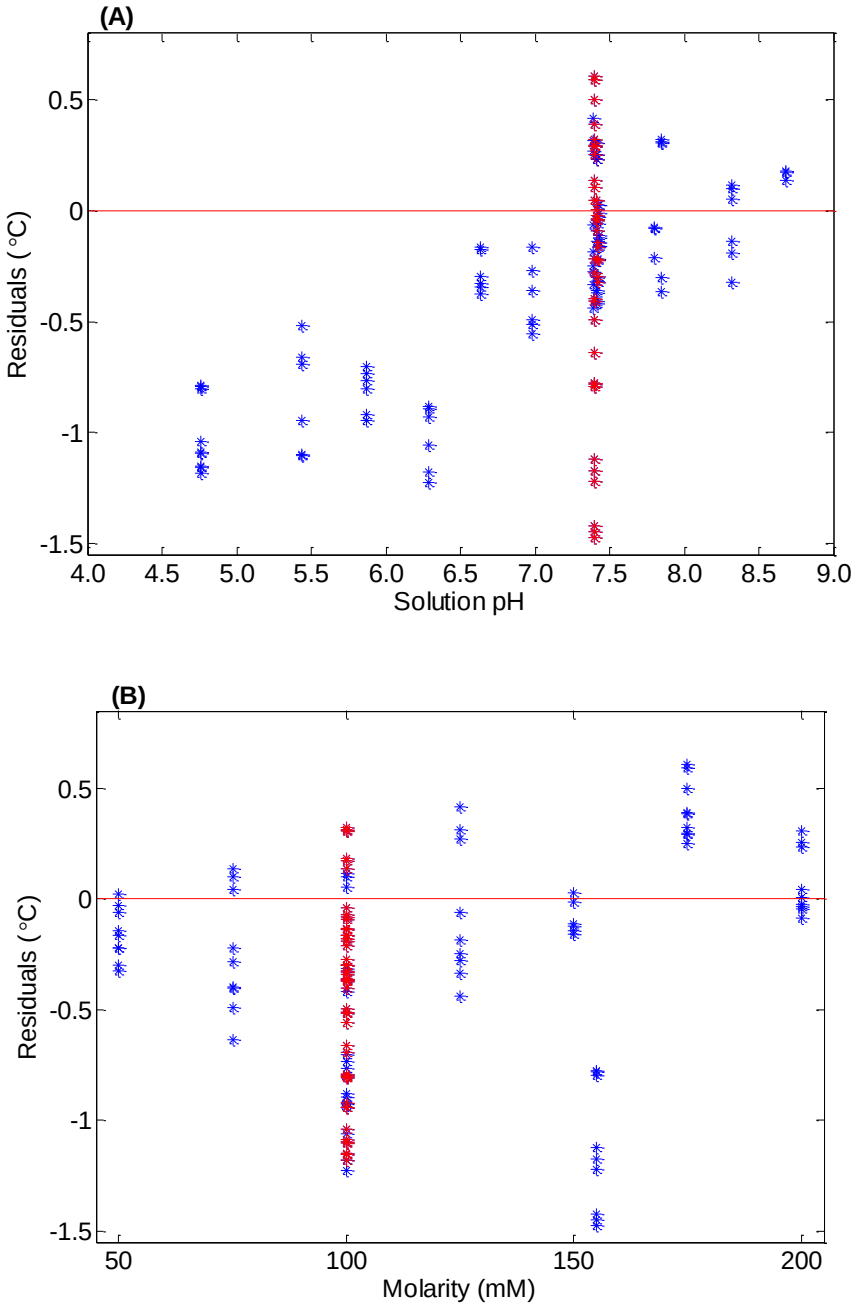

Figure 4-37. Effect of solution pH and molarity on temperature variations**.** Plots of residuals in predicted temperature vs. pH (**A**) and buffer molarity (**B**). The temperature model employed was based on 0.100 M, pH 7.40 phosphate buffer (Model 3 in Table 4-6). In each panel, the points marked in blue have a constant level of the alternate variable, while points plotted in red correspond to a different level of molarity (**A**) or pH (**B**).

respectively. This level of performance in calibration is similar to that obtained previously with fixed pH and buffer concentration. Two additional PLS factors are required (i.e., 3 vs. 1 latent variables), however, to account for the additional variation.

4.6.2 Prediction performance of temperature models for aqueous-based samples including pH and molarity variation

The prediction performance of these calibration models was assessed using two prediction sets of phosphate buffer spectra with varying pH and molarity values collected over two months. The SEP values for the prediction sets are summarized in Table 4-12. Both models gave SEP values ranging from 0.30 to 0.32 °C. This level of performance is consistent with previous results and suggests the effects on the spectra due to changes in both the molarity of the buffer and pH can be incorporated successfully into the temperature models.

Figures 4-39 through 4-41 display correlation and residual plots for the calibration and prediction data sets derived from Model 2 in Table 4-11. The correlations are visually very strong between estimated and reference temperatures. A slight linear ramp with increasing estimated temperature is observed in the residual plots for the prediction sets. This is a multiplicative effect different from the simple additive bias observed with the other prediction sets. The effect is quite small, however, as reflected in the low values of SEP.

4.6.3 Principal component analysis of calibration spectra

As a final evaluation step, PCA was performed on the preprocessed absorbance spectra (SNV + DWT (db5, seven levels of decomposition, only level 7 used in reconstruction) from the calibration set to gain further insight into the variation induced by changes in pH and buffer concentration. The spectral data matrix was mean centered before the PCA calculation and the wavenumber range of 4,725 to 4,150 cm^{-1} was used. Figures 4-42A and 4-43A are score plots based on PCs 1 and 2. Figures 4-42B and 4-43B are score plots based on PCs 2 and 3. The same data are represented in the four figures

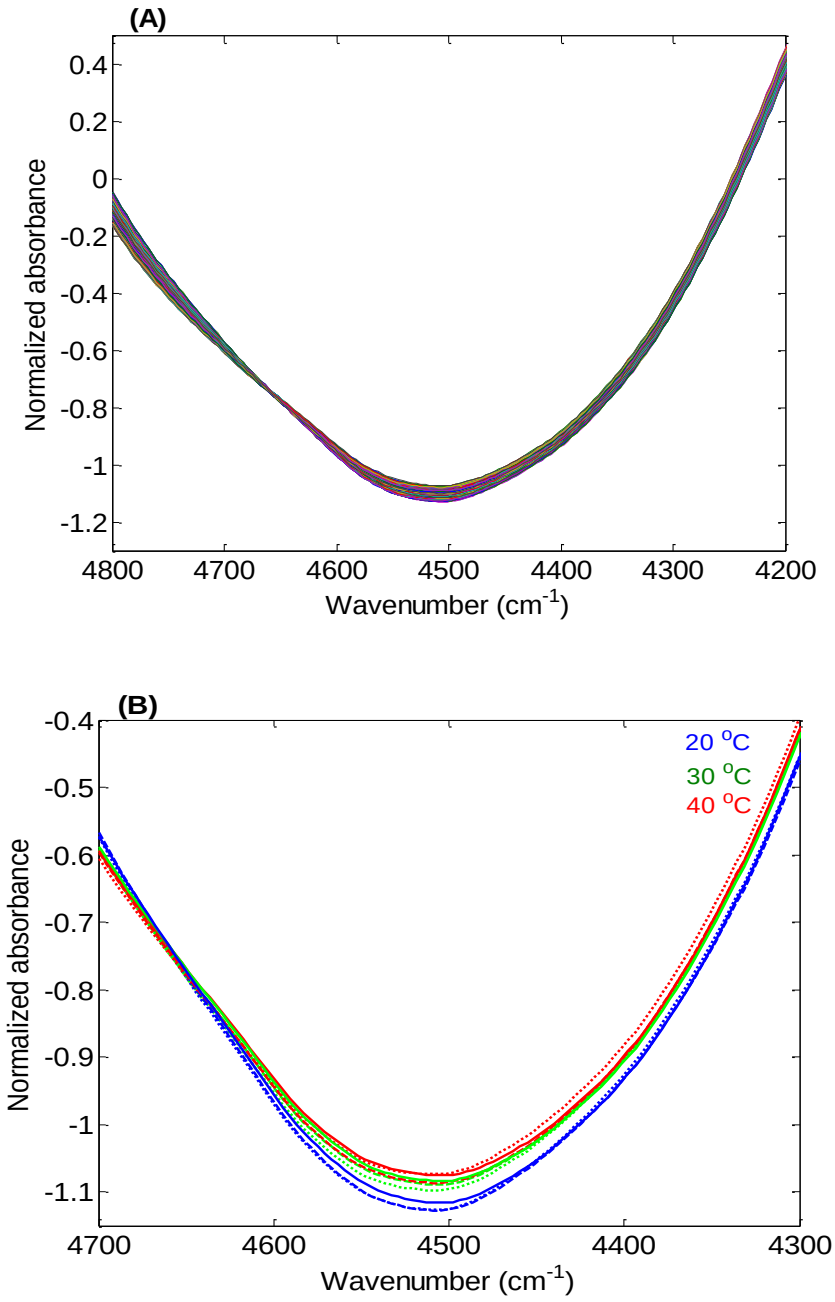

Figure 4-38. Preprocessed NIR spectra of phosphate buffer solutions collected over the range of 20.0 to 40.5 °C under conditions of varying pH and molarity. The SNV and DWT (db5, seven levels of decomposition, only level 7 used in reconstruction) methods were used. (A) represents the spectra collected over the range of 20.0 to 40.5 °C. **(B)** represents the same preprocessed spectra collected at 20.0, 30.0 and 40.0 °C. Plotted with dashed and dotted lines represent pH values of 4.7 and 8.6 at 0.100 M buffer, respectively, and solid lines represent a pH of 7.41 at 0.175 M buffer.

Table 4-11. Best PLS calibration models for temperature fluctuations in aqueous-based samples including pH and molarity variation

Model No.	Wavenumber range (cm^{-1})	Preprocessing method	Latent variables	SEC (°C)	CV-SEP (°C)
1	4,650-4,250	SNV & DWT (db5, 7 [7])[a]	3	0.21	0.24
2	4,725-4,150	SNV & DWT (db5, 7 [7])[a]	3	0.20	0.22

[a]Notation is wavelet family and order of wavelet function, number of levels of decomposition, and the levels used in the reconstruction of the spectrum.

Table 4-12. Prediction performance of PLS calibration models for temperature fluctuations in aqueous-based samples including pH and molarity variation

Data set	SEP (°C)	
	Model 1[a]	Model 2[a]
Calibration[b]	0.24	0.22
Prediction set 23 (PS23)	0.30	0.30
Prediction set 24 (PS24)	0.31	0.32

[a]Model numbers refer to Table 4-11.

[b]Statistics given for the calibration data are values of CV-SEP.

but with different symbols. The pH values are marked in Figure 4-42, while Figure 4-43 denotes the molarity values. Inspection of Figures 4-42A and 4-43A reveals that the majority (96.1 %) of the spectral variance can be explained by a single PC and that this factor is clearly related to temperature. A clear ordering of the data is seen with respect to temperature in the scores along the first PC.

In Figure 4-42B, some grouping of data related to pH values can be seen. Similarly, in Figure 4-43B, some grouping of the data related to molarity values can be seen. This suggests that any information related to pH and molarity changes is explained by the second and/or third PCs which together account for ~3.9 % of the spectral variance. However, no simple relationships are apparent among the levels of either pH or molarity.

4.7 Temperature predictions in flowing solutions

The final component of the temperature modeling study involved the investigation of temperature predictions in flowing solutions. As described previously, a set of calibration spectra and two prediction sets were collected from pH 7.40, 0.100 M phosphate buffer at each of three flow rates. As an initial assessment of the impact of a flowing sample on the temperature predictions, the calibration and prediction data for each flow rate were pooled to yield three sets of 147 spectra. These spectra were submitted to the previously computed calibration model developed from static solutions of the same buffer (Model 3 in Table 4-6). For flow rates of 68, 76, and 85 mL/min, the corresponding SEP values were 7.6, 7.5 and 7.7 °C, respectively. The time span of the data collected from the flowing samples was 20 months relative to the calibration spectra used to compute the temperature model. These SEP values indicate that calibration models developed from the static buffer solution spectra are not adequate to model temperature variations in a flowing solution.

Individual calibration models were next computed from the flow cell data for each flow rate. In this study, the SNV transform combined with the DWT were again used to

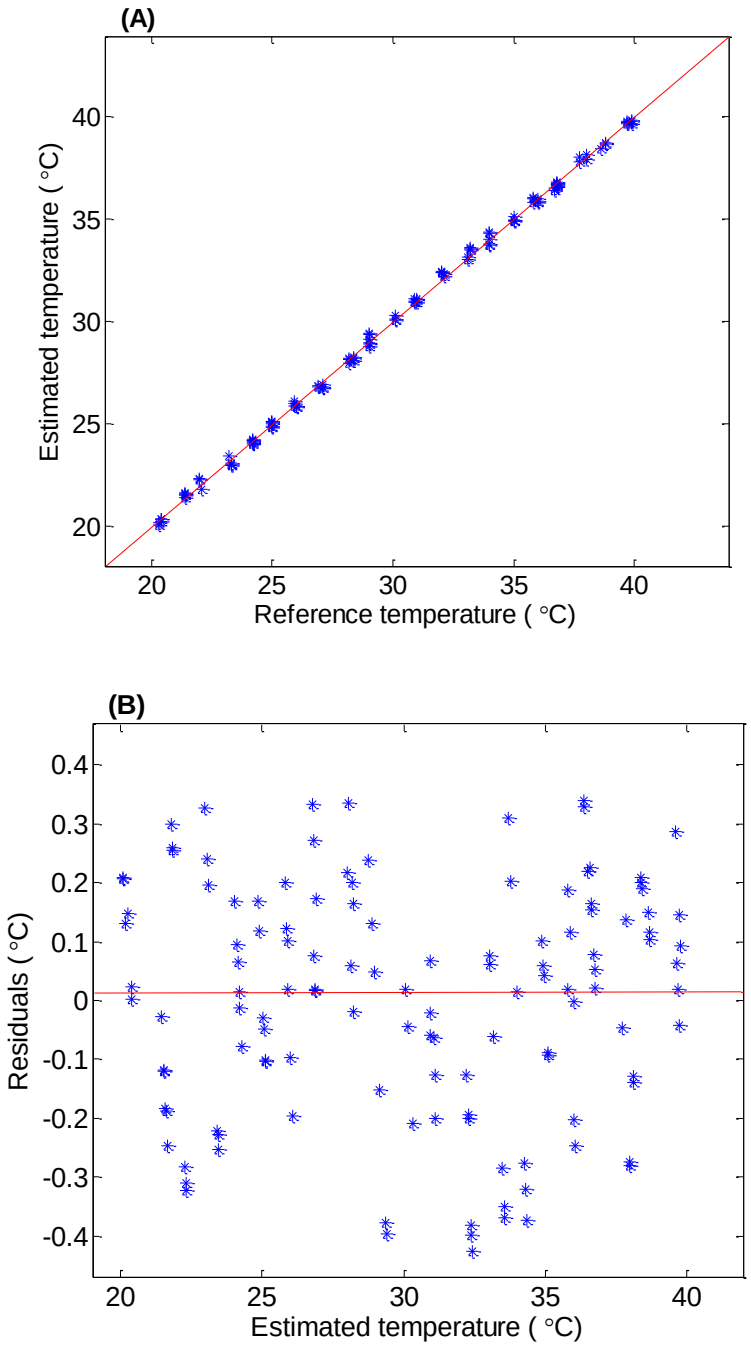

Figure 4-39. Correlation and residual plots for calibration. Correlation (**A**) and residual (**B**) plots for calibration spectra used to describe temperature fluctuations in buffer solutions that also incorporated variation in pH and buffer molarity. Model 2 in Table 4-11 was used. The red lines in panels A and B, respectively, correspond to perfect correlation between estimated and reference temperatures and 0.0 residuals.

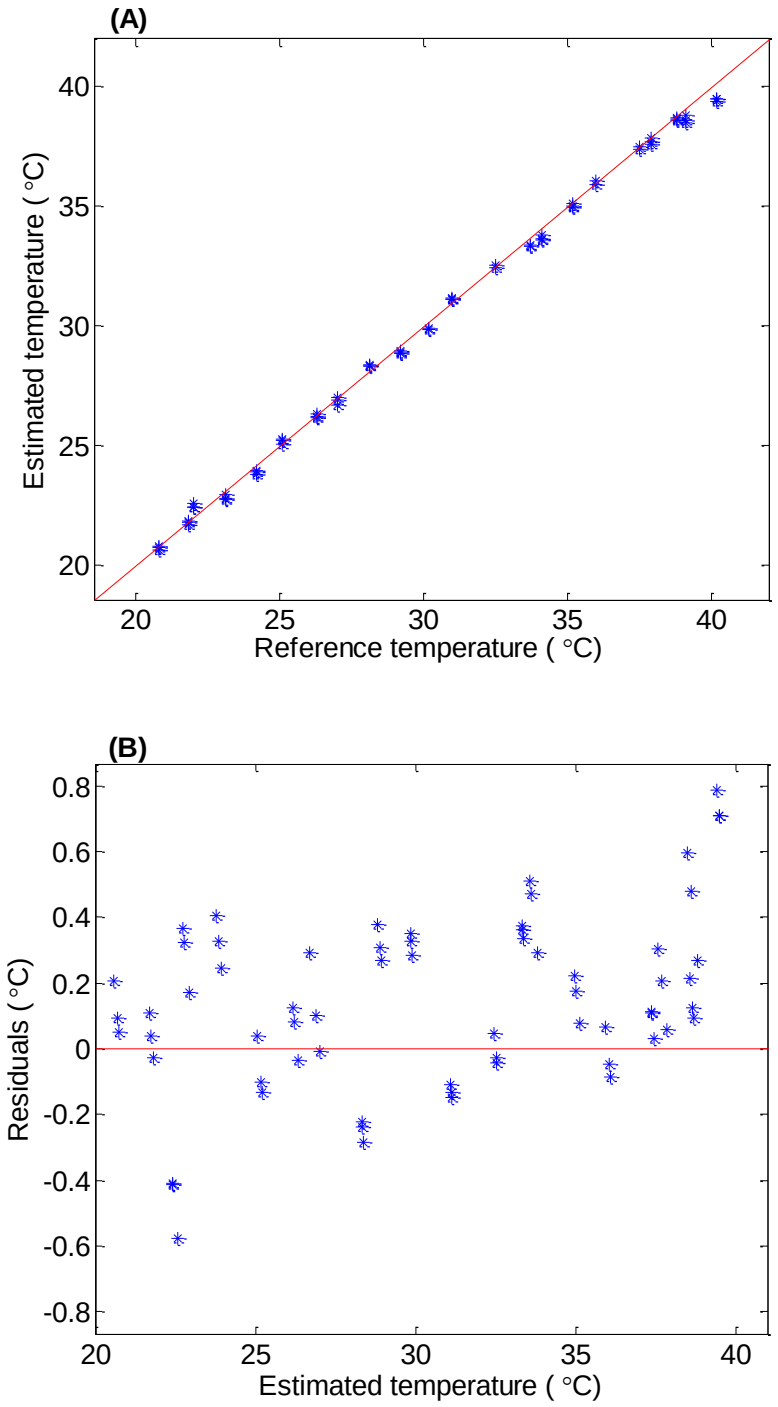

Figure 4-40. Correlation and residual plots. Correlation (**A**) and residual (**B**) plots for prediction set 23 (PS23). Model 2 in Table 4-11 was used. The red lines in panels A and B, respectively, correspond to perfect correlation between estimated and reference temperatures and 0.0 residuals.

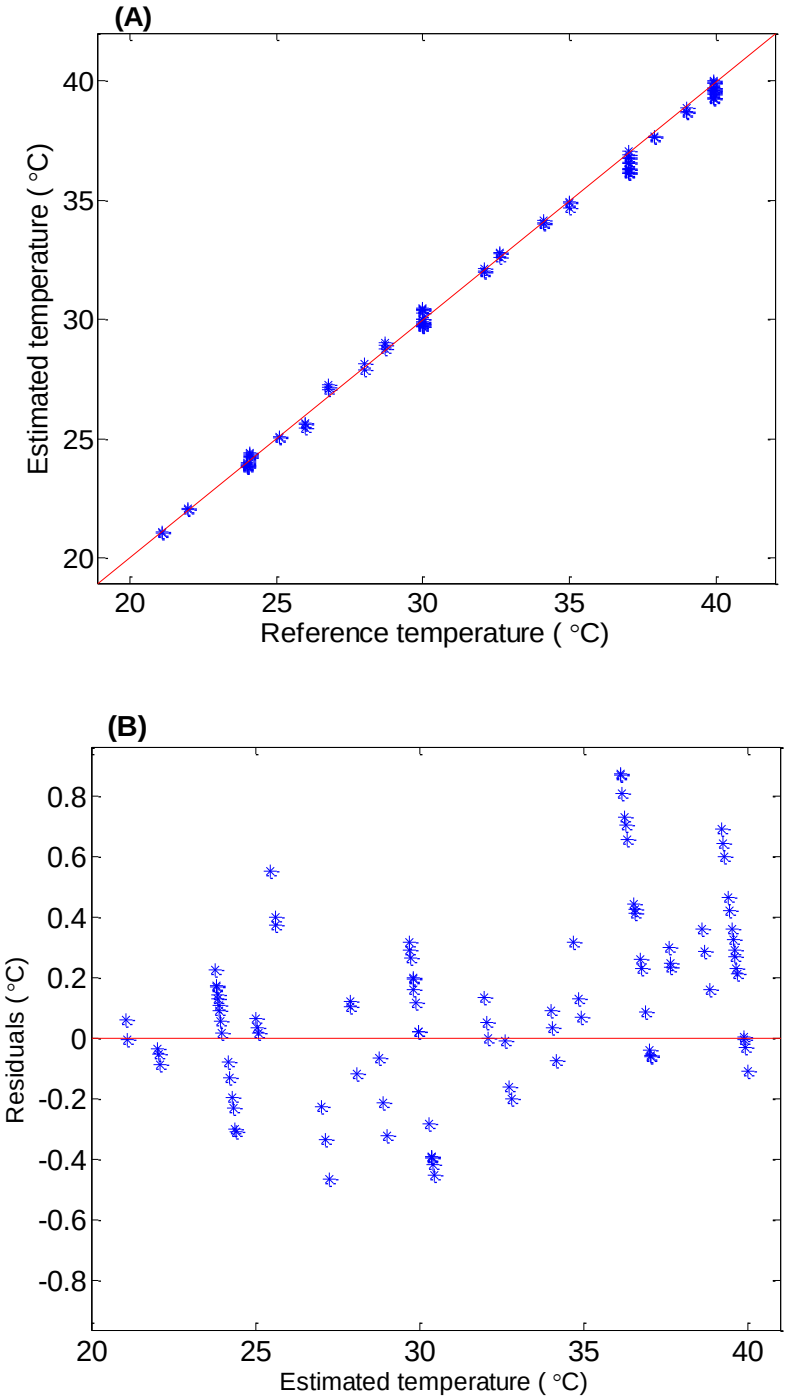

Figure 4-41. Correlation and residual plots. Correlation (**A**) and residual (**B**) plots for prediction set 24 (PS24). Model 2 in Table 4-11 was used. The red lines in panels A and B, respectively, correspond to perfect correlation between estimated and reference temperatures and 0.0 residuals.

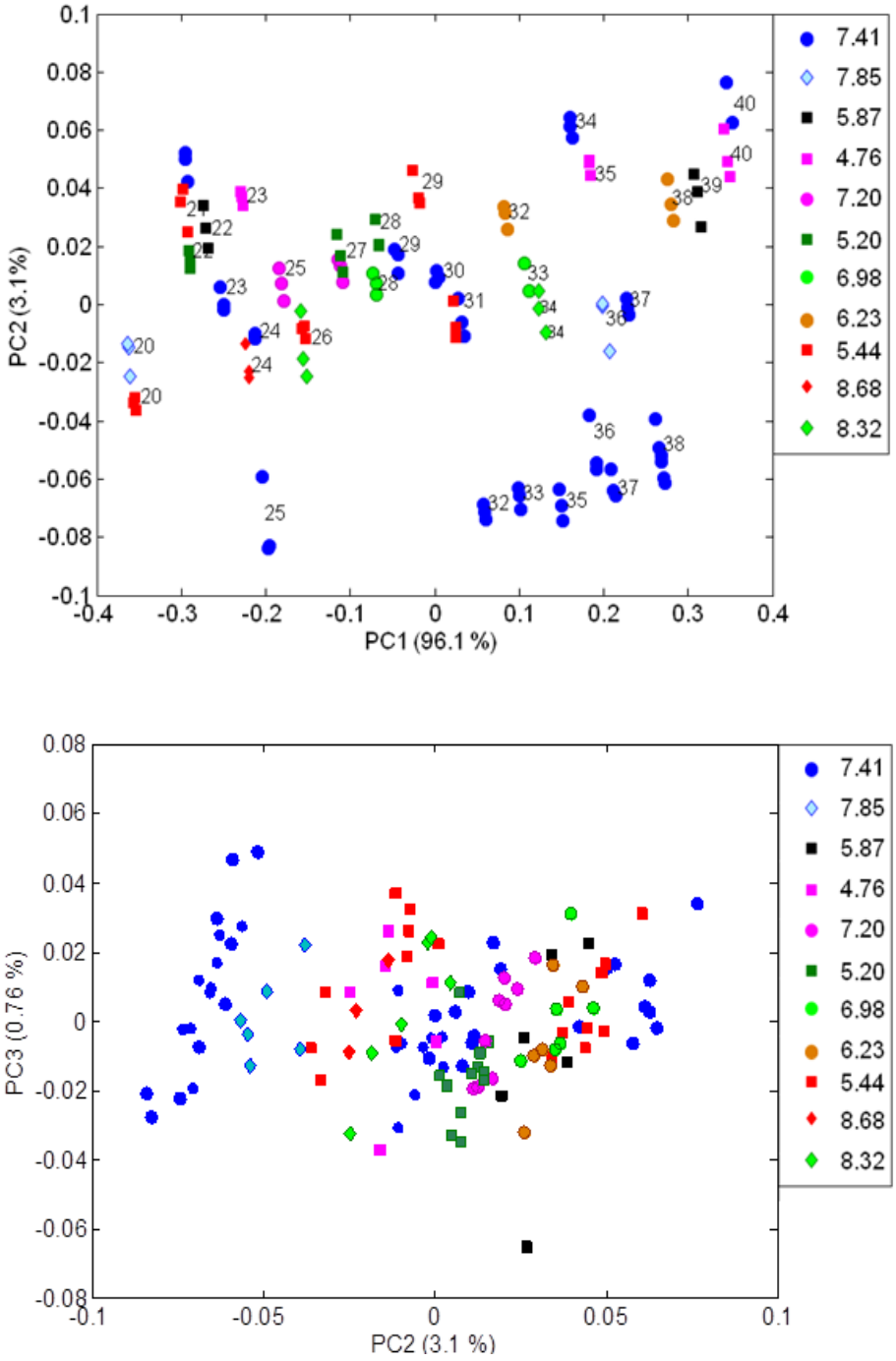

Figure 4-42. Principal component score plots. These plots represent preprocessed calibration spectra based on PCs 1 and 2 (**A**) and PCs 2 and 3 (**B**). Spectral preprocessing included the SNV and DWT methods (db5, seven levels of decomposition, level 7 only used in reconstruction). In both panels, the symbols represent the pH of the buffer solutions used. The data labels in panel **A** denote the sample temperatures. The percentage variance explained by each PC is given in the axis label.

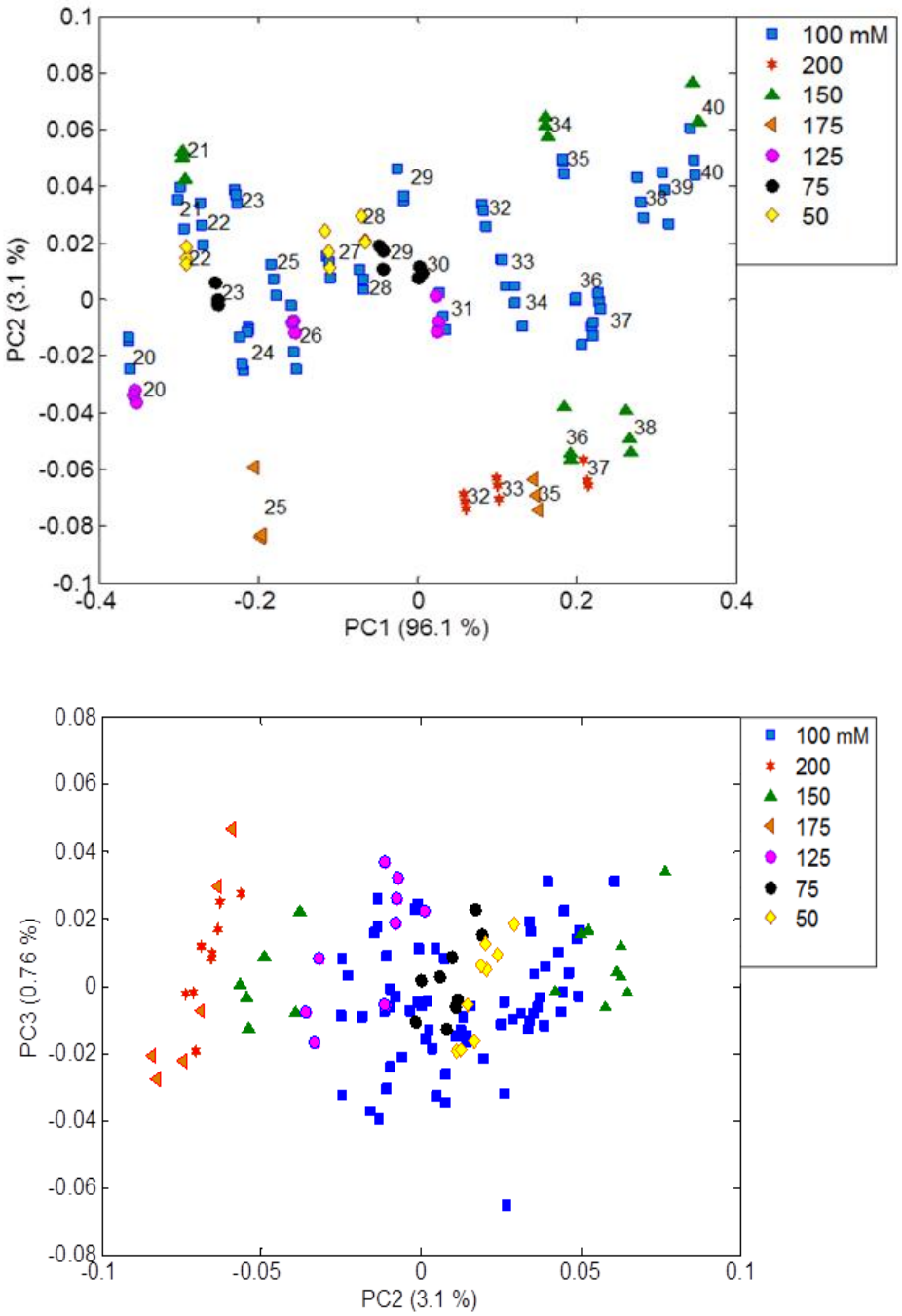

Figure 4-43. Principal component score plots. These plots represent preprocessed calibration spectra based on PCs 1 and 2 (**A**) and PCs 2 and 3 (**B**). Spectral preprocessing included the SNV and DWT methods (db5, seven levels of decomposition, level 7 only used in reconstruction). In both panels, the symbols represent the molarities of the buffer solutions used. The data labels in panel **A** denote the sample temperatures. The percentage variance explained by each PC is given in the axis label.

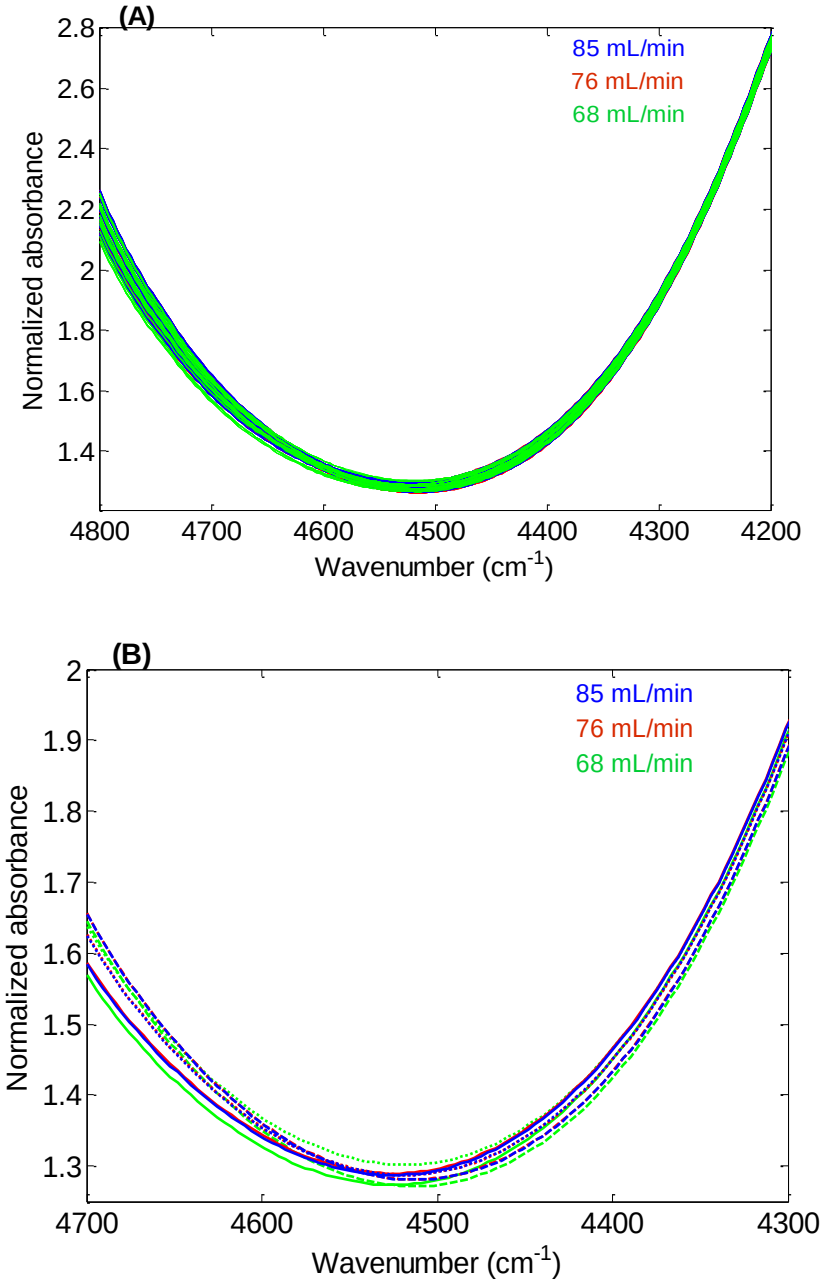

Figure 4-44. Preprocessed NIR absorbance spectra of phosphate buffer solutions (at three different flow rates) collected over the entire range of 20.0 to 40.5 °C. The preprocessing steps included the SNV and DWT calculations (db5, five levels of decomposition, level 5 only used in reconstruction). **(A)** represents the spectra collected over the range of 20.0 to 40.5 °C. **(B)** represents the same preprocessed buffer spectra collected at three different flow rates. The spectra corresponding to 20.0, 30.0 and 40.0 °C are shown with dashed, dotted and solid lines, respectively.

preprocess the absorbance spectra before submitting them to the PLS regression model. Wavelet functions from the Daubechies family were again used and the same optimization of the wavelet and PLS model parameters was performed as described previously. Figure 4-44 illustrates the preprocessed buffer absorbance spectra in the range of 20.0 to 40.5 °C obtained at different flow rates. Increased variation is noted in these spectra, as there is less clear separation in the data with respect to temperature when compared to spectra obtained from static samples (Figures 4-18, 4-31, 4-38).

4.7.1 Best calibration models for temperature fluctuations in flowing samples

The calibration models developed for each flow rate are summarized in Table 4-13. The optimal wavenumber range for spectra collected at 68 mL/min was 4,750 to 4,350 cm^{-1} with three PLS factors. At 76 mL/min, the optimal wavenumber range was 4,800 to 4,400 cm^{-1} with two PLS factors. The optimal wavenumber range for spectra collected at 85 mL/min was 4,850 to 4,375 cm^{-1} with three PLS factors. Differences in the spectral ranges found to be optimal across the three flow rates are likely not significant but rather a function of the similar results obtained with many different ranges.

For all models, the db5 wavelet function was again found to be optimal. Five levels of decomposition and the use of only level 5 in reconstruction were found to be the optimal wavelet parameters for each flow rate. The temperature models developed for the flowing solutions required either one or two additional PLS latent variables (i.e., 3 or 2 vs. 1) relative to the original model developed for static solutions. This suggests the need to characterize additional sources of spectral variance present in the spectra obtained from flowing solutions. It also helps to explain the poor performance of the model developed from static samples when it was applied to spectra collected with the flow system.

4.7.2 Prediction performance of temperature models for flowing solutions

The prediction performance of these calibration models was assessed by use of six prediction sets of buffer spectra (two prediction sets at each flow rate) collected over two weeks. Each model was applied to each prediction set to allow an assessment of how dependent the models were on the flow rate used for the spectra employed to build the model.

The SEP values for the prediction sets are summarized in Table 4-14. All the models gave SEP values ranging from 0.13 to 0.23 °C when applied to data at the same flow rate that formed the basis for the model. The average SEP value for this case was 0.17 °C. When models were applied to data at flow rates other than that used as the basis for the model, the SEP values ranged from 0.15 to 0.23 °C with an average of 0.18 °C. These results suggest that the computed models are relatively independent of the flow rate used.

Principal component analysis was applied to the three sets of calibration data to observe the relationships among the spectra as a function of flow rate. Preprocessed absorbance spectra were employed, the data were mean centered before submission to PCA, and the wavenumber range of 4,850 to 4,375 cm^{-1} was used (optimal wavenumber range for model based on 85 mL/min). Spectral preprocessing was performed with the SNV and DWT methods (db5, 5 levels of decomposition, level 5 only used in reconstruction).

Figure 4-45 is a score plot based on PCs 1 and 2. As observed previously in Figure 4-42, the first PC accounts for the great majority of the variance (~96%) and the primary information encoded in this PC appears to be the sample temperature. In general, for the same temperature, the spectra at the three flow rates tend to cluster together, with the 76 mL/min data appearing less similar to the other two flow rates. Overall, the score plot confirms the result that the three calibration models are relatively insensitive to flow rate.

The calibration model developed at 85 mL/min gave the best overall SEP value with an average of 0.135 °C. While the data collected here do not support a trend in SEP with respect to flow rate, the practical result from this work is to identify 85 mL/min as a workable flow rate for use in temperature predictions from flowing samples. This result will be utilized in the data collection protocol for the work described in Chapter 5. Figures 4-46 through 4-48 display correlation and residual plots for the calibration and prediction sets based on the data collected at 85 mL/min. As reflected in the low SEP values, the visual correlations between estimated and reference temperatures are excellent. Slight curvature is noted in the residual plots for the two prediction sets but the effect is minor when placed in context of the small magnitudes of the residuals.

4.8 Conclusions

A spectral preprocessing method using the SNV transform combined with the DWT, followed by PLS regression was utilized successfully in developing calibration models to determine the temperature of aqueous-based samples directly from their NIR spectra. These calibration models were developed from spectra of pH 7.40 phosphate buffer collected over the range of 20.0 to 40.5 °C. The spectral preprocessing strategy based on the DWT was successfully utilized to isolate the low-frequency baseline/background information which carries the spectral features due to temperature fluctuations in aqueous-based samples. Out of the two wavelet families studied, the Daubechies wavelets gave the most promising results. Under conditions of constant pH and buffer molarity, calibration models developed with wavelet preprocessing required only one PLS factor to explain temperature fluctuations and gave robust prediction results (SEP values ranging from 0.19 to 0.36 °C) with time, whereas buffer spectra with no preprocessing gave much higher SEP values (> 2°C) and performed poorly with time. The prediction performance of the temperature models in increasingly complex matrixes was assessed using seven prediction sets of sample spectra collected over six months. Buffer spectra with no preprocessing gave the higher SEP values (> 9 °C) and performed

Table 4-13. Best PLS calibration models for temperature fluctuations in flowing buffer solutions

Model No.	Flow rate (mL/min)	Wavenumber range (cm^{-1})	Preprocessing method	Latent variable	SEC (°C)	CV-SEP (°C)
1	68	4,750-4,350	SNV & DWT (db5, 5 [5])[a]	3	0.11	0.13
2	76	4,800-4,400	SNV & DWT (db5, 5 [5])[a]	2	0.14	0.14
2[b]	76	4,800-4,400	SNV & DWT (db5, 5 [5])[a]	3	0.13	0.14
3	85	4,850-4,375	SNV & DWT (db5, 5 [5])[a]	3	0.10	0.12

[a]Notation is wavelet family and order of wavelet function, number of levels of decomposition, and the levels used in the reconstruction of the spectrum.

[b]Model 2 with 3 PLS factors gave similar CV-SEP values to Model 2 with 2 PLS factors. Therefore the simpler model with 2 PLS factors was used in subsequent work.

Table 4-14. Prediction performance of PLS calibration models for temperature fluctuations in flowing solutions

Flow rate (mL/min)	Data sets	SEP (°C)		
		Model 1	**Model 2**	**Model 3**
68	Calibration[a]	0.13	N/A	N/A
	Prediction set 25 (PS25)	0.15	0.23	0.15
	Prediction set 26 (PS26)	0.15	0.21	0.16
76	Calibration[a]	N/A	0.14	N/A
	Prediction set 27 (PS27)	0.16	0.23	0.16
	Prediction set 28 (PS28)	0.17	0.23	0.16
85	Calibration[a]	N/A	N/A	0.12
	Prediction set 29 (PS29)	0.15	0.22	0.14
	Prediction set 30 (PS30)	0.15	0.20	0.13

[a]Statistics given for the calibration data are values of CV-SEP for the model generated with the data at the corresponding flow rate.

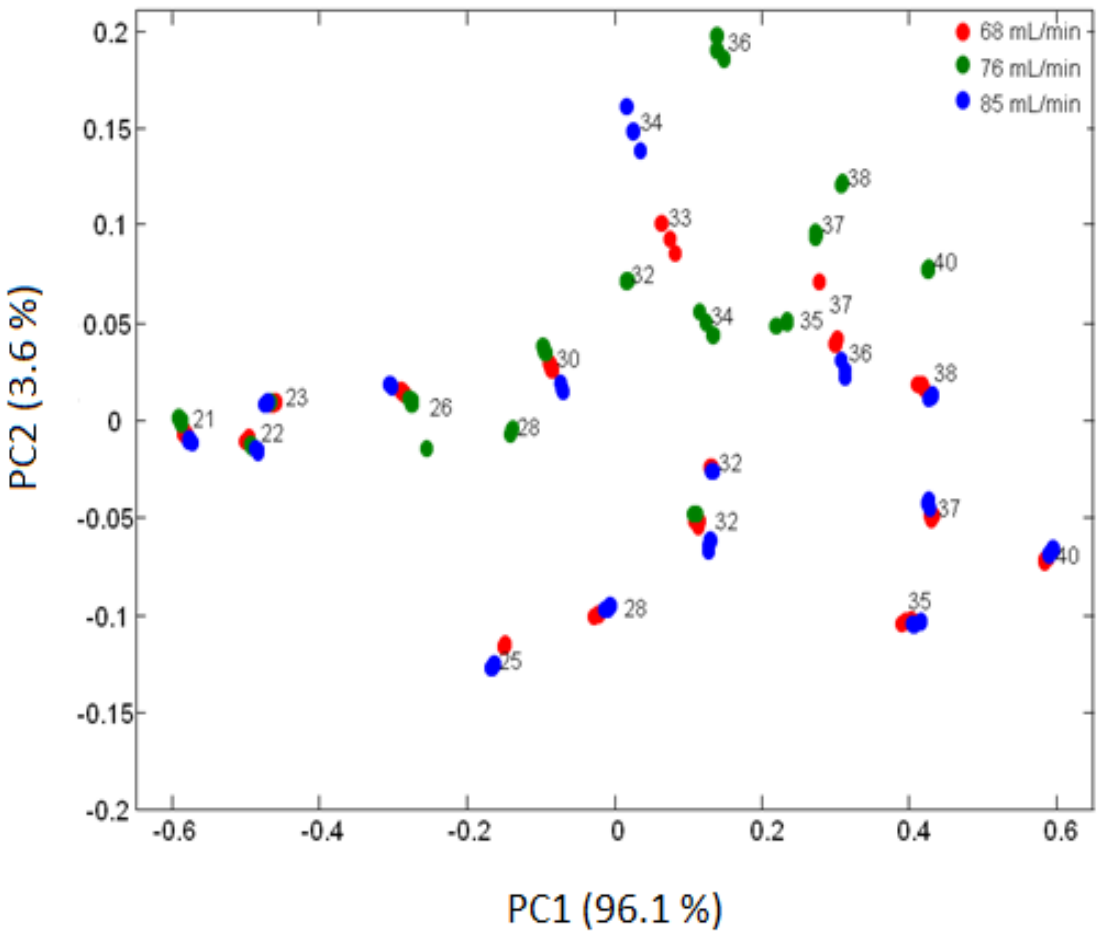

Figure 4-45. Principal component score plot of preprocessed calibration spectra based on PCs 1 and 2. The preprocessing steps included the SNV and DWT methods (db5, 5 levels of decomposition, level 5 only used in reconstruction). The symbol colors denote the flow rates and the data labels correspond to the reference temperatures of the samples. The percentage variance explained by each PC is given in the axis label.

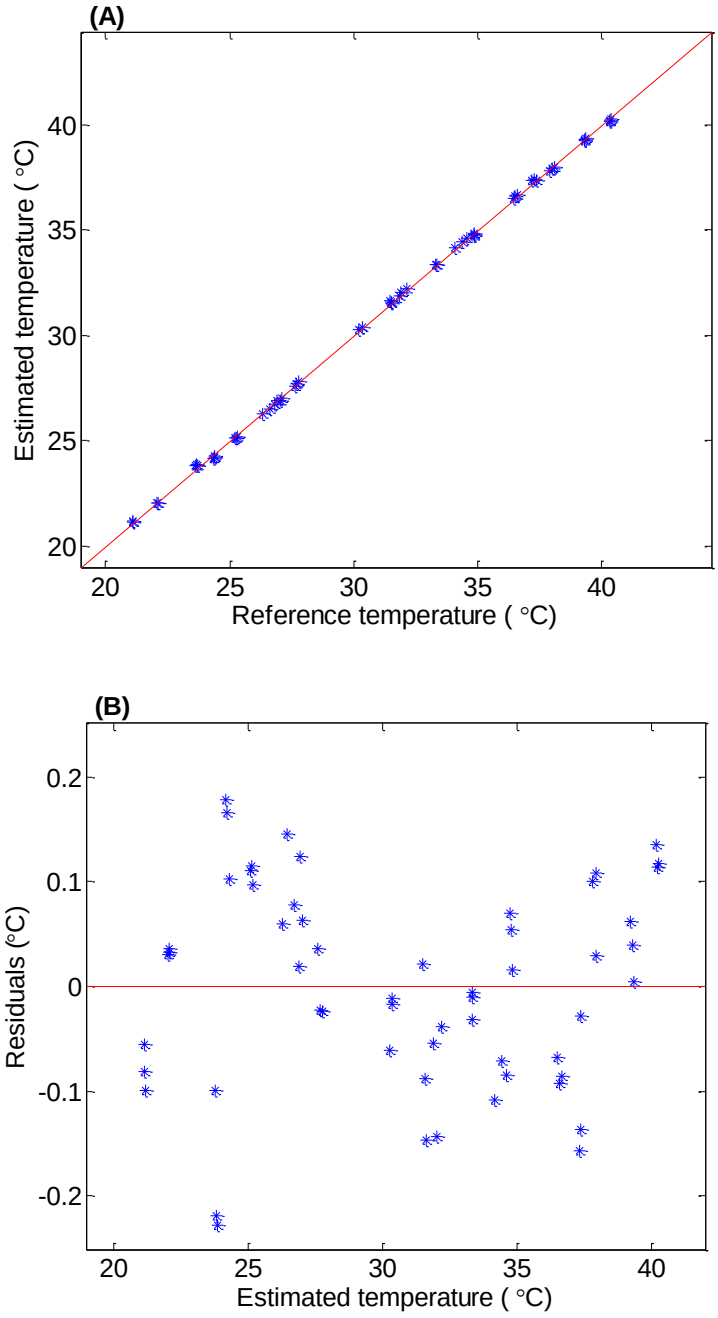

Figure 4-46. Correlation and residual plots for calibration. Correlation (**A**) and residual (**B**) plots for calibration spectra collected from pH 7.40, 0.100 M phosphate buffer solutions flowing at 85 mL/min. Model 3 in Table 4-13 was used to generate the results. The red lines in panels A and B, respectively, correspond to perfect correlation between estimated and reference temperatures and 0.0 residuals.

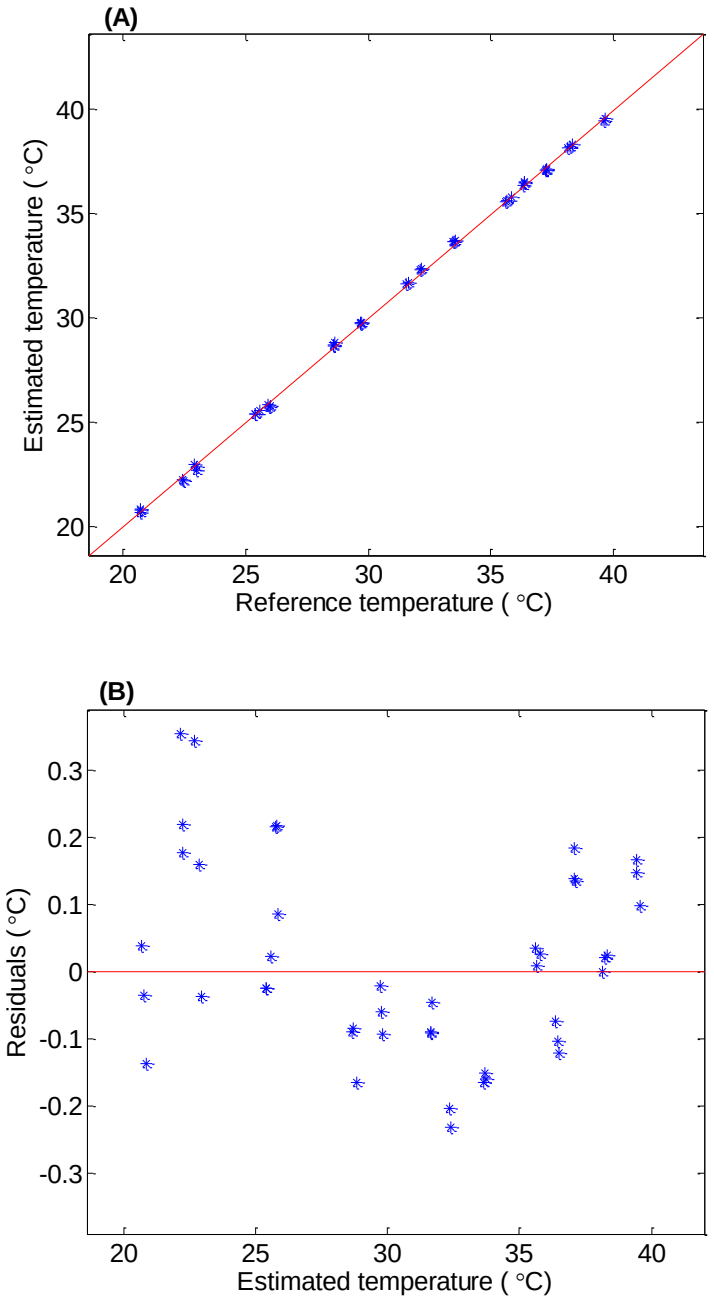

Figure 4-47. Correlation and residual plots. Correlation (**A**) and residual (**B**) plots for prediction set 29 (PS29). These spectra were collected from pH 7.40, 0.100 M phosphate buffer solutions flowing at 85 mL/min. Model 3 in Table 4-13 was used to generate the results. The red lines in panels A and B, respectively, correspond to perfect correlation between estimated and reference temperatures and 0.0 residuals.

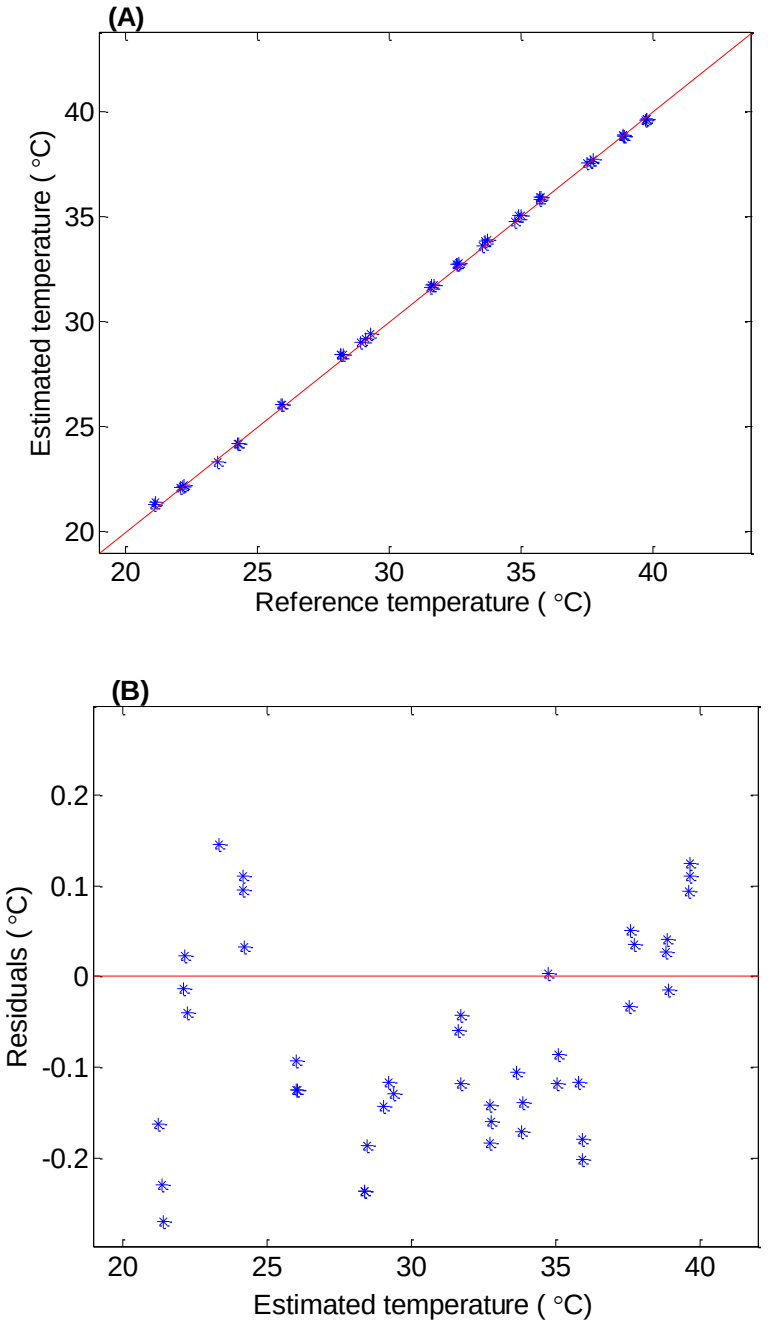

Figure 4-48. Correlation and residual plots. Correlation (**A**) and residual (**B**) plots for prediction set 30 (PS30). These spectra were collected from pH 7.40, 0.100 M phosphate buffer solutions flowing at 85 mL/min. Model 3 in Table 4-13 was used to generate the results. The red lines in panels A and B, respectively, correspond to perfect correlation between estimated and reference temperatures and 0.0 residuals.

poorly with the increasing complexity of the samples. Wavelet preprocessed buffer spectra gave SEP values ranging from 0.33 to 1.01 °C and performed well with the increasing complexity of the sample matrix. However, SEP values obtained for the BVP samples were the highest regardless of the calibration model. This could be due to the presence of dissolved proteins (globulins, albumins etc.) and different ionic species (K^+, Cl^-, Ca^{2+} etc.) in the plasma samples.

In order to investigate the ability to model temperature fluctuations in an aqueous-based sample in the presence of dissolved proteins, calibration models were developed based on a solution of HSA in pH 7.40 buffer. The best calibration model was obtained with DWT-preprocessed HSA spectra. It was observed that this calibration model required more latent variables (3 vs. 1) than the models generated using buffer alone. The prediction performance of the calibration model was assessed using both HSA and BVP samples. The SEP values obtained for both prediction sets were 0.29 and 0.18 °C, respectively.

Further investigations were conducted to investigate the ability to model temperature fluctuations in an aqueous-based sample including pH and molarity variation. For this purpose, calibration models were developed based on phosphate buffer solutions with varying pH and molrity values. The best calibration model was obtained with DWT-preprocessed buffer spectra. Temperature models developed to include pH and molarity variation needed more PLS latent variables (3) to explain the covariance between the spectral features and temperature than the models developed initially with constant pH and molarity. The prediction performance of the calibration model was assessed using two prediction sets. The SEP values obtained for both prediction sets were 0.30 and 0.31 °C, respectively.

In order to investigate the ability to model temperature fluctuations in a dynamic/ flowing solution, calibration models were developed using a pH 7.40 phosphate buffer solution in a custom made flow-cell system. This flow-cell design demonstrated excellent

performance in achieving and equilibrating at a desired temperature effectively. The best calibration models were again obtained with DWT-preprocessed buffer spectra. The prediction performance of these models was assessed using six prediction sets of buffer spectra obtained at three different flow rates. All the calibration models at different flow rates gave SEP values ranging from 0.13 to 0.23 °C, with the calibration model developed from data at 85 mL/min producing the lowest SEP values (average SEP of 0.135 °C). During the assessment of the effect of flow rate fluctuations on the calibration models, reasonably good prediction results were obtained (SEP values ranging from 0.15 to 0.23 °C) for prediction spectra that were collected at a different flow rate than that used in the collection of the calibration spectra. These results indicate that the temperature models are capable of tolerating some degree of fluctuation in flow rates.

Although the temperature range studied in these experiments ranged only from 20.0 to 40.5 °C, these models can be extended towards the entire temperature range in which water behaves as a liquid. This is possible due to the thermal behavior of the hydrogen-bonding network of liquid water being essentially the same regardless of the temperature range studied. Temperature modeling in an aqueous-based sample directly from the NIR spectrum has promising applications in situations in which it is difficult or inaccurate to use a conventional temperature probe. Such applications could be in the realm of measurements in the human body (e.g. non-invasive glucose sensing) but also could be found in environmental analysis, food and agricultural analyses, and process monitoring (e.g., bioreactors). Each of these areas is dominated by the need to analyze aqueous-based samples and there is a continuing interest in moving analyses from the laboratory to the field, chemical plant, etc.

CHAPTER 5
DEVELOPMENT OF TEMPERATURE CORRECTION STRATEGIES TO IMPROVE ANALYTE PREDICTION IN AQUEOUS-BASED SAMPLES

5.1 Introduction

The extreme temperature sensitivity of underlying water absorption peaks gives rise to large baseline variations in near-infrared (NIR) absorbance spectra of aqueous-based samples that have been measured relative to an aqueous background spectrum. This is due to the thermal behavior of the hydrogen-bonded network of water molecules. As described in Chapter 4, water absorption peaks shift to higher wavenumbers with increasing temperature.[6,37-39]

Temperature plays a key role as an external variable in many NIR measurements, especially those in clinically relevant studies and process control applications.[6.37-39,54-56] For example, our laboratory has a long-standing interest in the development of noninvasive glucose sensing based on NIR spectroscopy. Because an *in vivo* NIR measurement of body tissue is effectively the measurement of an aqueous sample, the temperature of the tissue influences the collected spectrum.

Rigorous temperature control is hard to achieve in many experimental settings. If precise temperature control during spectral collection is not ensured, these temperature fluctuations can translate to artifacts in the measured NIR spectra. Such artifacts are especially problematic in NIR spectra of samples which are primarily aqueous-based and can complicate the data analysis steps required to perform accurate quantitative analyses.[6,37-39]

In the NIR region, quantitative spectral analysis is always combined with multivariate calibration techniques due to the weak and overlapped nature of the spectral features found there.[3,24] Common multivariate techniques used for this purpose include

principal component regression (PCR) and partial least-squares regression (PLS).[3,24] Both of these methods are based on the linear additivity of absorbance. In simple terms, a mixture of components gives rise to a spectrum that is a linear combination of the pure-component spectra of the individual components that comprise the sample. Any deviation from linear additivity (e.g., peak shifts, etc.) demands either the use of nonlinear modeling methods or the inclusion of more linear factors/components in the model to help account for the nonlinearity. Both of these approaches tend to complicate the calibration process. Ultimately, the presence of temperature-induced spectral artifacts may negatively impact the prediction performance of the computed calibration models.[37,38]

5.2 Temperature correction strategies to improve predictions in aqueous samples

Different approaches to address this issue have been reported in previous studies.[37,59-60,63] A common method is to preprocess the data by digital filtering or other means to remove the artifactual information associated with changes in sample temperature. Studies carried out by Hazen et al. used digital Fourier filtering to remove the undesirable artifacts due to temperature. [37] Arimoto et al. used the linear variation in absorbance values of spectra due to temperature fluctuations to correct analyte concentrations[63] Wulfert et al. employed an approach based on continuous piecewise direct standardization to suppress the spectral artifacts due to temperature fluctuations.[60] Chen et al. used a similar approach based on loading space standardization to correct for temperature-induced spectral variations.[59] All of these methods have the disadvantage of possibly suppressing analyte information as the temperature-induced variation is suppressed. Also, these correction procedures are complex and the temperature levels studied are limited. Furthermore, corrections applied are limited to a given temperature value and cannot be adopted continuously across a range of temperatures.

In the work presented in this chapter, an alternative strategy is explored in which the sample temperature is measured first and then used as part of application of the

calibration model. The measurement of the sample temperature may be straightforward or not depending on the nature of the sample and experiment. For example, if an *in vivo* transmission spectroscopic measurement is made across a section of tissue, measurement of the temperature of the external surface of the tissue may not accurately reflect the internal temperature of the tissue through which the spectroscopic measurement is made. Similarly, while the circulation of blood within the human body helps to maintain a normal core temperature of 37 °C, the temperature of the dermal layer of a finger or hand may be different from the core temperature. Thus, in this application, use of a conventional temperature probe is impractical.

To address this issue, an attempt is first made to determine the temperature of an aqueous sample directly from its NIR spectrum. The estimated temperature information is then incorporated into the quantitative analyte prediction models. The first phase of this strategy, the development of models to determine the temperature of an aqueous-based sample directly from the NIR spectrum, was described in detail in Chapter 4. The current chapter focuses on a simple but effective correction strategy which is based on a second-order polynomial correction to the analyte concentration residuals, followed by an additive correction to the analyte prediction at a given temperature.

In the work presented here, separate PLS regression models are developed to model temperatures and glucose/lactate concentrations (1.0 to 20.0 mM) in laboratory-prepared solutions with a background matrix of pH 7.4 phosphate buffer. A temperature correction strategy is demonstrated to improve analyte predictions over the temperature range of 20.0 to 40.5 °C.

5.3 Experimental design

5.3.1 Apparatus and reagents

All the spectral data collections were performed with a Bruker Vertex 70 (Bruker Optics, Inc., Billerica, MA) Fourier transform (FT) spectrometer configured with a tungsten-halogen lamp source, a calcium fluoride (CaF_2) beam splitter and a liquid

nitrogen cooled indium antimonide (InSb) detector. A low-pass interference filter (OCLI, Inc., Santa Rosa, CA) was used to restrict the light beyond 5,000 cm^{-1}. A custom-made flow cell described previously in Chapter 4 (Section 4.3,1) was used in all spectral collections.

Phosphate buffer solutions (0.100 M) were prepared by dissolving appropriate amounts of reagent-grade sodium dihydrogen phosphate ($NaH_2PO_4.H_2O$, MW: 137.99 g/mol, Thermo Fisher Scientific, Inc., Waltham, MA) in reagent-grade water obtained with a Water Pro PS Station (Model 9000601, Labconco Corporation, Kansas City, MO). Sodium benzoate ($NaC_7H_5O_2$, MW: 144.11 g/mol, Thermo Fisher Scientific, Inc.) was added as a preservative (5g/L of buffer). The pH of the buffer solution was adjusted to 7.40 (± 0.01 pH units) using a 50 % (w/w) solution of sodium hydroxide (NaOH, Thermo Fisher Scientific, Inc.). All pH measurements were performed with an Orion Model 920A pH meter (Thermo Fisher Scientific, Inc.).

All glucose and lactate samples were prepared by dissolving appropriate amounts of reagent-grade *D*-glucose (dextrose) anhydrous ($C_6H_6O_6$, MW: 180.16 g/mol, Thermo Fisher Scientific, Inc.) or sodium-*L*-lactate ($NaC_3H_5O_3$, MW: 1112.06 g/mol, Sigma Aldrich, Inc., St. Louis, MO) in pH 7.40 phosphate buffer solution. Stock solutions of glucose and lactate (250. mM) were used to prepare the samples of glucose or lactate ranging from 1.0 to 20.0 mM. Glucose samples or mixtures of glucose and lactate were prepared *in situ* within the sample reservoir of the flow cell (Figure 4-3). This was done by adding appropriate volumes of the glucose and/or lactate stock solutions and pH 7.40 phosphate buffer to the sample reservoir and allowing them to equilibrate by circulation through the flow cell. A YSI Model 2300 Stat Plus glucose / lactate Analyzer (YSI Inc., Yellow Springs, OH) was used as a reference method to verify the glucose and lactate concentrations in each prepared sample.

5.3.2 Procedures

Two data collections were performed, corresponding to (1) samples of glucose in phosphate buffer and (2) mixture samples of glucose and lactate in buffer. For the study of solutions of glucose in buffer, 25 samples were prepared over the range of 1.0 to 20.0 mM (± 0.2 mM) for use in calibrating the system. Three replicate spectra were collected for each sample at 37.0 ^{o}C (± 0.1°C). To test the calibration, five prediction sets of sample spectra (glucose in pH 7.40 phosphate buffer) were collected over a time period of four weeks. Out of the five prediction sets, one was collected at 37.0 ^{o}C (± 0.1°C) while the others were collected to span a temperature range of 20.0 to 40.5 ^{o}C (± 0.1°C). In all the spectral collections, the glucose concentrations ranged from 1.0 to 20.0 mM (± 0.2 mM) and one target temperature from the range noted above was randomly assigned to each sample. The flow rate of the solution was set at 85 mL/min. This corresponds to the optimal flow rate determined in Chapter 4 (Section 4.7). A summary of the spectral collection protocol is given in Table 5-1.

For the data set based on mixtures of glucose and lactate, 34 samples were prepared in pH 7.40 phosphate buffer for use in calibration. The concentration range for each analyte was 1.0 to 20.0 mM (± 0.2 mM). Three replicate spectra were collected for each sample at 37.0 ^{o}C (± 0.1°C). To test the calibration, three prediction sets were collected over a period of three weeks. Out of the three prediction sets, one set was collected at 37.0 $^{\circ}$C (± 0.1°C) while the other two were collected to span a temperature range of 20.0 to 40.5 ^{o}C (± 0.1°C). For all the spectral collections, the glucose/lactate concentrations studied were again from 1.0 to 20.0 mM (± 0.2 mM) and a random target temperature from the range noted above was assigned to each sample. The flow rate of the solution was 85 mL/min. A summary of the data collection protocol is given in Table 5-2.

Temperatures and analyte concentrations were randomized with respect to time (i.e., the order of data collection) for all the spectral data collections described above to minimize the chance of correlations between these parameters and any time-dependent

Table 5-1. Summary of spectral collection protocol for glucose predictions in aqueous-based samples

Data set	Time since calibration (weeks)	Number of samples[a]/spectra	Temperature of spectral collection (°C)
Calibration	0	25/75	37.0
Prediction set 1 (PRD1)	0.5	19/57	37.0
Prediction set 2 (PRD2)	2	22/66	20.0 to 40.5
Prediction set 3 (PRD3)	3	20/60	20.0 to 40.5
Prediction set 4 (PRD4)	3.5	19/57	20.0 to 40.5
Prediction set 5 (PRD5)	4	17/51	20.0 to 40.5

[a]A sample is defined as a given chemical sample measured at one temperature.

Table 5-2. Summary of spectral collection protocol for glucose and lactate predictions in aqueous-based samples

Data set	Time since calibration (weeks)	Number of samples[a]/spectra	Temperature of spectral collection (°C)
Calibration	0	34/102	37.0
Prediction set 6 (PRD6)	0.5	17/51	37.0
Prediction set 7 (PRD7)	1	19/57	20.0 to 40.5
Prediction set 8 (PRD8)	3	30/90	20.0 to 40.5

[a]A sample is defined as a given chemical sample measured at one temperature.

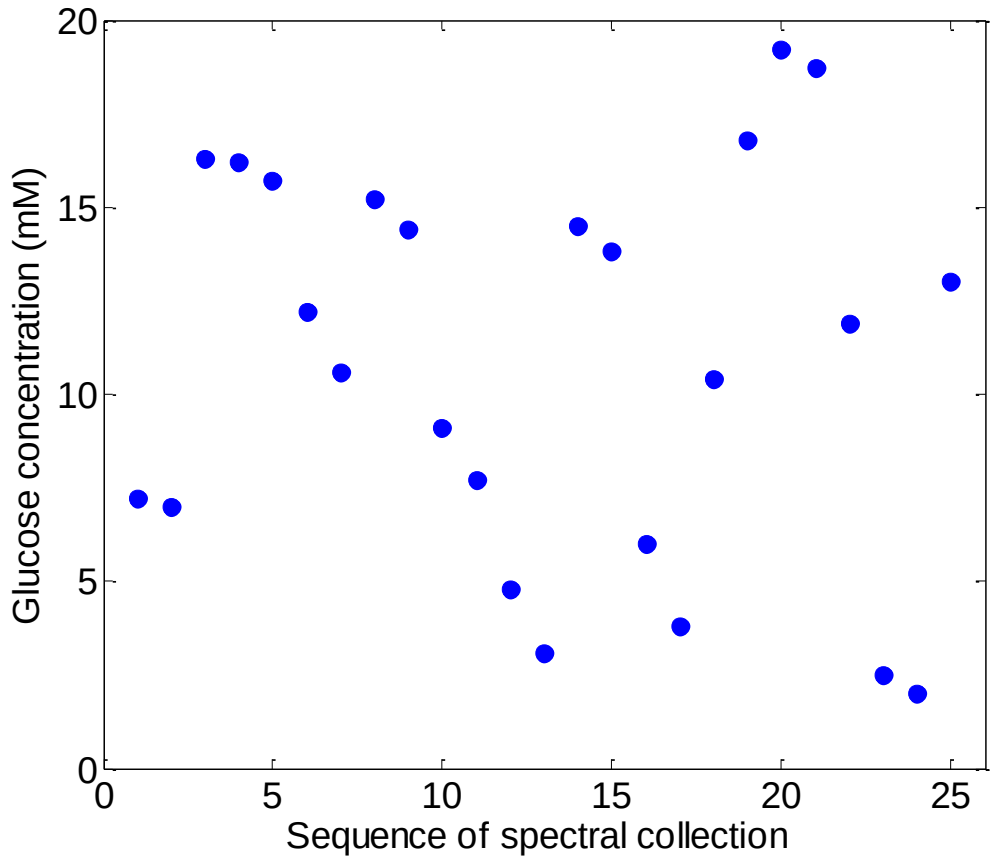

Figure 5-1. Randomization of glucose concentrations to minimize the correlation between glucose concentrations and time. The correlation coefficient is -0.113. The data plotted correspond to the calibration samples in the study of solutions of glucose in buffer. For this data set, all samples were measured at 37.0 ± 0.1 °C.

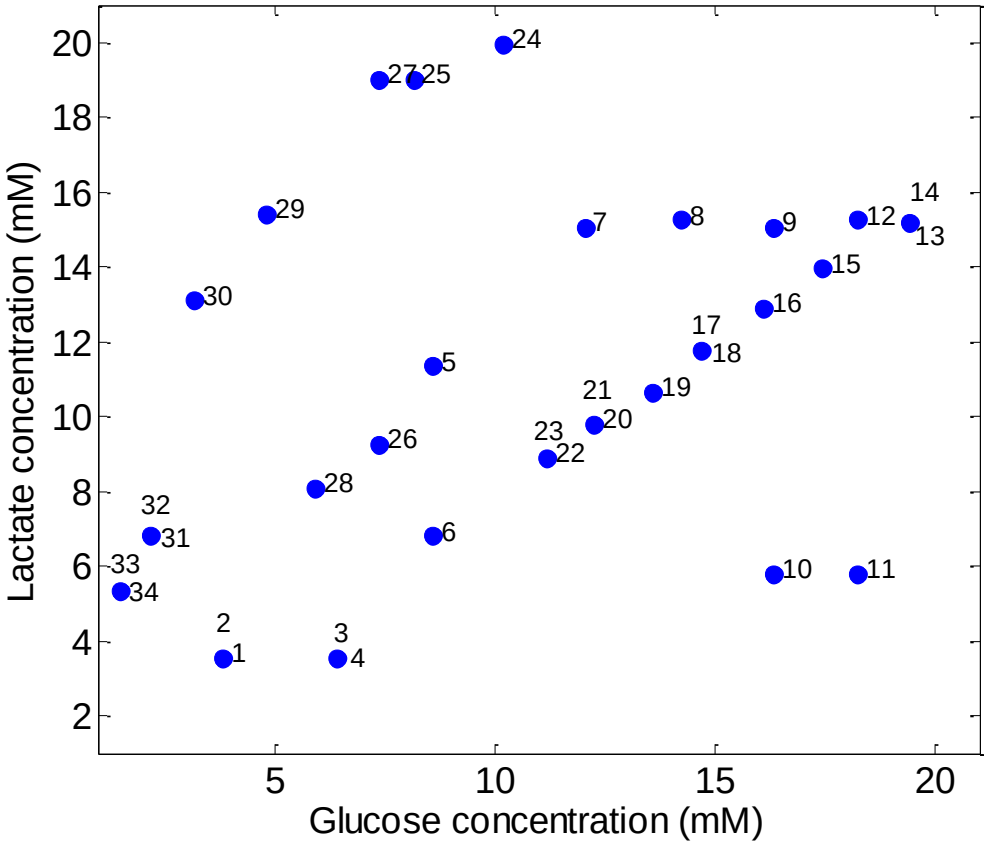

Figure 5-2. Correlation plot of glucose and lactate concentrations for calibration spectra. The correlation coefficient is 0.424. The data labels correspond to the order in which the samples were studied. For this data set, all samples were measured at 37.0 ± 0.1 °C.

data artifacts. As an example, Figure 5-1 shows the randomization of glucose concentrations with time for the set of calibration samples of glucose in buffer. Figure 5-2 is a correlation plot of the glucose and lactate concentrations for the calibration samples corresponding to the mixture solutions of glucose and lactate in buffer.

Open-beam air spectra were used as the spectral background in computing absorbance values for the collected spectra. For a given data collection session, eight warm-up air spectra were collected at the beginning of the day, eight intermediate air spectra were collected at the halfway point of the data collection, followed by another eight air spectra at the end of the day. A 6.3 % metal thin film neutral density filter (Rolyn Optics Co, Covina, CA) was used to attenuate the source intensity during the collection of the air spectra. The average of all the air spectra collected during a given data collection session was used in computing absorbance values for sample spectra collected during that session.

For the collection of the sample spectra, the sample to be measured was prepared in the reservoir of the flow system and the system was allowed to flow until the targeted temperature had stabilized. Experiments confirmed that this equilibration time was also adequate for the stabilization of the analyte concentrations (i.e., the prepared solution was sufficiently mixed).

After equilibration of the sample, three replicate spectra were collected consecutively. For both samples and backgrounds, the raw data consisted of 256 co-added double-sided interferograms containing 7,110 points collected at every zero crossing of the helium-neon (He-Ne) reference laser (15,800.45 cm^{-1}). The nominal spectral resolution was 8 cm^{-1}, and the setting of the source aperture was 6 mm. All interferograms were converted to single-beam spectra with a point spacing of 3.8575 cm^{-1} by applying two levels of zero filling, Blackmann-Harris 3-Term apodization and Mertz phase correction. The single-beam spectra were truncated to 4,000 to 5,000 cm^{-1} for use in subsequent calculations.

The Fourier processing calculations were performed with the Bruker Opus software (Version 6.5, Bruker Optics, Inc.) controlling the spectrometer. Further calculations were performed with Matlab (Version 7.4, The Mathworks, Inc., Natick, MA) on a Dell Precision 670 workstation (Dell Computer Corp., Round Rock, TX) operating under Red Hat Linux WS (Version 5.2, Red Hat, Inc., Raleigh, NC).

Both reference temperatures and concentrations were needed for each sample for use in building and testing calibration models. The temperature assigned to a given spectrum was the average of the readings of the thermocouples placed in the inflow and outflow of the optical transmission cell (Figure 4-2). Readings were taken before and after the collection of each replicate spectrum and used to assign the temperature to that spectrum.

To obtain the reference concentrations, samples were taken from the reservoir of the flow system before the start of the data acquisition and after the collection of the three replicate spectra. These samples were analyzed for glucose and/or lactate concentrations with the YSI analyzer. The average of the two concentration estimates was then assigned to all of the replicate spectra for that sample.

5.4 Results and discussion

5.4.1 Noise evaluations

The quality of the sample spectra in the calibration and prediction sets was determined by the average root mean square (RMS) noise computed from the replicate spectra in each data set. This calculation was performed by taking the ratio of each pairwise combination of the three replicate spectra for a given concentration/temperature combination, converting the resulting transmittance values to absorbance, and computing the RMS value in each noise absorbance spectrum. In computing the noise value to report, the spectral region from 4,500 to 4,300 cm^{-1} was fit to a third-order polynomial baseline function to remove systematic components from the noise spectrum. The

residuals about this fitted baseline served as the input to the RMS calculation. This calculation was summarized previously in Chapter 3 (Section 3.6).

The performance of the instrument itself was determined by the average RMS noise of air spectra collected on each day. This calculation was performed by taking the ratio of each pairwise combination of the replicate air spectra for a given day. In this study, the spectral region from 4,500 to 4,300 cm^{-1} was again used, and the noise was computed about a third-order polynomial baseline as described above.

Figures 5-3 and 5-4 show the average RMS noise values for sample and air spectra, respectively, corresponding to the study of solutions of glucose in pH 7.40 phosphate buffer. Figure 5-5 and 5-6 are the corresponding plots for the study of mixtures of glucose and lactate in buffer. The computed noise levels are consistent across the data sets.

5.4.2 Signal preprocessing

In this study, the discrete wavelet transform (DWT) was used to preprocess the computed absorbance spectra before submitting them to the PLS regression model. The DWT was discussed previously in Chapter 3 (Section 3.2.2). On the basis of results obtained in the temperature modeling work described in Chapter 4, wavelet functions from the Daubechies (db) family were used with a maximum decomposition level of 10. Parameters optimized included the order of the wavelet function, level of decomposition and number of levels used in the reconstruction of the signal. Figure 5-7 displays raw and preprocessed absorbance spectra. The specific optimization steps used to define the wavelet parameters are described in the next section.

5.4.3 Partial least-squares regression models for glucose predictions in pH 7.4 buffer samples

In order to assess the ability to predict glucose concentrations in pH 7.4 buffer under conditions of varying temperature, PLS calibration models were generated from the glucose absorbance spectra in the calibration data set. As noted previously, these

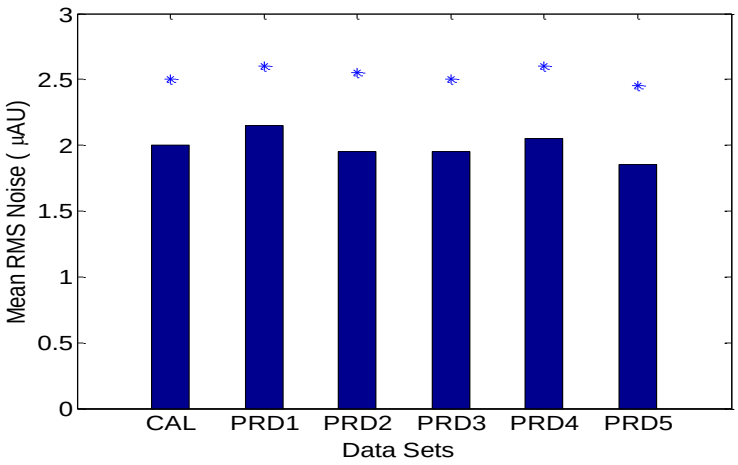

Figure 5-3. Average RMS noise values in units of microabsorbance (µAU) for glucose spectra in each spectral collection. The asterisks above the bars indicate one standard deviation from the average.

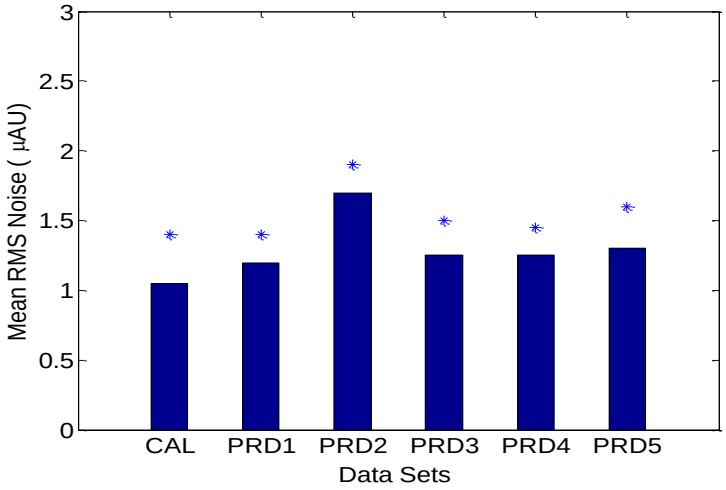

Figure 5-4. Average RMS noise values in units of microabsorbance (µAU) for air spectra in each spectral collection. The asterisks above the bars indicate one standard deviation from the average.

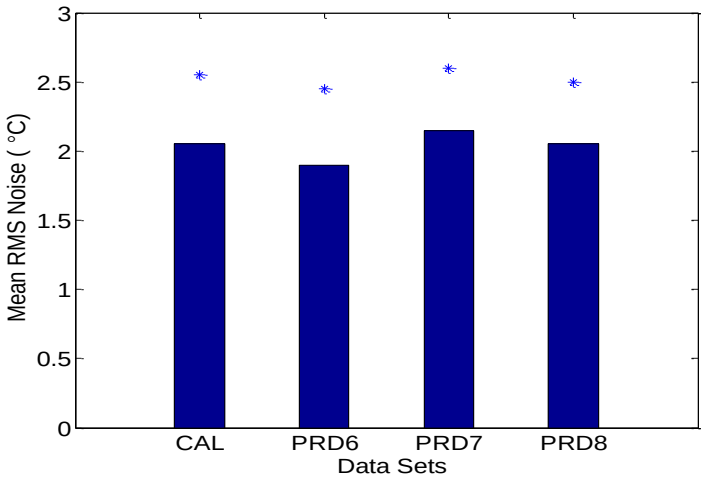

Figure 5-5. Average RMS noise values in units of microabsorbance (μAU) for glucose/lactate mixture spectra in each spectral collection. The asterisks above the bars indicate one standard deviation from the average.

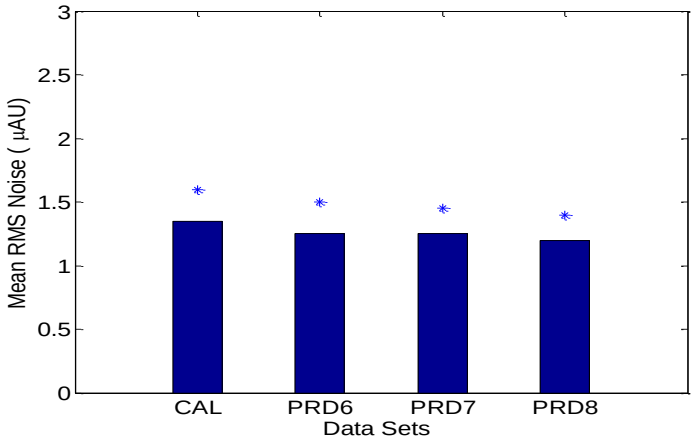

Figure 5-6. Average RMS noise values in units of microabsorbance (μAU) for air spectra in each spectral collection. The asterisks above the bars indicate one standard deviation from the average.

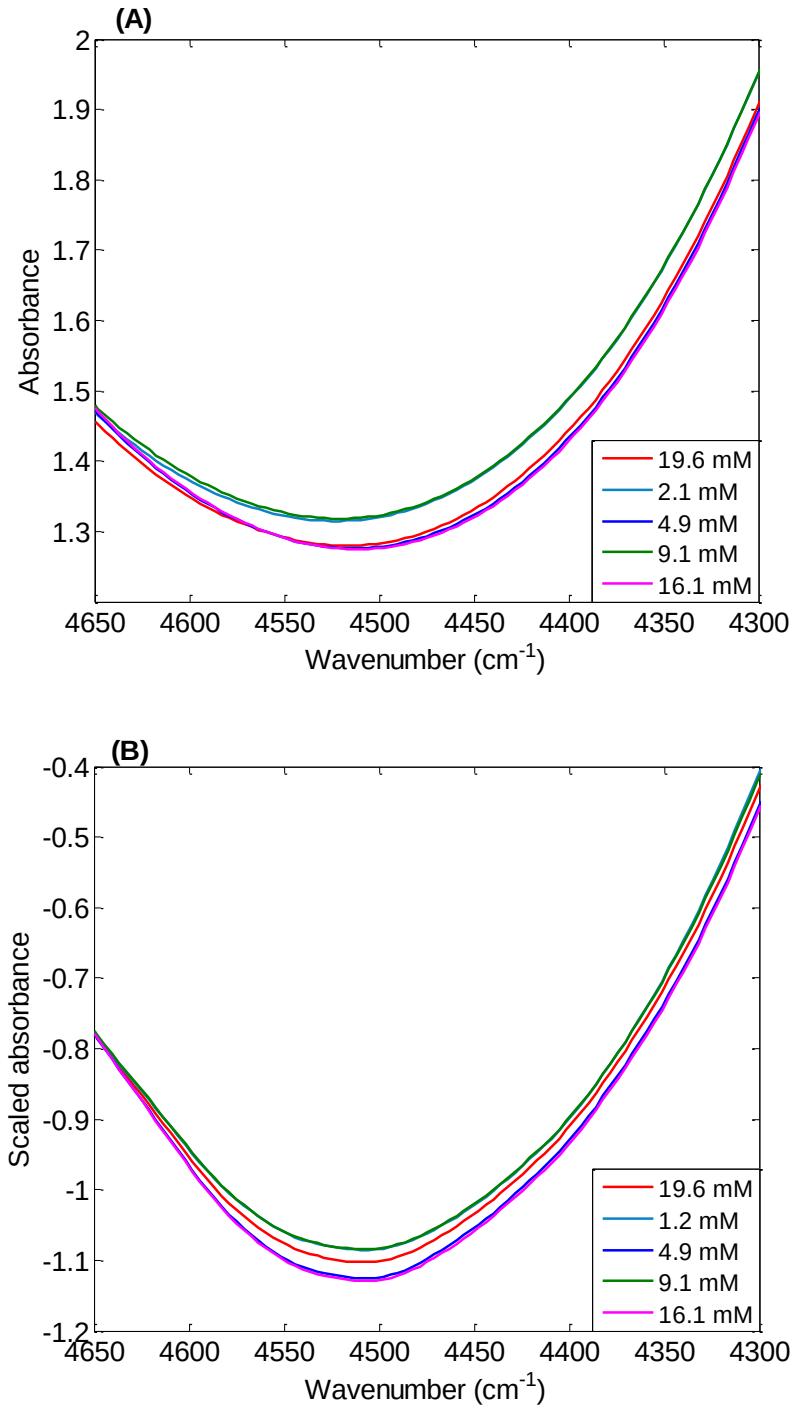

Figure 5-7. Absorbance spectra of glucose in pH 7.40 phosphate buffer. Raw (**A**) and preprocessed (**B**) spectra are shown. Preprocessing was based on application of the db6 wavelet, 8 levels of decomposition, and the use of the details from levels 2, 3, and 4 only in reconstructing the spectrum. No simple relationship is apparent between absorbance and glucose concentration in either the raw or preprocessed data.

absorbance spectra were computed using single-beam glucose spectra with respect to the average air spectrum of the day of spectral collection. Absorbance spectra were preprocessed with the DWT over the full spectral range of 4,000 to 5,000 cm^{-1} and then truncated to a specific wavenumber range before submitting them to the PLS calculation.

The PLS procedure included mean-centering the data matrix before the calculation of the first latent variable. Unlike the study described in Chapter 4, the standard normal variate (SNV) transform was not found useful as a preprocessing step. The SNV calculation scales the spectral intensities to a standard deviation of 1.0, thus removing information that is needed to model concentration.

A cross-validation procedure was used to validate the model performance. This involved leaving out 10 % of spectra together with their replicate measurements and generating a calibration model from the remaining spectra. The computed calibration model was then used to predict the withheld spectra. This calibration/prediction step was iterated 10 times such that all spectra were withheld once. As described in Chapter 3 (Section 3.4), the errors in predicted temperature were pooled to compute a cross-validated standard error of prediction (CV-SEP).

A grid-search procedure analogous to that described in Chapter 3 (Section 3.2.3) and Chapter 4 (Section 4.4.4) was used to define the optimal wavelet parameters and wavenumber range for the calibration models. The range study included scanning the wavenumber range from 4,200 to 4,800 cm^{-1} in steps of 25 cm^{-1} using window sizes from 300 to 600 cm^{-1} in steps of 25 cm^{-1}. For each wavenumber range investigated, models based on 1-10 latent variables (PLS factors) were computed.

For models based on preprocessed spectra, also incorporated into the cross-validation procedure was an investigation of the optimal parameters associated with spectral preprocessing via the DWT. Optimization of wavelet function (order), level of decomposition and levels of reconstruction was performed with a grid search. During this study, the gird search protocol used in wavelet optimization included scanning the

wavelet order from 2 to 8 (step size 1) for the Daubechies (db) family. For each wavelet order investigated, the degree of decomposition was scanned from levels 2 to 10 (step size 1). For each wavelet order and decomposition level studied, the best hierarchical combination of details to use in reconstructing the spectrum was evaluated. As an example, when the decomposition level was 5, the combinations of details evaluated were [2], [2, 3], [2, 3, 4], and [2, 3, 4, 5, 6]. For each combination of wavelet parameters studied, the same grid search of the spectral range and PLS latent variables described above was employed.

The level 1 details and the last level approximation were never included in the grid search as these coefficients were never found to be useful. Whereas the last level approximation was needed in the temperature modeling work described in Chapter 4, here the emphasis was on quantitative models for analyte concentration. In this case, the background information encoded in the last level approximation was not useful.

The minimum CV-SEP value was used to obtain the optimal wavenumber range, wavelet parameters, and number of PLS factors (latent variables). Once the wavenumber range and wavelet parameters were selected, an *F*-test at the 95% level was used to determine if the number of latent variables could be reduced without a statistically significant increase in CV-SEP. The final model size corresponded to the number of latent variables that produced a value of CV-SEP that was not statistically different from the minimum CV-SEP.

5.4.4 Best calibration models for glucose predictions in pH 7.40 buffer samples

Calibration models were developed separately for preprocessed and raw glucose absorbance spectra. The same optimization procedures were used for each model as described above, with the difference being whether or not the DWT was applied. In both cases, the best calibration model was selected using the minimum CV-SEP, followed by the *F*-test. These calibration models are summarized in Table 5-3. Listed in the table are the wavenumber ranges, number of PLS latent variables, and values of the standard error

of calibration (SEC) and CV-SEP. As described in Chapter 3 (Section 3.3), the SEC is the standard error in predicted concentrations achieved when all calibration spectra are included in the calculation of the model.

The optimal preprocessing method was determined to be the Daubechies-6 (db6) wavelet function at eight levels of decomposition and using only the details at levels 2, 3, and 4 for reconstruction. The presence of only lower-level details in the reconstruction indicates the DWT is removing broad spectral background features while preserving the narrower features that are related to the analyte absorption bands. The optimal wavenumber range and model size for preprocessed glucose spectra was determined to be from 4,650 to 4,350 cm^{-1} with 7 PLS factors.

The optimal parameters determined for the model based on raw glucose absorbance spectra were a spectral range of 4,625 to 4,300 cm^{-1} and 5 PLS factors. The CV-SEP values for the models based on preprocessed and raw absorbance spectra were 0.14 and 0.15 mM, respectively. These models performed equivalently with the calibration data.

5.4.5 Prediction performance of glucose models

The two computed models were used to predict glucose concentrations for spectra in the five prediction sets. Each model and prediction set produced a standard error of prediction (SEP) value (Chapter 3, Section 3.5) describing the standard error in predicted concentrations across the spectra in that prediction set. Both models performed equally well when applied to prediction set 1 which was collected at the same temperature (37.0 °C) as the calibration set. However, prediction sets 2 to 5 (PRD2 – PRD5) performed poorly (SEP > 8 mM) regardless of the calibration model used due to the variation introduced by temperature fluctuations.

The SEP values for the prediction sets are summarized in Table 5-4. Figures 5-8 and 5-9 show correlation plots of predicted vs. reference concentrations and residual plots for the calibration data and prediction set PRD1, respectively, when Model 1 in Table 5-3

was used. The correlation plots show excellent agreement between predicted and reference glucose concentrations. The plot of the residuals vs. predicted concentrations for the calibration data is random in appearance. The residual plot for prediction set PRD1 exhibits small values, although there is a clear bias that appears at the higher glucose concentrations. Overall, the good prediction results are expected because of the matching 37.0 °C temperatures between the calibration data and prediction set PRD1.

Figure 5-10 displays the correlation plot obtained for prediction set PRD3. Significant errors in predicted concentration are noted in Figure 5-10 as the sample temperature deviates from 37.0 °C. This is seen more clearly in Figure 5-11 which plots the concentration residuals in prediction set PRD3 as a function of sample temperature. A clear relationship between residual and temperature is observed in this plot.

5.4.6 Temperature correction strategy to improve glucose predictions

As discussed in Chapter 4 (Section 4.1), temperature variation introduced during the spectral data collection leads to baseline variation in analyte absorbance spectra. According to Figure 4-1, this effect is systematic because the water absorption peaks shift to higher wavenumber with increasing temperature. It is also observed that analyte bands not associated with O-H bonds do not shift with changing temperature.[37] Therefore, a correction strategy is needed to model the temperature-dependent baseline variation and incorporate this information into the concentration predictions.

According to Figure 5-11, variations in solution temperature introduce a systematic trend in the glucose residuals. The concentration residual for glucose at 37 °C is a minimum because the glucose model was developed at 37°C. However, as the temperature deviates further from 37°C, the concentration residuals become larger and more significant. The greater the deviation from 37°C, the greater the error observed in the glucose prediction. This systematic pattern between glucose residuals and temperature can be modeled using a simple polynomial function. Second-order and third-order polynomial corrections were used to model the relationship between glucose

Table 5-3. Best PLS calibration models for glucose predictions in buffer samples

Model No.	Wavenumber range (cm^{-1})	Preprocessing method	Latent variables	SEC[a] (mM)	CV-SEP[b] (mM)
1	4,650-4,350	DWT (db6, 8 [2,3,4])[c]	7	0.10	0.14
2	4,625-4,300	None	5	0.11	0.15

[a]Standard error of calibration.

[b]Cross-validated standard error of prediction.

[c]Notation is wavelet family and order of wavelet function, number of levels of decomposition, and the levels used in the reconstruction of the spectrum (details only).

Table 5-4. Prediction performance of PLS calibration models for glucose.

Data set	**Temperature of spectral collection (°C)**	**SEP[a] (mM)**	
		Model 1[b]	**Model 2[b]**
Calibration[c]	37.0	0.14[a]	0.15[a]
Prediction set 1 (PRD1)	37.0	0.13	0.20
Prediction set 2 (PRD2)	20.0 to 40.5	8.19	8.19
Prediction set 3 (PRD3)	20.0 to 40.5	8.56	8.56
Prediction set 4 (PRD4)	20.0 to 40.5	8.71	8.71
Prediction set 5 (PRD5)	20.0 to 40.5	9.14	9.14

[a]Standard error of prediction computed from the errors in predicted concentrations.

[b]Model numbers correspond to the entries in Table 5-3.

[c]Statistics given for the calibration data are values of CV-SEP.

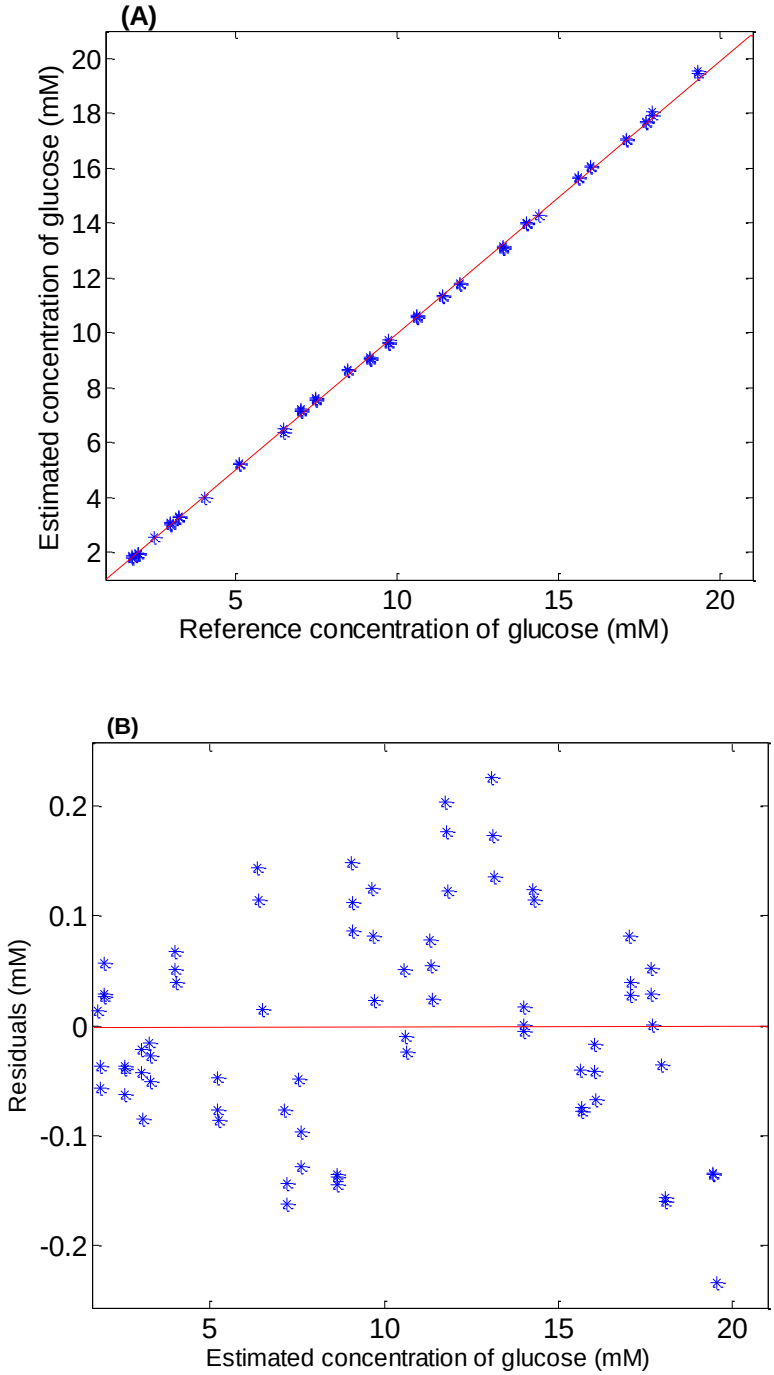

Figure 5-8. Correlation and residual plots for calibration. **(A)** Correlation plot of predicted vs. reference glucose concentrations for the calibration of glucose in pH 7.4 buffer at 37.0 °C. (**B**) Plot of residuals vs. predicted concentrations. Model 1 in Table 5-3 was used. The red lines in panels A and B, respectively, correspond to perfect correlation between estimated and reference concentrations and 0.0 residuals.

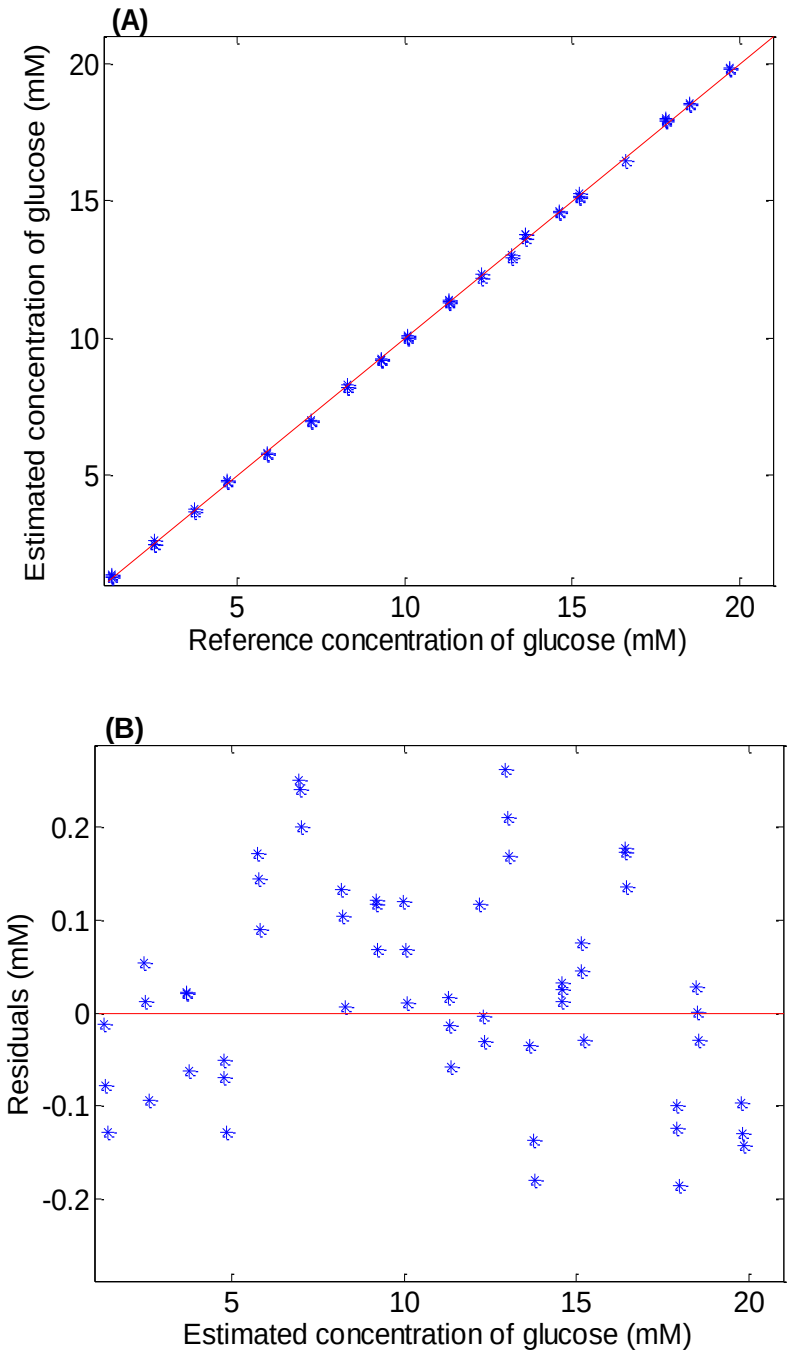

Figure 5-9. Correlation and residual plots. **(A)** Correlation plot of predicted vs. reference concentrations for prediction set 1 (PRD1). These data were collected at 37 °C. (**B**) Plot of residuals vs. predicted concentrations. Model 1 in Table 5-3 was used. The red lines in panels A and B, respectively, correspond to perfect correlation between estimated and reference concentrations and 0.0 residuals.

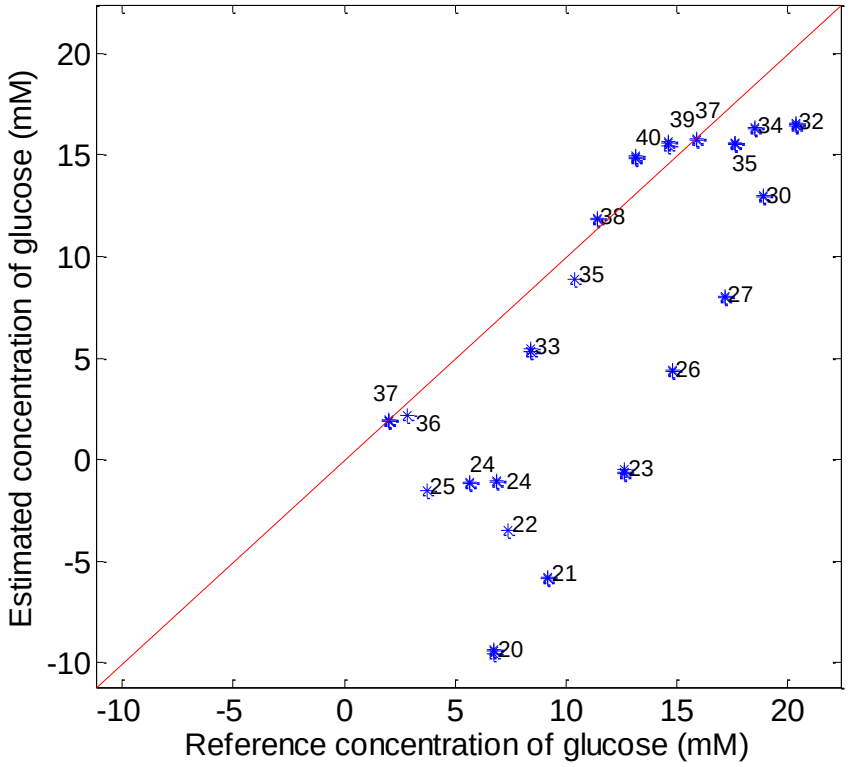

Figure 5-10. Correlation plot of predicted vs. reference concentrations for prediction set 3 (PRD3). Data labels correspond to the sample temperatures and the red line corresponds to perfect correlation between estimated and reference concentrations. Model 1 in Table 5-3 was used. Significant errors in predicted glucose concentrations are noted as the temperature deviates from 37 °C.

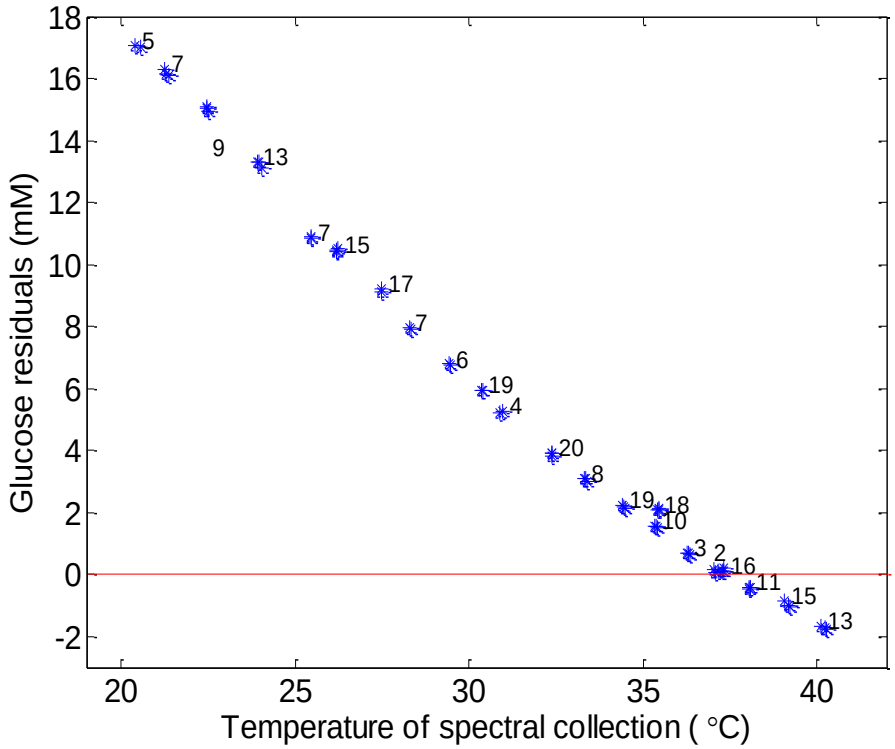

Figure 5-11. Glucose concentration residuals from prediction set 3 (PRD3) vs. sample temperature. Data labels are the reference glucose concentrations and the red line denotes a residual of 0.0. Model 1 in Table 5-3 was used. A clear relationship between residual and temperature is observed, whereas no relationship is apparent between the residuals and the reference glucose concentrations.

residuals from prediction set PRD2 and temperature. As noted in Table 5-1, these prediction data incorporated temperature variation from 20.0 to 40.5 °C. The polynomial models were computed by standard least-squares methods and are described in Table 5-5. Both models gave good fits. However, in the case of the third-order polynomial equation, the cubic term was not statistically significant (i.e., not statistically different from zero). A cutoff probability of 0.05 was used in making this determination. On the basis of these results, a second-order polynomial correction was chosen to be effective in modeling the relationship between glucose residuals and temperature. Fitted line and residuals plots for the second-order model are displayed in Figure 5-12.

The next step of the correction strategy was to utilize this polynomial fit effectively in obtaining accurate glucose predictions. Figures 5-13 and 5-14 are flow charts that explain the protocol for the proposed temperature correction strategy. This protocol has two phases: (1) a development phase and (2) an application phase. The development phase can be considered part of the overall calibration process, while the application phase is directed to the prediction of an unknown sample under conditions of variable sample temperature.

During the development phase, spectra of known analyte concentrations and temperatures are used. A quantitative calibration developed at 37.0 °C is used to predict the analyte concentrations corresponding to the above-mentioned spectra. The difference between each reference analyte concentration and associated predicted concentration provides the residual for the corresponding spectrum. Using the known sample temperatures recorded during the spectral collection (T), a second-order polynomial fit can be generated to model the relationship between concentration residuals and temperature. According to Figure 5-13, coefficients a, b and c can be obtained from the polynomial fit to compute a correction factor (ε) for a given temperature.

During the application phase, spectra of unknown analyte concentration are used. The sample temperatures corresponding to these spectra may or may not be known.

Table 5-5. Polynomial models for the relationship between glucose residuals and sample temperature[a]

Model	Fitted polynomial equation	R^2 [b]	Signficance levels for coefficients[c]
Second-order	$y = 0.0189\ x^2 - 2.11\ x + 52.7$	0.999	< 0.01, < 0.01, < 0.01
Third-order	$y = 0.000398\ x^3 - 0.0173\ x^2 - 1.04\ x + 42.4$	0.999	0.42, < 0.01, < 0.01, <0.01

[a]Model 1 in Table 5-3 was applied to prediction set PRD2 to generate the residuals.

[b]Coefficient of multiple determination expressing fraction of variance in the dependent variable explained by the computed model.

[c]Significance levels (two-tailed) associated with the *t*-values for the computed regression coefficients. Probabilities indicate the likelihood that the coefficient is not statistically different from zero. Coefficients with associated probabilities > 0.05 are judged to have little significance. In the table, probabilities are listed from highest to lowest polynomial order.

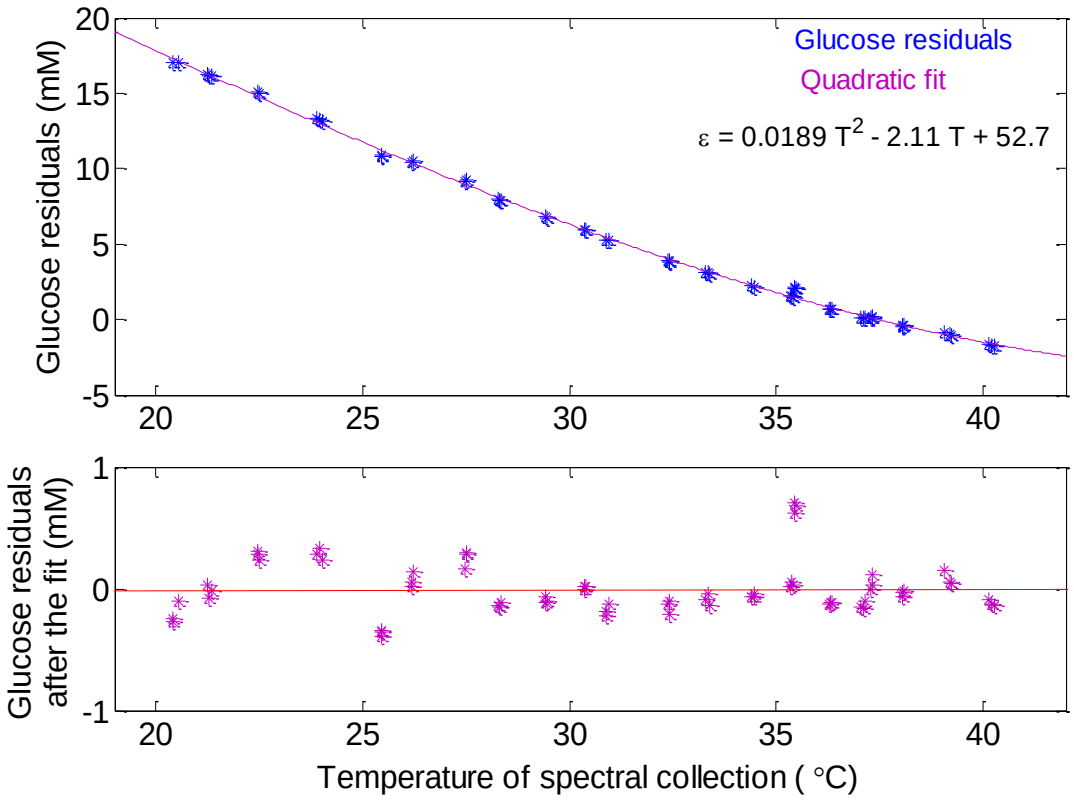

Figure 5-12. Second-order polynomial correction for glucose residuals and temperature. The top panel displays the concentration residuals from prediction set PRD2 (symbols) and the least-squares fitted equation (solid line). The bottom panel displays the residuals after the polynomial fit. Model 1 in Table 5-3 was used to generate the residuals. No obvious structure is apparent in the residuals after the fit.

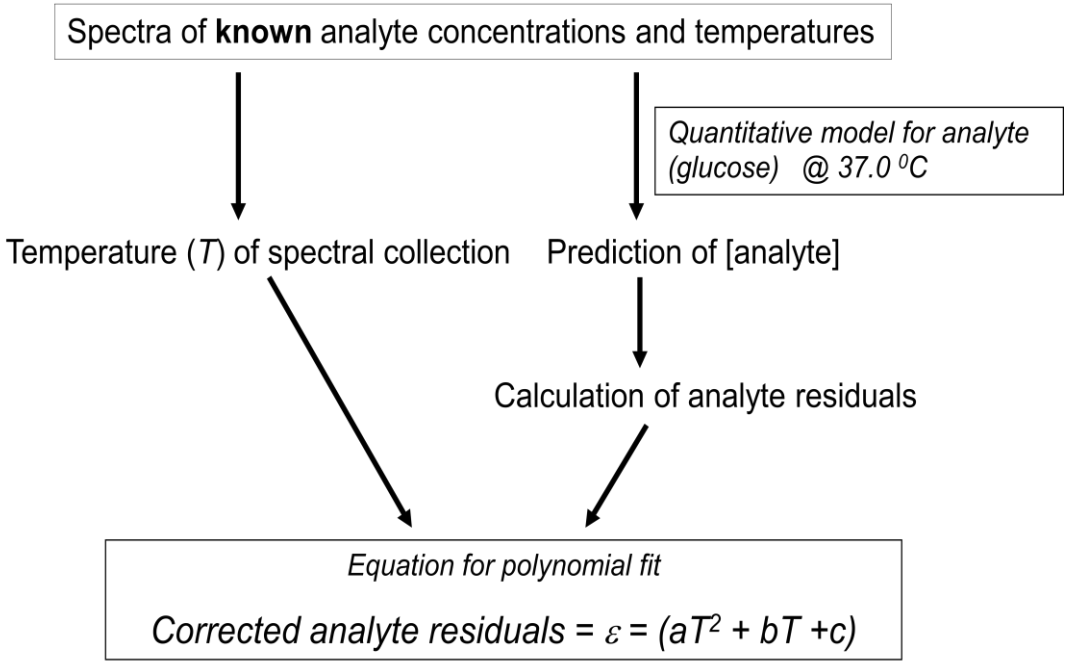

Figure 5-13. Development phase of the temperature correction strategy.

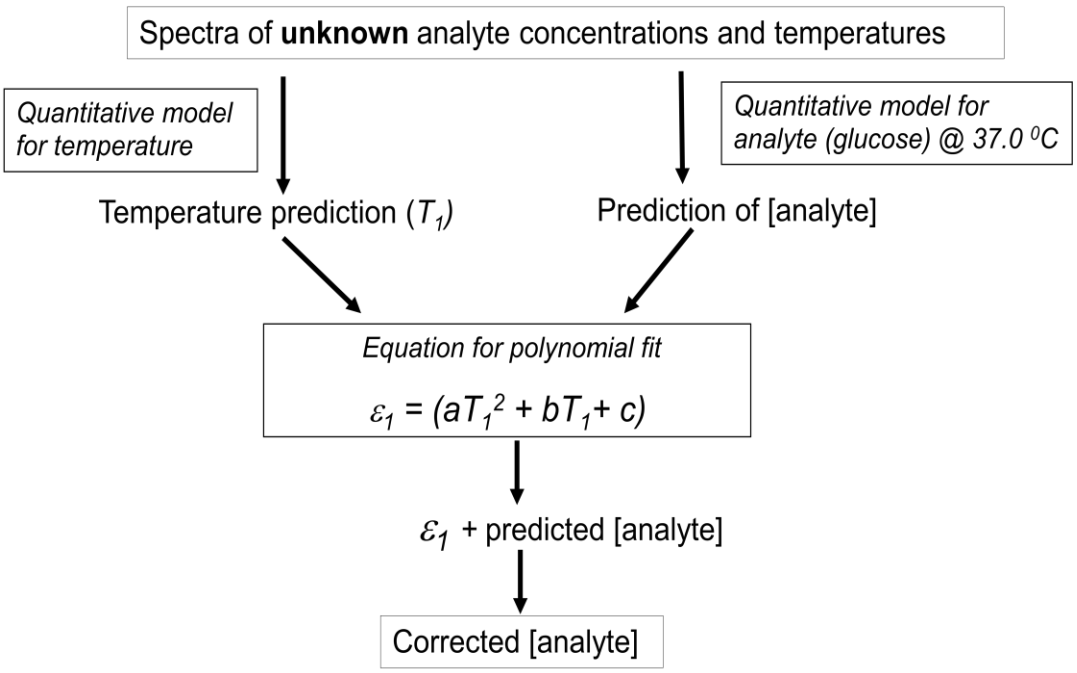

Figure 5-14. Application phase of the temperature correction strategy.

Using the quantitative calibration model developed at 37.0 °C, analyte concentrations are predicted. Then, using either the known sample temperature or the temperature predicted from a model such as those described in Chapter 4, a correction to the predicted concentration is obtained. This is done by combining the modeled coefficients (*a*, *b* and *c*) with the predicted or known temperature to obtain a predicted residual (correction factor). Addition of the correction factor to the predicted analyte concentration results in the corrected concentration.

5.4.7 Prediction performance after temperature correction

The temperature correction strategy based on the second-order polynomial fit of the concentration residuals was applied to prediction sets PRD1 to PRD5. The correction procedure was implemented first with the known sample temperatures recorded during the spectral acquisition. Table 5-6 summarizes the prediction results.

Next, the correction was applied using a temperature model. For this experiment, a temperature model was built with the preprocessed glucose spectra in prediction set PRD2. The details of parameter optimization and calibration model building were in accordance with the procedures developed during the work described in Chapter 4 (Section 4.4.4). The best temperature model included preprocessing with the SNV transform, followed by the DWT. In applying the DWT, the db5 wavelet was employed, five levels of decomposition were performed, and the spectral reconstruction used only the approximation and details from level 5. The optimal wavenumber range was 4,800 to 4,150 cm^{-1} with 3 PLS factors.

The prediction results corresponding to the use of this temperature model in implementing the temperature correction algorithm are displayed in Table 5-7. Also included in the table are the SEP values for the temperature predictions. Across the five prediction sets, the average SEP was 0.13 °C. This level of performance is analogous to that obtained in the temperature modeling work described in Chapter 4.

The average of the SEP values obtained before the temperature correction was applied was 8.65 mM across prediction sets PRD1 to PRD5. When the correction procedure was implemented with the measured reference temperatures, the average SEP value obtained for the five prediction sets was reduced to 0.23 mM (Model 1 in Table 5-3). When predicted temperatures were used, the average SEP was 0.26 mM for the case of Model 1. According to these results, SEP values obtained with the measured temperatures were only slightly better than the SEP values obtained with the predicted temperatures. This behavior is expected as the predicted temperatures carry an inherent error from the temperature calibration model which is larger than the error obtained with the measured temperatures. The SEP values obtained for prediction set PRD1 were the same regardless of whether or not the correction was applied. This is also expected as there is no temperature fluctuation to correct in this prediction set. Model 1 consistently outperformed Model 2 and the difference between the SEP values obtained with the two models increased with time. Preprocessing with the DWT proved useful in the removal of spectral background features that caused deterioration of the prediction results over time.

Figure 5-15 summarizes the prediction performance of the PLS calibration models for glucose before and after the temperature correction using predicted temperatures. Figures 5-16 and 5-17 show correlation plots of prediction sets PRD3 and PRD4 before and after the temperature correction. Excellent correlation is noted between predicted and reference concentrations after applying the correction procedure. Figure 5-18 displays the residuals vs. predicted glucose concentration after applying the correction. Both residual plots show randomly scattered residuals with slight bias evident with prediction set PRD4. In generating these plots, predicted temperatures were again used as inputs to the correction procedure and Model 1 in Table 5-3 was employed.

5.5 Development of temperature correction strategies to improve concentration predictions in mixture solutions of glucose and lactate

Table 5-6. Prediction performance of PLS calibration models for glucose after temperature correction using recorded sample temperatures

Data set	SEP after temperature correction[a] (mM)	
	Model 1[b]	Model 2[b]
Prediction set 1 (PRD1)	0.13	0.15
Prediction set 2 (PRD2)	0.20	0.23
Prediction set 3 (PRD3)	0.22	0.31
Prediction set 4 (PRD4)	0.23	0.32
Prediction set 5 (PRD5)	0.36	0.50

[a]Standard error of prediction computed from the errors in the corrected glucose predictions.

[b]Model numbers correspond to the entries in Table 5-3.

Table 5-7. Prediction performance of PLS calibration models for glucose after the temperature correction using predicted temperatures

Data set	SEP for temperature prediction[a] (°C)	SEP after temperature correction[b] (mM)	
		Model 1[c]	Model 2[c]
Prediction set 1 (PRD 1)	0.09	0.13	0.15
Prediction set 2 (PRD2)	0.11	0.20	0.23
Prediction set 3 (PRD3)	0.13	0.20	0.29
Prediction set 4 (PRD4)	0.15	0.24	0.32
Prediction set 5 (PRD5)	0.17	0.38	0.54

[a]Standard error of prediction computed from the errors in predicted temperatures.

[b]Standard error of prediction computed from the errors in the corrected glucose predictions.

[c]Model numbers correspond to the entries in Table 5-3.

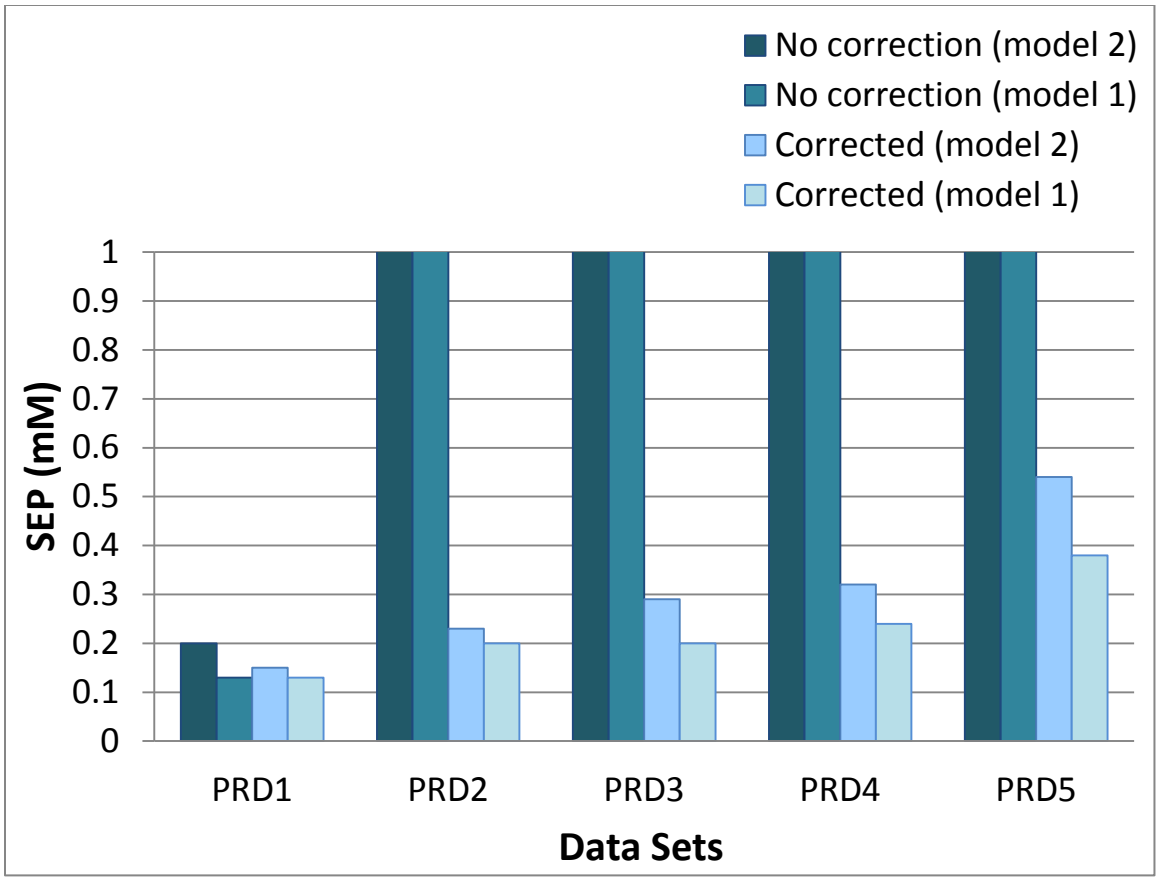

Figure 5-15. Prediction performance of PLS calibration models for glucose before and after the temperature correction. Results shown correspond to the use of predicted temperatures as inputs to the temperature correction procedure. The SEP axis is clipped at 1.0 mM for clarity.

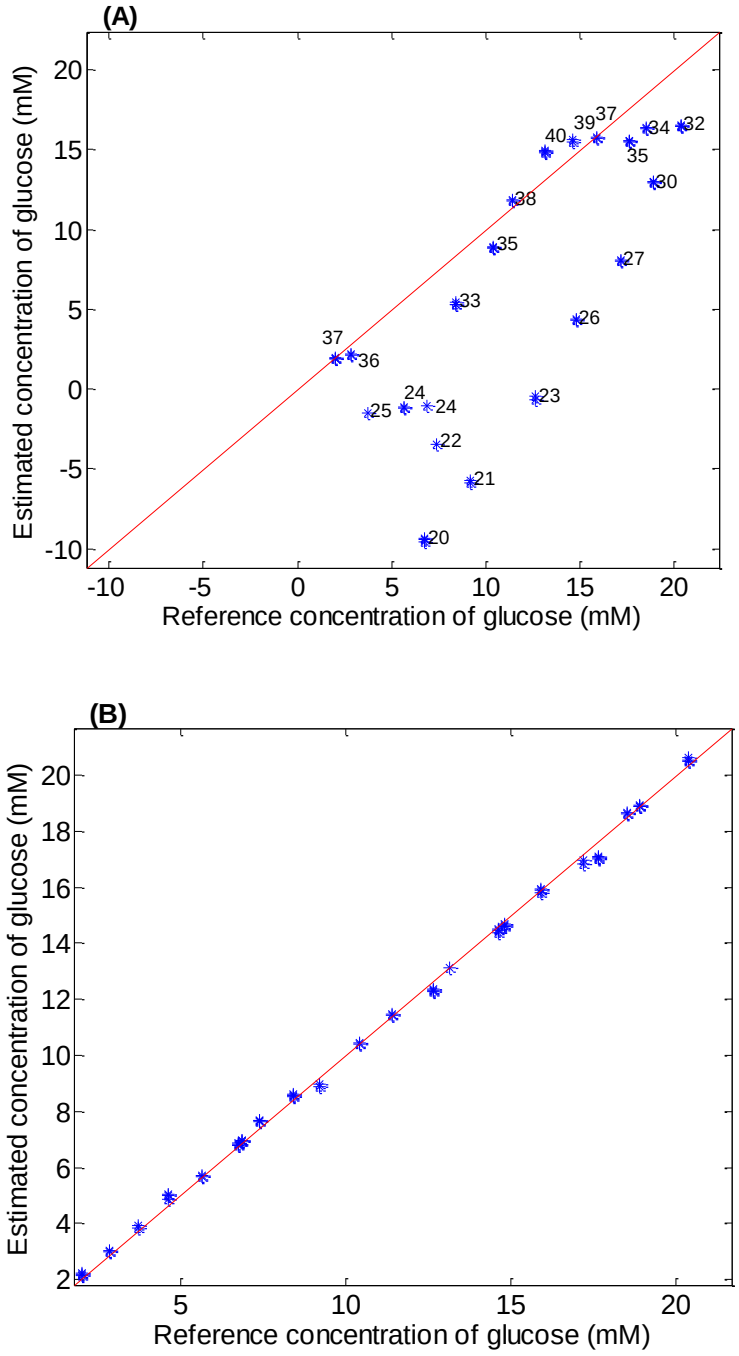

Figure 5-16. Effect of temperature correction strategy for prediction set 3. Correlation plot of prediction set PRD3 for glucose in pH 7.4 buffer from 20.0 to 40.5 °C before **(A)** and after **(B)** temperature correction. Model 1 in Table 5-3 was used and predicted temperatures were employed. Data labels in panel A are the sample temperatures, and the red lines in both panels correspond to perfect correlation between estimated and reference concentrations.

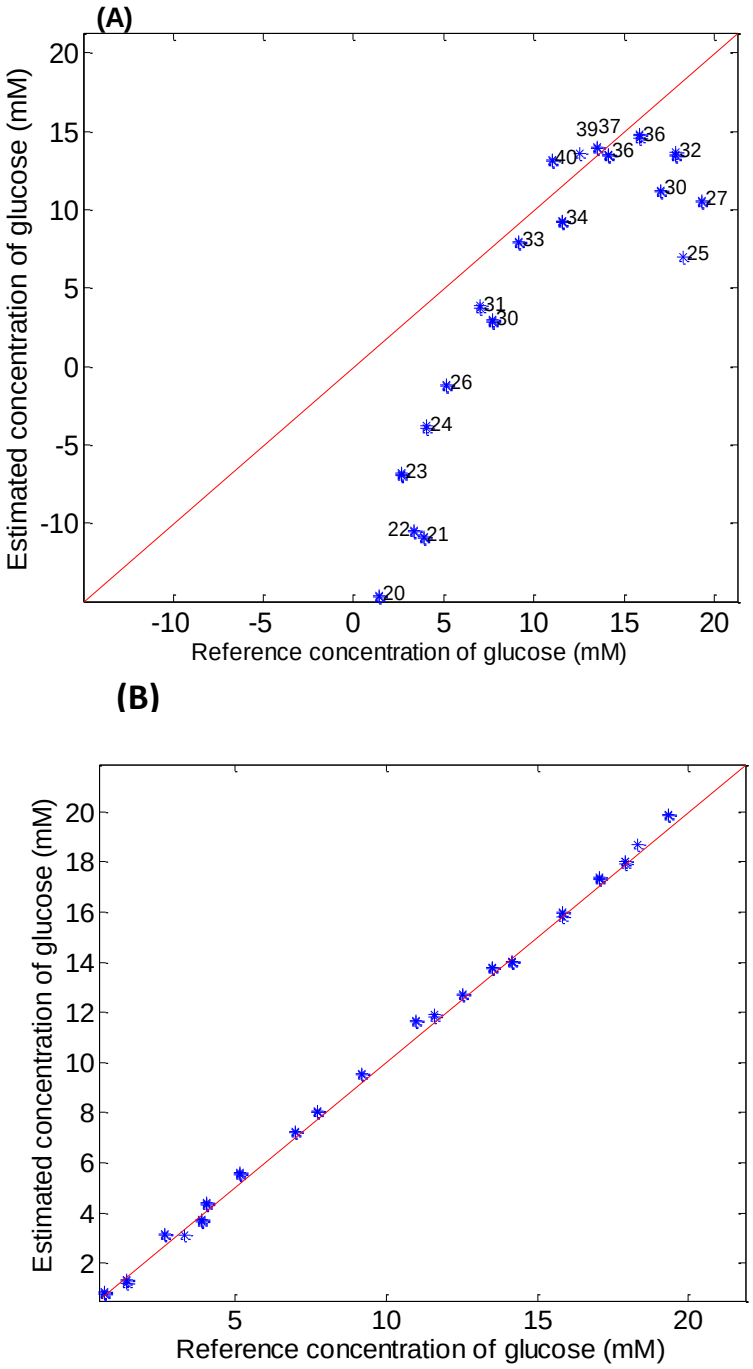

Figure 5-17. Effect of temperature correction strategy for prediction set 4. Correlation plot of prediction set PRD4 for glucose in pH 7.4 buffer from 20.0 to 40.5 °C before **(A)** and after **(B)** temperature correction. Model 1 in Table 5-3 was used and predicted temperatures were employed. Data labels in panel A are the sample temperatures, and the red lines in both panels correspond to perfect correlation between estimated and reference concentrations.

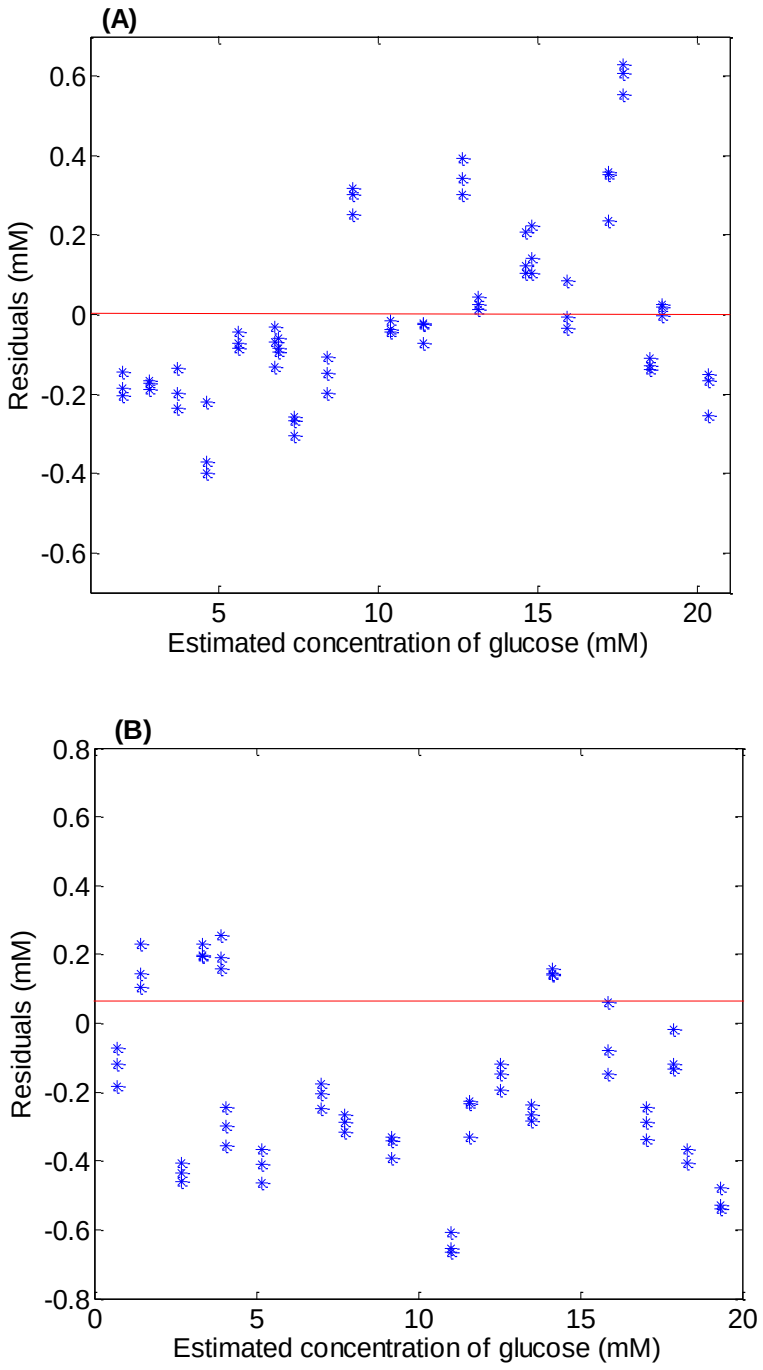

Figure 5-18. Plots of residuals after application of the temperature correction procedure vs. predicted corrected glucose values for prediction sets PRD3 and PRD4. The red lines in both panels denote residuals of 0.0. Predicted temperatures were used in the correction procedure and Model 1 in Table 5-3 was employed. (**A**) PRD3 and (**B**) PRD4.

Given the successful results obtained with solutions of glucose in buffer, an attempt was made to extend the temperature correction strategy to a multi-analyte system. In this work, PLS regression models were developed to predict glucose and lactate concentrations using laboratory-prepared mixture solutions of glucose and lactate (1.0 to 20.0 mM) in pH 7.4 buffer, followed by application of the temperature correction strategy to improve glucose and lactate predictions over the temperature range of 20.0 to 40.5 °C.

5.5.1 PLS regression models for glucose and lactate concentrations

In order to assess the ability to predict glucose and lactate concentrations in pH 7.4 buffer, PLS calibration models were generated separately for glucose and lactate using the absorbance spectra of the calibration samples recorded at 37.0 °C. These absorbance spectra were generated using single-beam glucose/lactate spectra with respect to an average air spectrum of the day of spectral collection. Absorbance spectra were preprocessed with the DWT before submitting them to the calibration model. The cross-validation procedure, spectral range study, and optimization of wavelet parameters discussed previously in Section 5.4.3 were used to optimize the parameters and select the best calibration models.

5.5.2 Best calibration models for glucose and lactate concentration predictions

Glucose calibration models were developed separately for preprocessed (Model 3) and raw (Model 4) absorbance spectra. These models are summarized in Table 5-8. The optimal wavenumber range for preprocessed spectra was 4,650 to 4,325 cm^{-1} with seven PLS factors. The optimal preprocessing method used the Daubechies-4 (db4) wavelet function at five levels of decomposition and employing the details at levels 2, 3 and 4 for reconstruction. When raw absorbance spectra were used, the optimal wavenumber range was 4,600 to 4,275 cm^{-1} with six PLS factors. The CV-SEP values for Models 3 and 4 were 0.13 and 0.14 mM, respectively. Difference in the number of factors found to be optimal are judged to be an artifact of the optimization procedure when only a single model is chosen from among many similar performing models.

Table 5-9 presents the corresponding results for the lactate calibration models. As with glucose, models were computed with preprocessed (Model 5) and raw (Model 6) absorbance spectra. The optimal wavenumber range for preprocessed spectra was 4,525 to 4,200 cm^{-1} with seven PLS factors. The optimal preprocessing method used the Daubechies-6 (db6) wavelet function at five levels of decomposition, employing the details at levels 2, 3 and 4 for reconstruction. When the raw absorbance spectra were used, the optimal wavenumber range was 4,750 to 4,375 cm^{-1} with five PLS factors. The values of CV-SEP for Models 5 and 6 were 0.13 and 0.10 mM, respectively. Again, no significance is attributed to the differences in models size between the cases of raw and preprocessed spectra.

5.5.3 Prediction performance of glucose and lactate models without temperature correction

In the case of glucose predictions, both prediction models performed equally well for prediction set 6 (PRD6) which was collected at the same temperature (37.0 °C) as the calibration set. However, prediction sets 7 and 8 (PRD7 and PRD8) performed poorly (SEP > 3 mM) regardless of the calibration model due to the spectral variation introduced by changing the sample temperature.

Similar results were obtained with the lactate models. Both calibration models performed equally well for prediction set PRD6 which was collected at the same temperature (37.0°C) as the calibration data. Prediction sets PRD7 and PRD8 performed poorly (SEP > 4 mM) with both models due to the effects of changing the sample temperature. Table 5-10 summarizes the SEP values for the glucose and lactate predictions.

5.5.4 Application of temperature correction strategy to glucose and lactate predictions

The same protocol described in Section 5.4.5 was used to correct the effects of temperature variation in the glucose and lactate predictions. Separate models were

computed to describe the relationships between glucose and lactate concentration residuals and temperature. Prediction set PRD6 was used for this purpose. Figures 5-19 and 5-20 illustrate the second-order polynomial fits for the glucose and lactate residuals, respectively. As observed in the work with the fit of the concentration residuals associated with the spectra of glucose in buffer, excellent correlation is obtained with the second-order polynomial model.

The fitted equations for the glucose and lactate residuals are quite similar. Relative to the model for the glucose residuals, coefficients *a*, *b*, and *c* differ by only 2., 3., and 8. % for the lactate model. The signs of the corresponding coefficients are the same between the two models. Comparison of the model for the glucose residuals with the model computed previously for solutions of glucose in buffer reveals similar magnitudes and signs for the coefficients but significant differences in the coefficient values. Relative to the model for the glucose residuals derived from the mixture solutions, coefficients *a*, *b*, and *c* differ by 15, 43, and 67 % for the model based on glucose/buffer solutions.

Similarities in the signs and magnitudes of the coefficients across the three models suggests the relationship between concentration residuals and sample temperatures has the same basic shape for the two sample matrixes investigated. This is assumed to derive from the effect of temperature on the background absorbance of water. The high similarity in the coefficients derived for the relationships of the glucose and lactate residuals with temperature for the glucose/lactate/buffer matrix further suggests the relationship between residual and temperature is matrix-dependent. The larger differences in the model coefficients for the glucose residuals across the glucose/buffer and glucose/lactate/buffer matrixes suggests that while the properties of water determine the basic functional form, the specific matrix components other than water do contribute to the relationship between concentration residuals and temperature.

Table 5-8. Best PLS calibration models for glucose concentrations in mixture solutions of glucose and lactate

Model No.	Wavenumber range (cm^{-1})	Preprocessing method	Latent variables	SEC[a] (mM)	CV-SEP[b] (mM)
3	4600-4325	DWT (db4, 5 [2,3,4])[c]	7	0.11	0.13
4	4600-4275	none	6	0.10	0.14

[a]Standard error of calibration.

[b]Cross-validated standard error of prediction.

[c]Notation is wavelet family and order of wavelet function, number of levels of decomposition, and the levels used in the reconstruction of the spectrum (details only).

Table 5-9. Best PLS calibration models for lactate concentrations in mixture solutions of glucose and lactate

Model No.	Wavenumber range (cm^{-1})	Preprocessing method	Latent variables	SEC[a] (mM)	CV-SEP[b] (mM)
5	4525-4200	DWT (db6, 5 [2,3,4])[c]	7	0.11	0.13
6	4750-4375	None	5	0.10	0.10

[a]Standard error of calibration.

[b]Cross-validated standard error of prediction.

[c]Notation is wavelet family and order of wavelet function, number of levels of decomposition, and the levels used in the reconstruction of the spectrum (details only).

Table 5-10. Prediction performance of PLS calibration models for glucose and lactate without temperature correction

Data set	Temperature of spectral collection (°C)	SEP for glucose (mM)		SEP for lactate (mM)	
		Model[a] 3	Model[a] 4	Model[b] 5	Model[b] 6
Calibration	37.0	0.13	0.14	0.13	0.10
Prediction set 6 (PRD6)	37.0	0.16	0.13	0.24	0.23
Prediction set 7 (PRD7)	20.0 to 40.5	3.78	3.78	4.22	4.22
Prediction set 8 (PRD8)	20.0 to 40.5	3.80	3.80	4.58	4.58

[a]Model numbers correspond to the entries in Table 5-8.

[b]Model numbers correspond to the entries in Table 5-9.

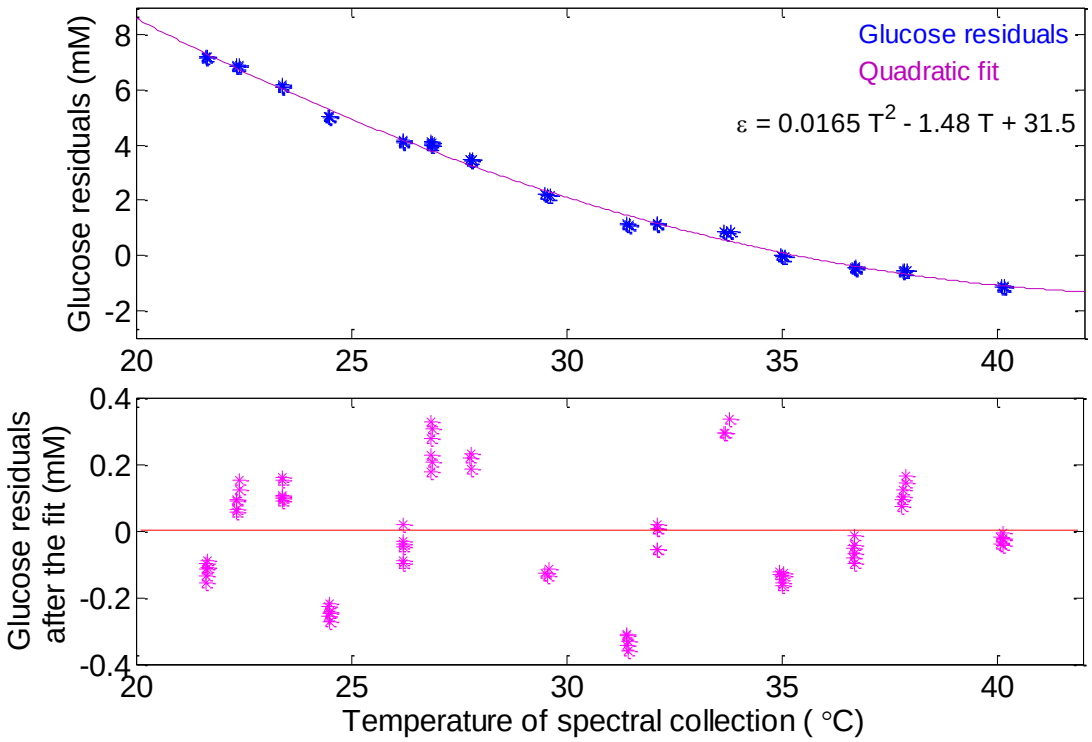

Figure 5-19. Second-order polynomial correction for glucose residuals vs. temperature in mixture solutions of glucose and lactate. Model 3 in Table 5-8 was applied to prediction set PRD6 to generate the residuals. The top panel displays the concentration residuals (symbols) and the least-squares fitted equation (solid line). The value of R^2 for the fit was 0.999. The bottom panel displays the residuals after the polynomial fit. No obvious structure is apparent in the residuals after the fit.

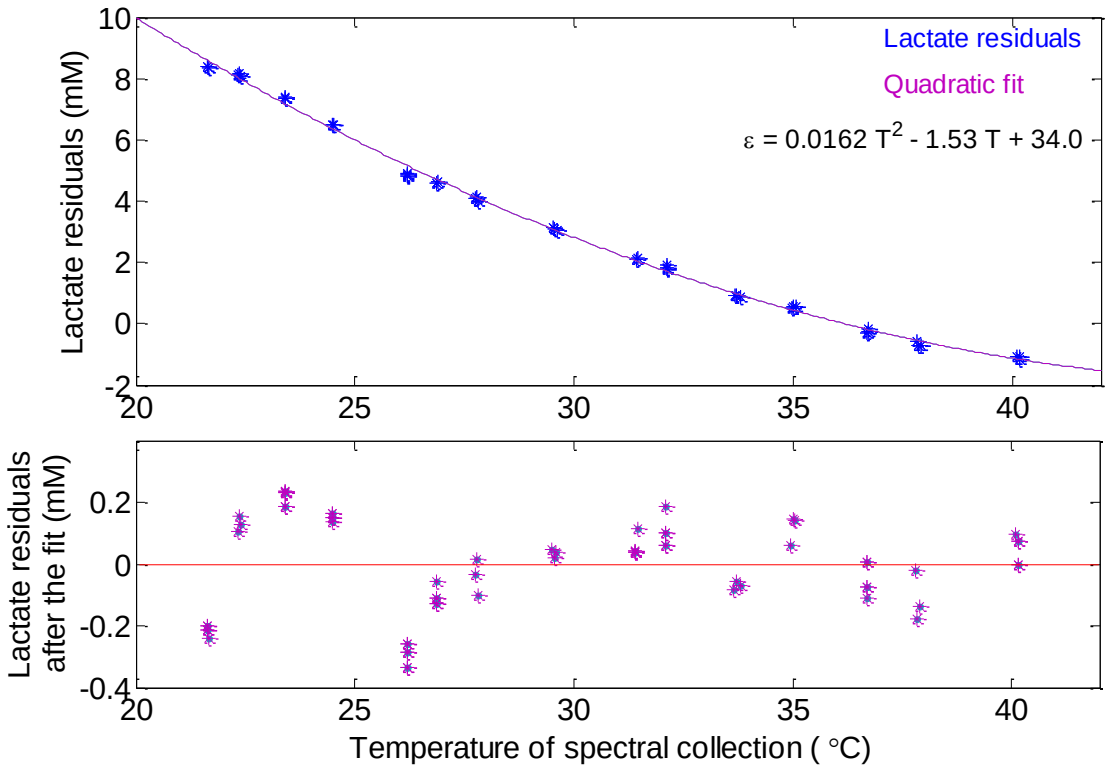

Figure 5-20. Second-order polynomial correction for lactate residuals vs. temperature in mixture solutions of glucose and lactate. Model 5 in Table 5-9 was applied to prediction set PRD6 to generate the residuals. The top panel displays the concentration residuals (symbols) and the least-squares fitted equation (solid line). The value of R^2 for the fit was 0.999. The bottom panel displays the residuals after the polynomial fit. No obvious structure is apparent in the residuals after the fit.

5.5.5 Prediction performance of glucose and lactate models after temperature correction

The temperature correction strategy based on the second-order polynomial fit improved the SEP values for both glucose and lactate prediction sets which were collected over the range of 20.0 to 40.5 ℃. In this work, predicted temperatures were used as the inputs into the temperature correction procedure.

A temperature model was built with preprocessed glucose and lactate mixture spectra from prediction set PRD6. The details of parameter optimization and calibration model building were in accordance with Chapter 4, Section 4.4.4. The best temperature model included the SNV transform and the DWT. The wavelet parameters included function db5, five levels of decomposition, and the use of only the approximation and details from level 5 in reconstructing the spectra. The optimal wavenumber range was 4,800 to 4,250 cm^{-1} with 3 PLS factors.

Table 5-10 summarizes the SEP values obtained for the glucose and lactate predictions after the temperature correction. The average SEP values obtained for glucose before the correction was 3.79 mM (across prediction sets PRD7 and PRD8). After temperature correction, the average SEP value obtained for glucose for the two prediction sets improved to 0.23 mM.. For the same prediction sets, the average SEP value obtained for lactate before the correction was 4.40 mM. After applying the correction, the average SEP value was reduced to 0.24 mM. Figure 5-21 summarizes the prediction performance of the PLS calibration models for glucose and lactate before and after the temperature correction. Figures 5-22 and 5-23 display correlation plots for glucose and lactate, respectively, for prediction set PRD8 before and after temperature correction was applied. Both figures are based on calibration models that included preprocessing (i.e., Model 3 in Table 5-8 and Model 5 in Table 5-9). Excellent correlation between predicted and reference concentrations is observed after applying the correction procedure.

Table 5-11. Prediction performance of PLS calibration models for glucose and lactate after temperature correction.

Data set	Temperature of spectral collection (°C)	SEP[a] (°C)	SEP for glucose after temperature correction[b] (mM)		SEP for lactate after temperature correction[b] (mM)	
			Model 3[c]	Model 4[c]	Model 5[d]	Model 6[d]
Prediction set 6 (PRD6)	37.0	0.09	0.16	0.13	0.24	0.23
Prediction set 7 (PRD7)	20.0 to 40.5	0.11	0.15	0.21	0.16	0.19
Prediction set 8 (PRD8)	20.0 to 40.5	0.13	0.32	0.33	0.34	0.29

[a]Standard error of prediction computed from the errors in predicted temperatures.

[b]Standard error of prediction computed from the errors in the corrected glucose predictions.

[c]Model numbers correspond to the entries in Table 5-8.

[d]Model numbers correspond to the entries in Table 5-9.

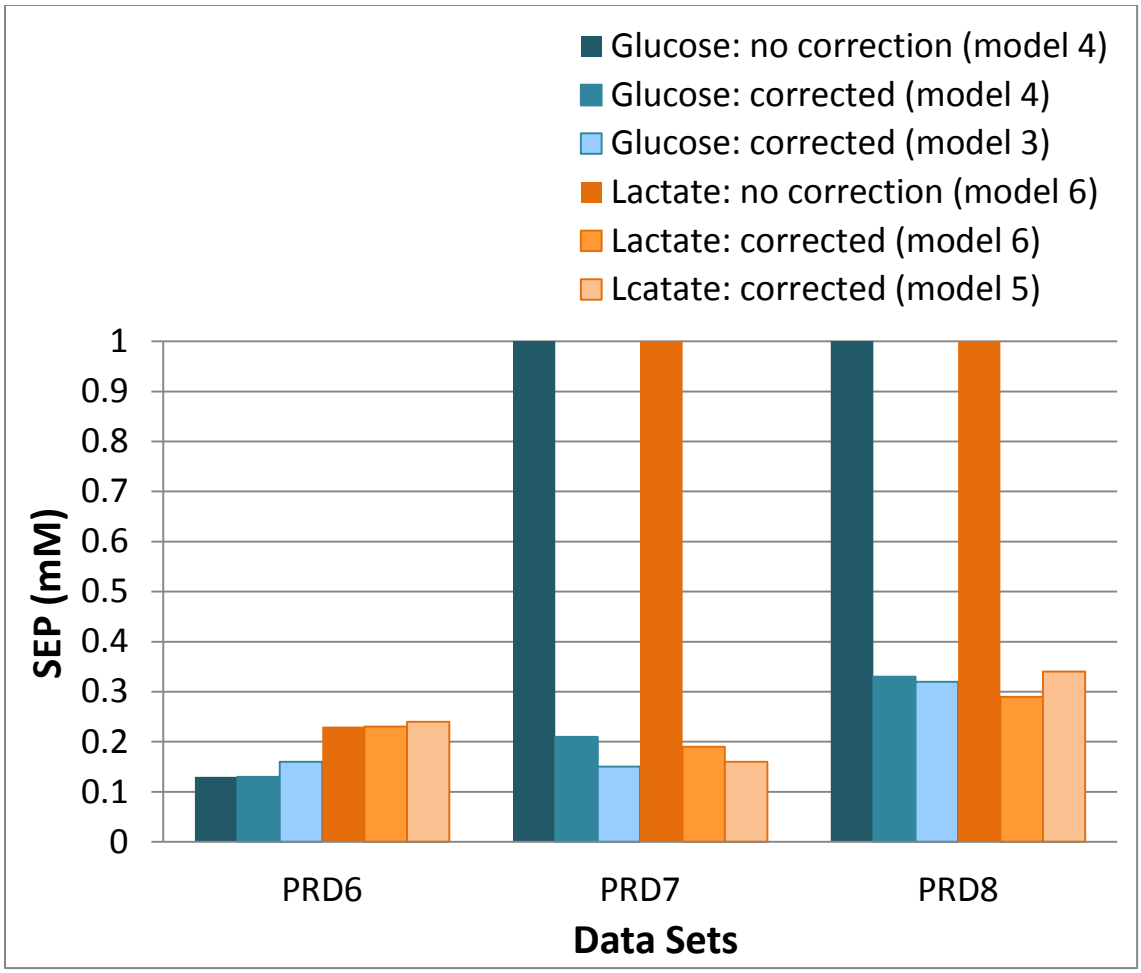

Figure 5-21. Prediction performance of PLS calibration models for glucose and lactate in mixture solutions of glucose and lactate in pH 7.4 buffer before and after the temperature correction. Results shown correspond to the use of predicted temperatures as inputs to the temperature correction procedure. The SEP axis is clipped at 1.0 mM for clarity. Model numbers refer to the results in Tables 5-8 and 5-9.

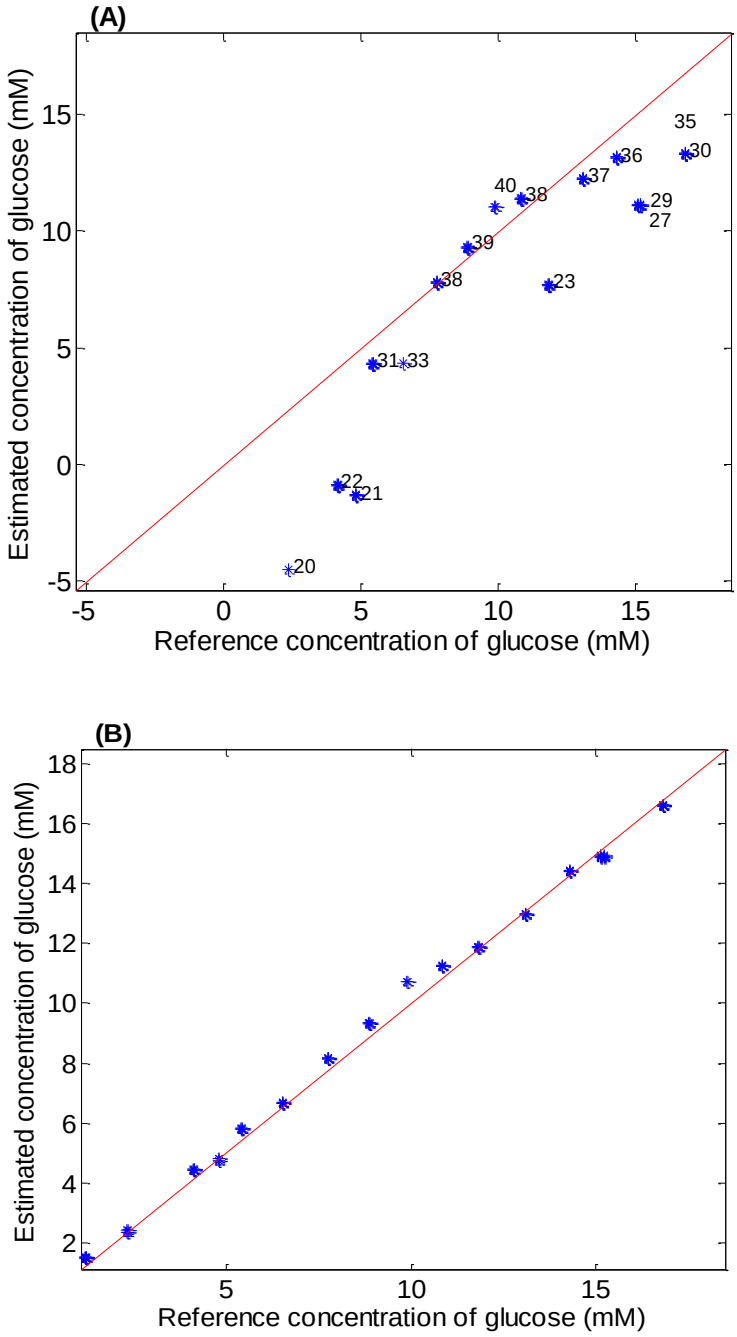

Figure 5-22. Effect of temperature correction strategy for prediction set 8. Correlation plot of prediction set PRD8 for glucose in mixture solutions of glucose and lactate from 20.0 to 40.5 °C **(A)** before and **(B)** after temperature correction. Model 3 in Table 5-8 was used and predicted temperatures served as the inputs to the temperature correction procedure.. Data labels in panel A correspond to the sample temperatures, and the red lines in both panels denote perfect correlation between predicted and reference concentrations.

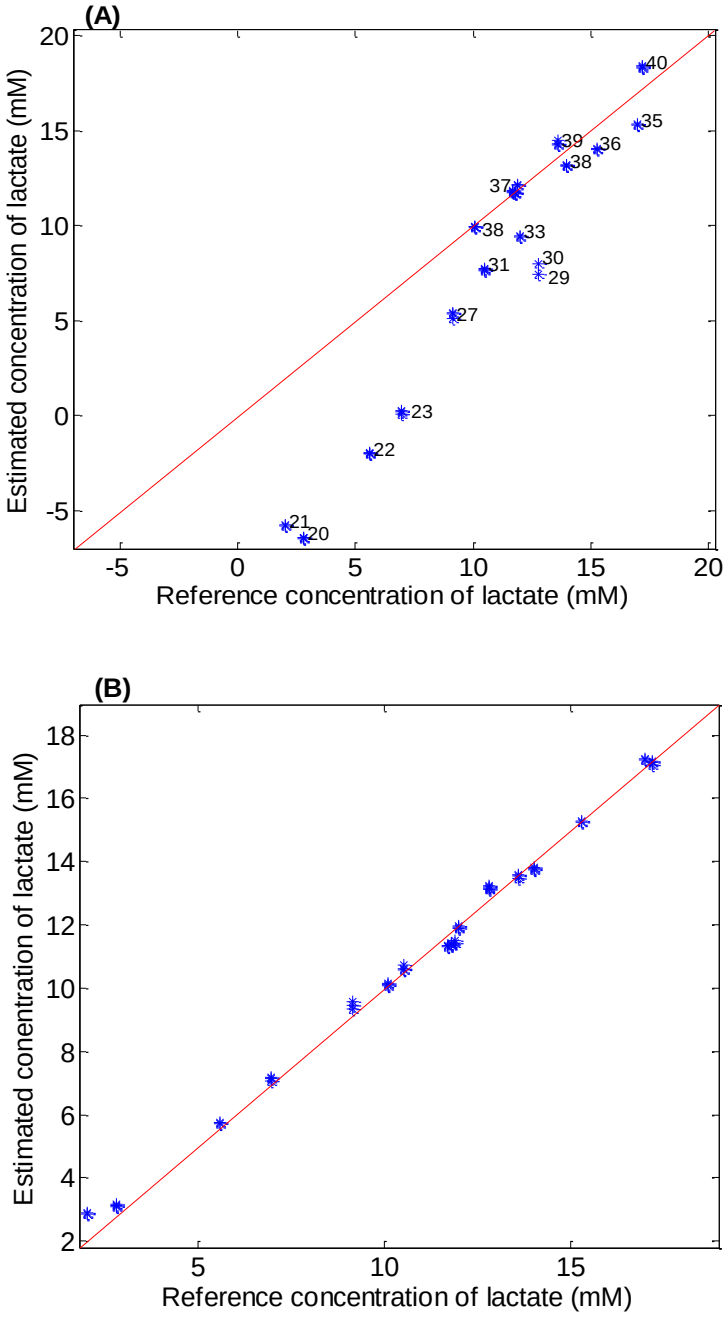

Figure 5-23. Effect of temperature correction strategy for prediction set 8. Correlation plot of prediction set PRD8 for lactate in mixture solutions of glucose and lactate from 20.0 to 40.5 °C **(A)** before and **(B)** after temperature correction. Model 5 in Table 5-9 was used and predicted temperatures served as the inputs to the temperature correction procedure. Data labels in panel A correspond to the sample temperatures, and the red lines in both panels denote perfect correlation between predicted and reference concentrations.

5.6 Comparison to alternative strategies for overcoming effects of temperature variation

Two other strategies were used as possible alternatives to overcome the effects of temperature fluctuation. The first strategy was to employ digital Fourier filtering as a possible signal preprocessing method to develop quantitative models for analyte predictions. This experiment is essentially the same as described in Section 5.4.4 with the only difference being the use of Fourier filtering instead of the DWT. As in the work described previously, the development of the calibration model employed only data collected at 37.0 °C.

The second strategy involved the incorporation of temperature variation into the data set used to build the calibration model. Through this procedure, a single calibration model was built to perform concentration predictions under conditions of changing sample temperatures. Both the DWT and Fourier filtering were evaluated as preprocessing procedures in this work.

5.6.1. Use of digital filtering in developing calibration models for glucose

Digital filtering is a signal processing method in which the raw spectra are modeled as a sum of sine and cosine frequencies by use of the Fourier transform. These Fourier domain spectra are then multiplied by a normalized Gaussian frequency response (filter) to remove unnecessary high (noise) and low (background drifts) frequencies. Then the filtered frequencies are converted back to the original data domain by applying the inverse Fourier transform.[14,15,57] Two parameters that need to be optimized for the Gaussian function are filter position and filter width at half-maximum.

For this work, the same data sets described in Table 5-1 were used. Calibration models for glucose were developed using digitally filtered glucose absorbance spectra collected at 37.0 °C (calibration data set, Table 5-1). Parameter optimization for the digital filter and PLS model was performed with a grid search. This grid-search procedure is analogous to that described in Chapter 3 (Section 3.2.3) and Chapter 4

(Section 4.4.4). During this grid search, optimal digital filter parameters, wavenumber range and number of PLS factors for the calibration models were optimized. The range study included scanning the wavenumber range from 4,200 to 4,800 cm^{-1} in steps of 25 cm^{-1} using window sizes from 300 to 600 cm^{-1} in steps of 25 cm^{-1}. For each wavenumber range investigated, models based on 1-10 latent variables (PLS factors) were computed.

Also incorporated into the cross-validation procedure was an investigation of the optimal parameters associated with spectral preprocessing via digital filtering. During this study, the gird search protocol was used to optimize the filter position from 0 to 1 in steps of 0.01 and filter width at half-maximum from 0.01 to 0.5 in steps of 0.05.

The minimum CV-SEP value was used to obtain the optimal wavenumber range, digital filter parameters, and number of PLS factors (latent variables). Once the wavenumber range and digital filter parameters were selected, an *F*-test at the 95% level was used to determine if the number of latent variables could be reduced without a statistically significant increase in CV-SEP. The final model size corresponded to the number of latent variables that produced a value of CV-SEP that was not statistically different from the minimum CV-SEP.

The best calibration model was obtained with digitally filtered glucose absorbance spectra when the filter position was set at 0.10 and the width of the filter at half-maximum was set at 0.16. These parameter values correspond to a normalized frequency bandwidth of 0 to 1. The optimized wavenumber range and the number of PLS factors for this model was 4,650 – 4,275 cm^{-1} and 4, respectively. The CV-SEP value obtained was 0.10 mM.

The prediction performance of the glucose model was assessed using the five prediction sets (PRD1-PRD5) described in Table 5-1. These results are summarized in Table 5-12. According to these results, digital filtering was not able to correct for temperature fluctuations introduced in prediction sets 2 through 5 (PRD2-PRD5).

Therefore, the same temperature correction strategy described in Section 5.4.5 was employed to correct for the temperature fluctuation. This correction was based on the second-order polynomial relationship developed using prediction set PRD2. The polynomial fit was $\varepsilon = 0.0189\ T^2 - 2.11\ T + 52.7$ (R^2=0.999). The temperature model used in this correction was the same as that described in Section 5.4.6. Table 5-12 summarizes the results for prediction sets PRD1-PRD5 after the temperature correction was performed. The SEP values obtained after the temperature correction (average SEP = 0.78 mM) with digital filtering was higher than the SEP values obtained after the temperature correction (average SEP = 0.23 mM) with wavelet preprocessing (Table 5-7, Model 1). The SEP value obtained for prediction set PRD5 was especially high. These results indicated that wavelet preprocessing was a more effective preprocessing strategy than Fourier filtering when coupled to the proposed temperature correction algorithm.

5.6.2. Development of calibration models for glucose including temperature fluctuations

The second strategy was to develop a calibration model for glucose incorporating variation in both glucose concentrations and sample temperatures. In order to develop this calibration model, prediction set two (PRD2, Table 5-1) was used as it contains both glucose and temperature variation. In this case, since the calibration model for glucose itself contains the information about temperature fluctuation, a separate correction for temperature is not expected. Both the DWT and digital Fourier filtering were used separately as signal preprocessing methods. A grid search based on cross-validation was again used to establish the optimal preprocessing and modeling parameters. This grid-search procedure is analogous to that described in Chapter 3 (Section 3.2.3) and Chapter 4 (Section 4.4.4).

During this grid search, optimal digital filter parameters/wavelet parameters, wavenumber range and number of PLS factors for the calibration models were optimized.

Table 5-12. Prediction performance of PLS calibration models for glucose developed with digital Fourier filtering.

Data set	SEP[a] before temperature correction (mM)	SEP[a] after temperature correction[b] (mM)
Prediction set 1 (PRD 1)	0.23	0.23
Prediction set 2 (PRD2)	8.10	0.17
Prediction set 3 (PRD3)	8.49	0.31
Prediction set 4 (PRD4)	8.63	0.34
Prediction set 5 (PRD5)	6.22	2.85

[a]Values of the standard error of prediction for the model developed using the digital filtering technique explained in Section 5.6.1

[b]Standard error of prediction computed from the errors in the corrected glucose predictions. Predicted temperatures were used in implementing the temperature correction algorithm.

The range study included scanning the wavenumber range from 4,200 to 4,800 cm^{-1} in steps of 25 cm^{-1} using window sizes from 300 to 600 cm^{-1} in steps of 25 cm^{-1}. For each wavenumber range investigated, models based on 1-10 latent variables (PLS factors) were computed. Also incorporated into the cross-validation procedure was an investigation of the optimal parameters associated with spectral preprocessing via DWT or digital filtering. For digital filtering, the gird search protocol was used to optimize the filter position from 0 to 1 in steps of 0.01 and filter width at half-maximum from 0.01 to 0.5 in steps of 0.05. The gird search protocol used in wavelet optimization included scanning the wavelet order from 2 to 8 (step size 1) for the Daubechies (db) family. For each wavelet order investigated, the degree of decomposition was scanned from levels 2 to 10 (step size 1). For each wavelet order and decomposition level studied, the best hierarchical combination of details to use in reconstructing the spectrum was evaluated. As an example, when the decomposition level was 5, the combinations of details evaluated were [2], [2, 3], [2, 3, 4], and [2, 3, 4, 5, 6].

For each combination of wavelet or filtering parameters studied, the same grid search of the spectral range and PLS latent variables described above was employed. The level 1 details and the last level approximation were never included in the grid search as these coefficients were never found to be useful.

The minimum CV-SEP value was used to obtain the optimal wavenumber range, digital filter/wavelet parameters, and number of PLS factors (latent variables). Once the wavenumber range and digital filter/wavelet parameters were selected, an *F*-test at the 95% level was used to determine if the number of latent variables could be reduced without a statistically significant increase in CV-SEP. The final model size corresponded to the number of latent variables that produced a value of CV-SEP that was not statistically different from the minimum CV-SEP.

When digital filtering was used as the preprocessing method, the best calibration model obtained for glucose incorporating temperature information had a filter position of

0.10, a width at half-maximum of 0.11, wavenumber range of 4,600-4,250 cm^{-1} and 6 PLS factors. When preprocessing was based on the DWT, the best calibration model obtained for glucose incorporating temperature information used the db5 wavelet, six levels of decomposition, and the details for levels 2, 3, and 4 in reconstructing the spectra. The optimal wavenumber range was 4,650-4,300 cm^{-1} and 7 PLS factors were employed.

The prediction performance of both of these models was assessed using three prediction sets (PRD3-PRD5, Table 5-1) and the results are summarized in Table 5-13. According to these results, both models gave reasonably good SEP values. The model based on wavelet preprocessing gave lower SEP values (average SEP = 0.29 mM) than the model based on digital Fourier filtering (average SEP = 0.34 mM). Both of these models gave slightly higher SEP values than the model developed with wavelet preprocessing and the separate temperature correction procedure (average SEP = 0.26 mM).

5.7 Conclusions

In the work presented in this chapter, a temperature-correction strategy to improve quantitative analyte predictions in aqueous-based samples was successfully developed. This correction strategy is based on the systematic pattern of analyte concentration residuals observed with respect to changes in temperature. The relationship between glucose or lactate concentration residuals and temperature was successfully modeled using a second-order polynomial fit which then led to an additive correction that ultimately resulted in corrected analyte predictions. This methodology was tested in solutions of glucose in buffer and glucose/lactate mixtures in buffer.

The basis for this correction strategy is the baseline artifacts introduced by the systematic shift of water absorption peaks with increasing temperature. The correction procedure incorporates temperature information into the calibration model without

Table 5-13. Prediction performance of PLS calibration models for glucose including temperature fluctuations

Data set	SEP[a] (mM)	SEP[b] (mM)
Prediction set 2 (PRD2)	0.14[c]	0.13[c]
Prediction set 3 (PRD3)	0.36	0.28
Prediction set 4 (PRD4)	0.38	0.28
Prediction set 5 (PRD5)	0.48	0.46

[a]Model developed using digital Fourier filtering explained in Section 5.6.2

[b]Model developed using wavelet preprocessing explained in Section 5.6.2

[c]Cross-validated standard error of prediction (CV-SEP) is reported

requiring a full-scale experimental design in which temperature is systematically varied together with analyte concentrations. In fact, the relatively simple relationship between concentration residuals and sample temperatures may allow the use of a significantly smaller data set than was employed here for establishing the polynomial correction function.

The correction procedure can be applied with or without an experimental measurement of the sample temperature. If no reference temperature is available, a temperature prediction model of the type developed in Chapter 4 can be used to estimate the sample temperature. Clearly, the effectiveness of the temperature correction strategy in this case is dependent on the prediction performance of the temperature model. As discussed in Chapter 4, however, temperature models for aqueous solutions can give good long-term prediction results and can tolerate some changes in the sample matrix.

Despite the effectiveness of the correction strategy, some deterioration of prediction performance was observed with time. This might be due to the degradation of analyte prediction models with time as the temperature prediction models were observed to be stable with time.

Calibration models developed using DWT-preprocessed spectra gave better prediction results than calibration models developed using raw absorbance spectra when combined with the temperature correction procedure. In the case of glucose predictions in laboratory-prepared glucose solutions, the glucose prediction model based on raw absorbance spectra gave an average SEP value of 0.34 mM whereas the model based on DWT preprocessed spectra gave an average SEP value of 0.26 mM. Similarly, in the case of glucose predictions in mixture solutions of glucose and lactate, the average SEP values obtained for glucose predictions using raw spectra was 0.27 mM. This value reduced 0.23 mM when the preprocessed spectra were used. Improvements in prediction performance for the model based on preprocessed spectra were less clear for lactate, however. In this case, the models based on raw and preprocessed spectra performed similarly.

An alternative strategy for overcoming the effects of temperature variation is to build both concentration variation and temperature variation into the calibration model. This approach was also evaluated in conjunction with spectral preprocessing based on both the DWT and digital Fourier filtering. The proposed temperature correction strategy performed favorably when compared to this alternative approach.

Finally, the temperature correction strategy developed in this work is not limited to biomedical applications such as glucose or lactate sensing or to aqueous-based samples. The method is general and can be applied to any sample matrix in which the temperature dependence of the concentration residuals can be modeled.

CHAPTER 6
DETERMINATION OF TEMPERATURE OF NYLON-6,6 POLYMER DIRECTLY FROM NEAR-INFRARED SPECTRA

6.1 Introduction

Nylon is the generic name given to a group of aliphatic polyamide polymers which form *via* condensation polymerization of a diamine with a dicarboxylic acid.[64-67] The United States, Canada and Mexico collectively produced 1,193 million pounds of nylon in 2012.[68]

As depicted in the reaction schematic shown in Figure 6-1, nylon-6,6 is a subgroup of nylon polymers synthesized by hexamethylenediamine and adipic acid monomers.[64-67] The repeating unit of the polymer is shown in Figure 6-2.

The nylon-6,6 polymer has no side chains. As depicted in Figure 6-3, the individual nylon-6,6 polymer chains are held together *via* hydrogen-bonding formed between the amide linkages.[65]

Nylon-6,6 is a thermoplastic polymer with a melting point of 265 °C. The density of nylon-6,6 is 1.14 g/mL and it has a refractive index of 1.5650. Nylon-6,6 provides great rigidity, high mechanical strength and durability, thereby making it one of the most widely used nylons in the world. Applications of nylon-6,6 can be found in self-lubricating bearing parts, apparel, tires, zip ties, ropes, conveyer belts, carpets, electro-insulating elements, airbags, pipes, hoses and in various machine parts.[69-74]

Mid-infrared (mid-IR) spectroscopy has been successfully used in the characterization of nylon polymers.[75-79] However, strong absorption of light in this region from the functional groups limits mid-IR spectroscopy to the analysis of thin polymer films.[80] Near-infrared (NIR) spectroscopy has been successfully used in polymer characterization for the past few years.[76,79,81-84] Foster et al. document the use of overtone and combination regions to study polymers such as nylons, polyethylenes and

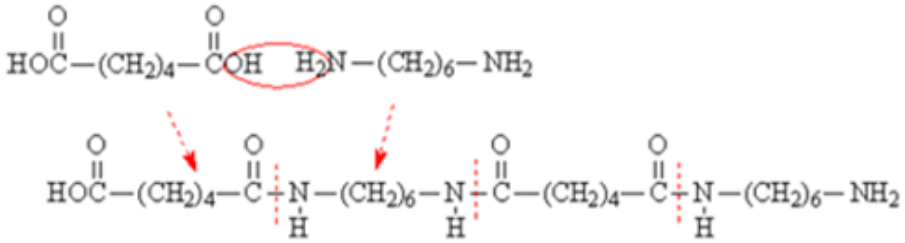

Figure 6-1. Formation of nylon-6,6 *via* the condensation reaction between hexamethylenediamine and adipic acid.[65]

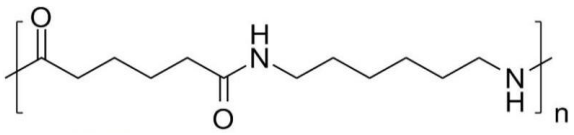

Figure 6-2. Repeating unit of nylon-6,6 polymer.

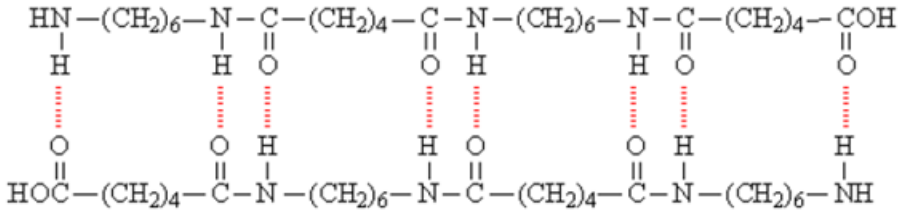

Figure 6-3. Schematic representation of intermolecular interactions (hydrogen-bonding) between individual nylon-6,6 fibers in a nylon-6,6 sheet.[65]

polyisobutylenes etc.[76] Orendroff et al. used NIR spectroscopy to study the effects of water and temperature on conformational order in nylon thin films.[79] Ghebremeskel et al used NIR spectroscopy to study specific interactions in polymer blends.[83] Rodgers et al. studied structural properties of Nylon-6,6 carpet yarns using NIR spectroscopy.[84] Wu et al. studied structural properties of amorphous polyamides using two-dimensional NIR spectroscopy.[81]

Spectral features in the NIR region include combinations and overtones of the fundamental vibrational bands associated with C-H, O-H and N-H bonds. The wavenumber region from 4,000 to 6,600 cm^{-1} contains first overtones of C-H bonds and combination bands involving C-H, N-H and O-H bonds. Previous studies regarding polymer characterization have identified characteristic peaks for nylon polymers in the NIR region.[80-82] Combination bands of symmetric and asymmetric stretches of C-H bonds are located in the region of 4,100 to 4,400 cm^{-1}. The combination band of a fundamental N-H bend and the Amide III fundamental vibration can be found at 4,611 cm^{-1}. The third overtone of the Amide II fundamental vibration occurs at 4,659 cm^{-1}, while the combination band of a fundamental N-H bend and the Amide II fundamental vibration can be found at 4,877 cm^{-1}. Peaks related to amide linkages are expected to be broader than the other spectral features because the amide linkages are involved in hydrogen bonding between the individual nylon chains.[80-82]

Near-infrared spectroscopy is a non-destructive analysis technique which requires little to no sample preparation.[3,24] It is also compatible with polymer samples with considerable thickness (in the mm range) as the NIR region exhibits reduced absorption when compared to the mid-IR region. However, the weak and highly overlapped spectral features in the NIR region complicate quantitative determinations as a single wavelength or single spectral band can rarely be used alone for the implementation of a quantitative calibration. This factor demands the use of multivariate calibration techniques such as partial least-squares (PLS) regression when quantitative methods are developed.[3,24]

The research presented here is an extension from Chapters 4 and 5. The primary motivation for this work was to develop methods to predict the temperature of a given solid material directly from NIR spectra. Such methods could be used for temperature determinations of solid materials in applications where it is inaccurate or inconvenient to determine the temperature with a conventional probe such as a thermocouple thermometer. The methodology used in Chapters 4 and 5 is extended towards common materials which are no longer liquids. Since nylon polymers are a widely used group of materials, it is interesting to investigate the ability to predict the temperature of a nylon sample directly from its NIR spectrum.

In this work, PLS regression was used to develop calibration models to determine the temperature of a given piece of nylon-6,6 polymer directly from its NIR spectrum. The prediction performance of these temperature models was assessed for robustness with time and the ability to predict the temperature across different sheets of nylon-6,6.

6.2 Thermal behavior of nylon

Nylon-6,6 polymers are not good heat conductors. Linear expansion of nylon-6,6 due to heating is negligible. The following statistics about nylon-6,6 document the above properties. The coefficient of thermal expansion of nylon-6,6 is 90 x 10^{-6} K^{-1} and its specific heat capacity is 1,670 $JK^{-1}kg^{-1}$. The thermal conductivity of nylon-6,6 at 23 °C is 0.25 $Wm^{-1}K^{-1}$.[71,72,85]

Changes in temperature primarily affect the intermolecular hydrogen-bonding network that exists between the nylon polymer chains. However, it is also observed that temperature changes can influence the structure of the hydrocarbon chains.[81,86,87] Upon heating of nylon, overtones and combination peaks that arise due to hydrogen-bonded amide linkages as well as combination peaks that arise due to symmetric and asymmetric stretches of C-H bonds are expected to deviate.

6.3 Experimental design

6.3.1 Apparatus and reagents

The spectral data collection described here was performed with a Bruker Vertex 70 Fourier transform (FT) spectrometer configured with a tungsten-halogen lamp source, a calcium fluoride (CaF_2) beam splitter and a liquid nitrogen cooled indium antimonide (InSb) detector (Bruker Optics, Billerica, MA). A low-pass filter (OCLI, Santa Rosa, CA) was used to restrict the light beyond 5,000 cm^{-1}. Commercially obtained nylon-6,6 samples (McMaster-Carr, Elmhurst, IL) were used in this analysis. A metal sample holder was used to hold the samples. A custom-made brass heater (described below) was employed to heat the nylon samples to a desired temperature. Figure 6-4 provides an overall schematic of the experimental setup.

An Omega Model 670 digital thermocouple thermometer (Omega Engineering, Inc., Stamford, CT) equipped with Type T thermocouples was used to obtain temperature measurements. A Mettler AE200 analytical balance (Mettler-Toledo, Inc., Columbus, OH) was used to obtain the weight measurements of the nylon pieces. A Fisher Scientific Isotemp Model 655G oven (Fisher Scientific, Pittsburgh, PA) and a glass desiccator equipped with drierite (W.A. Hammond Drierite Co, Ltd., Xenia, OH) were used for drying purposes.

6.3.2 Brass heater design details

Figure 6-5 displays a schematic of the heating system used to control the temperature of the nylon sample during the spectroscopic measurement. A cartridge heater (McMaster-Carr, PN3618K211) was used as the heating element in this heater design. The cartridge heater was enclosed in a block of brass (3.5 × 2.0 × 1.5 in). Two brass plates were mounted on the two metal sample holder plates to increase the thermal conductivity of the assembly. The nylon sample was sandwiched between the two sample holder plates. Three points of contact were made on one brass plate to input the three T-type thermocouples (5TC-GG-T-20-72, Omega Engineering, Inc.) used to obtain the temperature of the nylon at a given time. An Omega (CN7500 series, Omega

Engineering, Inc.) temperature controller was employed to set the temperature of the cartridge heater to a desired value.

6.3.3 Procedures

Four pieces of nylon-6,6 (A, B, C and D) were used in the spectral data collection. As denoted in Table 6-1, these nylon samples were obtained from four different sheets of nylon-6,6. The average dimensions of the nylon pieces were 35. × 35. × 0.40 ± 0.01 mm and the average weight was 0.5215 ± 0.0001 g.

Two methods were evaluated for assigning reference temperatures to the nylon samples during the spectral acquisition. The first was simply to take the average of the readings of the three thermocouples depicted in Figure 6-5:

$$T_{avg} = \frac{T_1+T_2+T_3}{3} \pm 0.06\ ^\circ C \qquad (6\text{-}1)$$

In Eq. 6-1, T_{avg} is the average temperature associated with a given nylon spectrum and T_1, T_2, T_3 are the temperature readouts from thermocouples 1, 2 and 3, respectively.

The second approach took into consideration that in the configuration of the heater assembly, the heating element was located in closer proximity to thermocouple T_1 than to the other two thermocouples, T_2 and T_3. In Eq. 6-2, T_{avg1} is the reference temperature associated with a given nylon spectrum using the alternate method and T_1, T_2, T_3 are the temperature readouts from thermocouples 1, 2 and 3, respectively.

$$T_{avg1} = \frac{[(T_2+T_3)/2]+T_1}{2} \pm 0.06\ ^\circ C \qquad (6\text{-}2)$$

Comparison of the two methods yielded that the close proximity of T_1 to the heating element did have a slight bias towards the contribution of T_1, especially at higher temperatures. This is shown in Figure 6-6 in which the temperatures produced by Eqs. 6-1 and 6-2 are plotted with respect to the set point of the temperature controller.

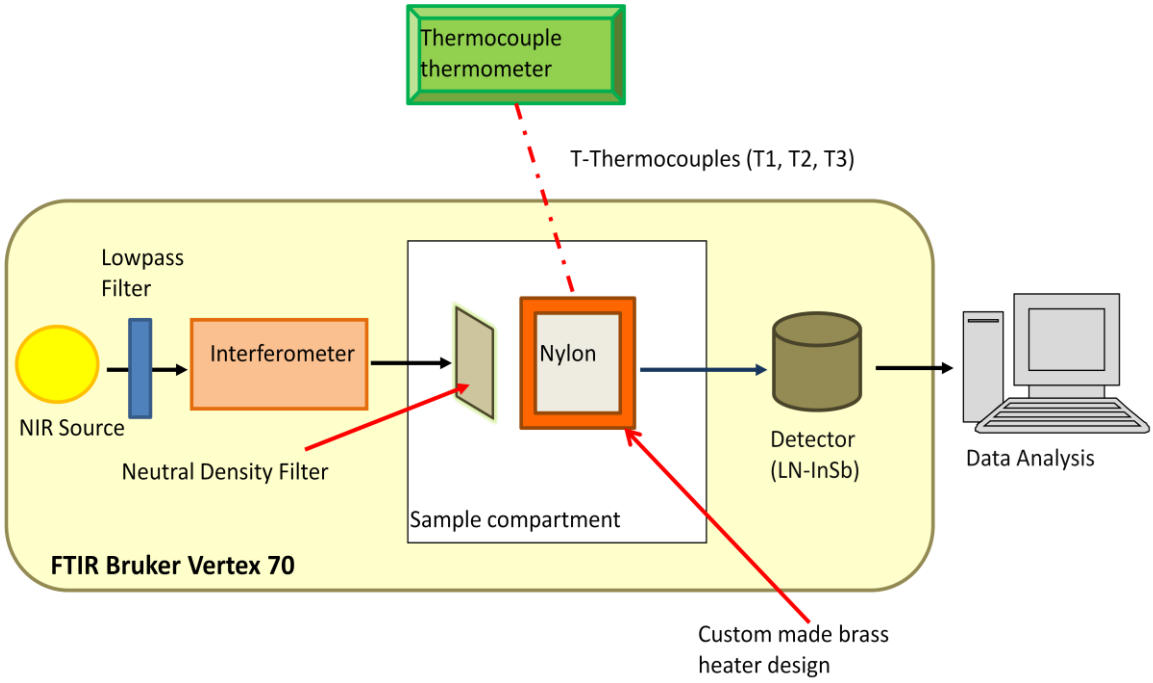

Figure 6-4. Schematic diagram of the experimental set up for collecting NIR spectra of nylon-6,6 at a given temperature.

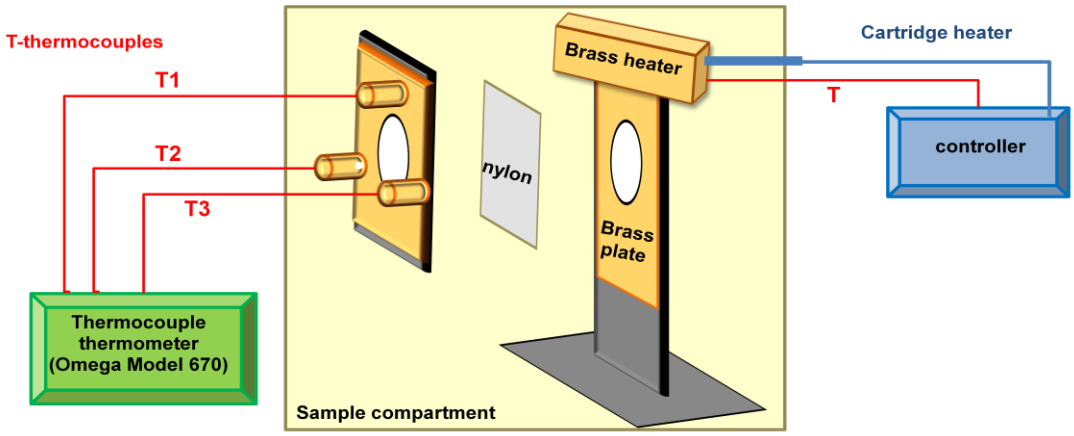

Figure 6-5. Schematic diagram of the custom-made brass heater used to obtain desired temperatures of the nylon samples.

Table 6-1. Summary of nylon-6,6 samples used in the experiment.

Nylon piece	Nylon sheet
A	1
B	2
C	3
D	4

Linear regression was performed on both sets of data in Figure 6-6 to characterize the differences in response. The fitted equations and associated statistics are provided in Table 6-2. The slopes and intercepts both differ by approximately 2%. When the 95 % confidence intervals for the slope and intercept were considered, however, neither the slopes nor the intercepts were statistically different. On the basis of this evaluation, the two methods were judged to be equivalent. Equation 6-1 was adopted for its simplicity and used to establish the reference temperatures recorded for each collected spectrum.

To build calibration models to relate spectral intensities to the reference temperatures, a set of 72 nylon spectra were collected using nylon-6,6 piece A over a temperature range from room temperature (~21.0 °C) to 105.0 °C. This corresponded to three consecutive replicate spectra collected at 24 different temperature levels between 21.0 °C and 105.0 °C. In order to assess the long-term predictive ability of the temperature models, 10 sets of nylon spectra were collected using nylon-6,6 pieces B, C and D over the same temperature range over a period of seven weeks. Table 6-3 summarizes the data sets collected.

All calibration and prediction spectra were obtained with dry (0 % moisture uptake) nylon-6,6. Each nylon-6,6 piece used in the data collection was dried in the oven to remove any moisture before the experiment. Weight measurements were obtained both before and after the spectral collection to verify that dry conditions were maintained. The brass heater described previously was used to heat the nylon sample to a given temperature. The temperatures employed during the spectral collection were randomized to minimize the correlation of temperature with time. Figure 6-7 illustrates the randomization of temperatures during a spectral collection session. Similar randomization procedures were used during the collection of the calibration and prediction data.

Open-beam air spectra were used as backgrounds in the calculation of absorbance spectra of the nylon samples. For a given spectral collection session, eight warm-up air spectra were collected at the beginning of the day and six air spectra were collected at the

end of the day. A 6.3% neutral density filter (Rolyn Optics, Covina, CA) was used to attenuate the source intensity during the collection of the open-beam air spectra. The average of the 14 air spectra was used as the background in computing absorbance spectra of the nylon samples measured during the corresponding data collection session.

The raw data consisted of 256 co-added double-sided interferograms containing 14,220 points collected at every zero crossing of the helium-neon reference laser (15,800.45 cm^{-1}) with a nominal spectral resolution of 4 cm^{-1} and an aperture setting of 6 mm.

All interferograms were converted to single-beam spectra with a point spacing of 1.9288 cm^{-1} by applying two levels of zero filling, Blackmann-Harris 3-term apodization and Mertz phase correction. The Fourier processing was performed with the Opus software (Version 6.5, Bruker Optics, Inc.) controlling the spectrometer. After Fourier processing, single-beam spectra were reduced to the range of 5,000 to 4,000 cm^{-1}. Further calculations were performed with Matlab, (Version 7.4, The Mathworks, Inc., Natick, MA) on a Dell Precision 670 computer (Dell Computer Corp., Round Rock, TX) operating under Red Hat Linux WS (Version 5.2, Red Hat, Inc., Raleigh, NC).

6.4 Results and discussion

6.4.1 Noise evaluations

The quality of the spectra in the calibration and prediction sets was determined by the average root-mean-square (RMS) noise of the spectra in each data set. This calculation was discussed previously in Chapter 3 (Section 3.6). In brief, the ratios were taken of each pairwise combination of the three replicate spectra corresponding to a given temperature. The performance of the instrument was determined by the average RMS noise of the air spectra collected each day. This calculation was performed by taking the ratio of each pairwise combination of the replicate air spectra for a given day.

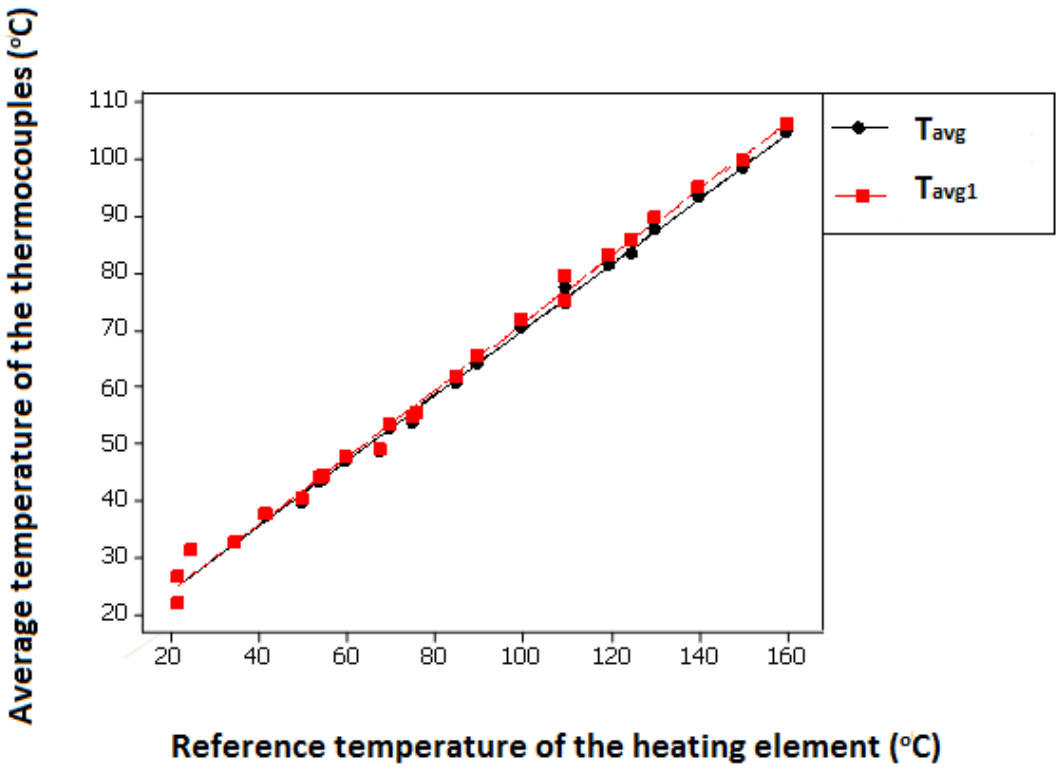

Figure 6-6. Plot of average temperatures (T_{avg} and T_{avg1}) calculated using the two methods described by Eqs. 6-1 and 6-2, respectively, vs. the set point of the temperature controller. The solid lines represent the fitted regression equations for the two sets of data. The two lines slightly diverge at higher temperatures, indicating that T_1 has a small bias toward higher temperatures.

Table 6-2. Regression models and statistics related to comparison of temperature calculations

Average temperature (°C)	**Linear fit**[a]	**Regression coefficients**	**95 % confidence interval**[b]
T_{avg}[c]	$y = 12.23 + 0.58\,x$	12.23 (y-intercept)	(10.98, 13.48)
		0.58 (slope)	(0.56, 0.59)
T_{avg1}[d]	$y = 12.02 + 0.59\,x$	12.02 (y-intercept)	(10.69, 13.34)
		0.59 (slope)	(0.58, 0.60)

[a]The regression equation was based on the computed reference temperatures (y) as a function of the setpoint temperature (x). Slope values < 1 indicate the inefficiency of heating nylon and the loss of heat to the surroundings.

[b]Upper and lower 95% confidence limits for the corresponding regression coefficient.

[c]Temperature computed with Eq. 6-1.

[d]Temperature computed with Eq. 6-2.

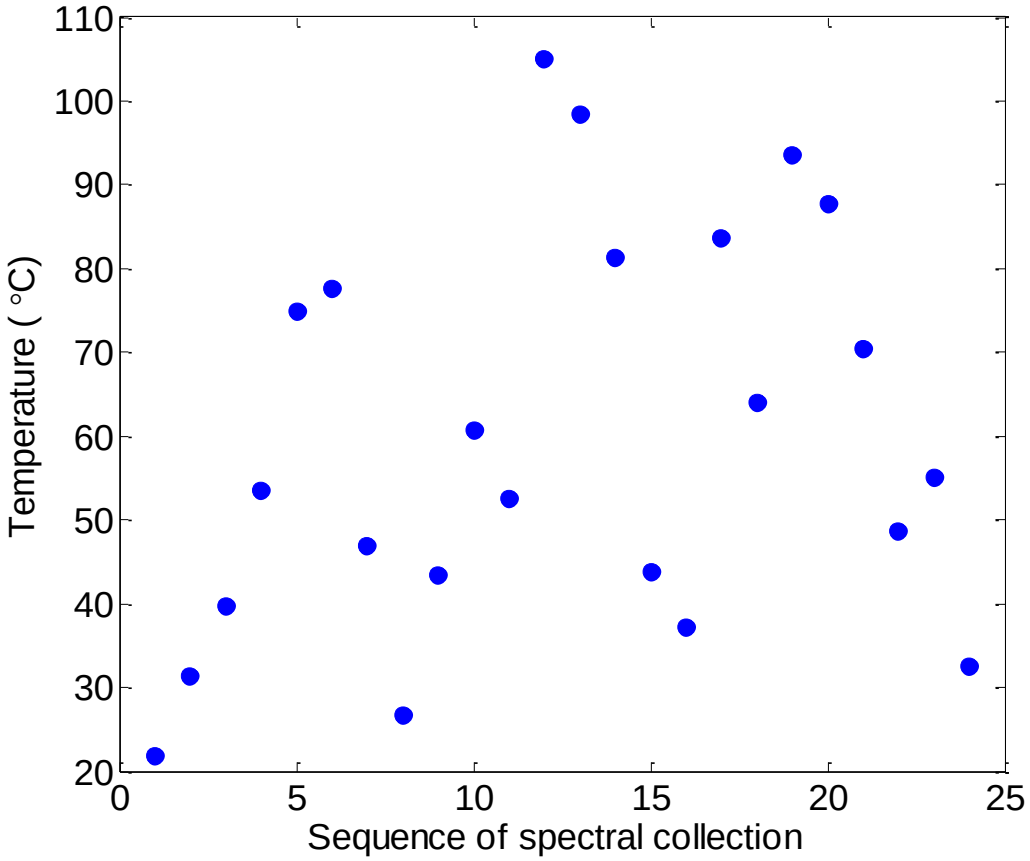

Figure 6-7. Randomization of temperature values to minimize the correlation between temperature and data acquisition time.

Table 6-3. Summary of spectral collection protocol for the temperature models of nylon-6,6 polymer

Data set	Nylon piece used	Number of samples/spectra collected[a]	Time since calibration (weeks)
Calibration	A	24/72	0
Prediction set 01 (PS01)	D	15/45	0.5
Prediction set 02 (PS02)	D	14/42	1.5
Prediction set 03 (PS03)	B	14/42	2.0
Prediction set 04 (PS04)	C	14/42	3.0
Prediction set 05 (PS05)	C	14/42	3.0
Prediction set 06 (PS06)	B	13/39	3.5
Prediction set 07 (PS07)	D	14/42	3.5
Prediction set 08 (PS08)	B	14/42	5.0
Prediction set 09 (PS09)	C	14/42	6.0
Prediction set 10 (PS10)	D	13/39	7.0

[a]A sample corresponds to one specific setting of the temperature controller.

Noise spectra were converted to absorbance units (AU) and fit to a third-order polynomial to remove systematic variation. In this study, the spectral region from 4,800 to 4,200 cm^{-1} was used to compute RMS noise values.

Figure 6-8 represents the average RMS noise values computed for nylon-6,6 and air spectra for each spectral data set. The noise levels are consistent across the data sets. Higher noise levels for the air spectra relative to those reported previously in Chapters 4 and 5 reflect the different wavenumber range used here in the calculation. The corresponding higher noise levels reported for the nylon samples relative to those associated with the solution samples described previously in Chapters 4 and 5 reflect both differences in the transmission properties of the samples and the wavenumber range used in the calculation.

6.4.2 Spectral preprocessing methods

In this study, the standard normal variate (SNV) transform combined with the discrete wavelet transform (DWT) were used to preprocess the nylon-6,6 absorbance spectra before submitting them to the PLS regression model. These preprocessing methods were described in detail in Chapter 3 (Sections 3.2.1 and 3.2.2, respectively).

Optimization of the wavelet function (order), level of decomposition and levels of details and approximations used in reconstructing the spectra was performed with a grid search. A detailed description of a grid search is given in Chapter 3 (Section 3.2.3). Spectra preprocessed with the SNV transform were used as inputs to the grid search, and the DWT was applied to the entire spectral range of 4,000 to 5,000 cm^{-1}. Details regarding the levels of each parameter studied will be given in Section 6.4.4 below.

6.4.3 Near-infrared spectra of nylon-6,6 at different temperatures

Figure 6-9 illustrates spectra collected at different temperatures and preprocessed with the SNV and DWT methods. The Daubechies 6 (db6) wavelet function was used, implemented as five levels of decomposition and the use of the details in levels 2, 3, and 4 only in reconstructing the spectra. Spectral features centered at 4,350 and 4,600 cm^{-1}

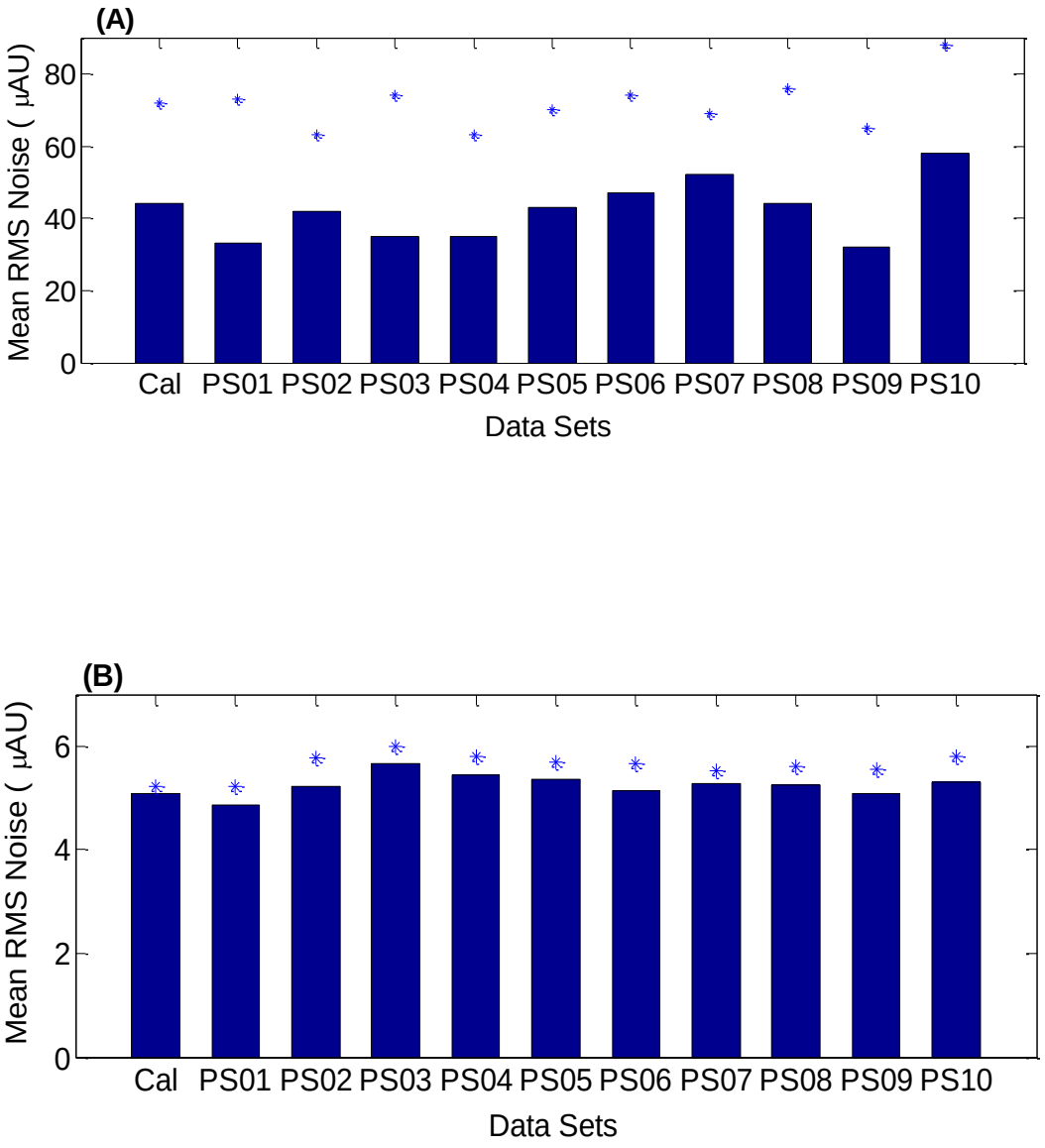

Figure 6-8. Average RMS noise values (in units of microabsorance – µAU).
(A) nylon-6,6 spectra and **(B)** air spectra for a given spectral collection. The * symbols represent one standard deviation from the average. The large variation in the noise levels for the nylon samples reflects the possible scattering of light due to the solid sample.

show changes in intensity and peak position as the temperature changes. Combination peaks that arise due to symmetric and asymmetric stretches of C-H bonds are centered at 4,350 cm^{-1}, whereas combination peaks that arise due to hydrogen-bonded amide linkages are centered at 4,600 cm^{-1}. Thus, the observed spectral changes confirm the influence of temperature change both in the hydrogen-bonding network and the hydrocarbon chains in nylon-6,6.

6.4.4 PLS regression models for temperature changes in nylon-6,6

In order to model the temperature changes in nylon-6,6 samples, PLS calibration models were generated from the computed nylon-6,6 absorbance spectra. Section 3.3.2 in Chapter 3 discusses the basics of PLS regression. As noted previously, these absorbance spectra were generated using single-beam nylon-6,6 spectra with respect to an average air spectrum of the day of data collection. Absorbance spectra were preprocessed with the SNV and DWT methods before submitting them to the calibration model, and the calibration data matrix was mean-centered before the PLS calculation. A grid search protocol was used to optimize the wavelet parameters, as well as the spectral range submitted to the PLS calculation and the number of PLS latent variables (factors) used in the temperature model.

During this study, the grid search protocol used in the wavelet optimization included scanning the wavelet order from 2 to 8 for the Daubechies (db) family (step size of 1). For each wavelet order investigated, the degree of decomposition was scanned from level 3 to level 8 (step size of 1). For each wavelet order and decomposition level studied, the best hierarchical combination of details to use in reconstructing the spectrum was evaluated. As an example, when the decomposition level was 5, the combinations of details evaluated were [2], [2, 3], [2, 3, 4], and [2, 3, 4, 5]. The level 1 details and the last level approximation were never included in the grid search as these coefficients were never found to be useful.

For each combination of wavelet parameters studied, a further grid search was used to optimize the wavenumber range and the number of factors used in building the PLS model for temperature. The second grid search included scanning the wavenumber range from 4,050 to 4,950 cm^{-1} in steps of 25 cm^{-1} using window sizes from 300 to 800 cm^{-1} in steps of 25 cm^{-1}. For each wavenumber range investigated, models based on 1-10 PLS factors were computed.

A cross-validation (CV) procedure was used to validate the performance of each set of parameters related to the DWT, spectral range, and number of PLS factors. As described in Chapter 3 (Section 3.4), this procedure involved leaving out 10% of spectra with their replicate measurements and generating a temperature calibration model from the remaining spectra. The computed calibration model was then used to predict the temperatures corresponding to the withheld spectra and the process was repeated until all spectra had been withheld once. A standard error of prediction (SEP) was pooled from the residuals of the predicted temperatures. The value is termed the cross-validated standard error of prediction (CV-SEP) and was presented previously in Chapter 3 as Eq. 3-22. The minimum CV-SEP value was used as the criterion for selecting the optimal parameters for the calibration model. Once the optimal wavelet parameters and spectral range were established, a final selection of the number of latent variables was performed by assessing whether models with fewer latent variables than that producing the minimum CV-SEP were statistically equivalent (i.e., not statistically different). An *F*-test at the 95% level was used to make this determination.

6.4.5 Calibration model for temperature changes in nylon-6,6 polymer

Calibration models were generated for temperature variations in nylon-6,6 polymer using PLS regression. Models were developed separately for preprocessed (i.e., application of the SNV and DWT procedures) and raw nylon absorbance spectra. For models built with raw absorbance spectra, the same grid search described above was used for the optimization of the wavenumber range submitted to the PLS calculation and the

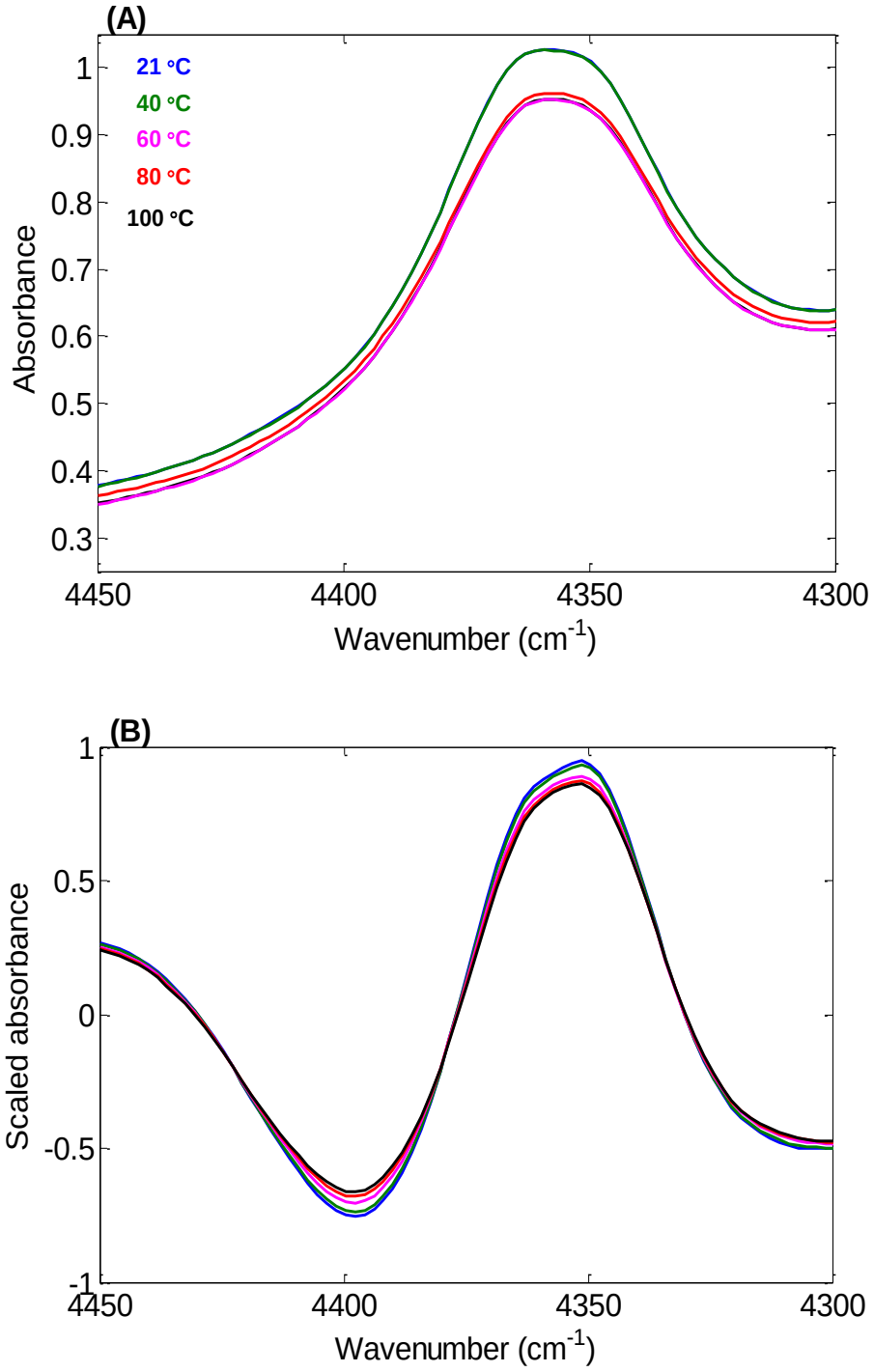

Figure 6-9. Raw and preprocessed nylon-6,6 absorbance spectra collected at 21, 40, 60, 80, and 100 °C over the wavenumber range 4,300 – 4,450 cm^{-1}. Preprocessing was based on application of the SNV transform, followed by the DWT. The db-6 wavelet was employed at five levels of decomposition, followed by the use of the details from levels, 2, 3, and 4 only in reconstructing the spectra. **(A)** Raw spectra **(B)** preprocessed spectra.

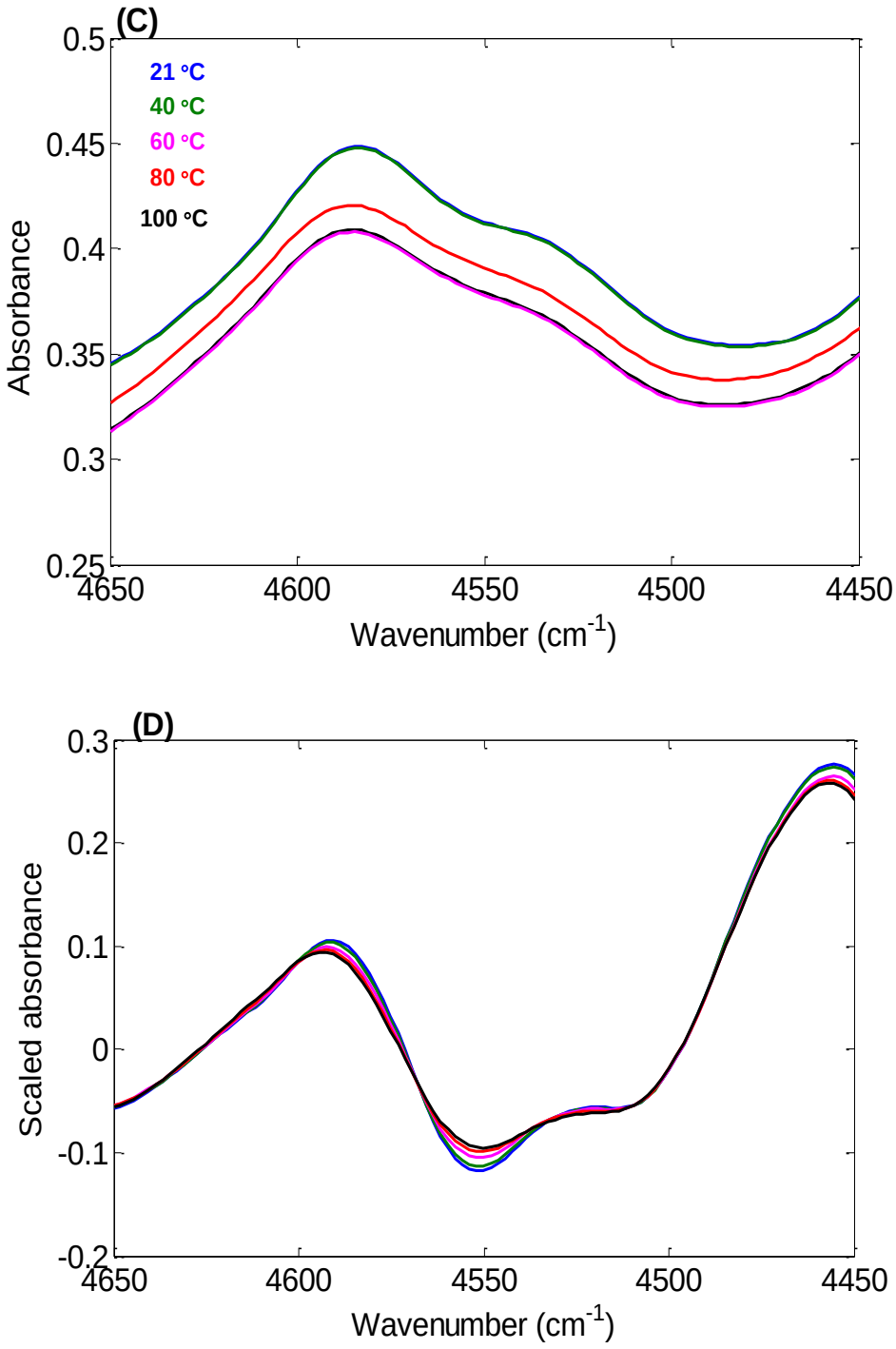

Figure 6-9 continued.
(C) Raw nylon-6,6 absorbance spectra in the wavenumber range 4,450 – 4,650 cm^{-1}
(D) Preprocessed nylon-6,6 absorbance spectra in the wavenumber range 4,450 – 4,650 cm^{-1}.

number of PLS factors used in the final model. These computed models are summarized in Table 6-4. Listed in the table are the wavenumber ranges, number of PLS latent variables, and values of the standard error of calibration (SEC) and CV-SEP. As described in Chapter 3 (Section 3.3), the SEC is the standard error in predicted temperature achieved with the calibration data when all spectra were included in the calculation of the model.

The optimal wavenumber range for preprocessed spectra was 4,650 to 4,300 cm^{-1} with three PLS factors used to construct the model. The DWT preprocessing used the Daubechies-6 (db6) wavelet function at five levels of decomposition, with levels 2, 3 and 4 only used for reconstructing the spectra. These are the parameters used to preprocess the spectra displayed in figure 6-9. The best calibration model gave a CV-SEP value of 0.75 °C. By comparison, the optimal wavenumber range for raw spectra was 4,800 to 4,500 cm^{-1} with five PLS factors. The best calibration model gave a CV-SEP value of 0.68 °C. Figure 6-10 is a PLS score plot that illustrates the data variance encompassing the preprocessed nylon spectra used to compute the calibration model. Scores along the first two PLS factors are plotted. The first PLS factor explains about 97 % of the spectral variance. Spectra collected at a given temperature tend to cluster together. However, as shown by the superimposed ellipses, temperature information appears to be encoded in three prominent bands of increasing temperature from the lower left to the upper right of the figure. These three bands seem to be clustered according to the time of data collection. The band to the left contains the spectra collected at the beginning of the data collection and the band to the right contains the spectra at the end of the data collection.

Figure 6-11 illustrates the three spectral loadings computed for the PLS calibration model based on the preprocessed nylon-6,6 spectra. These can be interpreted as the abstract spectral components whose contributions to the nylon spectra are reflected in the PLS scores used to build the calibration model. While challenging to interpret precisely, the three spectral loadings indicate features between 4,300 cm^{-1} – 4,400 cm^{-1} and 4,550 –

4,600 cm^{-1} which contains peaks due to asymmetric and symmetric C-H stretches and combination bands of amide linkages, respectively.

6.4.6 Prediction performance of temperature models for nylon-6,6

The long-term prediction performance of the calibration models was assessed using ten prediction sets of nylon-6,6 spectra collected over a period of two months. These results are summarized in Table 6-5. The prediction performance of the calibration model based on the raw nylon absorbance spectra was poor, with SEP values exceeding 6 °C after 3 weeks. The calibration model based on preprocessed spectra gave good prediction results with SEP values ranging from 0.70 to 2.65 ºC. Moreover, the model based on preprocessed spectra was able to predict temperatures across different sheets of nylon-6,6. Nylon piece C gave the highest SEP values (average SEP of 2.23 °C) when compared to the other pieces of nylon (average SEP of 0.857 and 1.44 °C for pieces B and D, respectively).

Figure 6-12 summarizes the CV-SEP and SEP values for the models computed with and without spectral preprocessing. No significant degradation of performance in the calibration model based on preprocessed spectra is noted over time. The model based on raw absorbance data degrades noticeably as the time since calibration increases.

For the models based on preprocessed spectra, Figure 6-13 plots the CV-SEP and SEP values color-coded by the nylon piece. From an inspection of this plot, the specific piece of nylon has a clear influence on the temperature prediction. Within the results for a given nylon piece, there is no obvious degradation in model performance with time.

6.4.7 Effects of signal preprocessing

As indicated in Table 6-5, the prediction performance of the temperature model based on the preprocessed nylon-6,6 spectra was much better than the corresponding model computed with raw absorbance spectra. For the calibration data and prediction sets PS01, PS04, PS06, PS07, and PS10, Figure 6-14 is a principal component score plot that illustrates the improved data clustering observed after spectral preprocessing with the

Table 6-4. Summary of the best PLS calibration models for temperature changes in nylon-6,6 polymer

Wavenumber range (cm^{-1})	**Number of factors**	**Preprocessing method**	**SEC (°C)**	**CV-SEP (°C)**
4,650 – 4,300	3	SNV & DWT (db6, 5 [2 3 4])[a]	0.61	0.75
4,800 – 4,500	5	None	0.50	0.68

[a]Notation is wavelet family and order of wavelet function, number of levels of decomposition, and the levels of details used in the reconstruction of the spectrum.

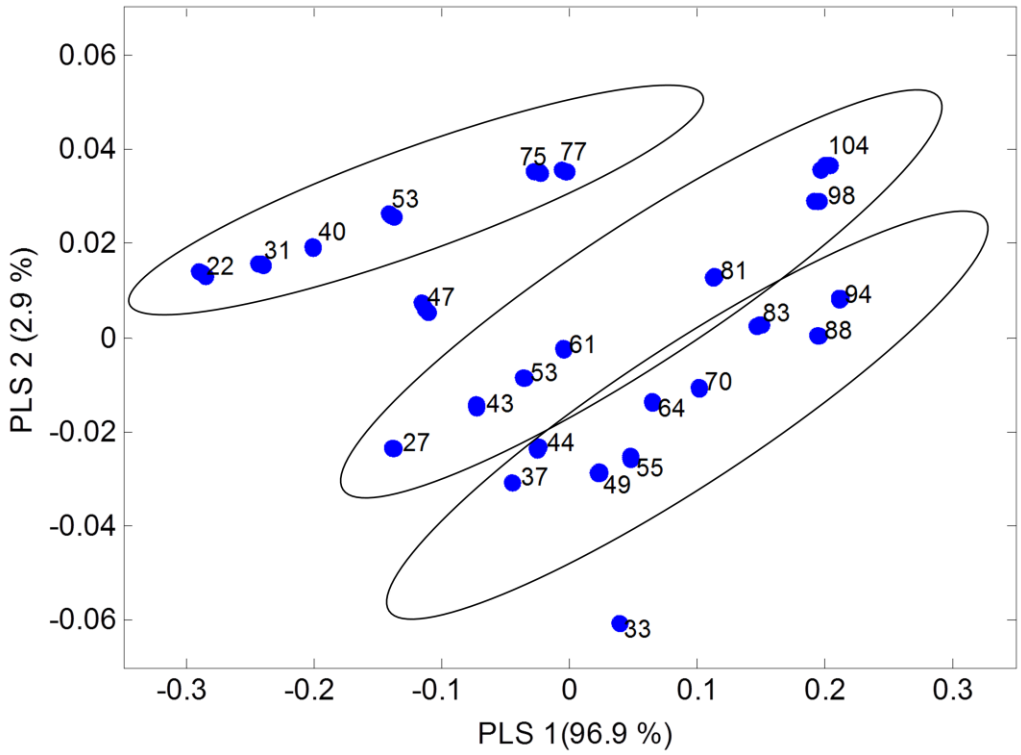

Figure 6-10. Partial least-squares scores along the first two latent variables for the preprocessed nylon-6,6 spectra used in the calibration model. Data labels are the corresponding sample temperatures, and the axis labels include the % variance in the calibration data matrix explained by the corresponding PLS factor. As shown by the superimposed ellipses, temperature information appears to be encoded in three prominent bands of increasing temperature from the lower left to the upper right of the figure. These three bands seem to be clustered according to the time of data collection. The band to the left contains the spectra collected at the beginning of data collection and the band to the right contains the spectra at the end of the data collection.

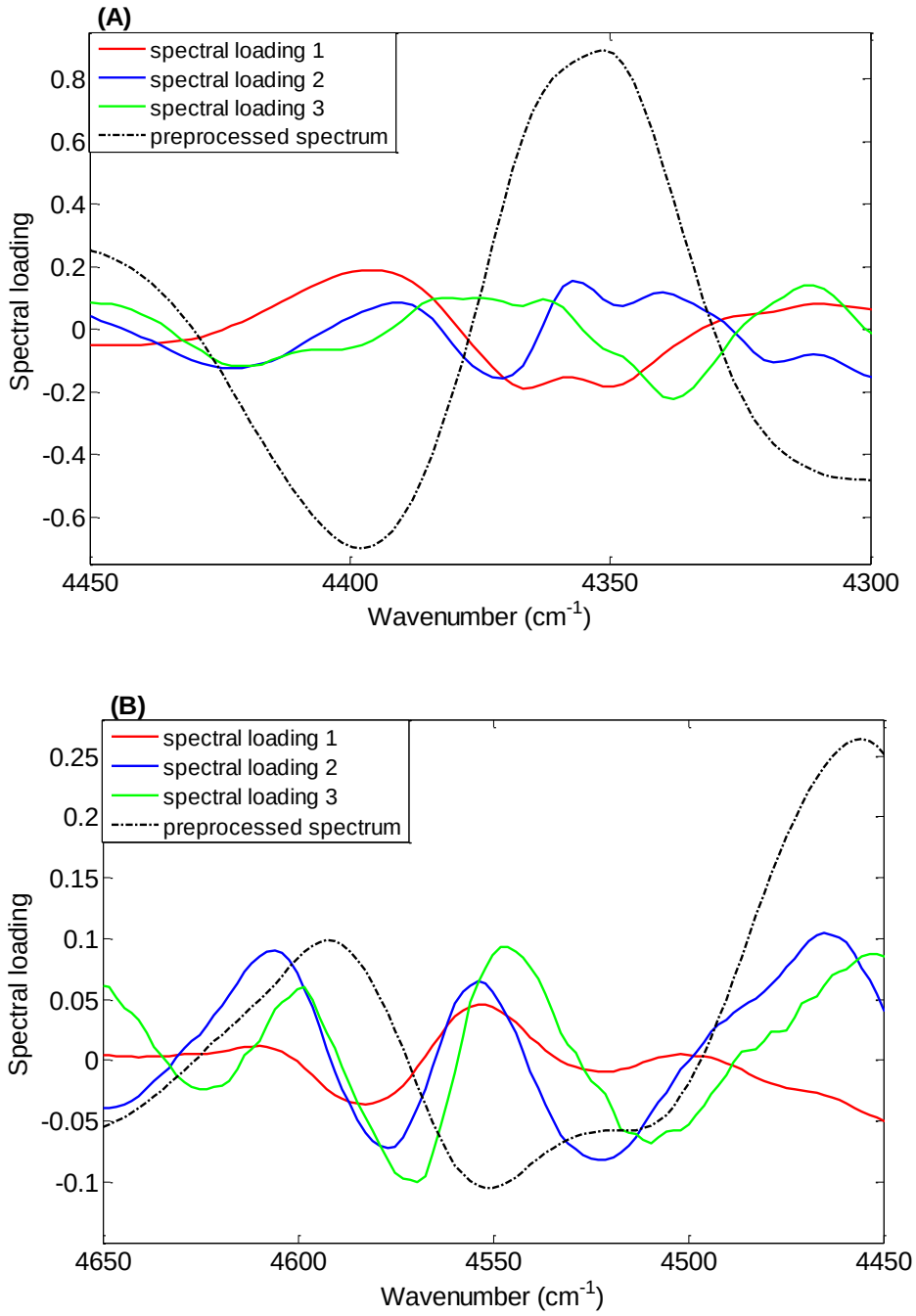

Figure 6-11. Spectral loadings computed for the PLS calibration model using preprocessed nylon spectra. For clarity, separate ranges of the loadings are displayed in panels **A** and **B**. The black dashed line in both panels is a preprocessed nylon spectrum.

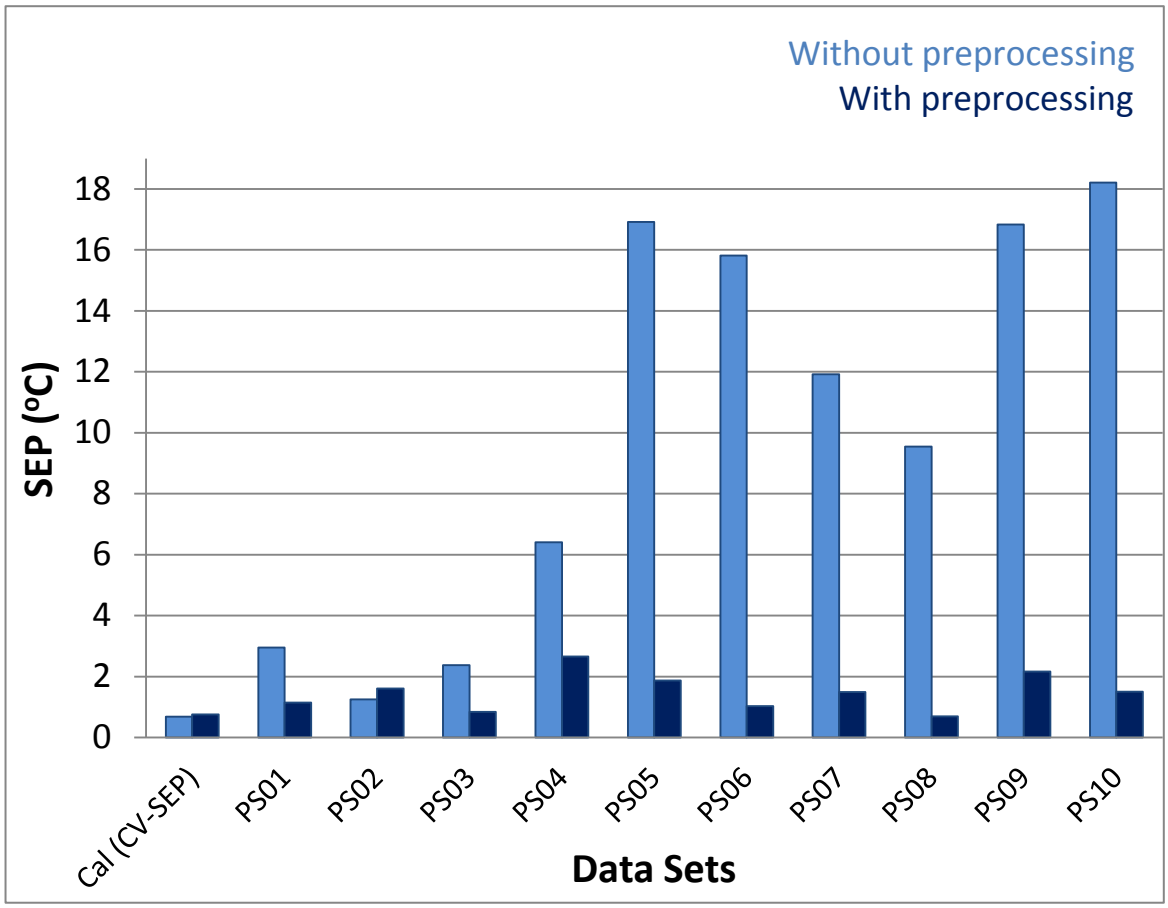

Figure 6-12. Prediction performance of PLS calibration models for temperature changes in nylon-6,6. The models based on preprocessed spectra clearly outperform those based on raw absorbance spectra.

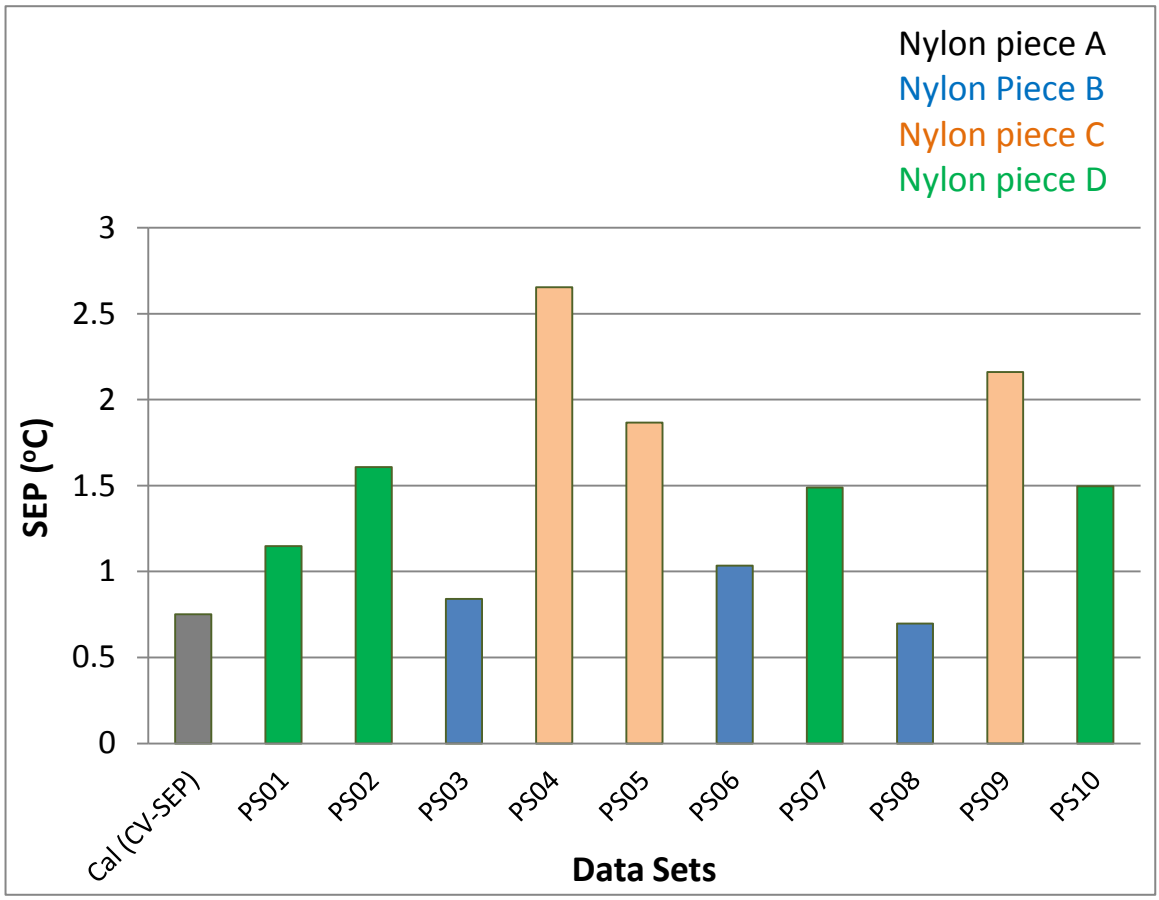

Figure 6-13. Prediction performance of the PLS calibration model based on preprocessed spectra for temperature changes in nylon-6,6. Bars are color-coded with respect to the piece of nylon used in collecting the spectra. The results appear to be grouped by the piece of nylon rather than by time since the collection of the calibration spectra.

Table 6-5. Prediction performance of PLS calibration models for temperature changes in nylon-6,6.

Data set	Nylon piece used	SEP for preprocessed spectra (°C)	SEP for raw spectra (°C)
Calibration[a]	A	0.75	0.68
Prediction set 01 (PS01)	D	1.15	2.95
Prediction set 02 (PS02)	D	1.61	1.25
Prediction set 03 (PS03)	B	0.84	2.37
Prediction set 04 (PS04)	C	2.65	6.40
Prediction set 05 (PS05)	C	1.87	16.9
Prediction set 06 (PS06)	B	1.03	15.8
Prediction set 07 (PS07)	D	1.49	11.9
Prediction set 08 (PS08)	B	0.70	9.55
Prediction set 09 (PS09)	C	2.16	16.8
Prediction set 10 (PS10)	D	1.50	18.2

[a]Results given for the calibration data are values of CV-SEP.

SNV and DWT methods. The technique of principal component analysis was discussed previously in Chapter 3 (Section 3.3.1). The data sets chosen include all four pieces of nylon and encompass the total time span of the data collection. The improved data clustering is judged to be a contributing factor to the excellent prediction performance of the calibration model with time.

6.4.8 Correlation and residual plots

Figure 6-15 presents correlation and residual plots for the calibration data used to build the model for temperature changes in nylon-6,6. The figure is derived from the preprocessed spectra. Excellent correlation between predicted and observed temperatures is observed throughout the temperature range. The residual plot appears randomly scattered with no obvious indicators of deficiency in the model.

Figures 6-16 through 6-18 are similar correlation and residual plots for a subset of the prediction sets (PS04, PS06, PS10). These figures are also based on the preprocessed nylon-6,6 absorbance spectra. The results in Figures 6-16, 6-17, and 6-18 correspond to nylon pieces C, B, and D, respectively. These figures also span the times of 3.0, 3.5, and 7.0 weeks removed from the calibration data. While the predictions are successful when placed into context of the ~80 °C temperature range of the data, some bias is observed with each set of predicted values. This appears to be primarily related to the nylon sheet, suggesting that a more robust model may require the representation of different sheets of nylon in the calibration data.

6.5 Conclusions

In the research discussed here, the methodology developed in Chapters 4 and 5 was successfully extended towards samples other than liquids. In doing so, a signal preprocessing method combining the SNV and DWT procedures followed by PLS regression was utilized to develop calibration models to determine temperatures of a given piece of nylon-6,6 polymer directly from its NIR transmission spectrum. Near-infrared spectra at different temperatures show deviations in intensity and peak position

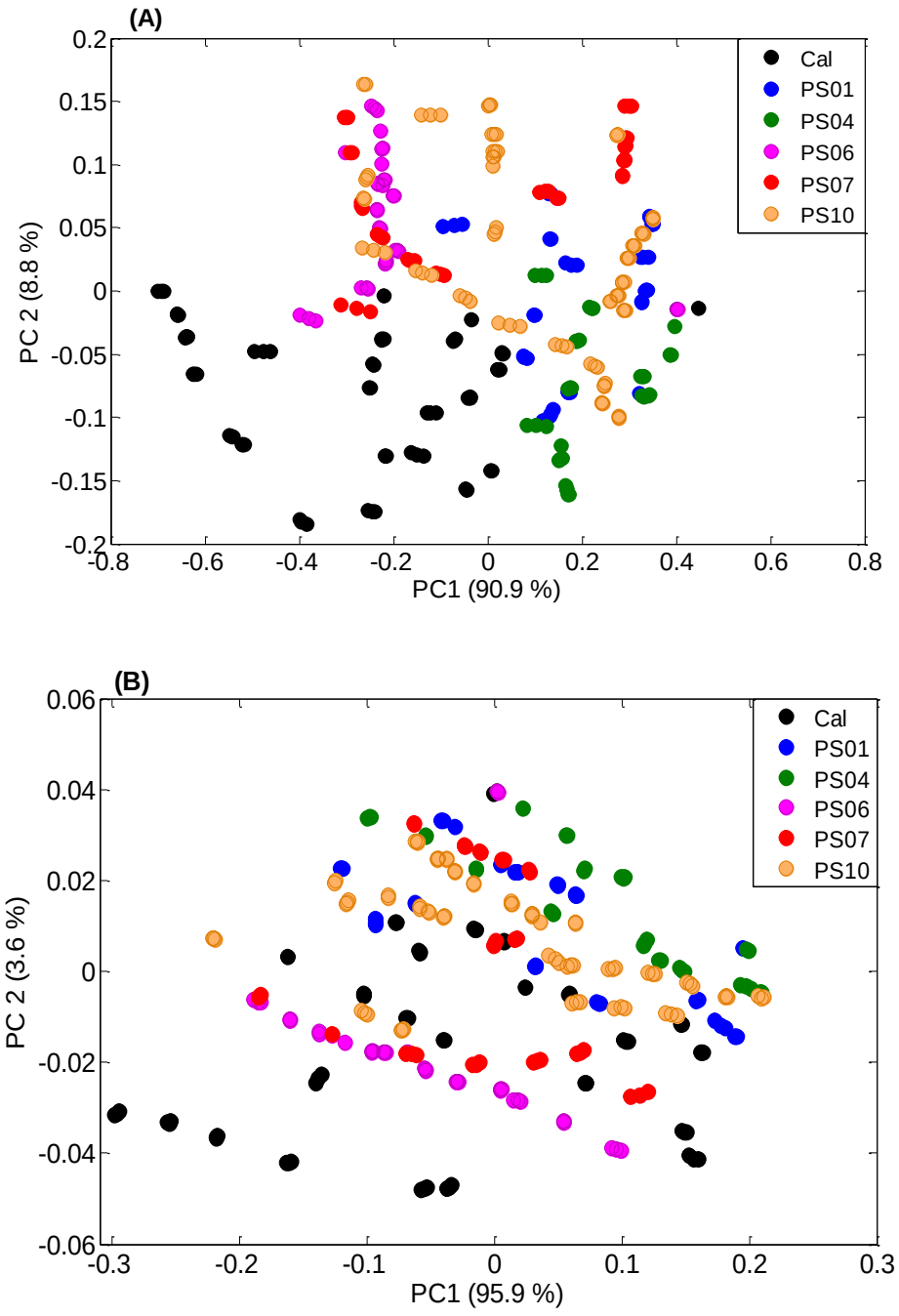

Figure 6-14. Principal component (PC) score plots (PC 2 vs. PC 1). These PC scores are computed from raw absorbance **(A)** and preprocessed (SNV and DWT) spectra **(B)**. In both plots, two PCs account for >99% of the data variance. The spectral data sets were mean-centered before the PCs were computed. Greater overlap between the calibration and prediction data sets is observed in the preprocessed spectra.

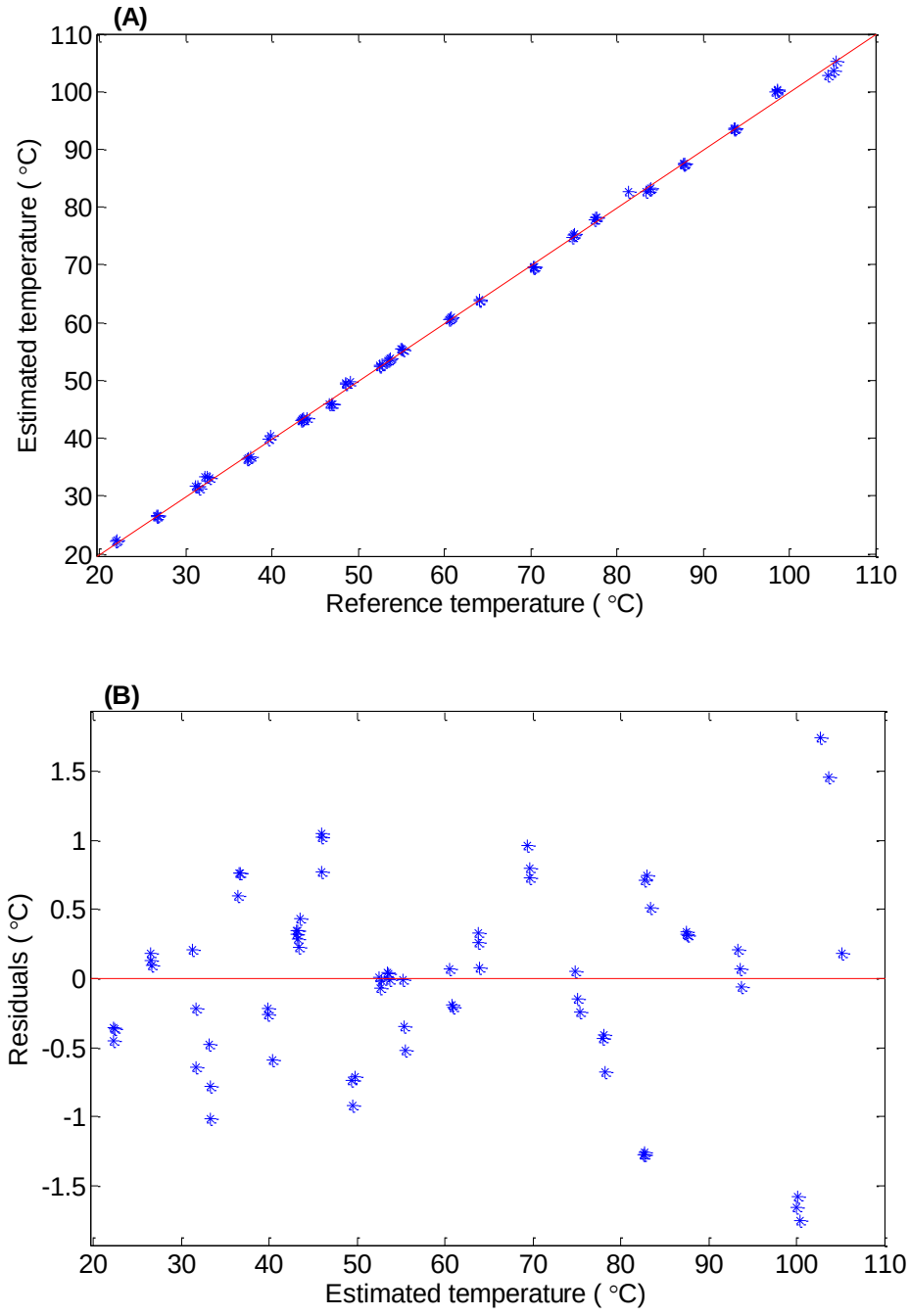

Figure 6-15. Correlation and residual plots for calibration. Correlation **(A)** and residual **(B)** plots for the calibration data used to build the model for temperature changes in nylon-6,6. The red lines in panels A and B denote perfect correlation between estimated and reference temperatures and residuals of 0.0 °C, respectively. Both plots show a good correlation and randomly scattered unbiased residuals.

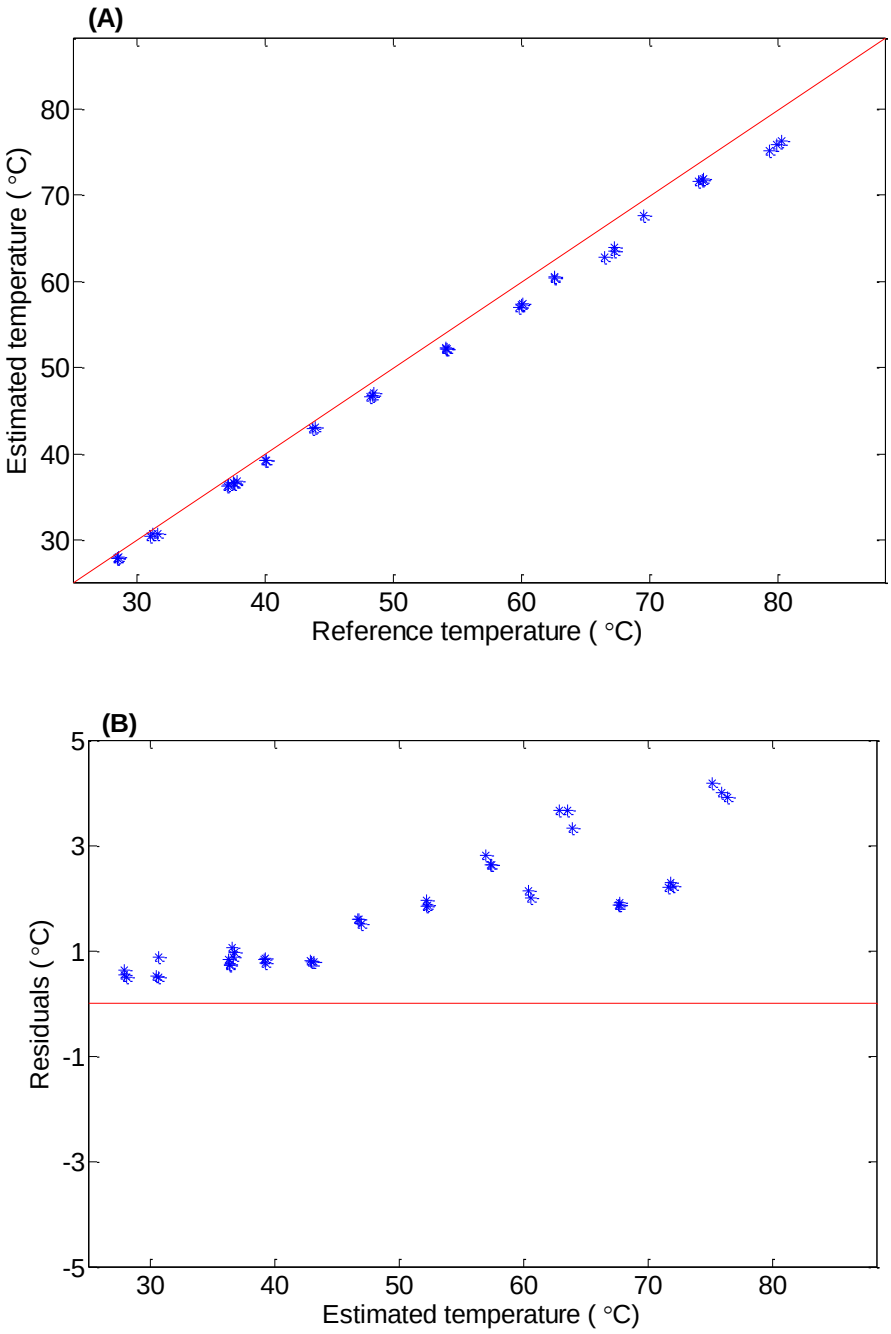

Figure 6-16. Correlation and residual plots. Correlation **(A)** and residual **(B)** plots for prediction set 4 (PS04) for temperature changes in nylon-6,6. The red lines in panels A and B denote perfect correlation between estimated and reference temperatures and residuals of 0.0 °C, respectively. Nylon piece C was used in this prediction and the duration was 3.0 weeks after calibration. A clear bias is shown in both the correlation and residual plots.

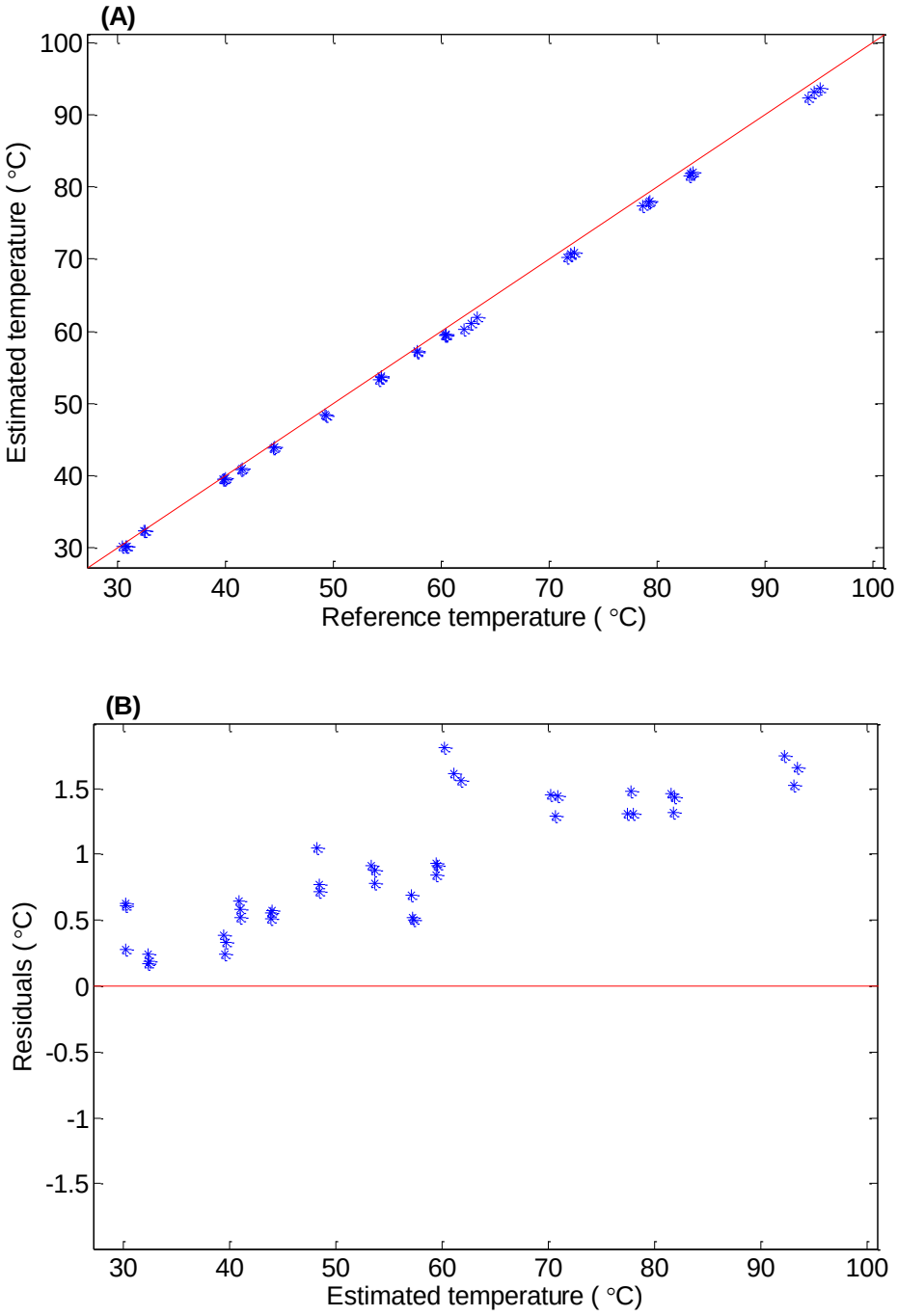

Figure 6-17. Correlation and residual plots. Correlation **(A)** and residual **(B)** plots for prediction set 6 (PS06) for temperature changes in nylon-6,6. The red lines in panels A and B denote perfect correlation between estimated and reference temperatures and residuals of 0.0 °C, respectively. Nylon piece B was used in this prediction and the duration was 3.5 weeks after calibration. A slight bias is observed for both correlation and residual plots.

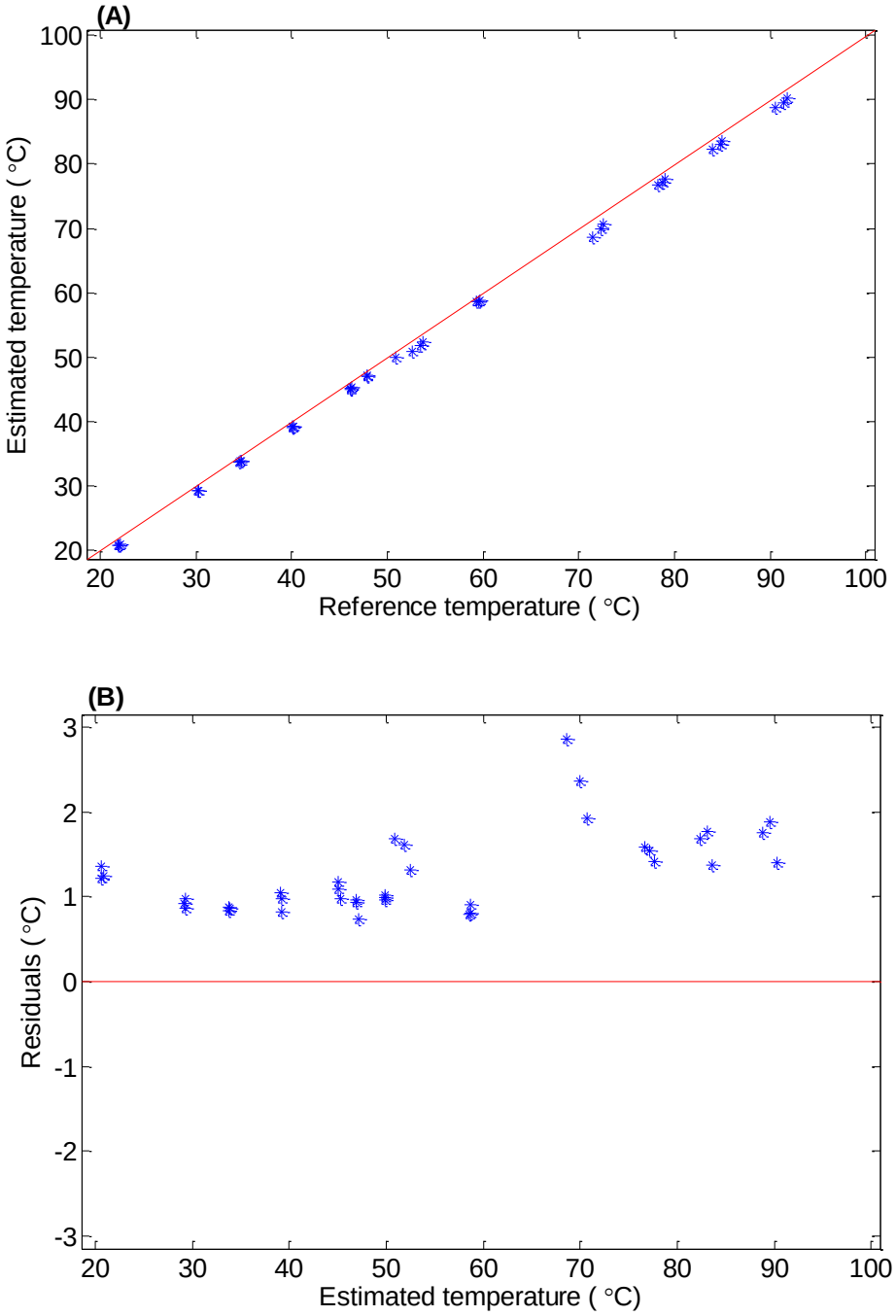

Figure 6-18. Correlation and residual plots. Correlation **(A)** and residual **(B)** plots for prediction set 10 (PS10) for temperature changes in nylon-6,6. The red lines in panels A and B denote perfect correlation between estimated and reference temperatures and residuals of 0.0 °C, respectively. Nylon piece D was used in this prediction and the duration was 7.0 weeks after calibration. A clear bias is shown in both correlation and residual plots.

which arise due to the changes in hydrogen-bonded amide groups and hydrocarbon chains.

Long-term prediction performance of the temperature models was assessed using 10 prediction sets of nylon-6,6 spectra at different temperatures spanning a time period of seven weeks. The temperature model based on raw nylon absorbance spectra gave very high SEP values (> 6 °C) after prediction set PS04 (3 weeks since calibration) whereas the model based on preprocessed spectra provided improved SEP values (0.697 to 2.65 °C) with time.

Use of wavelet functions significantly improved the performance of the temperature model with time and also improved prediction performance across different sheets of nylon. Principal component analysis of the preprocessed and raw spectra further showed the effectiveness of this preprocessing approach. Temperature models based on preprocessed spectra also gave similar SEP values across the different nylon sheets. However, nylon piece C gave high SEP values (average SEP: 2.23 °C) when compared to the other three pieces of nylon (average SEP: 1.19 °C). This might be due to the inhomogeneous nature of different sheets of nylon at a microscopic level.

In principle, these temperature models are not limited to nylon-6,6 polymers, but could be applied to other nylons as well since all the nylon polymers contain the same basic chemical structure. This represents a potential area for further investigation.

CHAPTER 7
DETERMINATION OF MOISTURE CONTENT OF NYLON-6,6 POLYMER DIRECTLY FROM NEAR-INFRARED SPECTRA

7.1 Introduction

Nylons are widely used polyamide polymers. Chapter 6 provided an introduction regarding nylon polymers and the chemical reactions associated with nylon-6,6 polymerization. In addition, physical properties and applications of nylon-6,6 polymers were discussed.

Nylon polymers have hygroscopic properties, meaning they absorb water/moisture from the surrounding environment.[71,80,82] The degree of affinity for water depends on the chemical structure of the nylon species considered. Most common techniques used in the determination of moisture content of a given nylon polymer are based on thermal analyses such as thermogravimetric analysis (TGA), differential scanning calorimetry (DSC) and loss-on-drying (LOD). Although these methods are reliable and easy to conduct, they are time-consuming and destructive. Hence, they cannot be used in on-line analyses.[80] Among chemical analysis methods, the Karl-Fischer titration is also used to determine the moisture content of nylon polymers. Similar to the thermal analysis techniques, this method is also time-consuming, incompatible with on-line analyses and requires hazardous chemicals.[80]

Vibrational spectroscopy has also been used to characterize moisture content in nylon. This approach is attractive because it is non-destructive, requires little or no sample preparation and is potentially amenable to on-line analyses. Among the methods applied, both mid-infrared and near-infrared (NIR) measurements have been performed. Mid-infrared approaches have the advantage of the use of fundamental vibrations, but strong absorption of light in this region from both water and the functional groups of the polymer limits these measurements to the analysis of thin films.[80,82]

By contrast, NIR spectroscopy is compatible with polymer samples with considerable thickness (in the mm range) as the NIR region exhibits reduced absorption when compared to the mid-infrared. As described in Chapter 6, the NIR spectra of nylons have distinctive combination and overtone bands associated with C-H and N-H groups. However, as also discussed in previous chapters, the weak and highly overlapped spectral features in the NIR region present challenges when quantitative analyses are performed. Relating NIR spectral intensities to quantitative measures such as moisture content requires the use of multivariate calibration techniques such as partial least-squares (PLS) regression.[3,24]

In previous work, Lachenal investigated the potential of NIR spectroscopy to be used in the analysis of water content, degree of crystallinity, inter- and intra-molecular interactions of nylons, polyethylene terephthalate (PET), and polyurethane polymers.[82] Miller et al. used NIR spectroscopy and chemometrics to analyze the morphology, amount of absorbed water and the amount of adhesive present in polyethylene/nylon laminates.[89] Both of these studies focused on studying the spectral features of specific polymers as they were subjected to changes in moisture content, temperature, etc. Neither investigated the ability to develop quantitative models to predict the moisture content of a given polymer.

Camacho et al. used NIR spectroscopy and chemometrics to determine the moisture content of recycled nylon-6,6 polymers using spectral features in the 4,500 to 9,000 cm^{-1} region.[80] This work documented the use of PLS regression to develop calibration models to predict moisture content of nylon-6,6 polymers. In this study, however, the reference methods used for developing the calibration models were destructive methods such as TGA, DSC and LOD. This limits the integration of the method with routine non-destructive analysis procedures. Furthermore, the long-term predictive ability of the developed calibration models was not assessed.

In the work reported in this chapter, the methodology reported by Camacho was extended in several respects. Partial least-squares regression models were developed to determine the moisture content of nylon-6,6 polymers directly from NIR spectra. The prediction performance of these moisture models was assessed for robustness with time and the ability to predict moisture uptake across different sheets of nylon-6,6 polymers. The reliability of using an analytical balance as an alternative to time-consuming TGA measurements to obtain reference weight measurements was also demonstrated in this work.

7.2 Moisture uptake on nylon

Moisture absorption of nylon polymers has been a topic of interest for many years.[79,80,82] Nylon polymers are sensitive to moisture due to their ability to form hydrogen bonds with water molecules using the polar amide groups.[70,71,73,80,88] This hydrogen bonding process is illustrated in Figure 7-1. Also, water molecules are believed to displace nylon molecules, thereby resulting in swelling of the nylon molecular matrix.[71] Water can act as a plasticizer which increases toughness and flexibility while reducing the tensile strength and modulus of nylon polymers. Ultimately, absorption of moisture results in deterioration of electrical properties and poor dimensional stability in an environment of changing relative humidity.[73]

Water has a fundamental O-H stretching peak centered at 3,800 cm^{-1} and the first overtone of this O-H stretching vibration is centered at 6,900 cm^{-1}. A combination band of O-H fundamental stretching and bending modes is centered at 5,200 cm^{-1}. All of these peaks are broad in nature due to the hydrogen-bonding network of water molecules.[6,37] Upon uptake of water, the overtones and combination peaks of nylon that arise due to the amide linkage are expected to deviate as a result of hydrogen bonding. Also, the intensities of the water bands themselves are expected to increase upon moisture uptake of nylon. Commercially available nylon-6,6 polymers absorb up to an average of 8-10 % of water by dry weight upon saturation.[71] Moisture uptake on nylon is a reversible

process. The rates of moisture uptake and moisture loss vary with the relative humidity, temperature and the chemical structure of nylon considered.[71,88]

7.3 Experimental design

7.3.1 Apparatus and reagents

All spectral data collections were performed with a Bruker Vertex 70 (Bruker Optics, Inc., Billerica, MA) Fourier transform (FT) spectrometer configured with a tungsten-halogen lamp source, a calcium fluoride (CaF_2) beam splitter and a liquid nitrogen cooled indium antimonide (InSb) detector. A low-pass filter (OCLI, Santa Rosa, CA) was used to restrict the light beyond 5,000 cm^{-1}. Commercially obtained nylon-6,6 samples (McMaster-Carr, Elmhurst, IL) were used in this analysis. A metal sample holder was used to hold the samples. Weight measurements of the nylon pieces were obtained with a Mettler AE200 analytical balance (Mettler-Toledo, Inc., Columbus, OH). A Fisher Scientific Isotemp Model 655G oven (Fisher Scientific, Pittsburgh, PA) and a glass desiccator equipped with drierite (W.A. Hammond Drierite Co, Ltd., Xenia, OH) were used for drying purposes. Relative humidity measurements were obtained from a TES 1364 humidity-temperature meter (TES Electrical Electronic Corp., Taipei, Taiwan). Figure 7-2 provides a schematic representation of the experimental setup.

7.3.2 Procedures

Six pieces of nylon-6,6 (A, B, C, D, E and F) were used in the spectral data collections. These nylon samples were cut from three different commercially available sheets of nylon-6,6 polymer. The average dimensions of the six nylon pieces were 25 × 20 × 0.40 ± 0.01 mm, and the average weight was 0.2350 ± 0.0001 g. All the spectral data collections were performed at ambient temperature conditions (~21 – 22 °C). Nylon pieces were exposed to several methods of moisture uptake and drying. Methods of moisture uptake included soaking the nylon in water, placing the nylon piece in a humidity chamber and exposing the nylon to ambient temperature and humidity conditions in the laboratory. Methods of drying included drying in a desiccator, drying

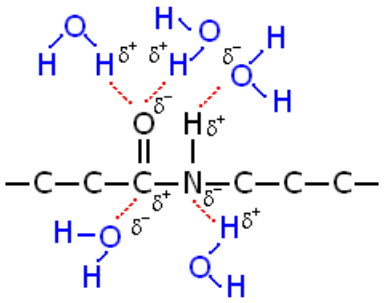

Figure 7-1. Schematic representation of moisture uptake on nylon polymers.[88] Water molecules form hydrogen bonds with polar amide groups in nylon.

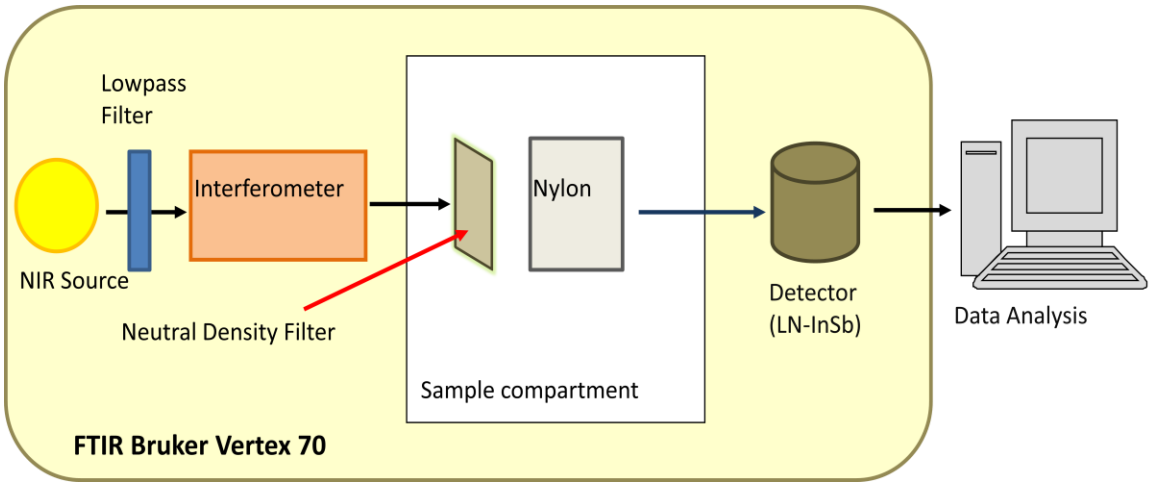

Figure 7-2. Schematic diagram of the experimental setup used for collecting NIR spectra of nylon.

in an oven (~80 °C and ~100 °C) and exposing the nylon to ambient temperature and humidity conditions in the laboratory.

Moisture uptake was assessed by weighing the nylon piece before and after exposure to water. The percentage moisture uptake of a given piece of nylon at a given time was calculated using two different expressions. The first method was based on the dry weight of nylon and is given in Eq. 7-1.

$$\%\, moisture\ uptake = \frac{W_{wet\ nylon} - W_{dry\ nylon}}{W_{dry\ nylon}} \times 100 \qquad (7\text{-}1)$$

In the equation, $W_{wet\ nylont}$ is the weight of a given piece of nylon with some absorbed moisture and $W_{dry\ nylon}$ is the weight of the piece of nylon at 0 % moisture uptake.

The second approach was based on expressing the moisture uptake as a fraction of the weight of the wet nylon piece. This calculation is summarized in Eq. 7-2.

$$\%\, moisture\ uptake = \frac{W_{wet\ nylon} - W_{dry\ nylon}}{W_{wet\ nylon}} \times 100 \qquad (7\text{-}2)$$

The terms in Eq. 7-2 are the same as those defined in Eq. 7-1.

A summary of the spectral collection protocol is given in Tables 7-1 and 7-2. For calibration purposes, spectra were collected from 76 nylon samples over three consecutive days using nylon-6,6 pieces A and E. For this discussion, a nylon sample is considered to be a piece of nylon subjected to a given set of moisture uptake conditions. Three consecutive spectra were collected from the nylon sample after placing it in the spectrometer. A total of 3×76 = 228 calibration spectra were thus obtained. Each nylon piece was weighed at the start and end of the spectral acquisition to allow the assessment of moisture loss during the six minutes of data acquisition time. This issue will be discussed in detail in Section 7.4.4.

In order to assess the long-term predictive ability of the quantitative moisture models, 10 sets of nylon spectra were collected using the other nylon-6,6 pieces (B, C, D and F) over a period of six months. Three replicate spectra were again collected for each nylon sample.

Moisture uptake values were randomized in the calibration and prediction sets to minimize the correlation of moisture uptake with time. Randomization of the moisture uptake values is illustrated in Figure 7-3. The method of moisture uptake and drying selected for a given piece of nylon was also randomized to assess the prediction performance of the moisture uptake model across different sheets of nylon.

Open-beam air spectra were used as the background in the calculation of absorbance values throughout the data collection For a given data collection session, eight warm-up air spectra were collected at the beginning of the day and three intermediate air spectra were collected after the measurement of every fourth nylon sample. An additional six air spectra were collected at the end of the day. The average of the air spectra collected on a given day was used in calculating the absorbance values for nylon spectra collected on that day. A 6.3% metal thin-film neutral density filter (Rolyn Optics Co., Covina, CA) was used to attenuate the source intensity during the collection of the open-beam air spectra.

The raw data consisted of 256 co-added double-sided interferograms containing 14,220 points collected at every zero crossing of the helium-neon (He-Ne) reference laser (15,800.45 cm^{-1}). The nominal spectral resolution was 4 cm^{-1} and an aperture setting of 6 mm was used. All interferograms were Fourier processed to single-beam spectra by use of the Bruker Opus software controlling the spectrometer (Version 6.5, Bruker Optics, Inc.). The single-beam spectra were computed with a point spacing of 1.9288 cm^{-1} by applying two levels of zero filling, Blackmann-Harris 3-Term apodization and Mertz phase correction. The wavenumber range selected for this study was from 4,000 to 5,000 cm^{-1}.

Further calculations were performed with Matlab (Version 7.4, The Mathworks, Inc., Natick, MA) on a Dell Precision 670 workstation (Dell Computer Corp., Round Rock, TX) operating under Red Hat Linux WS, (Version 5.2, Red Hat, Inc., Raleigh, NC). Nonlinear curve fitting to assess moisture loss with respect to time was performed with Microsoft Excel (Version 2007, Microsoft, Inc., Redmond, WA).

Before quantitative modeling of moisture uptake was investigated, the single-beam spectra of the nylon samples were converted to absorbance units by use of the appropriate open-beam air background. The resulting spectra were normalized by use of the standard normal variate (SNV) transform. This method was described previously in Chapter 3.

7.4 Results and discussion

7.4.1 Complementary weight measurements with TGA

To assess the reliability of assigning moisture uptake values on the basis of measurements with the analytical balance, a set of parallel measurements was performed with TGA. Four pieces of nylon-6,6 (average weight: 12.4 ± 0.1 mg) were dried in the oven to remove any moisture and subsequently weighed with the analytical balance. They were then soaked in water until the nylon pieces were saturated. Weight measurements were then made on the saturated nylon pieces right before they were introduced to the TGA (Model Q500-0305, TA Instruments, New Castle, DE). The temperature range analyzed in these experiments was from 20 to 600 ^{o}C with a linear ramp of 5.00 ^{o}C/min. The composition of the purge gas used with the TGA was 19 to 23% O_2 in N_2. Once the nylon piece was completely decomposed, the first derivative of the mass loss (peak centered at 100 °C) with temperature was computed to calculate the % mass loss due to evaporation of water.

Moisture uptake percentages obtained with the TGA method were well matched to moisture uptake values commonly reported in commercial literature.[71] Also, moisture uptake percentages obtained with the TGA method were well correlated with the

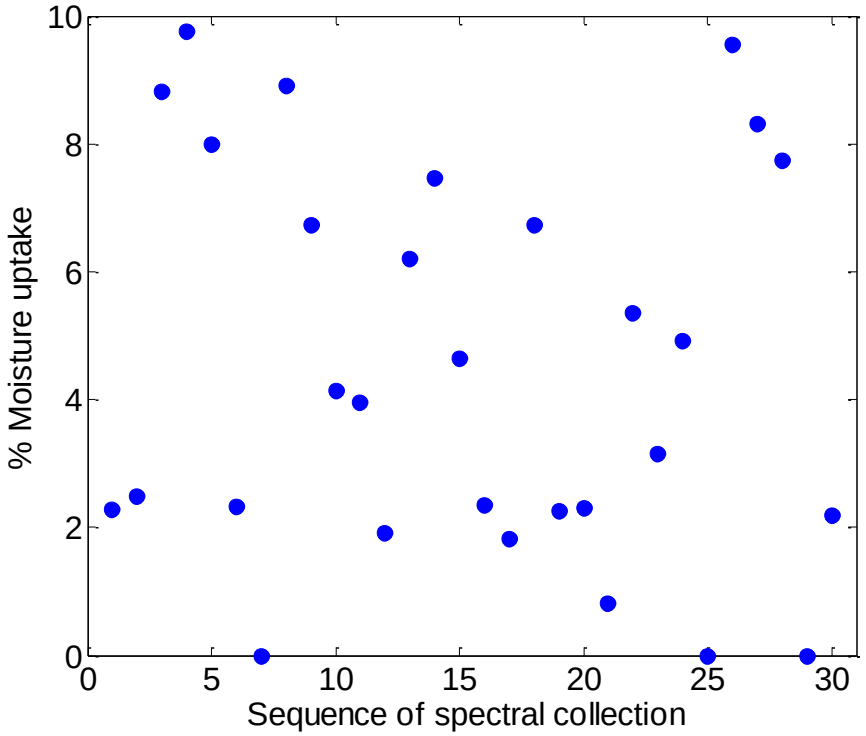

Figure 7-3. Randomization of moisture uptake values to minimize the correlation between moisture uptake and time. Moisture uptake values were computed with Eq. 7-1. The first 30 of the 76 samples in the calibration data set are displayed in this plot.

Table 7-1. Summary of nylon-6,6 samples used in the experiment

Nylon piece	Nylon sheet
A	1
B	2
C	3
D	1
E	2
F	3

Table 7-2. Summary of spectral collection protocol for the moisture uptake models

Data set	Number of Samples[a]	Number of spectra collected	Time since calibration (weeks)
Calibration	76	228	0
Prediction set 1 (PS01)	42	126	0.5
Prediction set 2 (PS02)	41	123	1
Prediction set 3 (PS03)	45	135	2
Prediction set 4 (PS04)	43	132	3
Prediction set 5 (PS05)	43	132	4
Prediction set 6 (PS06)	48	144	6
Prediction set 7 (PS07)	45	135	8
Prediction set 8 (PS08)	40	120	14
Prediction set 9 (PS09)	48	144	18
Prediction set 10 (PS10)	46	138	23

[a]A sample is defined as a piece of nylon subjected to a given level of moisture uptake.

moisture uptake values obtained with the analytical balance. Table 7-3 summarizes the % moisture uptake (based on dry weight of nylon) values for each piece of nylon measured with the analytical balance and TGA. As indicated in the last column in the table, the percentage difference between the two methods ranged from -1.65 to +0.78, with the mean absolute value of the percentage differences equal to 0.74%. A pairwise *t*-test (two-tailed) to compare the two sets of % moisture uptake values is only significant at 47% (mean and standard deviation of differences equal to -0.35 and 1.00%, respectively). These results suggest that the weight measurements obtained with the analytical balance were consistent with the TGA measurements and that the precision of the % moisture uptake values is on the order of ±1%. On the basis of these results, weight measurements obtained from the analytical balance were used subsequently in the development of calibration models for moisture uptake in nylon.

7.4.2 Moisture uptake of nylon-6,6 and relative humidity

Two pieces of nylon-6,6 (average weight: 0.2376 ± 0.0001 g) were dried in the oven to remove any moisture and weighed using the analytical balance. The two nylon pieces were then exposed to ambient relative humidity (RH) and temperature conditions in the laboratory for 20 days. Weight measurements were made on the nylon pieces each day using the analytical balance, and relative humidity and temperature measurements were performed with the humidity-temperature meter. As described by Eq. 7-3, the moisture uptake pattern of the nylon-6,6 pieces was expressed each day in relative terms compared to the previous day.

$$\%\ change\ in\ moisture\ uptake = \frac{W_{day\,2} - W_{day\,1}}{W_{day\,1}} \times 100 \qquad (7\text{-}3)$$

In Eq. 7-3, W_{day2} is the weight of the piece of nylon on a given day and W_{day1} is the corresponding weight of the nylon piece on the previous day.

Table 7-3. Comparison between % moisture uptake values obtained with the analytical balance and TGA

Nylon piece	Moisture uptake on nylon (%)		% Difference[a]
	Analytical balance measurements	TGA measurements	
1	9.282	9.210	0.78
2	8.694	8.711	-0.20
3	8.950	9.100	-1.65
4	9.618	9.652	-0.35

[a]Percentage difference computed relative to the TGA measurements.

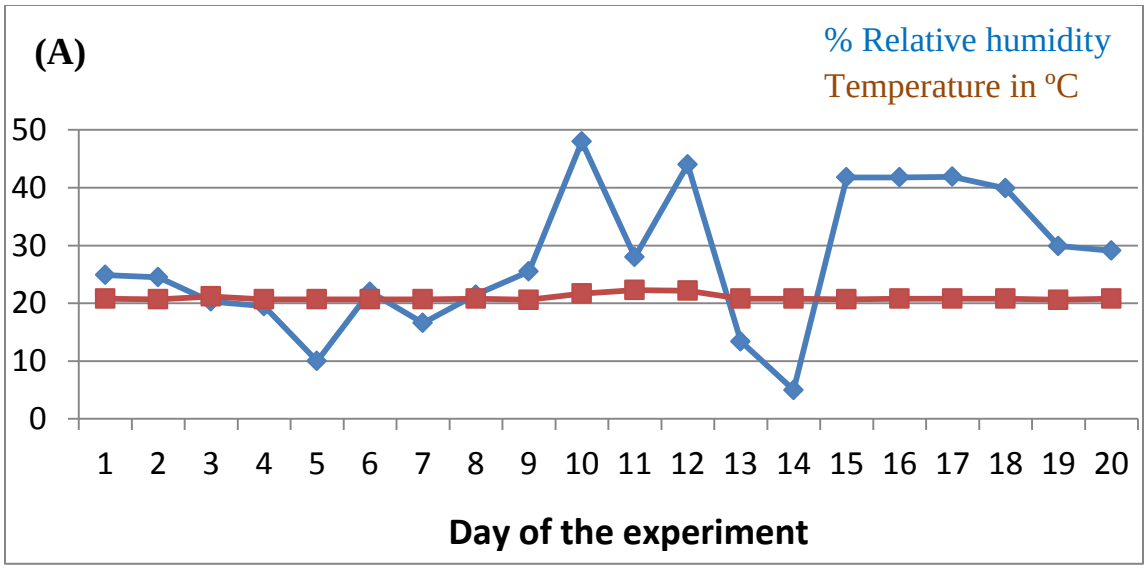

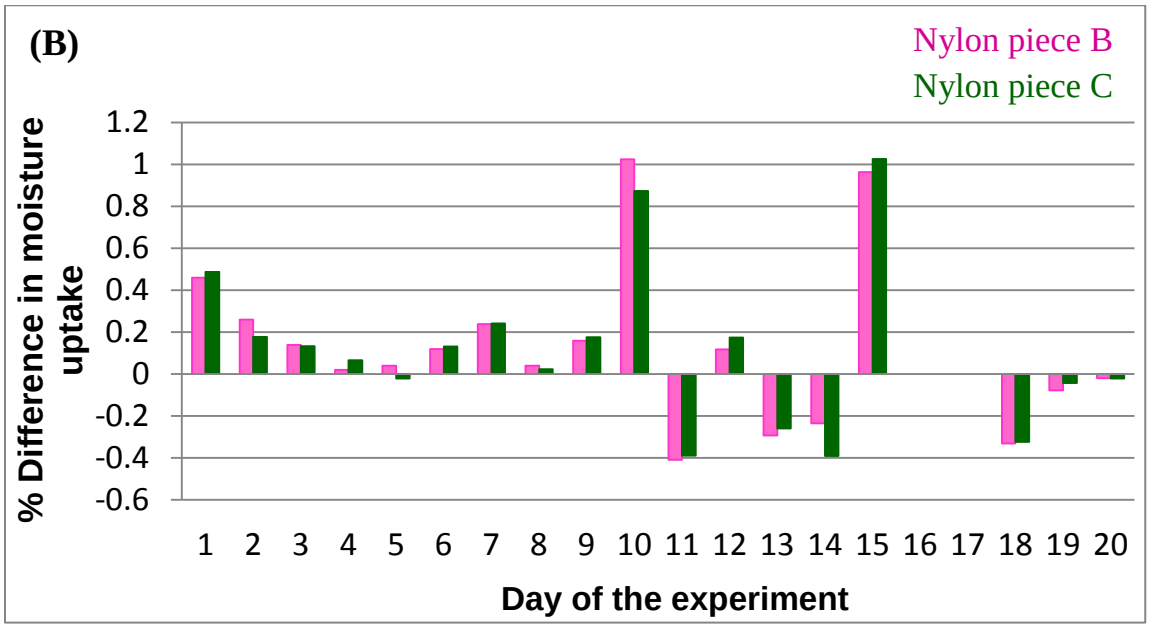

Figure 7-4. Ambient % relative humidity and temperature conditions and their effect on moisture uptake of nylon-6,6. **(A)** Ambient % relative humidity and temperature measurements obtained over the 20-day time period. **(B)** Moisture uptake pattern of nylon-6,6 pieces B and C over the 20-day time period.

The trend in the moisture uptake pattern shown in Figure 7-4 clearly indicates the reversible nature of moisture uptake in nylon and its dependence on the relative humidity of the environment. For this experiment, the contribution of temperature was negligible as the laboratory temperature showed no significant change over the period of data collection.

7.4.3 Near infrared spectra of nylon-6,6 upon water uptake

Figure 7-5 illustrates NIR absorbance spectra of nylon-6,6 obtained at different levels of moisture uptake. The displayed spectra were normalized with the SNV transform. It can be observed that the intensity of absorption near 4,000 cm^{-1} and 5,000 cm^{-1} is increasing with increasing moisture content. This is due to the presence of the two dominant water absorption peaks centered at 3,800 cm^{-1} (fundamental O-H stretching) and 5,200 cm^{-1} (combination band of O-H fundamental stretching and bending).

Principal component analysis (PCA, Chapter 3, Section 3.3.1) was used to investigate the spectral differences in nylon-6,6 polymers upon moisture uptake. This was performed using a collection of 78 dry (0% moisture uptake) and 66 saturated (99% moisture uptake) nylon-6,6 absorbance spectra. The wavenumber range of 4,000 to 4,400 cm^{-1} was used in the calculation, the spectra were scaled with the SNV transform, and the spectral data matrix was mean centered before submission to PCA. Figure 7-6 is a score plot based on the first two principal components (PCs). It illustrates the clear clustering of dry and wet nylon spectra, confirming the differences in the spectral features of nylon-6,6 that arise upon moisture uptake.

7.4.4 Application of a correction strategy for moisture loss during spectral acquisition

Possible moisture loss inside the spectrometer was of a concern as the relative humidity inside the sample compartment was measured to be 2 - 4%. This was particularly problematic when the nylon pieces had a considerable amount of moisture on

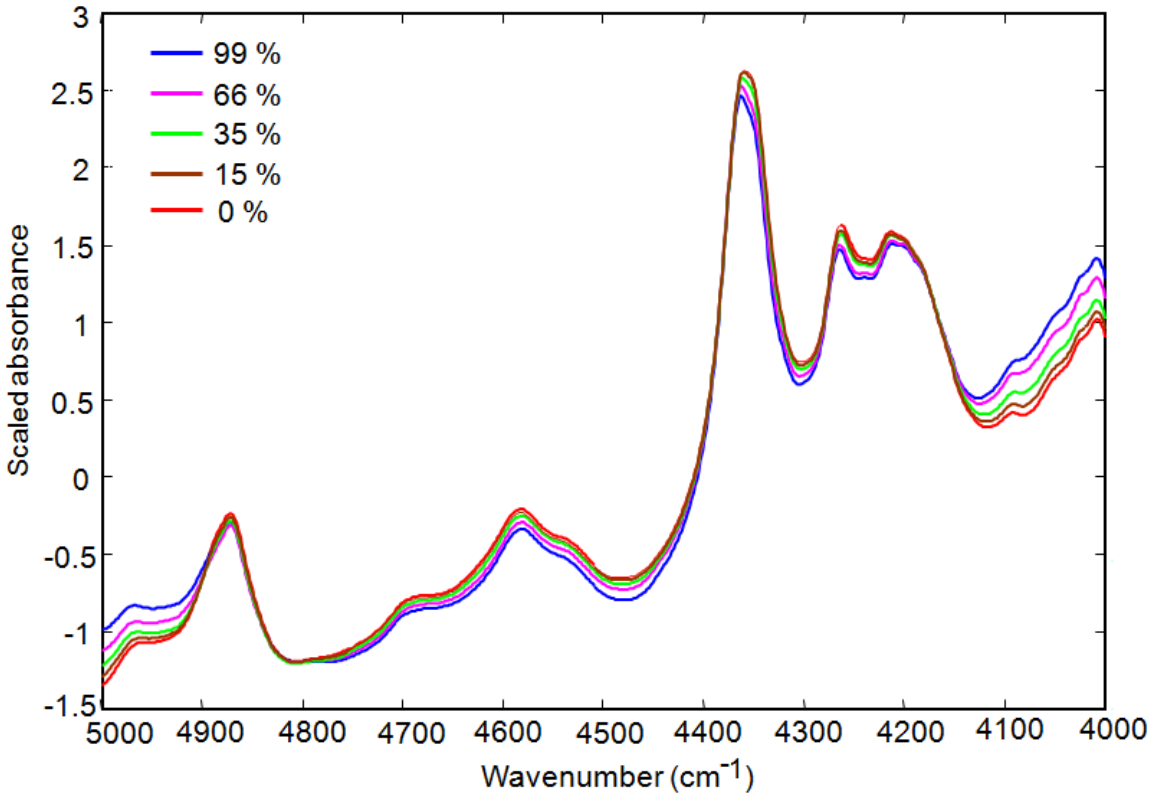

Figure 7-5. Near infrared spectra of nylon-6,6 in the range of 4,000 to 5,000 cm^{-1} obtained at different levels of moisture uptake (Eq. 7-1). Spectra were normalized with the SNV transform. Ordering of the spectra with respect to moisture uptake is observed at the two extremes of the plot as a consequence of the strong absorption bands of water near 3,800 and 5,200 cm^{-1}.

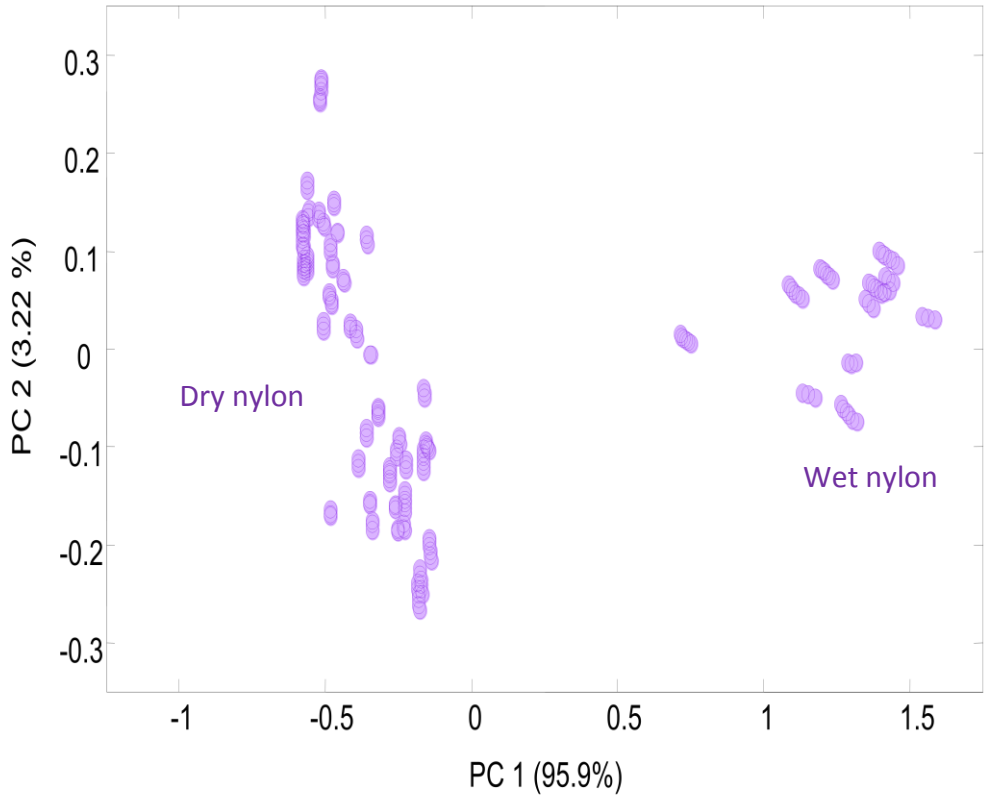

Figure 7-6. Principal component score plot (PCs 2 vs. 1) obtained from nylon-6,6 absorbance spectra corresponding to dry and wet (i.e., saturated) nylon. Spectra were scaled with the SNV transform and the spectral data matrix was mean centered before the PCs were computed. Together, the first two principal components account for greater than 99% of the data variance.

them. Moisture loss during the spectral collection was investigated on the basis of assuming either a linear or an exponential decay. In order to test the two hypotheses, three pieces of nylon-6,6 polymer corresponding to initial values of 80, 65, and 45 % moisture uptake (Eq. 7-1) were exposed to the dry conditions inside the sample compartment and weight measurements were obtained every two minutes for a total of 12 minutes. This time spacing corresponds to the collection of one replicate spectrum.

As described in Eqs. 7-4 to 7-6, the moisture loss process was defined on the basis of *Z*, the % moisture remaining to be lost during the exposure to dry air. As a function of time, *t*, *Z* is defined as:

$$Z_t = \frac{\Delta w_{t-max} - \Delta w_t}{\Delta w_{t-max}} \times 100 \tag{7-4}$$

$$\Delta w_{t-max} = w_{initial} - w_{t-max} \tag{7-5}$$

$$\Delta w_t = w_{initial} - w_t \tag{7-6}$$

In Eq. 7-4, $\Delta w_{t\text{-max}}$ corresponds to the total weight loss from time zero to the maximum time of the experiment (i.e., 12 minutes in the example described here). This is defined in Eq. 7-5 as the difference between the initial weight, $w_{initial}$, and the weight after the maximum time, $w_{t\text{-max}}$. Experimentally, these initial and final weights are averages of three consecutive weight measurements taken at the beginning and end of the experiment, respectively. Similarly, Δw_t corresponds to the weight loss at a given time, *t*, and is defined in Eq. 7-6 as the difference between the initial weight, $w_{initial}$, and the weight at time, *t*, w_t.

The experimental results (Figure 7-7) suggest that moisture loss from the nylon pieces follows an approximate exponential decay. If just the first six minutes are considered as the time required to collect three replicate spectra, about 49 % of the total moisture loss occurred during the acquisition of the first replicate spectrum while about 36 % and 15 % of the total moisture loss occurred during the collection of the second and third replicate spectra, respectively.

On the basis of this experiment, an exponential decay correction was performed in order to assign a more accurate weight to the nylon piece at the time of spectral collection. The data displayed in Figure 7-7 were fit to a simple exponential decay function, yielding the fitted result displayed in Eq. 7-7 and represented as the solid line in Figure 7-7.

$$Z_t = 55.5e^{-0.00432t} \tag{7-7}$$

This expression allows the value of Z to be estimated for any time (in seconds) within the range of 0 to the defined maximum time (i.e., six minutes in the context of acquiring three spectra). Given this estimated value along with the initial and final weights of the nylon piece (i.e., $w_{initial}$ and $w_{t\text{-max}}$, respectively), Eqs. 7-4, 7-5, and 7-6 can be combined and rearranged to solve for w_t:

$$w_t = \frac{Z_t}{100}(w_{initial} - w_{t-max}) + w_{t-max} \tag{7-8}$$

As an example, at Z = 50 %, Eq. 7-8 simplifies to the weight at the time corresponding to the average of the initial and final weights.

$$w_t = 0.5(w_{initial} - w_{t-max}) + w_{t-max} = 0.5w_{initial} + 0.5w_{t-max} = \frac{W_{initial} + W_{t-max}}{2} \tag{7-9}$$

Given the estimated weight at time t, Eqs. 7-1 or 7-2 can be used to estimate the corresponding % moisture uptake that corresponds to that time

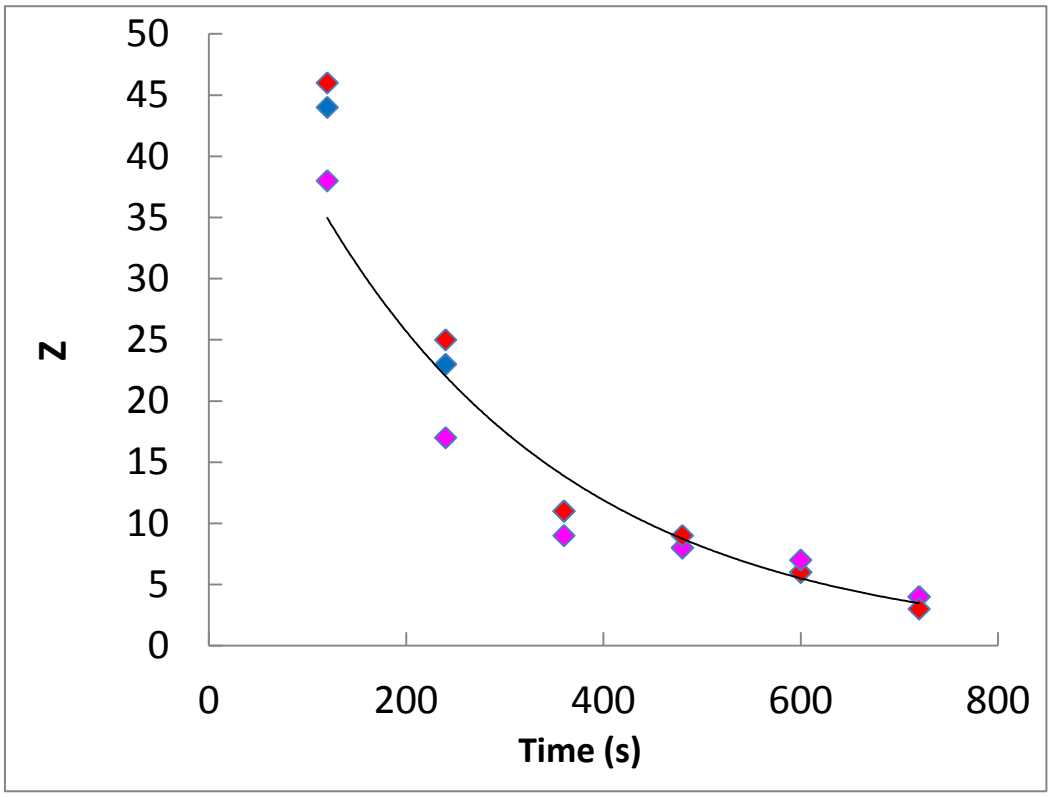

Figure 7-7. Values of Z (Eq. 7-4) obtained from three nylon pieces (shown in blue, red and magenta) with respect to time of exposure to the dry atmosphere of the sample compartment of the spectrometer. The blue, red, and magenta symbols correspond to 80, 65, and 45 initial values of % moisture uptake (Eq. 7-1), respectively. The solid line represents the results of fitting the data to an exponential decay function ($y = 55.5e^{-0.00432x}$). The value of r^2 corresponding to the fitted equation was 0.944. No blue symbols are apparent for the last four time points due to overlap with the red and magenta symbols. The last data points do not reach $Z = 0$ because $w_{t=\max}$ (Eq. 7-5) is computed as the average of three replicate weights and is typically smaller than the single weight at the last time point due to further evaporation of water during the weighing procedure.

Assessment of the effect of the exponential decay correction was performed by developing separate PLS calibration models for exponentially corrected and uncorrected % moisture uptake values. In addition, a third model was built based on a simple linear decay function. For the linear function, the starting and ending weights and their corresponding times relative to the start of data acquisition (i.e., 0 and 6 min) were fit to a two-parameter linear model, and the resulting slope and intercept were used to assign a weight to each spectrum on the basis of its average collection time (i.e., 1, 3, and 5 min after the start of data collection). Table 7-4 provides an example that compares the corrected weights and corresponding values of *Z* obtained with the linear and exponential corrections.

The SNV-normalized absorbance spectra were used in computing the three models and both the wavenumber region submitted to the PLS procedure and the number of PLS model terms (latent variables) were optimized for each model by a grid-search procedure. This optimization involved scanning the wavenumber range from 4,000 to 5,000 cm^{-1} in steps of 25 cm^{-1} using window sizes from 300 to 800 cm^{-1} in steps of 25 cm^{-1}. For each wavenumber range investigated, models based on 1-10 latent variables were computed. Cross-validation (CV) based on leaving out 10% of the calibration spectra per iteration was used to identify the optimal model. In this case, the CV procedure builds a model with 90% of the data and uses that model to predict the 10% withheld. By cyling through the withheld spectra, a cross-validated standard error of prediction (CV-SEP) can be computed to describe the model performance. The CV-SEP is an error estimate based on pooling the errors in predicted % moisture uptake for each of the spectra withheld from the calculation of the models. The CV procedure was discussed in detail in Chapter 3 (Section 3.4).

Once the spectral range associated with the minimum CV-SEP was determined, the optimal number of latent variables was taken as that which produced a value of CV-SEP not statistically different from the minimum CV-SEP. This determination was made

Table 7-4. Comparison of linear and exponential corrections to sample weights[a]

Correction method used	Spectrum 1		Spectrum 2		Spectrum 3	
	Weight[b] (g)	***Z*[c] (%)**	**Weight[b] (g)**	***Z*[c] (%)**	**Weight[b] (g)**	***Z*[c] (%)**
Linear correction	0.2434	83	0.2428	50	0.2422	17
Exponential correction	0.2427	43	0.2424	26	0.2422	15

[a]The initial and final weights of the nylon piece for this example were 0.2437 and 0.2419 g, respectively.

[b]Weights for spectra 1, 2, and 3 correspond to times of 1, 3, and 5 minutes, respectively.

[c]Values for *Z* (% moisture remaining to be lost) were computed with Eqs. 7-4 to 7-6 for the linear correction procedure and with Eq. 7-7 for the exponential correction. This accounts for the discrepancy between values of *Z* for corresponding weights.

by use of an *F*-test at the 95 % confidence level. This procedure was used previously in the work described in Chapters 4-6.

As presented in Table 7-5, the CV-SEP obtained for the exponentially corrected data was superior to that of the uncorrected and linearly corrected data. This suggests that the exponential decay correction addresses the moisture loss during the spectral collection effectively, thereby improving the predictive ability of the model. All further work reported here was performed with the exponentially corrected sample weights.

7.4.5 Noise evaluation

The quality and consistency of the spectra in the calibration and prediction sets was determined by the average root-mean-square (RMS) noise of spectra in each data set. As described in Chapter 3 (Section 3.6), this calculation was performed by taking the ratio of each pairwise combination of the three replicate single-beam spectra corresponding to a given moisture uptake level. The performance of the instrument itself was determined by the average RMS noise of air spectra for each day. This calculation was performed by taking the ratio of each pairwise combination of the replicate air spectra collected on a given day.

After taking the ratio, the resulting spectra were converted to absorbance units for the noise calculation. In this study, the spectral region from 4,800 to 4,200 cm^{-1} was used to compute the RMS noise. Systematic components in the noise spectra were removed by fitting the selected spectral region to a third-order polynomial function and computing the RMS noise in the resulting spectral residuals. Figures 7-8 and 7-8 show the average RMS noise values in each data set for the nylon and air spectra, respectively. The noise values are reported in microabsorbance units (μAU). In both plots, noise levels are consistent across the time span of the data collection. Noise levels for the air spectra match those reported previously in Chapter 6 for the same wavenumber range. The noise levels observed for the nylon spectra are higher than those reported in Chapter6. This reflects the additional reduction in transmitted light intensity caused by the presence of water on

Table 7-5. Performance of PLS calibration models based on corrected and uncorrected values of % moisture uptake

Correction method	**Wavenumber range (cm^{-1})**	**Latent variables**	**SEC [b] (%)**	**CV-SEP[c] (%)**
None[a]	4,350 – 4,000	5	0.917	1.93
Linear decay	4,650 – 4,350	6	0.902	1.13
Exponential decay	4,400 – 4,000	3	0.649	0.841

[a]No correction corresponds to assigning the average weight of the nylon piece (i.e., the average of the weights obtained at the beginning and end of the acquisition of three spectra) to each of the three replicate spectra of the nylon sample.

[b]Standard error of calibration describing standard error in predicted values of % moisture content when all spectra were included in the calculation of the model. This calculation is described in Chapter 3 (Section 3.3)

[c]Cross-validated standard error of prediction resulting from predicting moisture uptake for each calibration spectrum when it was excluded from the calculation of the model.

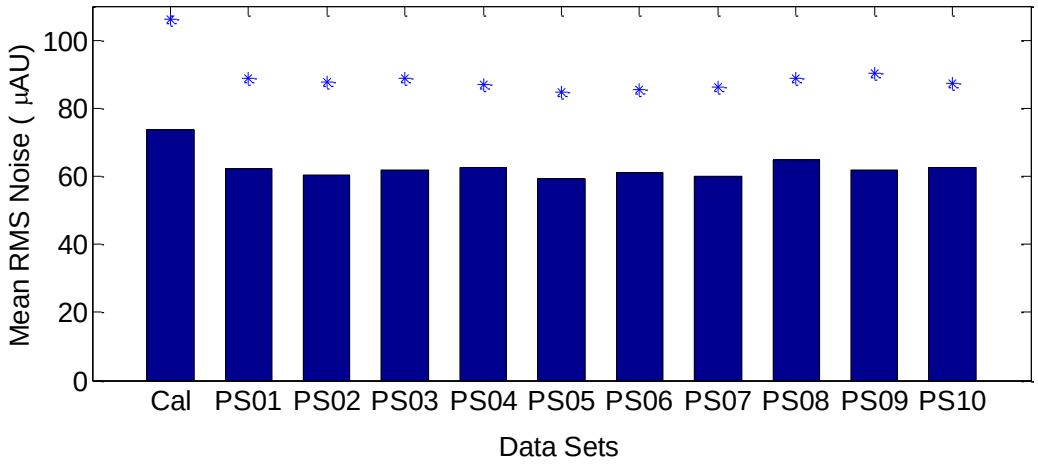

Figure 7-8. Average RMS noise values in units of microabsorbance (µAU) for nylon-6,6 spectra in each data set. The asterisks above each bar represent one standard deviation from the average. The individual data sets are described in Table 7-2.

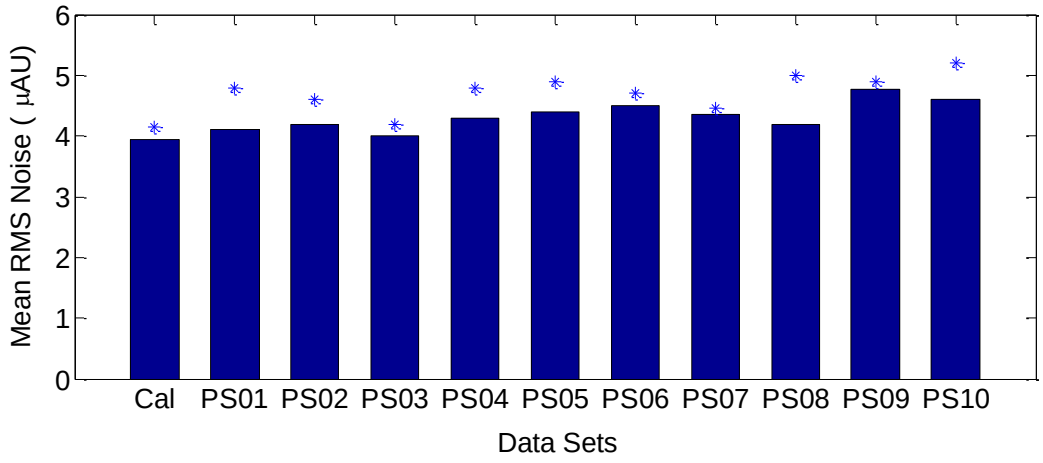

Figure 7-9. Average RMS noise values in units of microabsorbance (µAU) for air spectra collected with each data set. The asterisks above each bar represent one standard deviation from the average.

the nylon. The larger standard deviations also reflect the variation in water content across the nylon samples measured in a given data set.

7.4.6 Calibration models for moisture uptake on nylon-6,6

In order to assess the ability to predict moisture uptake on nylon-6,6 samples, PLS calibration models were generated from the SNV-normalized nylon absorbance spectra in the calibration set and then applied to the 10 prediction sets. As described previously, a cross-validation procedure based on leaving out 10% of the calibration spectra per iteration was used to guide the optimization of the wavenumber range and number of latent variables.

Two calibration models for moisture uptake were generated separately on the basis of the two methods of computing % moisture uptake (Eqs. 7-1 and 7-2). Table 7-6 summarizes the best calibration models found. The optimal wavenumber range was from 4,400 to 4,000 cm^{-1} for both models with three PLS factors. Using the % moisture uptake values in Eqs. 7-1 and 7-2, both models performed equally well with CV-SEP values of 0.649% and 0.661%, respectively.

Figure 7-10 is a score plot that illustrates the variance explained by the first two PLS factors computed from the optimized wavenumber range of the calibration spectra. The first PLS factor explains 98 % of the variance which is primarily the contribution from water itself. Figure 7-11 illustrates the PLS spectral loadings computed for the calibration models and the spectral differences between dry and wet nylon. It can be observed that the first spectral loading primarily explains the difference between dry and wet nylon and thus encodes the contribution from water.

7.4.7 Prediction performance of moisture uptake models for nylon-6,6

The long-term prediction performance of the moisture uptake models was assessed using the 10 prediction sets of nylon-6,6 spectra collected over six months. The prediction performance of the models is summarized in Table 7-7 and Figure 7-12. The standard error of prediction (SEP) values reported in the table are a reflection of the

Table 7-6. Best PLS calibration models for moisture uptake on nylon-6,6

Calculation of % moisture uptake	**Wavenumber range (cm^{-1})**	**Latent variables**	**SEC[a] (%)**	**CV-SEP[b] (%)**
Method 1 (Eq. 7-1)	4,400 – 4,000	3	0.649	0.841
Method 2 (Eq. 7-2)	4,400 – 4,000	3	0.661	0.874

[a]Standard error of calibration describing standard error in predicted values of % moisture content when all spectra are included in the calculation of the model. This calculation is described in Chapter 3 (Section 3.3)

[b]Cross-validated standard error of prediction resulting from predicting moisture uptake for each calibration spectrum when it is excluded from the calculation of the model.

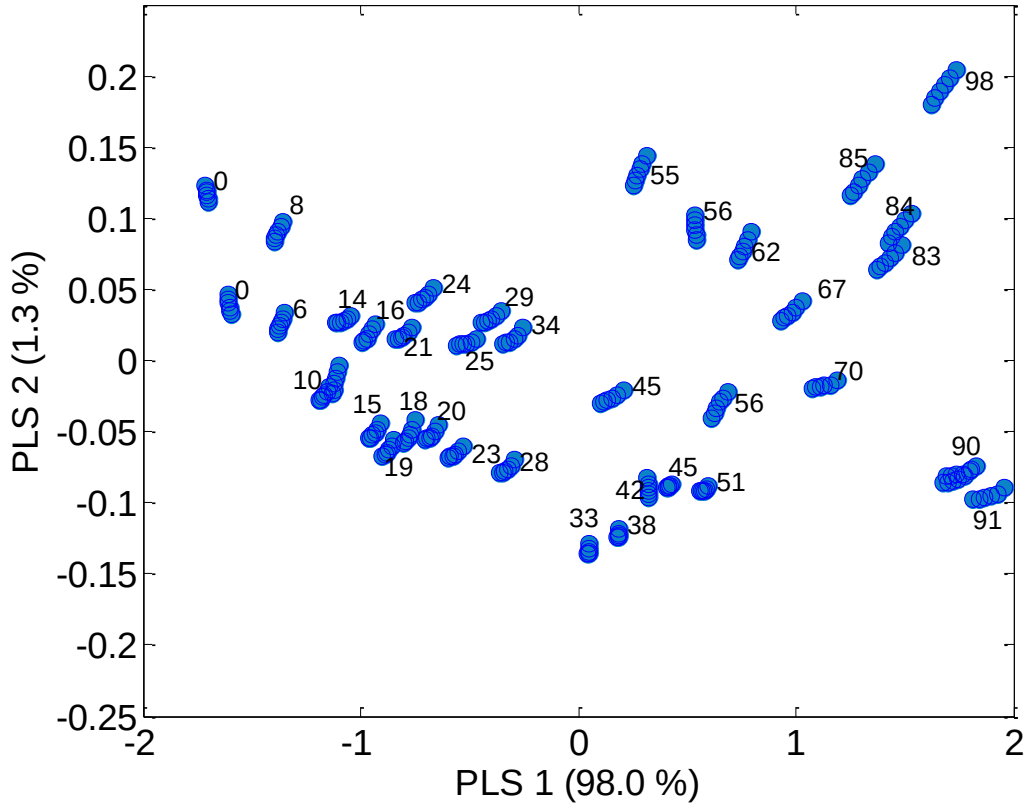

Figure 7-10. Partial least-squares score plot for factors 1 and 2 of nylon-6,6 spectra used in the calibration model. Data labels are % moisture uptake values. More than 99 % of the variance in the calibration data matrix is explained by the first two PLS latent variables.

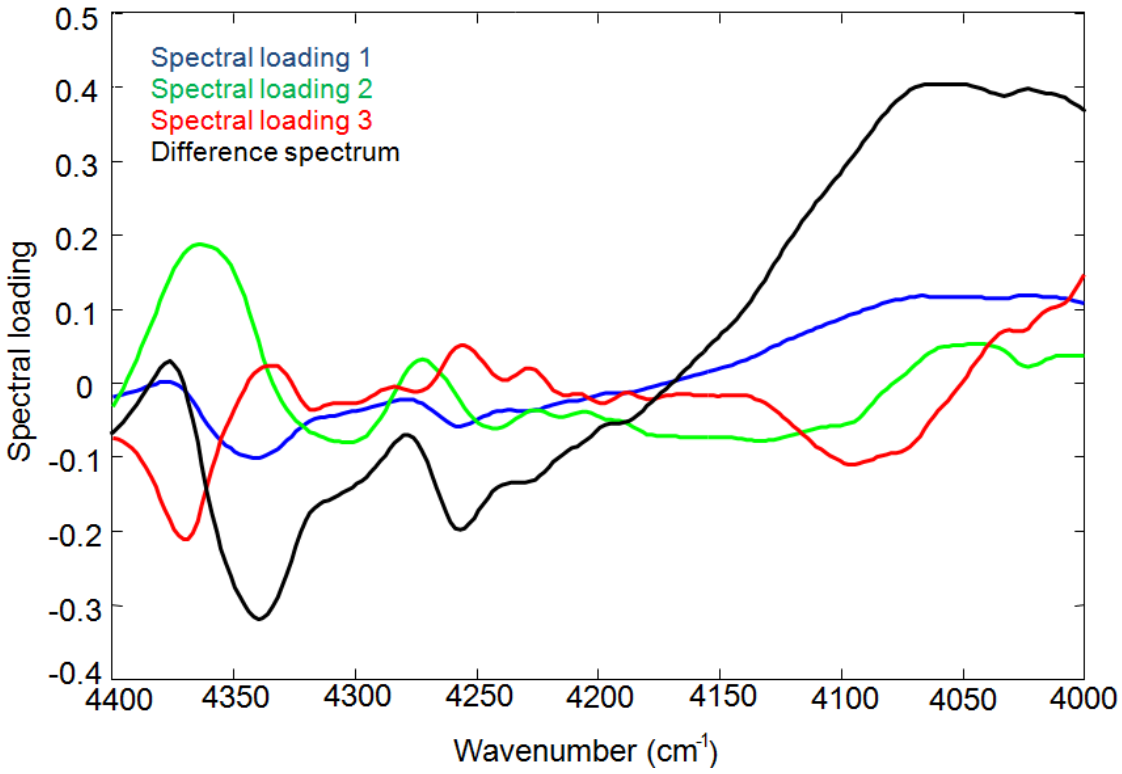

Figure 7-11. Spectral loadings of the PLS calibration model for moisture uptake. The black trace represents the difference spectrum of saturated and dry nylon spectra. Similarity in overall shape between the blue and black traces suggests that the first spectral loading is largely responsible for modeling the spectral changes induced by the presence of water.

standard deviation in the residuals (errors) between predicted and assigned (i.e., weight-based) values of % moisture uptake. These SEP values must be considered in the context of the 0 (dry) to 100% (saturated) range of the % moisture uptake values and the absolute error of roughly ±1% in the assigned values.

Both calibration models gave good prediction results (SEP values ranging from 0.958 to 2.09%) which is indicative of the robustness of the models with time. These low SEP values also confirm the ability of the models to predict moisture uptake across different sheets of nylon-6,6 polymers. While there is a gradual increase in SEP with time, we consider a 2% or smaller absolute error in % moisture uptake over six months to be a result good enough for practical use.

Figure 7-13 is a plot of PLS scores computed from the calibration spectra and prediction sets PS03, PS05, PS07 and PS10. Only five sets of prediction spectra were represented in the figure for purposes of clarity. This plot illustrates the good clustering of the nylon-6,6 calibration and prediction spectra, confirming the similarity in spectral shapes across the time span of the data collection. This helps to explain the excellent prediction performance of the calibration models with time.

Figure 7-14 displays correlation and residual plots for the spectra used in generating the calibration model for moisture uptake of nylon-6,6. Figures 7-15 through 7-17 present the corresponding plots for a selected subset of the prediction sets. All of these figures are based on % moisture uptake values calculated using Eq. 7-1. Figure 7-14A shows a good correlation between the reference % moisture uptake values and estimated values for the calibration data. The residual plot in Figure 7-14B shows randomly distributed residuals from the calibration model. As seen in Figures 7-15 to 7-17, the prediction sets exhibited good correlations and random residuals. However, as the time span increases relative to the calibration data (Figure 7-17), both correlation and residual plots exhibit some degradation in the model performance.

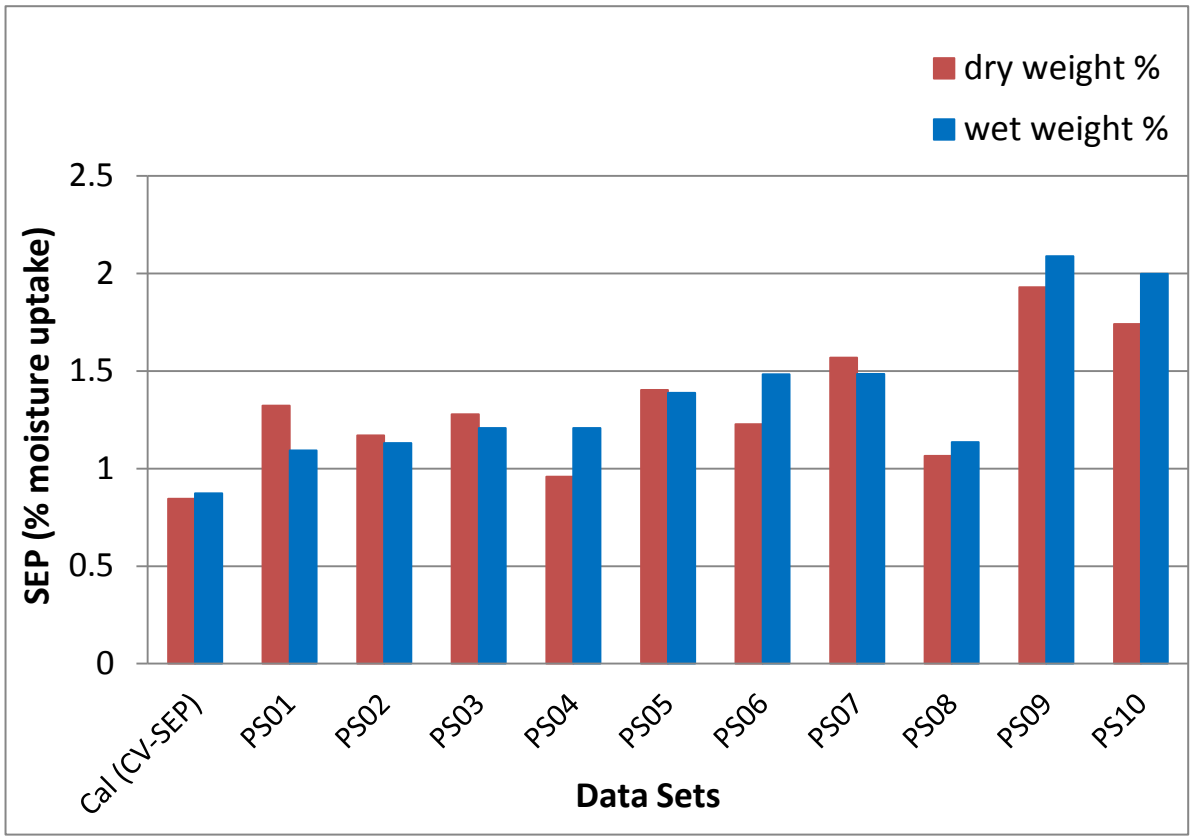

Figure 7-12. Prediction performance of PLS calibration models for moisture uptake on nylon-6,6. Consistent performance is noted between the two methods for computing moisture uptake.

Table 7-7. Prediction performance of PLS calibration models for moisture uptake on nylon-6,6.

Data set	**Method 1**[a] **SEP (%)**	**Method 2**[a] **SEP (%)**
Calibration[b]	0.841	0.874
PS01	1.32	1.09
PS02	1.17	1.13
PS03	1.28	1.21
PS04	0.958	1.21
PS05	1.40	1.39
PS06	1.23	1.48
PS07	1.57	1.48
PS08	1.06	1.14
PS09	1.93	2.09
PS10	1.74	2.00

[a]Methods 1 and 2 correspond to the use of Eqs. 7-1 and 7-2, respectively, for the calculation of values of % moisture uptake.

[b]Results reported for the calibration data are CV-SEP values.

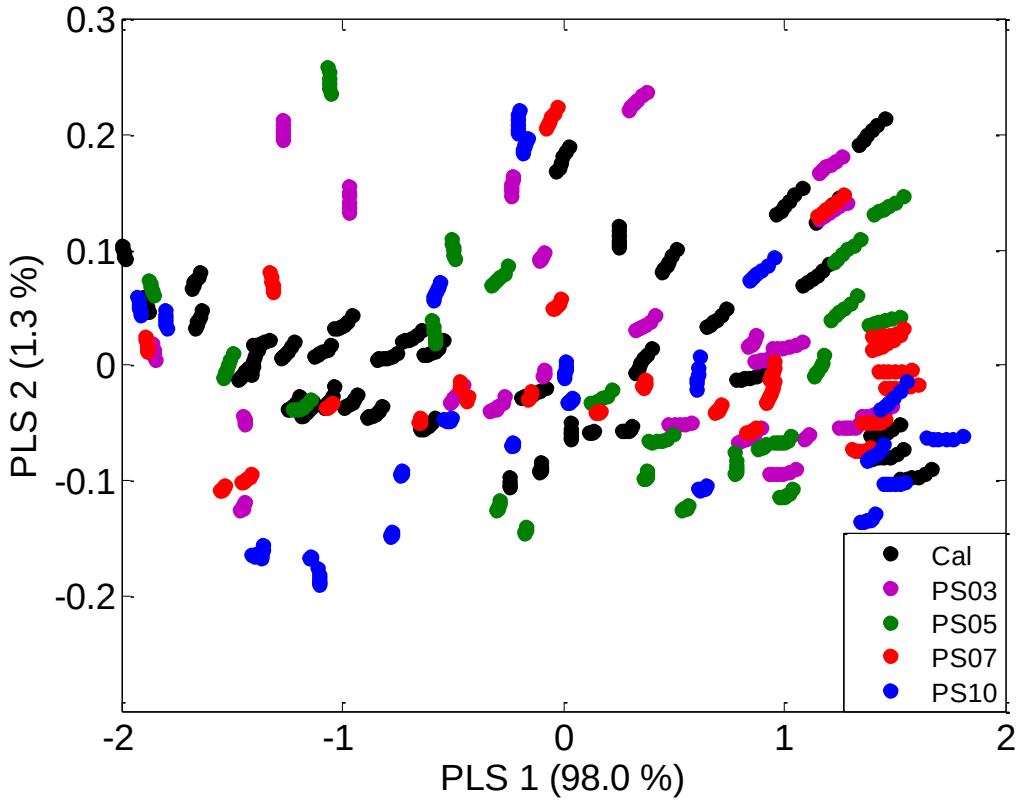

Figure 7-13. Plot of PLS scores along factors 1 and 2 corresponding to the calibration data and the data from prediction sets PS03, PS05, PS07, and PS10. These factors account for greater than 99% of the data variance. Good overlap is observed between the calibration and prediction data sets.

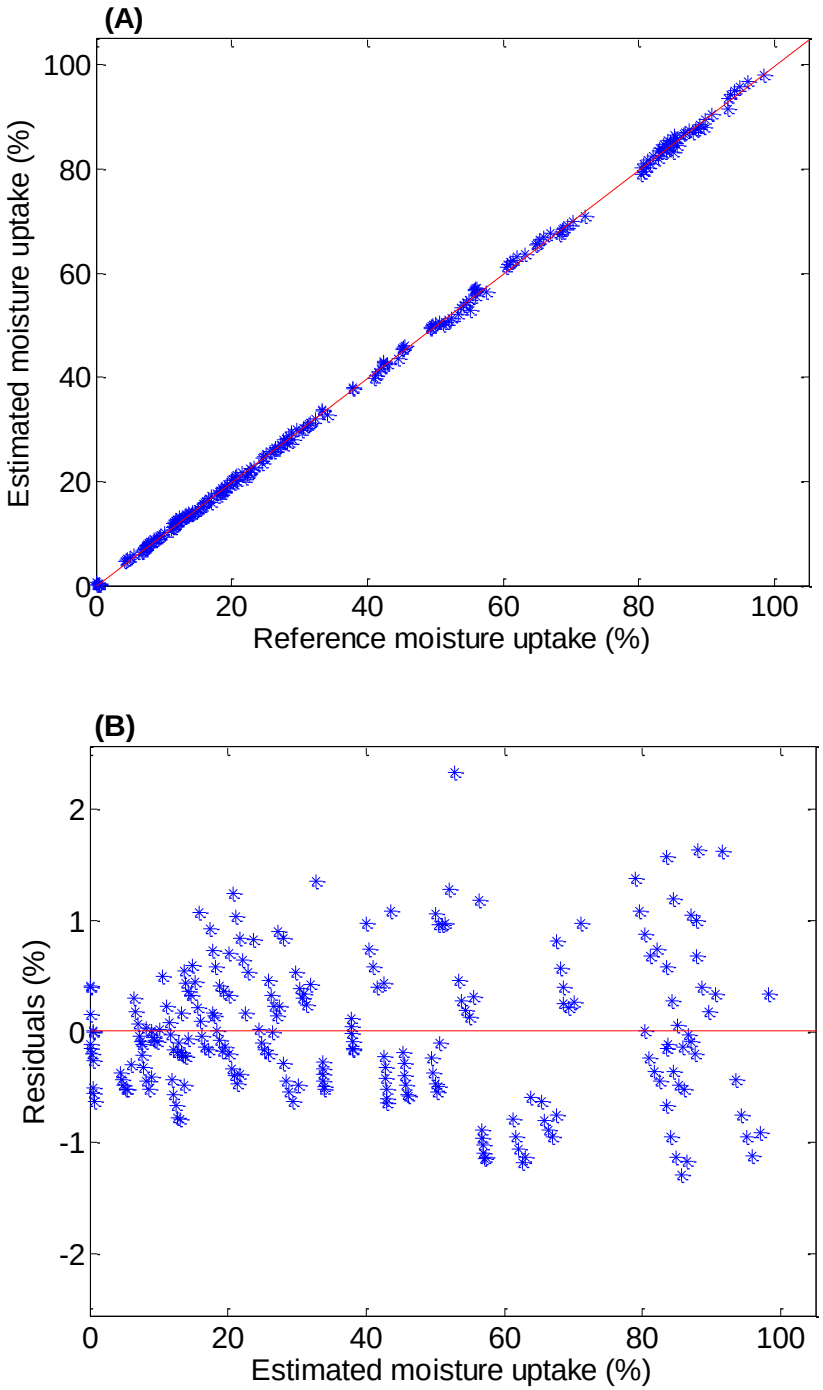

Figure 7-14. Correlation and residual plots for calibration. **(A)** Correlation and **(B)** residual plots for the spectra used in generating the calibration model for moisture uptake of nylon-6,6. The red lines in panels A and B correspond to perfect correlation between estimated and reference values of % moisture uptake and residuals of 0.0 %, respectively.

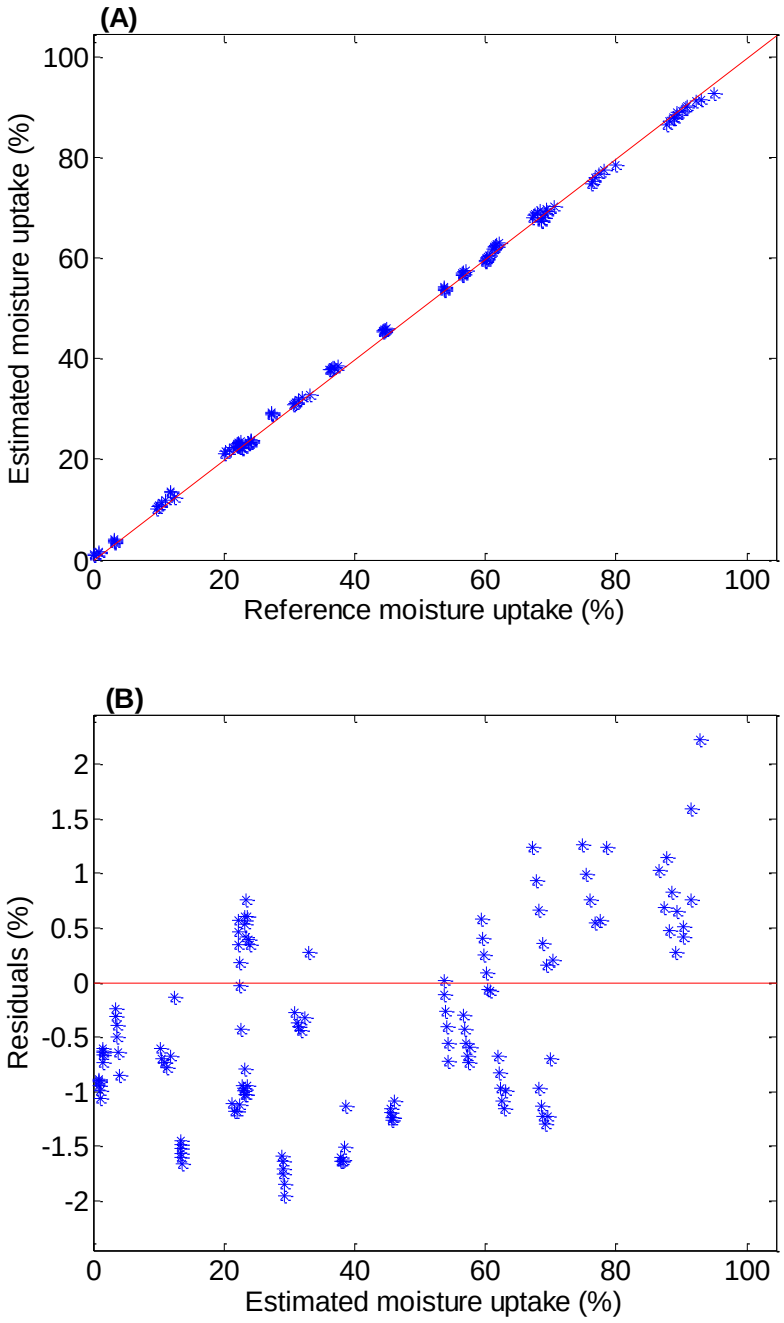

Figure 7-15. Correlation and residual plots. **(A)** Correlation and **(B)** residual plots for % moisture uptake in prediction set PS04. The red lines in panels A and B correspond to perfect correlation between estimated and reference values of % moisture uptake and residuals of 0.0 %, respectively.

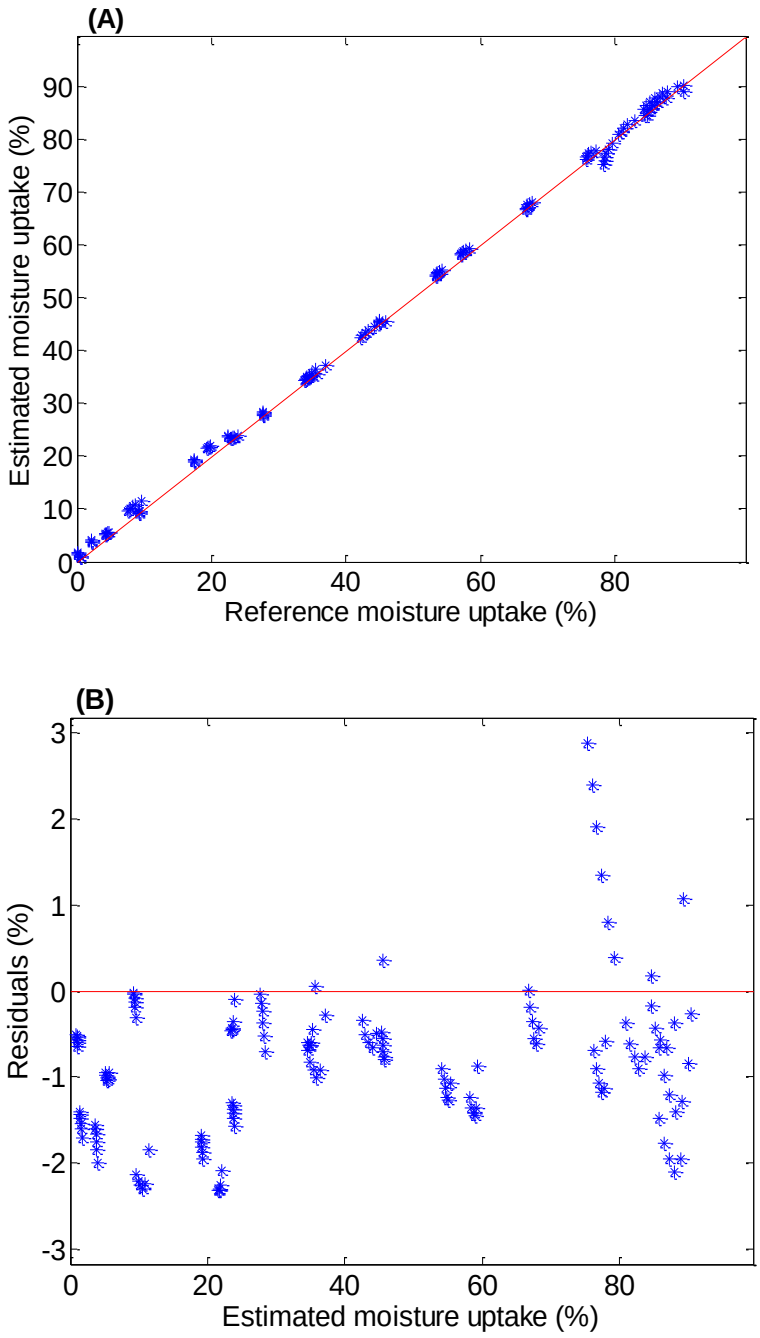

Figure 7-16. Correlation and residual plots. **(A)** Correlation and **(B)** residual plots for % moisture uptake in prediction set PS06. The red lines in panels A and B correspond to perfect correlation between estimated and reference values of % moisture uptake and residuals of 0.0 %, respectively.

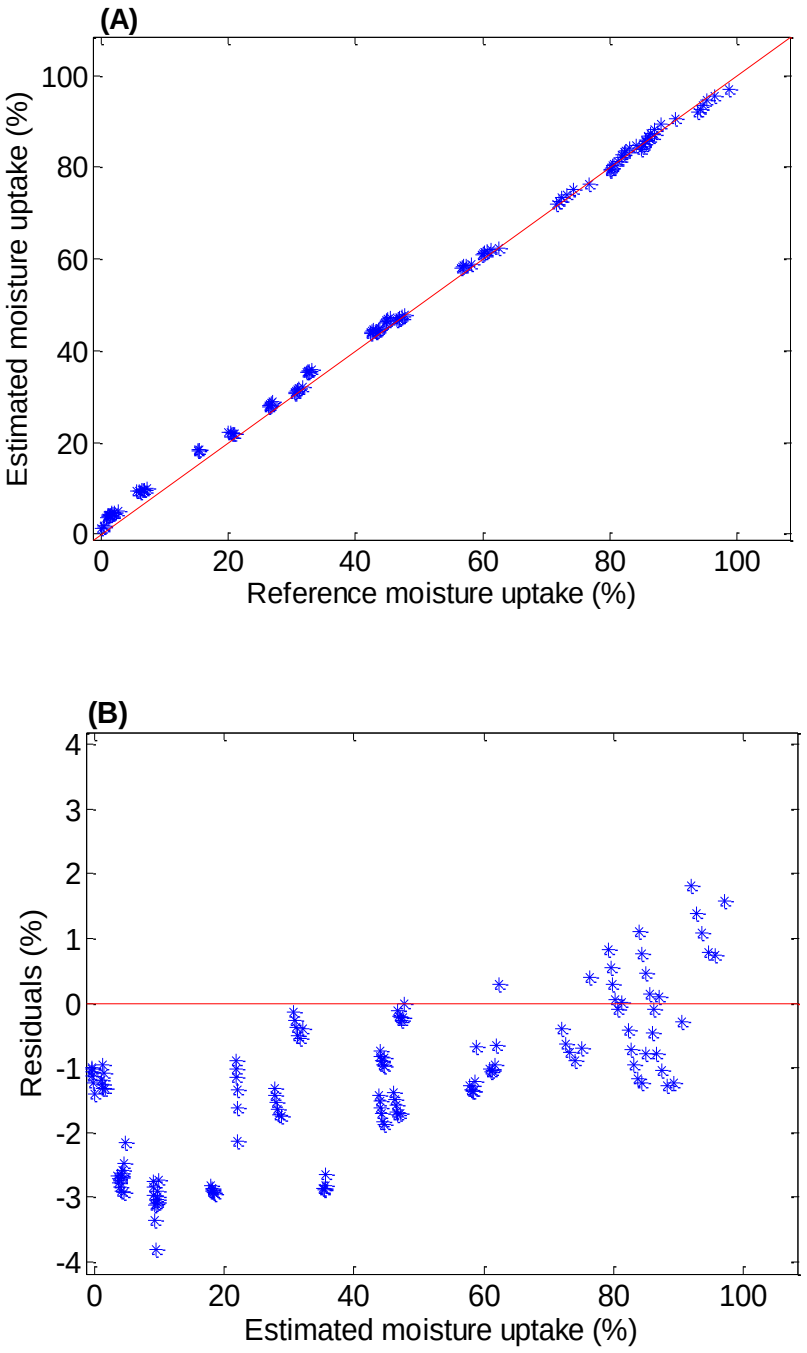

Figure 7-17. Correlation and residual plots. **(A)** Correlation and **(B)** residual plots for % moisture uptake in prediction set PS10. Some bias is evident in both plots. The red lines in panels A and B correspond to perfect correlation between estimated and reference values of % moisture uptake and residuals of 0.0 %, respectively.

7.5 Conclusions

Experimental results obtained in this study clearly indicate the reversible nature of moisture uptake of nylon and its dependence on the percentage relative humidity of the environment as explained in previous studies. Experimental results also demonstrate that commercially available nylon-6,6 polymers are capable of absorbing up to an average of 8-10 % of water (relative to their dry weight) upon saturation.

The amount of moisture loss during the spectral data collection was explained in terms of an exponential decay correction. This proposed exponential decay correction was able to addresses the moisture loss during the spectral acquisition effectively, thereby improving the predictive ability of the computed quantitative models for moisture uptake.

The combination of spectral preprocessing by the SNV transform and PLS regression was utilized successfully in developing calibration models to determine the moisture content of nylon-6,6 polymers directly from their NIR spectra. Two calculation methods were used to determine the moisture uptake percentage of a given piece of nylon at a given time. Both methods performed equally well, providing CV-SEP values of 0.841% and 0.874% respectively. These moisture models are primarily based on the amount of water that is absorbed by the nylon. This was evident from the first PLS factor (98.01% variance explained) which mainly explained the contribution from water.

The long-term predictive performance of these moisture models was assessed using 10 prediction sets of nylon-6,6 spectra at different moisture levels spanning a time period of six months. The SEP values obtained for these prediction sets ranged from 0.958 % to 2.09 %, with an average ± standard deviation of 1.4 ± 0.3 %. These models were successful in predicting the moisture uptake across different sheets of nylon-6,6 polymers. It was also observed that the performance of both models deteriorated slightly in PS09 (18 weeks) and PS10 (23 weeks).

When compared to existing techniques, (TGA, DSC, LOD etc.), NIR spectroscopy combined with PLS regression provides a reliable and fast method to

determine the moisture content of a given nylon polymer. This methodology could be easily integrated with on-line analyses. This method can be applied to reasonably thick polymer sheets (e.g., in the mm range) as opposed to methods based on mid-infrared spectroscopy.

The methodology developed in this work is not limited to nylon-6,6 polymers, but could be applied to other nylon polymers as well since all nylon polymers contain the amide linkage which is responsible for absorbing moisture. Furthermore, the methodology could be extended to other condensation polymers such as polyesters since they contain an ester linkage that follows a similar mechanism of moisture uptake as polyamides.

CHAPTER 8

INVESTIGATION OF MOISTURE UPTAKE AND YELLOWING OF NYLON-6,6 POLYMER USING INFRARED MICROSCOPY

8.1 Introduction

Fourier transform infrared microscopy (FTIR microscopy) combines FTIR spectrometry with microscopic analysis in order to obtain chemical information from samples which are very small (physical dimensions in the range of 10 to 500 μm).[1,4,12,13,90,93] Fourier transform IR microscopes were first manufactured in the 1980's and the technique has become very useful and popular in many fields since then.[1,4,12,13]

Successful applications of FTIR microscopy can be found in clinical chemistry, earth sciences, forensic sciences, archeology, and the polymer, textile and electronics industries.[4,12,13,90,93] As examples, Zhang et al. used FTIR microscopic imaging in combination with cluster analysis and artificial neural networks to classify cancer cells among human breast cells.[91] Alexeeva et al. used FTIR microscopy to analyze rat skin tissue heterogeneity in noninvasive glucose sensing measurements.[92] Yang et al. reported the use of FTIR microscopy in kinetic analysis of thermal oxidation of metallocene cyclic olefin copolymer composites.[96] Chalmers et al. and Sahlin et al. described the use of specular reflectance and near-field FTIR imaging methods to improve spatial resolution in polymer characterization studies.[94,95]

Fourier transform infrared microscopes can be equipped with either single-channel or multichannel detectors. A single-channel detector records the IR intensity for a single location on the sample, while a multichannel detector consists of an array of individual detector elements that can simultaneously (i.e., at the speed of the sampling electronics) record separate intensities across a grid of locations on the sample. Use of a

multichannel detector eliminates the need for translating the sample to acquire an image.[4,12,13] Multichannel detectors used in FTIR microscopy are termed focal plane array (FPA) detectors because the two-dimensional detector array is positioned in the focal plane of the microscope.[4,12,13] Infrared microscopes can operate in both transmittance and reflectance modes depending on the nature of the sample. A visible light beam and associated imaging detector is also used to visually locate the sample to be studied with the IR beam.[4,12] A detailed discussion about the principles of FTIR microscopy and FPA detectors is provided in Chapter 2 (Section 2.6).

The research presented in this chapter is an extension from that of Chapters 6 and 7. In Chapter 6, a signal preprocessing method combining the standard normal variate (SNV) transform and the discrete wavelet transform (DWT), followed by partial least-squares (PLS) regression was utilized to develop calibration models to determine temperatures of a given piece of nylon-6,6 polymer directly from its near-infrared (NIR) transmission spectrum. Good prediction results were obtained across three different nylon pieces. However, one piece of nylon (nylon piece C) gave high values of the standard error of prediction (SEP) (average SEP: 2.23 °C) when compared to the other two pieces of nylon (average SEP: 1.19 °C). It was hypothesized that this might be due to the inhomogeneous nature of different sheets of nylon at a microscopic level.

In a closer inspection, nylon sheets show different surface features. These could be a result of the molding and processing procedures employed to create them. Figure 8-1 represents the three nylon-6,6 pieces (B, C, D in Table 6-3) used for testing the temperature model developed in Chapter 6. These images were obtained using a polariscope (Nortel Manufacturing Ltd., Toronto, Canada) in order to easily visualize the features.

It was also observed that nylon pieces developed a yellow coloration with time and this yellowing phenomenon was accelerated by the heating involved in the experiments associated with temperature modeling. Figure 8-2 represents two nylon-6,6

pieces obtained from the same sheet. One of these pieces (1) was subjected to temperatures of ~100 °C overnight while the other piece (2) was exposed to ambient temperature conditions in the laboratory. It can be seen that in Figure 8-2, nylon piece 1 has developed a considerable amount of yellow color due to heating.

Several theories have been discussed regarding the origin and effect of yellowing in nylon polymers.[67,86,99,100] Thermal degradation of nylon polymers usually occurs via a free radical mechanism.[67,86,99,100] These radicals can be free carbonyl radicals or free methylene radicals. Once generated, these radicals continue on more radical attacks that leads to bond scissions and rearrangements of hydrocarbon polymer chains. Common products of such radical reactions are ring structures such as cyclopentanone and small hydrocarbon chains.[86,99] It is reported that the yellow coloration is a likely indication of the production of a conjugated structures due to structural rearrangements. This process leads to loss of crystalanity.[99]

In Chapter 7, a combination of spectral preprocessing by the SNV transform and PLS regression was utilized successfully in developing calibration models to determine the moisture content of nylon-6,6 polymers directly from their NIR spectra. These moisture uptake models provided good prediction results across different nylon pieces. Moreover, experimental results obtained in this study clearly indicate the reversible nature of moisture uptake of nylon-6,6 and its dependence on the percentage relative humidity of the environment as explained in previous studies. In the work described here, this observation was examined further in an attempt to understand the moisture uptake process at a microscopic level.

The research presented in this chapter involved a series of very preliminary investigations conducted with FTIR microscopy to study the moisture uptake patterns and yellowing of nylon-6,6 polymers at a microscopic level. In addition, thermogravimetric analysis (TGA) was used to provide further insight into the moisture uptake process as TGA studies are widely employed in determining moisture uptake of polymers.[80,98] While

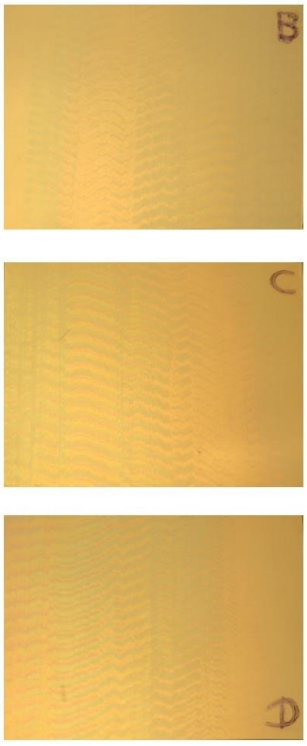

Figure 8-1. Features of nylon-6,6 pieces observed under polarized light.

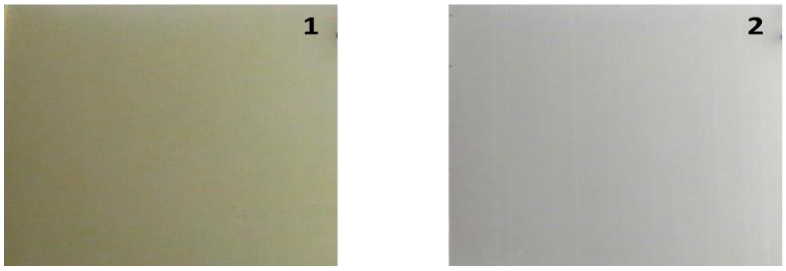

Figure 8-2. Yellowing of nylon-6,6. **(1)** Yellowed nylon piece upon exposure to a temperature of 100 °C overnight. **(2)** No yellow coloration is developed in the nylon piece which is exposed to ambient laboratory conditions.

this work remains in its initial stages, it is included in this dissertation to provide formal documentation of the research such that future studies are facilitated.

8.2 Experimental design

8.2.1 Apparatus and reagents

The experimental work described in this chapter consisted of measurements performed with a thermogravimetric analyzer and an IR imaging system. The instrument used for the TGA measurements was a TA Model Q500-0305 (TA Instruments, New Castle, DE). All IR images were acquired with a Hyperion 3000 IR Microscope (Bruker Optics, Inc., Billerica, MA) combined with a Bruker Vertex 70 (Bruker Optics, Inc.) Fourier transform (FT) spectrometer configured with a globar source (U-shaped silicon carbide rod), a potassium bromide (KBr) beam splitter and a liquid nitrogen cooled focal plane array (FPA) detector configured with 128×128 mercury cadmium telluride (MCT) detector elements. A gold coated micro-slide (Thermo Electron Corporation, Madison, WI) was used as the background reference throughout the data collection. A 15× objective was used to magnify the samples and a 340×340 μm^2 sample area with a pixel resolution of 2.7 μm was studied at a given time. All the IR imaging data were collected in the reflectance mode at a frame rate of 1,610 Hz and an integration time of 0.120750 ms. Visible images were collected with a SONY EXWAVEHAD color digital video camera integrated into the Hyperion 3000 microscope.

Commercially obtained nylon-6,6 samples (McMaster-Carr, Elmhurst, IL) were employed in all the measurements described here. A Mettler AE200 analytical balance (Mettler-Toledo, Inc., Columbus, OH) was used to obtain all weight measurements. A Fisher Scientific Isotemp Model 655G oven (Fisher Scientific, Pittsburgh, PA) was used for heating purposes.

8.2.2 Procedures

Thermogravimetric (TGA) analysis was initially performed to assess water uptake in nylon. Fourteen pieces of nylon-6,6 with an average weight of 10.0 ± 0.1 mg and an

average thickness of 0.40 ± 0.01 mm were dried in the oven to remove any moisture and subsequently weighed. They were then treated with different moisture uptake/loss methods which included soaking in water, placing in a humidity chamber, exposing to ambient temperature and relative humidity conditions in the laboratory and drying in the oven. Table 8-1 summarizes the procedure for this experiment.

After obtaining a constant weight for each nylon piece, they were then introduced individually into the TGA instrument. The temperature range analyzed in these experiments was from 20 to 600 ^{o}C with a linear ramp of 5.00 ^{o}C / min. The composition of the purge gas used with the TGA was 19 to 23% O_2 in N_2. Once the nylon piece was completely decomposed, the first derivative of the trace of mass loss (peak centered at 100 °C) with temperature was computed to calculate the % mass loss due to evaporation of water. The software controlling the instrument was used to perform these calculations.

To assess the effect of the thickness of the nylon samples on the results, the TGA measurements were repeated with twelve additional pieces of nylon-6,6 with an average weight of 9.0 ± 0.1 mg and an average thickness of 0.30 ± 0.01 mm. The same experimental methods and procedures described above were used.

Infrared imaging measurements were then employed to study the moisture uptake patterns of nylon-6,6 polymers**.** Two pieces of nylon-6,6 (N_1 and N_2) were used in the spectral data collections. These nylon samples were cut from two different commercially available sheets of nylon-6,6 polymer. The average dimensions of the two nylon pieces were 35×30×0.40 ± 0.01 mm. All the spectral data collections were performed at ambient temperature and relative humidity conditions (~21 – 22 °C, ~30 % RH). These nylon pieces were dried in the oven prior to the experiment to remove any residual moisture. Weights of the two nylon pieces (N_1 and N_2) at 0 % moisture uptake were 0.2523 and 0.2418 g, respectively. These nylon pieces were then exposed to moisture by placing them in a humidity chamber. As the nylon pieces were absorbing moisture, FTIR microscopic data were collected at eight different moisture uptake values. Table 8-2

summarizes the levels of moisture uptake by each nylon piece. Moisture uptake percentages were computed as described in Chapter 7 (Eq. 7-1). A limitation of this study was that the IR images were collected consecutively with increasing moisture content rather than by randomizing moisture content with respect to the order of data collection.

For each of the 128×128 detector pixels, the raw data consisted of 128 co-added double-sided interferograms containing 1,184 points collected at every zero crossing of the helium-neon (He-Ne) reference laser (15,800.45 cm^{-1}). Interferograms were sampled in rapid-scan mode and collected on both forward and backward scans of the moving mirror. The nominal spectral resolution was 16 cm^{-1} and an aperture setting of 6 mm was used. Collection and Fourier processing of one image (i.e., one set of 128×128 spectra) required approximately 20 minutes.

All interferograms were Fourier processed to single-beam spectra by use of the Bruker Opus software controlling the spectrometer (Version 5.5, Bruker Optics, Inc.). The single-beam spectra were computed with a point spacing of 5.1428 cm^{-1} by applying two levels of zero filling, Blackmann-Harris 3-Term apodization and Mertz phase correction. After Fourier processing, spectra were truncated to 3,990 to 946 cm^{-1}. Further calculations were performed with Matlab (Version 7.4, The Mathworks, Inc., Natick, MA) on a Dell Precision 670 workstation (Dell Computer Corp., Round Rock, TX) operating under Red Hat Linux WS, (Version 5.2, Red Hat, Inc., Raleigh, NC).

Before analysis of the IR images was attempted, the sets of 128×128 single-beam spectra of the nylon samples (collected in reflectance mode) were converted to relative reflectance (R) by taking the ratios to the corresponding set of 128×128 single-beam background spectra acquired from the gold slide. These background spectra were obtained at the beginning of each data collection. All spectra were then converted to pseudo-absorbance units ($\log_{10}(1/R)$) and normalized by use of the standard normal variate (SNV) transform. The SNV transform was described previously in Chapter 3 (Section 3.2.1).

Table 8-1. Moisture uptake methods employed in the TGA analysis

Number of nylon-6,6 pieces	Method of moisture uptake/loss
3	Soaked in water
3	Placed in humidity chamber
5	Exposed to relative humidity conditions in the laboratory
3	Dried in oven

Table 8-2. Levels of moisture uptake by nylon pieces used in infrared imaging studies

Percentage moisture uptake levels studied (%)[a]	
N_1(sheet 1)	N_2 (sheet 2)
0	0
11	12
22	21
30	42
47	51
64	70
78	79
88	88

[a]Values obtained with Eq. 7-1.

For each nylon piece, two imaging points were selected. These were identified as $N_{1,1}$ and $N_{1,2}$ for nylon piece N_1 and $N_{2,1}$ and $N_{2,2}$ for nylon piece N_2. For nylon piece, N_1, three consecutive (replicate) images were collected at each level of moisture uptake. A single replicate was collected for each level of moisture uptake with nylon piece, N_2.

Figure 8-3 summarizes the visible images of the four selected points of interest. Moisture uptake was assessed by weighing the nylon piece before and after exposure to water. The percentage moisture uptake of a given piece of nylon at a given time was calculated as described previously using Eq. 7-1.

To study the yellowing of nylon-6,6 polymers, one piece of nylon-6,6 (N_3) was used in the spectral data collections. The dimensions of the nylon piece were 45×40×0.40 ± 0.01 mm. All the spectral data collections were performed at ambient temperature and relative humidity conditions (~21 – 22 ℃, ~31% RH). The nylon piece was dried in the oven prior to the experiment to remove any residual moisture. The weight of the nylon piece (N_3) at 0 % moisture uptake was 0.3252 g. This nylon piece was then heated in the oven at four different temperatures (85, 120, 150 and 180 ℃ respectively). As the nylon piece was developing the yellow color, FTIR microscopic data were collected at the four levels of yellow coloration. The same data collection procedures described above was used. One imaging measurement was taken at each temperature condition. There was no randomization of the temperature conditions and the order of data collection.

Table 8-3 summarizes the hues of yellow developed by the nylon piece at each temperature. For this nylon piece, only one imaging point was selected. This was identified as $N_{3,1}$ and Figure 8-3E displays the visible images of the selected point of interest. The point of interest was an artificially made scratch that was placed in the nylon to facilitate both locating the imaging position and observing any acceleration in degradation.

Table 8-3. Temperatures used in the yellowing study and the degree of coloration developed by the nylon piece with increasing temperature

Temperature (°C)	Weight (g)	Color
85	0.3252	White
120	0.3251	Light yellow
150	0.3246	Yellow
180	0.3220	Light brown

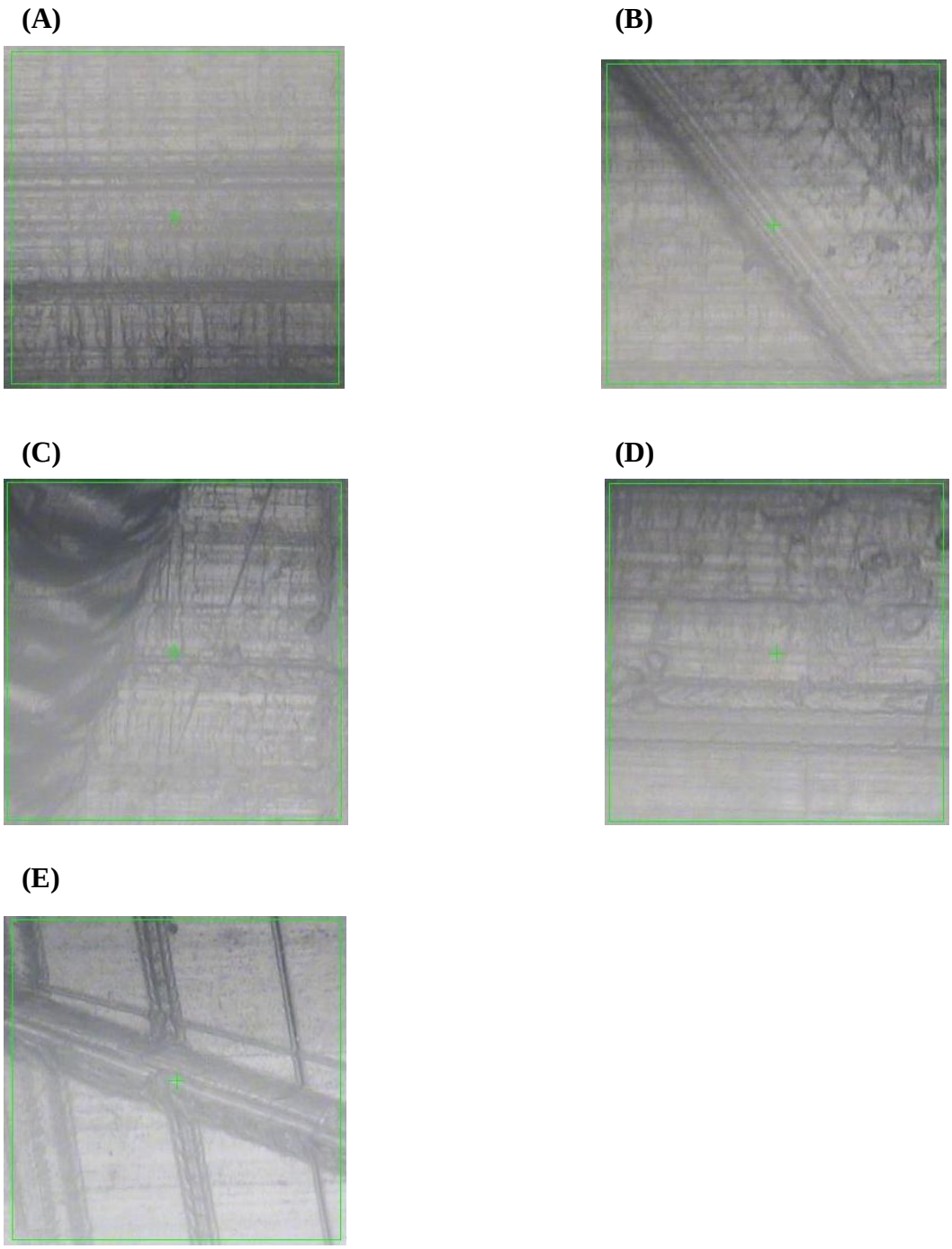

Figure 8-3. Visible images of the four selected points of interest of the two nylon pieces used in the moisture uptake experiment and visible image of the nylon piece used in the yellowing experiment. **(A)** $N_{1,1}$ **(B)** $N_{1,2}$ **(C)** $N_{2,1}$ **(D)** $N_{2,2}$ **(E)** $N_{3,1}$

8.3. Results and Discussion

8.3.1 Moisture uptake patterns of nylon-6,6 determined from TGA measurements

Nylon-6,6 polymers are hygroscopic in nature. Chapter 7 discusses this phenomenon in detail. According to Figure 7-1, hydrogen bonding between water molecules and the amide linkage in nylon polymers are responsible for their hygroscopic nature. According to the experimental results documented in Section 7.4.2, moisture uptake is reversible and directly dependent on the percentage relative humidity (% RH) of the environment. This observation suggests that the degree and stability of hydrogen-bonding should in turn be dependent on the percentage relative humidity of the environment.

The TGA measurements were used to test this hypothesis. Figure 8-4 provides an example TGA curve obtained for a nylon-6,6 piece with a thickness of 0.40 ± 0.01 mm. The green trace represents the % mass loss and the blue trace represents the first derivative of mass loss (% per °C). In both traces, mass loss around 100 °C is attributed to moisture loss and mass loss around 400 °C is attributed to the decomposition of nylon itself.

Figure 8-5 summarizes the first derivative of mass losses for the fourteen nylon-6,6 pieces used in the initial TGA measurements. The temperature axis is truncated at 250 °C to enhance the peak around 100 °C which is responsible for the moisture loss from the nylon pieces. According to these results, it is observed that the three dried nylon pieces show no evidence of moisture loss. For the five nylon pieces exposed to relative humidity conditions in the laboratory, a maximum moisture loss is indicated around 120 °C. The amount of moisture uptake is between 2-3 % by dry weight of nylon which is in accordance with moisture uptake values typically obtained in the laboratory conditions reported in Chapter 7.

For the three nylon pieces exposed to the humidity chamber, a maximum moisture loss is indicated around 103 °C. The amount of moisture uptake is between 9-10 % by dry

weight of nylon. For the three nylon pieces soaked in water, a maximum moisture loss is indicated around 100 °C. The amount of moisture uptake is again between 9-10 % by dry weight of nylon which is in accordance with the moisture uptake values typically obtained for nylon-6,6 polymers as reported in Chapter 7.

Results obtained with the nylon pieces of 0.30 mm thickness were similar to those displayed in Figure 8-5. These results are summarized in Figure 8-6. Differences in the temperature at which the maximum moisture loss was observed indicate a pattern in moisture uptake on nylon. It can be hypothesized that the nature of hydrogen-bonding observed at ambient conditions is stronger than that of hydrogen-bonding observed at saturated conditions. It could also be that at saturation, additional water molecules add up as a layer by making hydrogen bonds with an existing layer of water molecules. A third possibility is that water molecules are displacing nylon molecules, causing swelling of the matrix as suggested previously.[71] In order to further examine these possibilities at a microscopic level, FTIR microscopy was employed.

8.3.2 Fourier transform infrared microscopic studies of nylon-6,6 polymers

The collected sets of IR spectra were analyzed in an attempt to gain further insight into the patterns of moisture uptake on nylon-6,6. An evaluation of the overall spectral quality was performed first, followed by the generation and analysis of images created from the IR data.

8.3.2.1. Noise evaluations

The quality and consistency of the spectra were determined by the average root-mean-square (RMS) noise of spectra collected in each experiment. This calculation was performed by taking the ratio of each pairwise combination of the three replicate single-beam spectra collected at each image pixel for each measurement with nylon piece, N_1. The performance of the instrument itself was determined by the average RMS noise computed from the single-beam reflectance spectra of the gold background. This

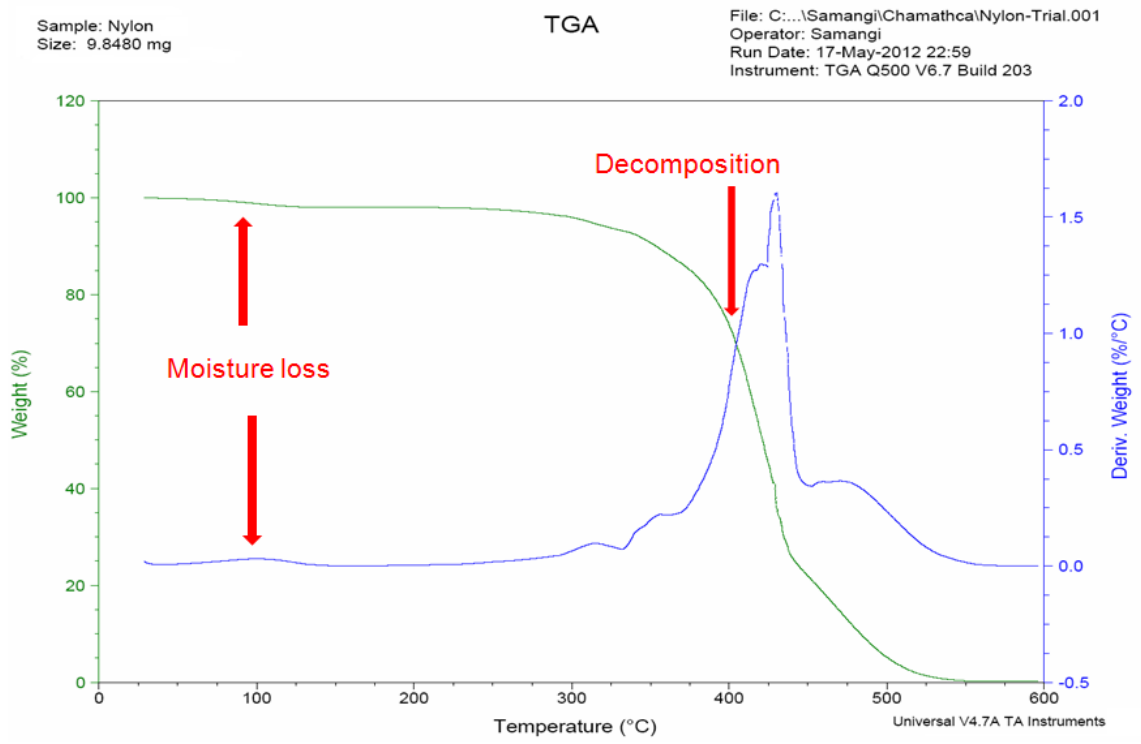

Figure 8-4. An example TGA curve obtained for a 0.40 ± 0.01 mm thick nylon-6,6 piece.

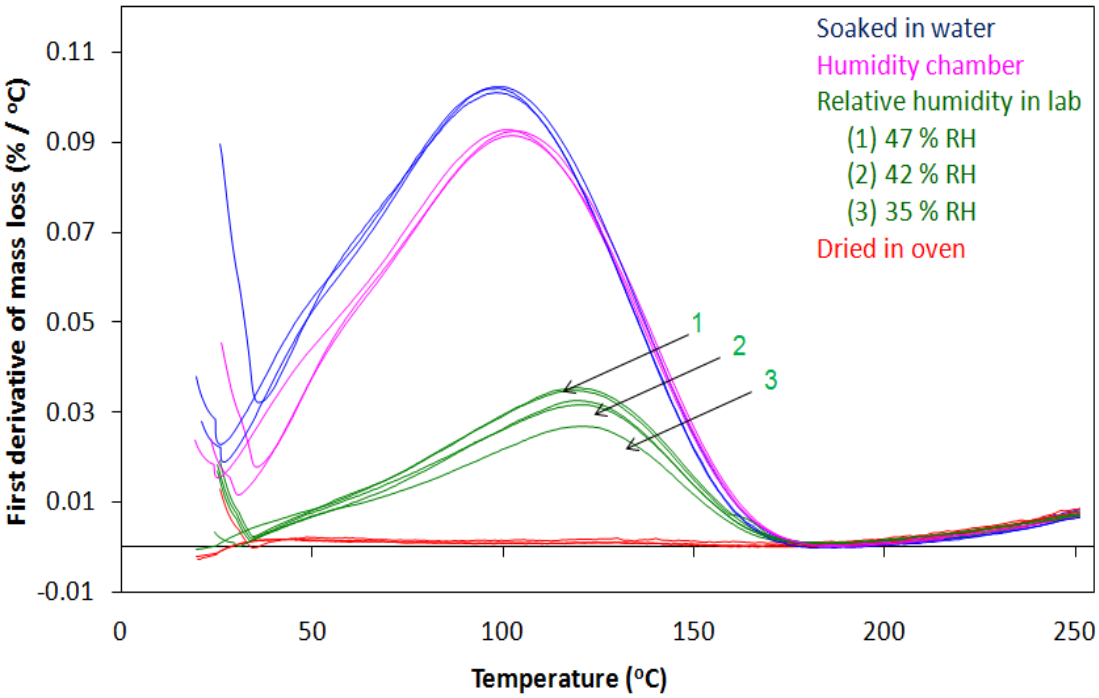

Figure 8-5. The first derivative of mass losses from the TGA analysis for the 14 nylon-6,6 pieces with 0.40 ± 0.01 mm thickness.

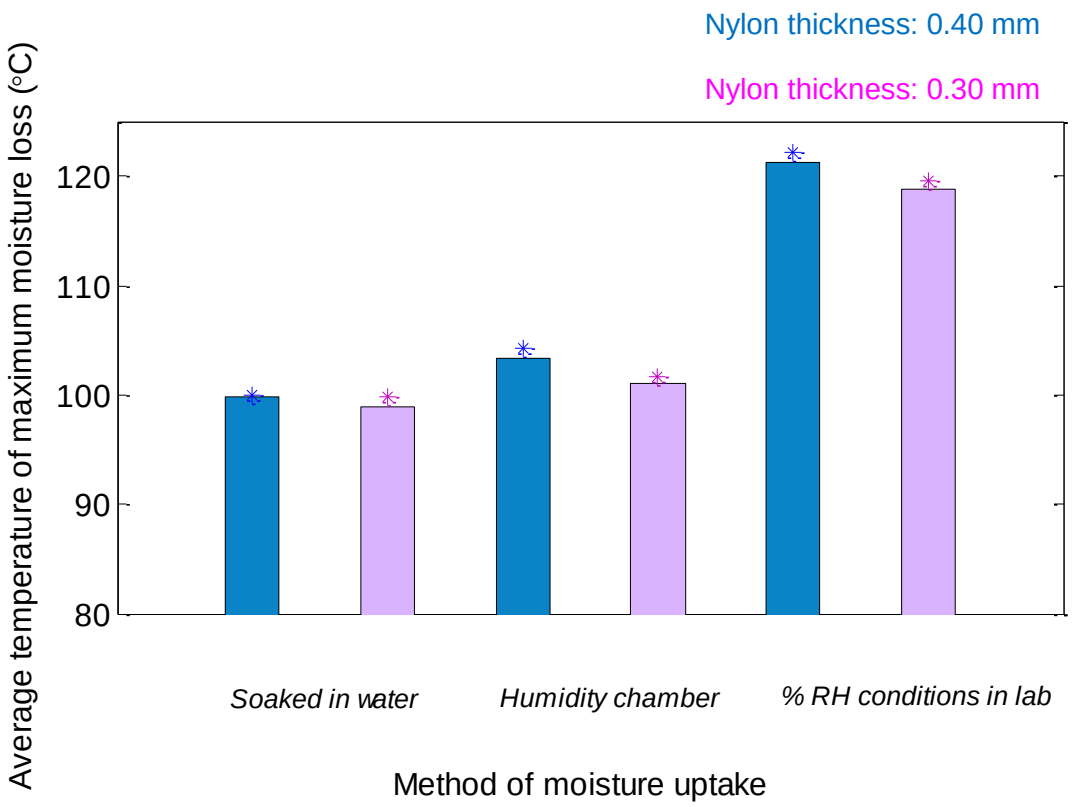

Figure 8-6. Average temperature at which the maximum moisture loss occurs for the nylon pieces used in the TGA analysis. The asterisks above each bar represent one standard deviation from the average.

calculation was performed by taking the ratio of each pairwise combination of the replicate gold spectra collected on a given day. The spectral ratios were converted from transmittance to absorbance units for the noise calculation. In this study, the spectral regions from 1,200 to 1,700 cm^{-1} and 2,800 cm^{-1} to 3,500 cm^{-1} (separate noise computed for each range and averaged) were used to compute the RMS noise. Systematic components in the noise spectra were removed by fitting the selected spectral region to a third order polynomial function and computing the RMS noise in the resulting spectral residuals. The noise values are reported in microabsorbance units (μAU). The RMS noise calculation is described in detail in Chapter 3 (Section 3.6).

The average RMS noise value obtained for the gold spectra ranged from 5,092 – 5,384 μAU for both the moisture uptake and yellowing studies. The average RMS noise value obtained for nylon-6,6 spectra ranged from 6,696 – 8,103 μAU for both the moisture uptake and yellowing studies. These noise values are high when compared to the previous studies reported in Chapters 4-7. The increased noise arises from the lower signal levels obtained in this experiment. Lower signals arise from the reflectance mode of the data collection and the small size of the individual detector elements in the FPA. Figure 8-7 displays images constructed from the computed noise values across the 128×128 pixels of the FPA for gold (A) and nylon (B) spectra.

8.3.2.2 Fourier transform infrared microscopic spectra of nylon-6,6 polymers

Several important spectral features of nylon polymers can be found in the inspected wavenumber range. These include fundamental stretching modes of the amide carbonyl (~1,630 cm^{-1}), amide II (1,540 cm^{-1}), amide III (1,300 cm^{-1}), the fundamental stretching mode of N-H (~3,300 cm^{-1}), and the fundamental symmetric and asymmetric stretching modes of C-H (~2,800 – 2,950 cm^{-1}). The stretching mode of the N-H bond exhibits a broad feature often extending from ~3,100 to 3,500 cm^{-1} due to the presence of hydrogen bonding. Moreover, the fundamental stretching and bending modes of O-H

exhibit spectral features at ~3,300 cm^{-1} and 1,640 cm^{-1}, respectively. These features can also exhibit broad bands due to the presence of hydrogen bonding.[75,97]

During this experiment, two main spectral regions were targeted. The first region was from 1,200 to 1,700 cm^{-1} which includes stretching modes of the amide carbonyl, amide II, amide III and the bending mode of water. The second region was from 2,800 to 3,500 cm^{-1} which includes the stretching modes of N-H, O-H and C-H.

Figure 8-8 represents four pseudo-absorbance spectra of a nylon-6,6 polymer sample obtained with the FTIR microscope. These spectra were generated by taking the ratios of single-beam nylon-6,6 spectra (nylon piece N_1 at 0 % moisture uptake at pixel numbers 8130,8131,8132,8133) to the corresponding single-beam gold spectrum. The gold spectrum was scaled to suppress the peak at 2,349 cm^{-1} due to atmospheric CO_2. The resulting spectrum was converted to $\log_{10}(1/R)$ units and normalized with the SNV transform. Among the clearly visible features are the amide carbonyl (~1630 cm^{-1}), amide II (~1540 cm^{-1}), symmetric and asymmetric stretching of C-H (~ 2800 and 2900 cm^{-1}) and stretching of N-H (~3300 cm^{-1}).

8.3.2.3 Fourier transform infrared microscopic imaging of nylon-6,6 polymers

In order to generate IR microscopic images, SNV-preprocessed nylon-6,6 spectra were subjected to principal component analysis (PCA). As described in Chapter 3 (Section 3.3.1), the PCA method allows the generation of lower-dimensional representations of high-dimensional data. For the work described here, this allowed the extraction of spectral information across the two wavenumber regions of interest into a small number of principal component (PC) scores. The spectral data matrix was mean centered before it was submitted to PCA. Separate PCA calculations were done on the two regions.

For the moisture pattern analysis, in each case, PCA was performed on the nylon spectra which had the highest moisture content to compute the loading vectors. Then, the rest of the nylon spectra were projected onto these loading vectors to generate the

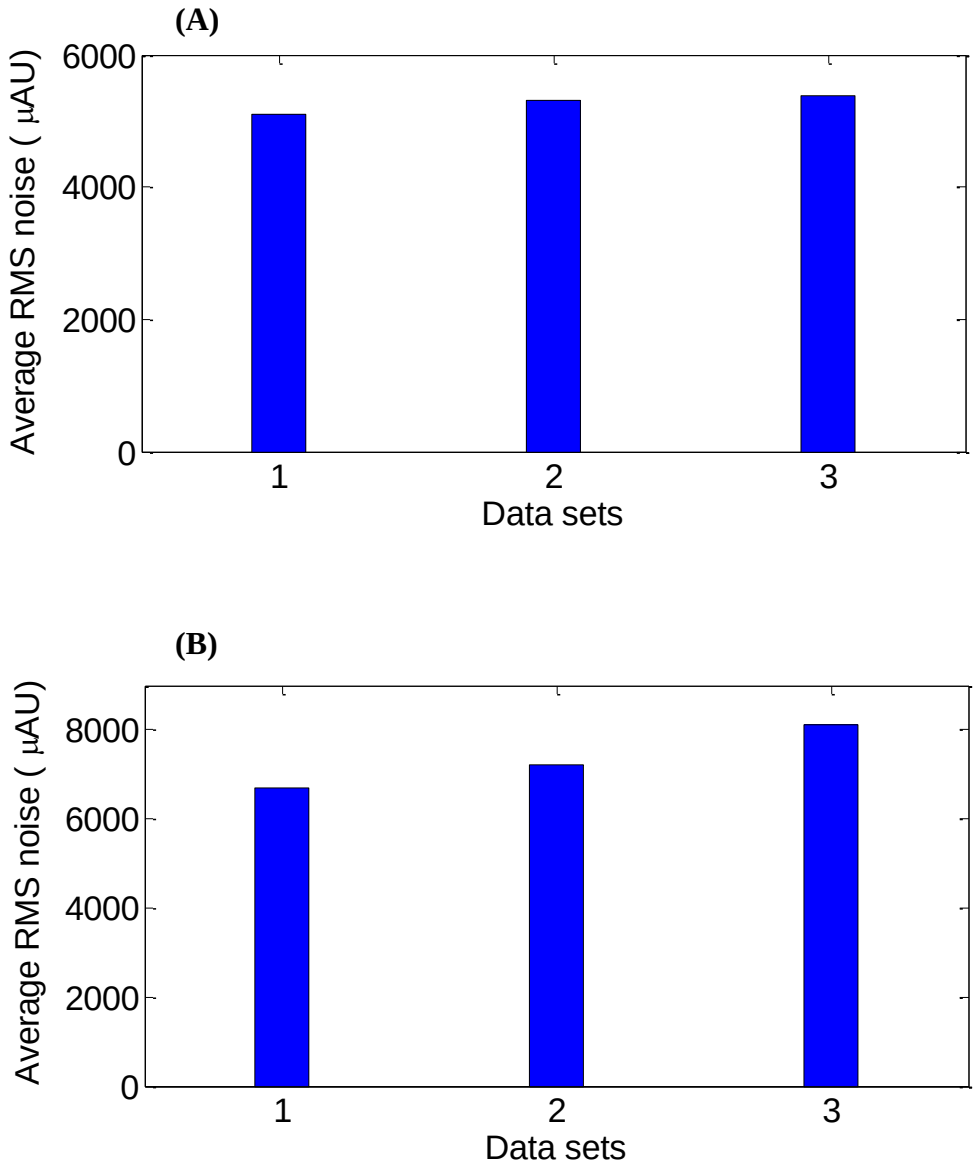

Figure 8-7. Images displaying average RMS noise values computed across the detector array for spectra collected from the gold slide **(A)** and nylon pieces at 0 % moisture uptake **(B)**. Data sets 1, 2 and 3 correspond to data collection carried out with nylon pieces N_1, N_2 and N_3 respectively.

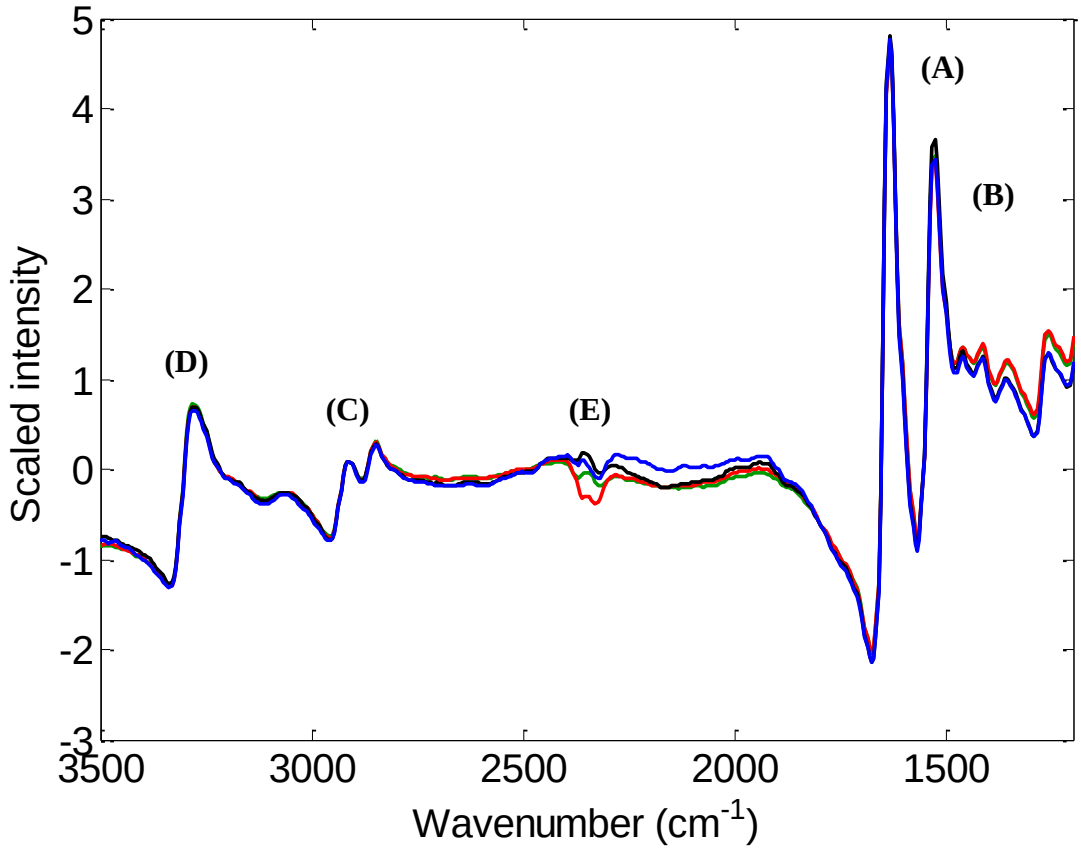

Figure 8-8. Spectra of nylon-6,6 polymer obtained with the FTIR microscope. These spectra were referenced to a gold background and scaled with the SNV transform. The following bands can be identified: **(A)** amide carbonyl (~1,630 cm^{-1}), **(B)** amide II (~1,540 cm^{-1}), **(C)** symmetric and asymmetric stretching of C-H (~2,800 and 2,900 cm^{-1}) and **(D)** stretching of N-H (~3,300 cm^{-1}). The residual of the corrected CO_2 peak is also observed **(E)**. Spectra obtained at pixel numbers 8130, 8131, 8132 and 8133 are represented in blue, red, green and black respectively.

respective PC scores corresponding to nylon spectra collected at other moisture levels. The score along the first PC was then used to generate an IR image of each nylon piece at each moisture level. To produce images for display, the minimum and maximum scores computed across all the images were mapped onto the range of 1-63. This corresponded to a standard color map that ranged from blue (1) to red (63). All the IR images were thus generated with the same color map. Same PC score calculation procedure was performed with each replicate and the IR image that resembles the features in the visible image the best was chosen for further evaluations.

The same procedure was followed for the yellowing analysis. In this case, the loading vectors were generated from the nylon spectra obtained with white nylon (85 °C). In order to assess any changes in the images, regions of 20×20 pixels were selected and an average pixel value was computed for each moisture level/yellow hue. Then, plots of pixel value vs. moisture level/temperature were generated to investigate any trends in the images.

8.3.2.4 Moisture uptake patterns of nylon-6,6 polymers

For the moisture uptake pattern experiment, better images were obtained with the wavenumber region of 2,800 to 3,500 cm^{-1}. In this context, "better" refers to IR images in which the surface features evident in the corresponding visible images (Figure 8-3) could be observed. The selection of the 2,800 to 3,500 cm^{-1} region supports the phenomenon of hydrogen bond formation of water molecules with the amide linkages in the nylon polymer during moisture uptake. Some changes were observed with the pixel values (colors) in the IR images with increasing moisture content. These changes may be attributed to the structural changes occurring during moisture uptake.

Figures 8-9, 8-10, 8-11 and 8-12 summarize the IR images obtained for the four selected points $N_{1,1,}$ $N_{1,2,}$ $N_{2,1,}$ $N_{2,2}$ respectively, with increasing moisture content. In each case, only four images are shown corresponding to four selected levels of moisture uptake for simplicity. No changes were observed in the visible images. Two visible

images (0 % and 88 % moisture uptake) are also shown in the figure for comparison purposes. Although there were some observable changes in the IR images, the trends obtained in the spectral features or pixel values among the four points inspected with the two nylon pieces were less generalized and clear. Figure 8-13 summarizes the FTIR microscopic spectra obtained for $N_{1,1}$with increasing moisture content. Although these spectra indicate some spectral variation, no clear trends were obtained with them. Similar images were obtained with $N_{1,2,}$ $N_{2,1,}$ $N_{2,2}$ as well. Figures 8-14, 8-15, 8-16 and 8-17 depict the average pixel value vs. moisture uptake trends in $N_{1,1,}$ $N_{1,2,}$ $N_{2,1,}$ and $N_{2,2}$, respectively. Although there are trends in changes in the pixel values, they cannot be generalized. Further investigations are needed in order to establish a valid conclusion about the moisture uptake patterns of nylon-6,6.

8.3.2.5 Yellowing of nylon-6,6 polymers

For the yellowing experiment, better images were also obtained with the wavenumber range of 2,800 to 3,500 cm^{-1}. This supports the hypothesis of changes/degradation in the hydrocarbon chains of the nylon polymer as the cause of yellowing. Some changes were observed with the pixel values (colors) in the IR images with increasing yellowing. These changes may be attributed to the structural changes occurring during the yellowing process. Figure 8-18 summarizes the IR images obtained for the selected point, $N_{3,1}$, with increased yellowing. No changes were observed in the visible images. Two visible images (85 and 180 °C) are also shown in the figure for comparison purposes.

Although there were some observable changes in the IR images, the trends obtained in the spectral features or pixel values were less generalized and clear. Figure 8-19 summarizes the FTIR microscopic spectra obtained for $N_{3,1}$ with increasing yellowing. Although these spectra indicate some spectral variation, no clear trends were obtained with them.

Figure 8-20 depicts the average pixel value vs. temperature trends in $N_{3,1}$. However, the trends obtained in the spectral features or pixel values for one nylon piece are not adequate to generalize the trends. Further investigations are needed in order to establish a valid conclusion about the yellowing and degradation of nylon-6,6. Moreover, it was observed that the weight of the nylon piece decreased as the temperature increased. About 1 % of weight was (with respect to initial weight of nylon piece) lost once the nylon piece was heated to 180 °C. This may be due to the production of some gaseous degradation products formed at elevated temperature as suggested elsewhere.[99]

8.4 Conclusions and future work

The research presented in this chapter includes preliminary investigations conducted with FTIR microscopy to study the moisture uptake patterns and yellowing of nylon-6,6 polymers at a microscopic level. This work was motivated by the research described in Chapters 6 and 7. In Chapter 6 it was observed that pieces of nylon obtained with different sheets of nylon-6,6 polymers gave different prediction results when used in the temperature prediction model. Furthermore, nylon pieces developed a yellow coloration upon heating. It was also observed that different nylon sheets have different features on them when observed under polarized light. This inhomogeneous nature at a microscopic level can influence the macroscopic properties such as thermal behavior and degradation (rate and degree of yellowing) of nylon-6,6 polymers.

In Chapter 7 it was observed that moisture uptake of nylon-6,6 polymers is reversible and dependent on the percentage relative humidity conditions of the surrounding environment. Further investigations with TGA revealed that the temperature at which the maximum moisture loss was observed indicates a pattern and it also was dependent on the percentage relative humidity conditions of the surrounding environment. This could be due to the nature of hydrogen bonding observed at different relative humidity conditions along with the inhomogeneous nature of the nylon polymers themselves.

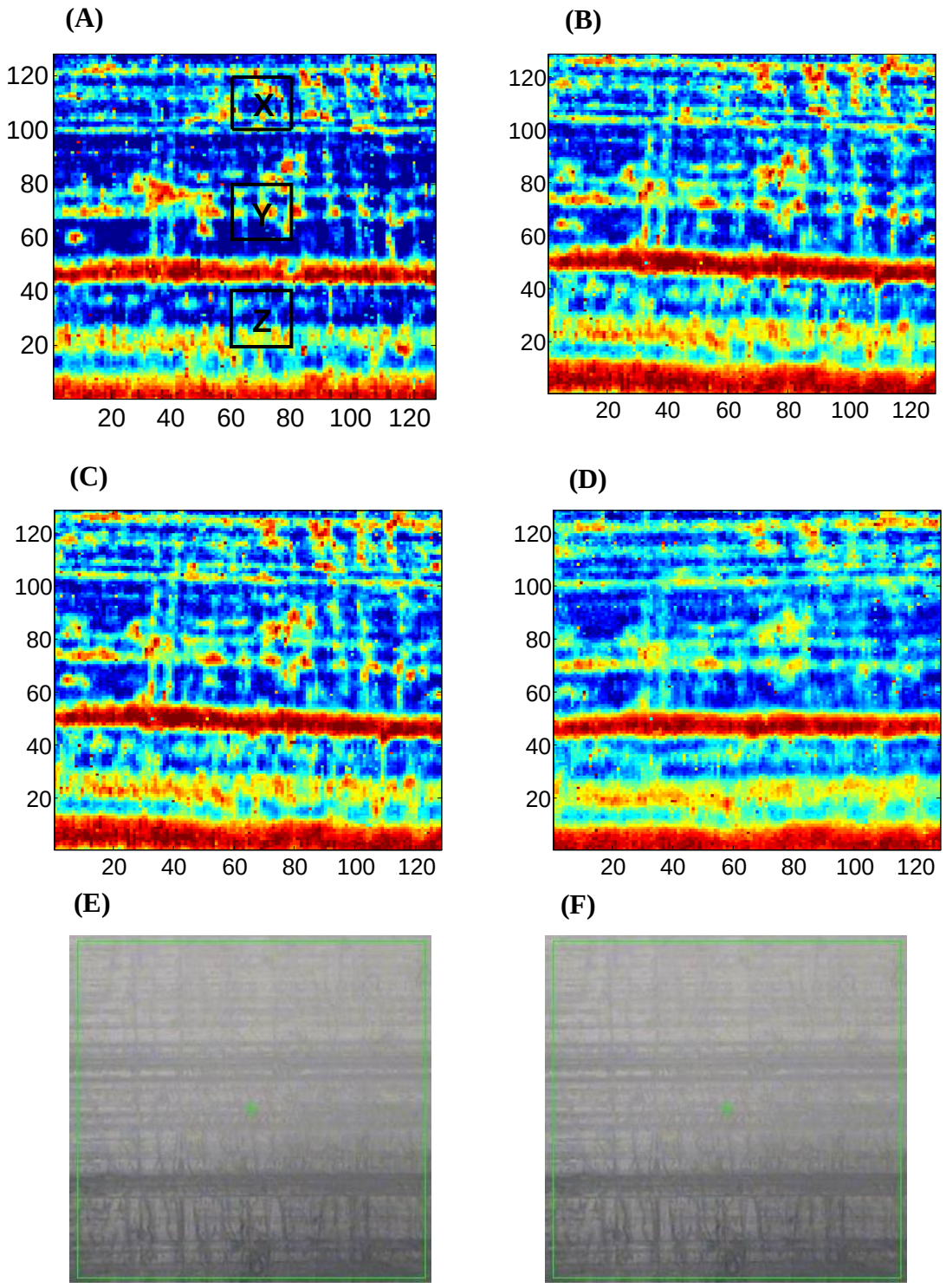

Figure 8-9. Infrared images obtained for the first selected point in nylon piece $N_{1,1}$. These images were obtained at **(A)** 0 %, **(B)** 30 %, **(C)** 64 % and **(D)** 88 % moisture uptake. Visible images obtained at **(E)** 0 % **(F)** 88 % moisture uptake. Regions X, Y and Z indicated in panel A were used in the average pixel value calculation.

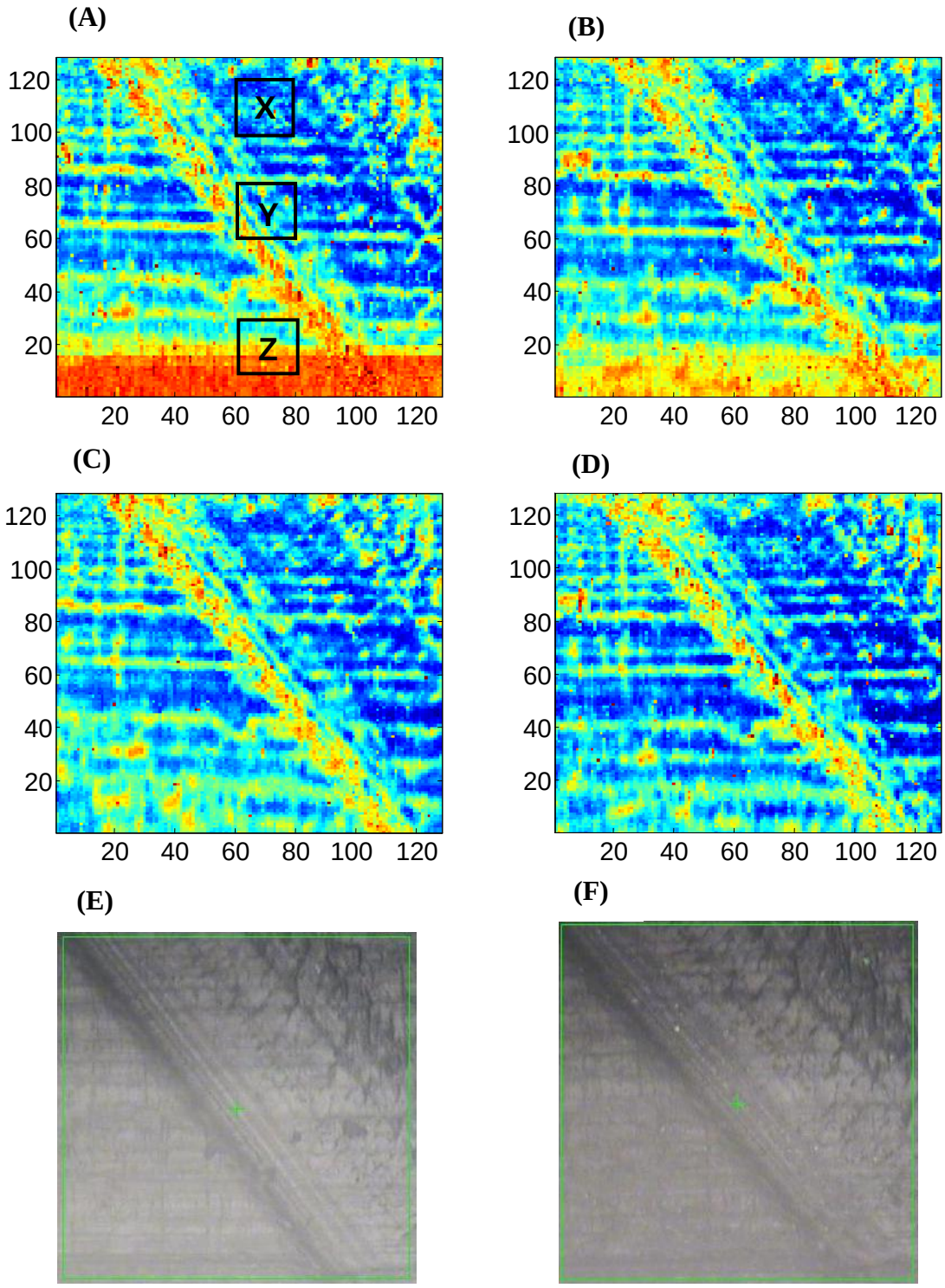

Figure 8-10. Infrared images obtained for the second selected point in nylon piece $N_{1,2}$. These images were obtained at **(A)** 0 %, **(B)** 30 %, **(C)** 64 % and **(D)** 88 % moisture uptake. Visible images obtained at **(E)** 0 % **(F)** 88 % moisture uptake. Regions X, Y and Z were used in the average pixel value calculation.

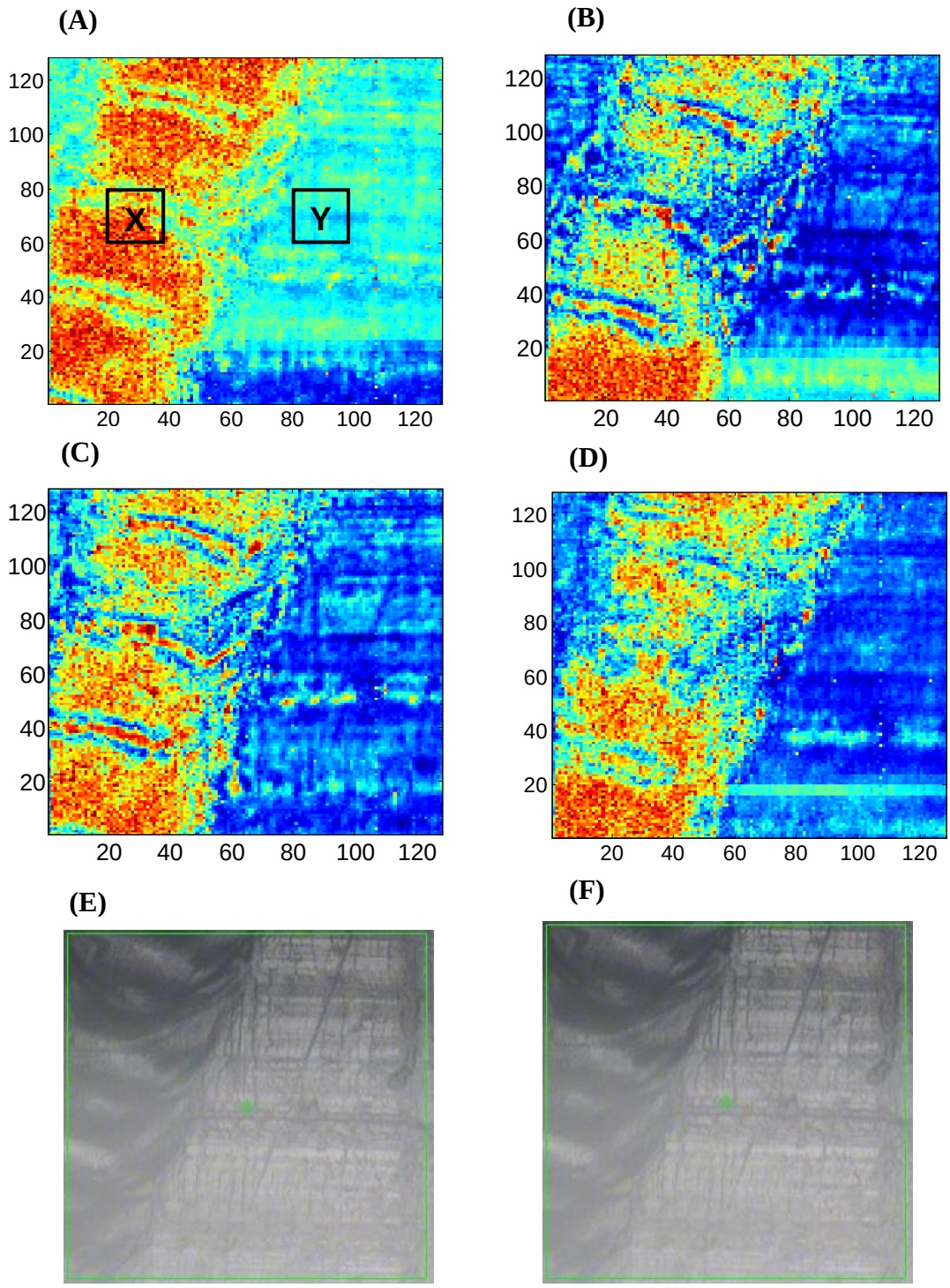

Figure 8-11. Infrared images obtained for the first selected point in nylon piece two ($N_{2,1}$). These images were obtained at **(A)** 0 %, **(B)** 42 %, **(C)** 70 % and **(D)** 88 % moisture uptake. Visible images obtained at **(E)** 0 % **(F)** 88 % moisture uptake. Regions X and Y were used in the average pixel value calculation.

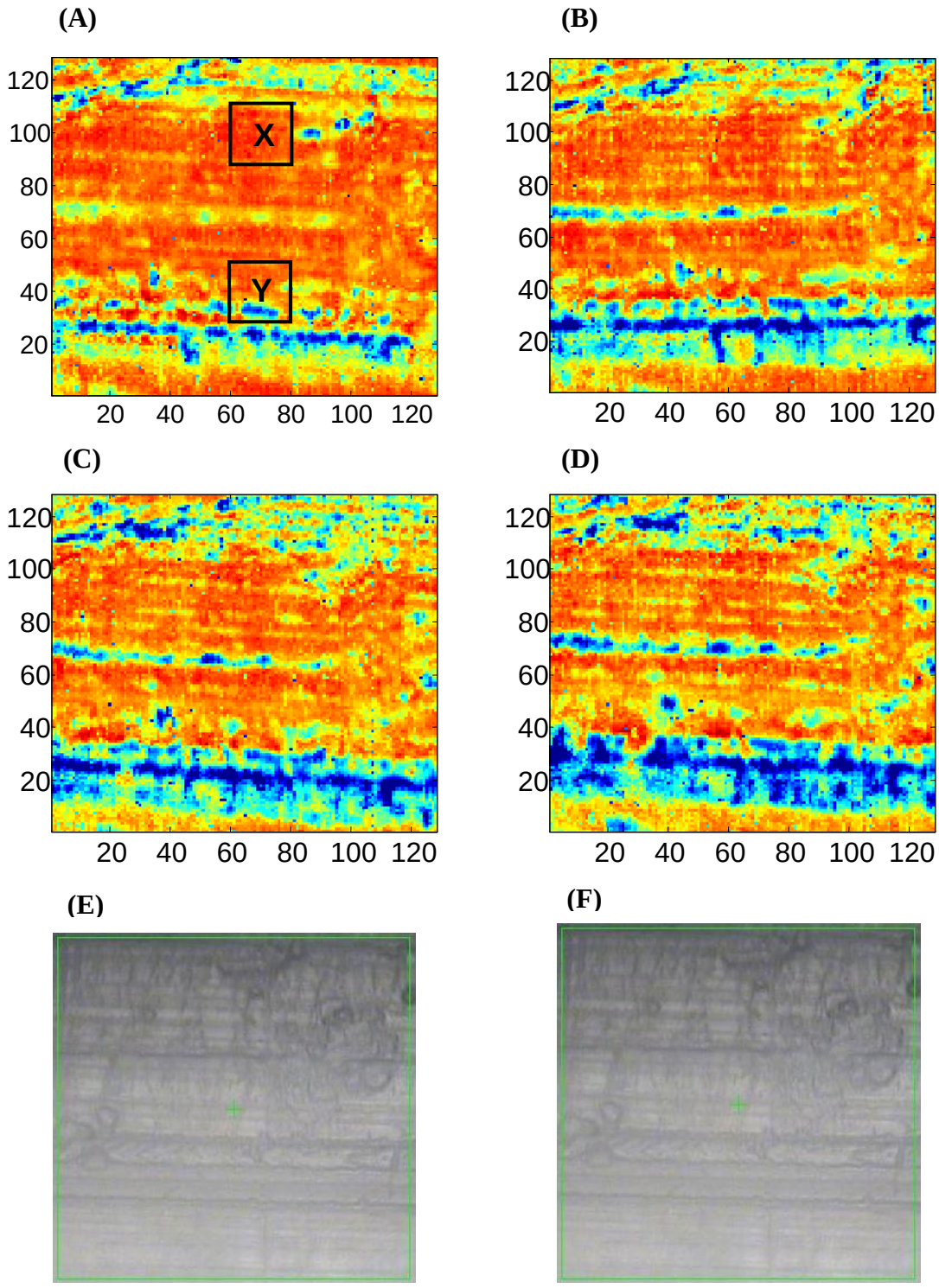

Figure 8-12. FTIR images obtained for second selected point in nylon piece two ($N_{2,2}$). These images were obtained at **(A)** 0 %, **(B)** 42 %, **(C)** 70 % and **(D)** 88 % moisture uptake. Visible images obtained at **(E)** 0 % **(F)** 88 % moisture uptake. Regions X and Y were used in the average pixel value calculation.

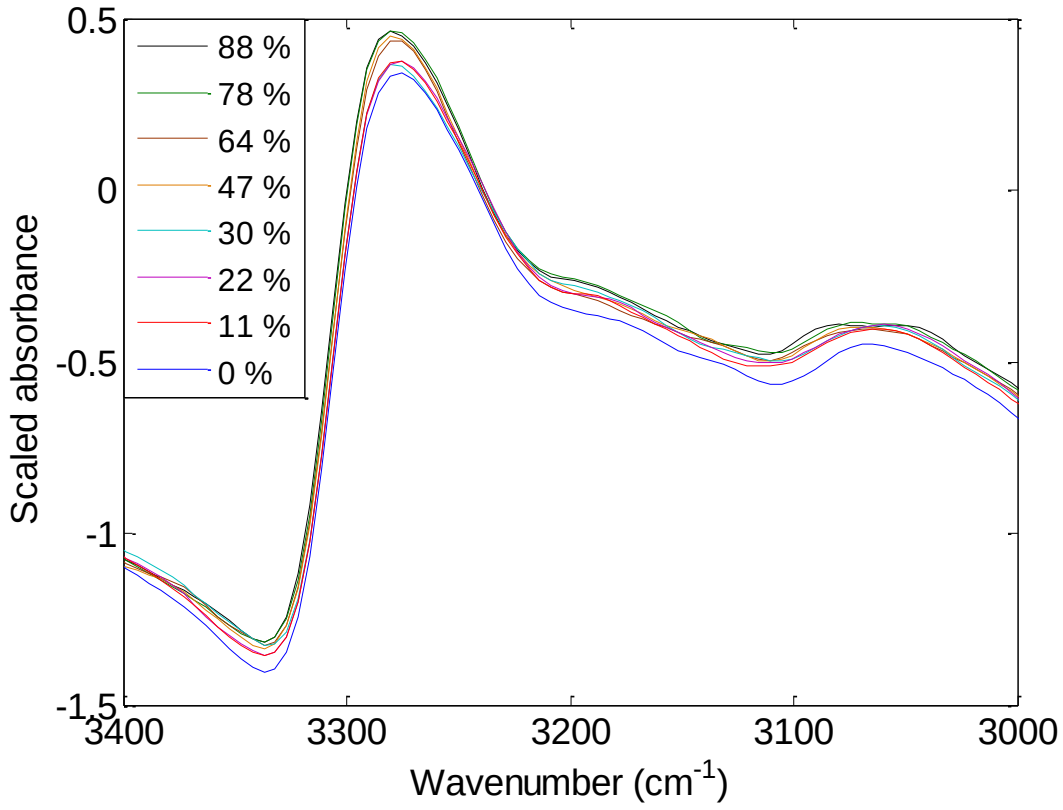

Figure 8-13. FTIR microscopic spectra obtained for $N_{1,1}$ with increasing moisture content. Some spectral variation is visible at the N-H stretching band around 3,300 cm^{-1}.

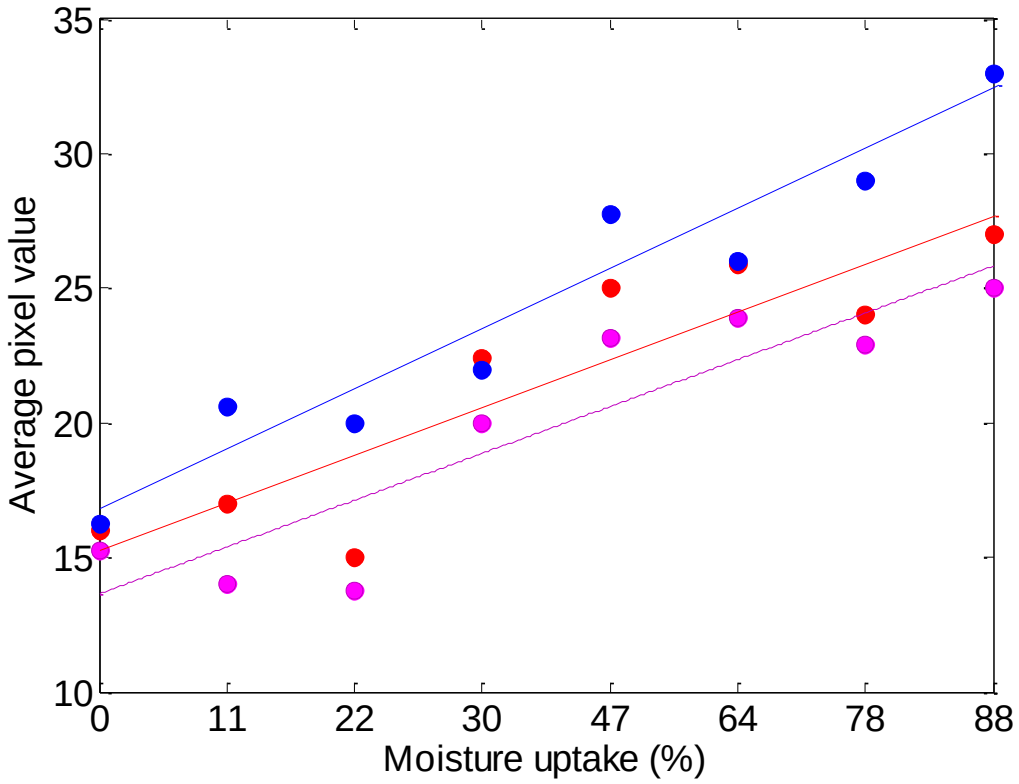

Figure 8-14. Average pixel value obtained for regions X (purple), Y(red), Z(blue) depicted in Figure 8-9 with increasing moisture uptake. A gradual but non-smooth increase in pixel colors was observed with increasing moisture content. A fitted linear regression line is superimposed on the plot to help illustrate the trending.

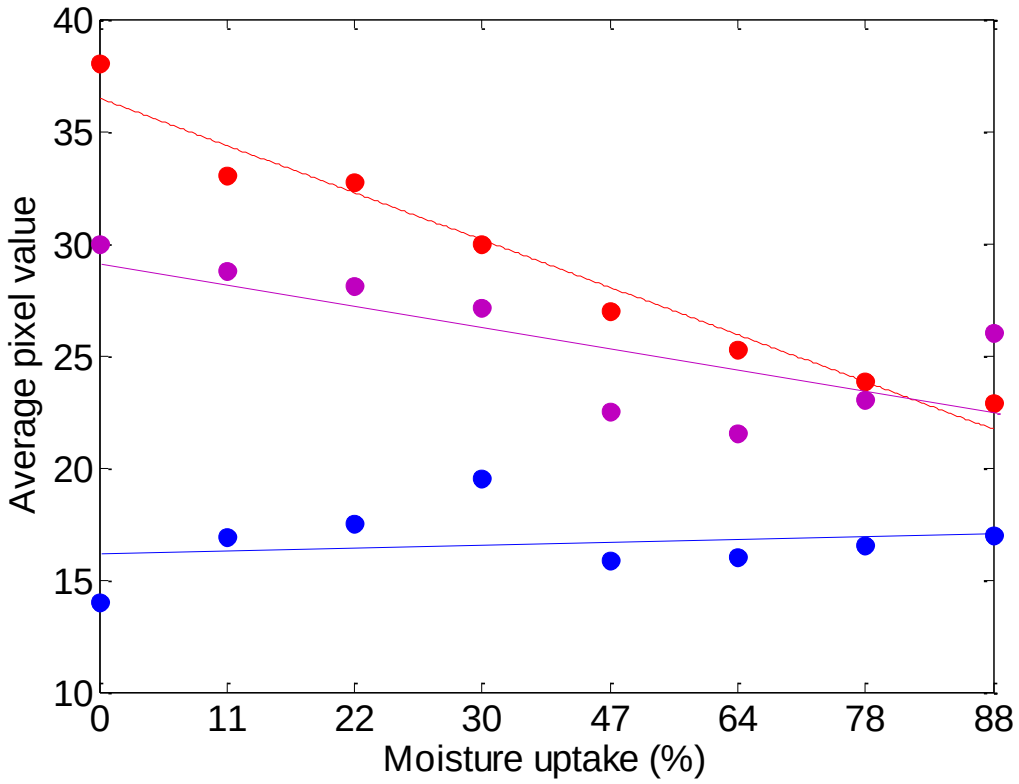

Figure 8-15. Average pixel value obtained for regions X (blue), Y(purple), Z(red) depicted in Figure 8-10 with increasing moisture uptake. A gradual decrease in pixel colors was observed with increasing moisture content for regions Y and Z, but region X exhibited only a slight change. A fitted linear regression line is superimposed on the plot to help illustrate the trending.

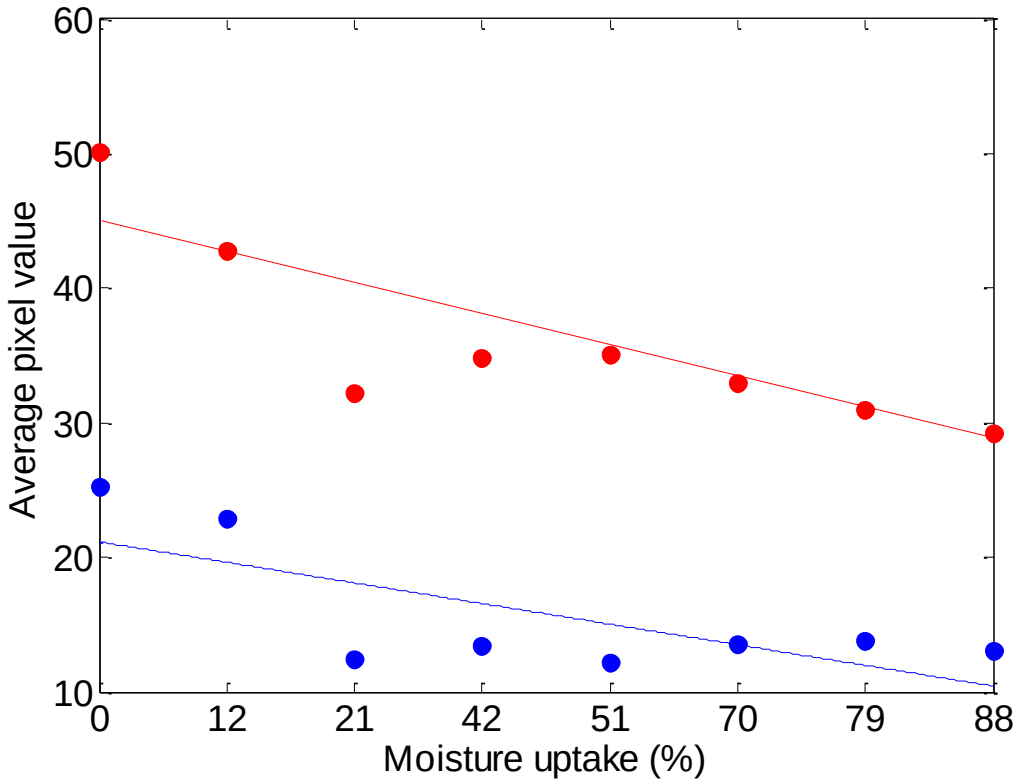

Figure 8-16. Average pixel value obtained for regions X (red) and Y (blue) depicted in Figure 8-11 with increasing moisture uptake. A gradual decrease in pixel colors was observed for both regions until 21 % and then the average pixel value remained constant with increasing moisture content.

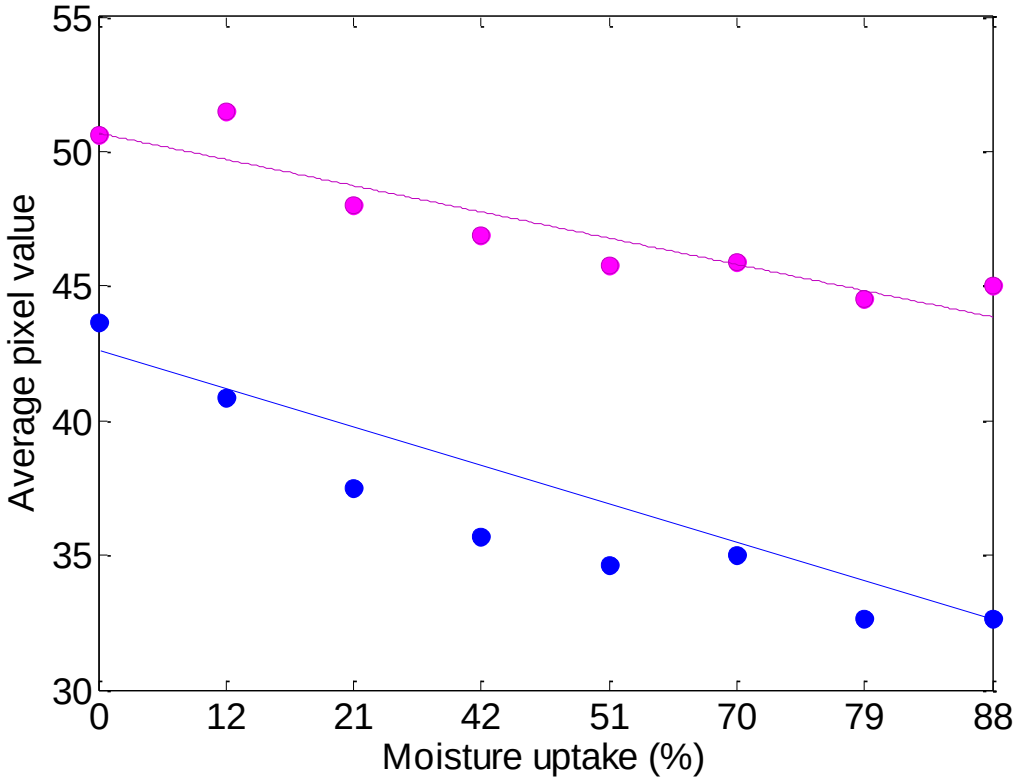

Figure 8-17. Average pixel value obtained for regions X (magenta) and Y (blue) depicted in Figure 8-12 with increasing moisture uptake. A gradual decrease in pixel colors was observed with increasing moisture content.

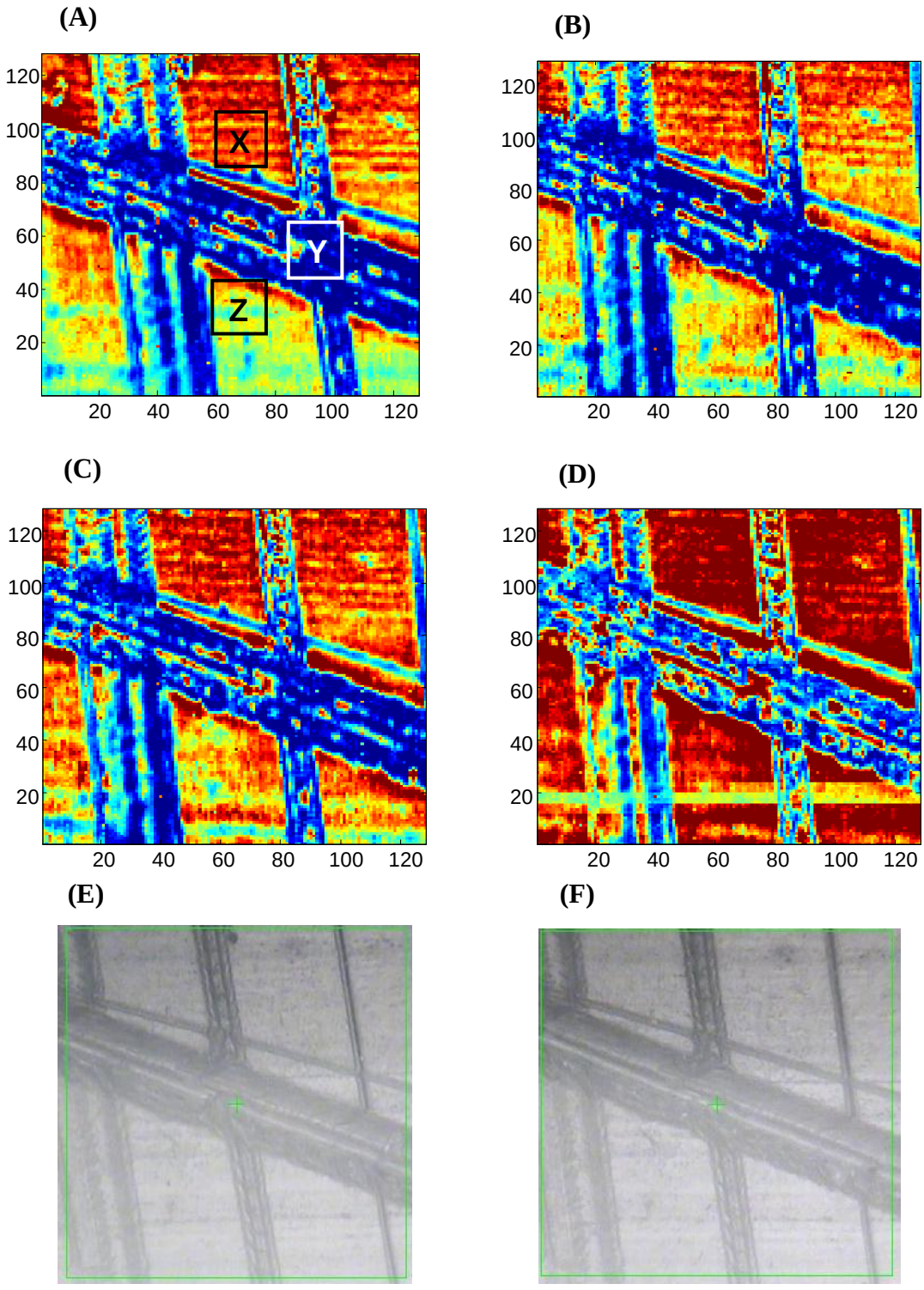

Figure 8-18. Infrared mages obtained for the selected point in nylon piece three ($N_{3,1}$). These images were obtained at **(A)** 85 °C, **(B)** 120 °C, **(C)** 150 °C and **(D)** 180 °C. Visible images obtained at **(E)** 85 °C **(F)** 180 °C. Regions X and Y were used in the average pixel value calculation.

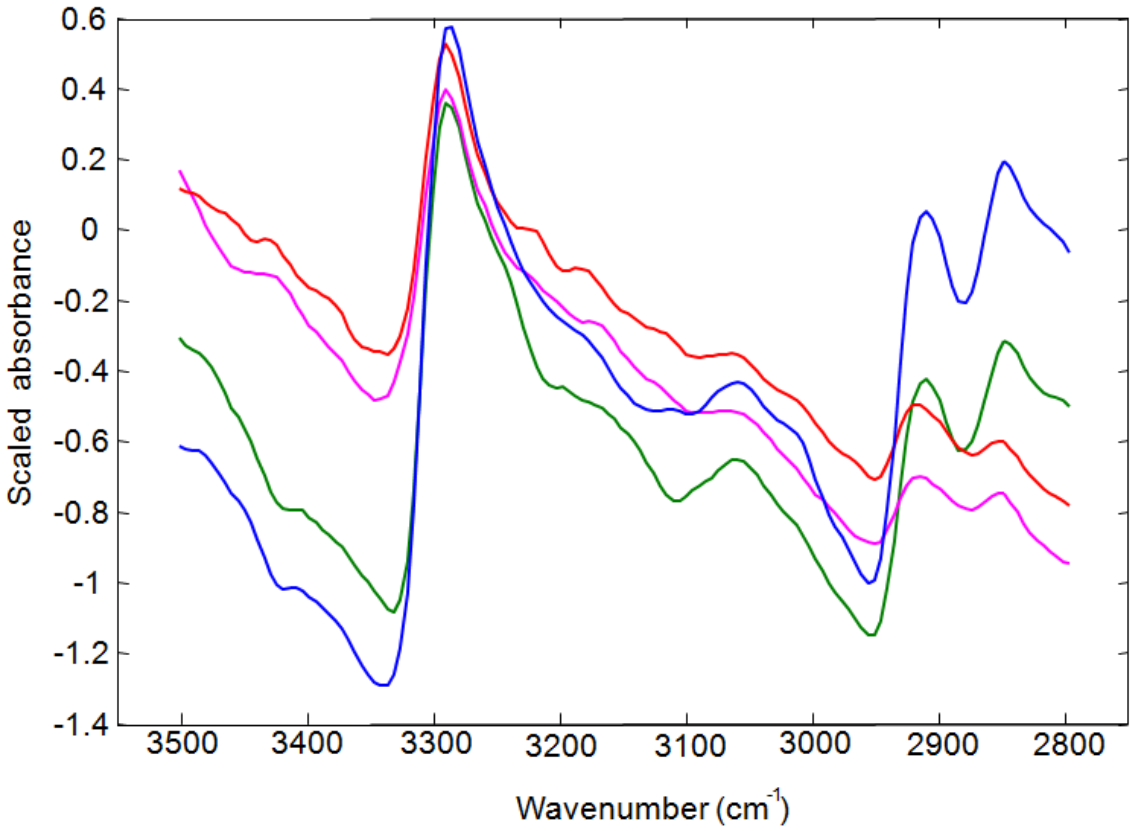

Figure 8-19. Infrared microscopic spectra obtained for $N_{3,1}$ with increasing yellowing at 85 °C (blue), 120 °C (green), 150 °C (magenta) and 180 °C (red). Some spectral variation is visible in the C-H stretching bands around 2800 -2900 cm^{-1}, as well as in the N-H stretching band around 3300 cm^{-1}

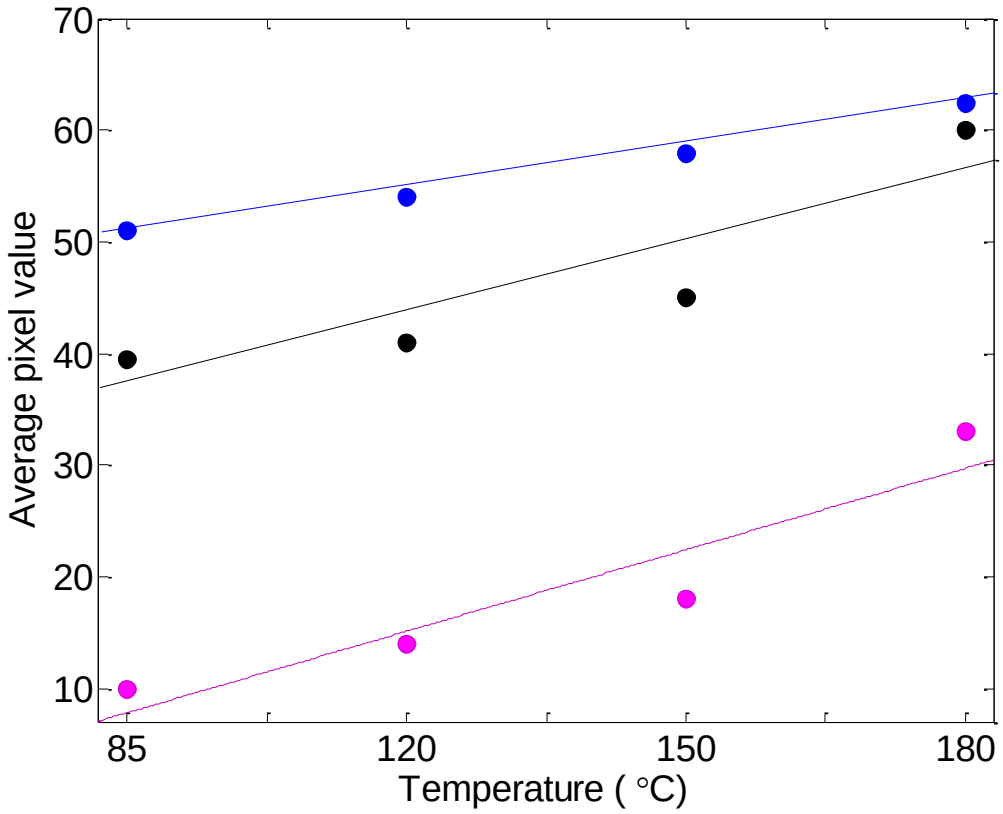

Figure 8-20. Average pixel value obtained for regions X (blue), Y (magenta), Z (black) depicted in Figure 8-18 with exposure to increasing temperature. A gradual increase in pixel colors was observed with increasing yellowing in all regions.

Therefore, the goals of the work described in this chapter were to use FTIR microscopy to investigate the effect of the inhomogeneous nature of nylon-6,6 on moisture uptake and thermal degradation, the nature of hydrogen bonding between water and nylon-6,6 polymer as a function of moisture content and the microscopic nature of yellowing/thermal degradation of nylon-6,6 polymers. During this work, a spectral preprocessing method using the SNV transform combined with PCA was used to generate FTIR images for both moisture uptake and yellowing experiments. Values of the first principal component score were used and an appropriately scaled color map was employed in generating the images.

For both moisture uptake and yellowing experiments, the wavenumber range of 2,800 to 3,500 cm^{-1} produced images that showed the best reproduction of the surface features observed in the corresponding visible images. This indicates that spectral variation in the N-H and C-H stretching frequencies are useful in understanding the microscopic nature of nylon polymers as they uptake moisture as well as degrade due to heat. Changes in the pixel values (colors) in the FTIR images were observed as the amount of moisture content was varied. Similarly, changes in the pixel values (colors) in the images were observed as the degree of yellowing in the nylon varied. Features in the FTIR microscopic spectra also indicated a considerable amount of spectral variation for both moisture uptake and yellowing experiments.

However, the trends were not well understood in both cases. The relationship between the average pixel values for selected regions of the FTIR images and moisture content gave different patterns for each of the four points of interest. These relationships indicated a clear change in the nylon polymer as the moisture content varied, yet no clear trend was established. The relationship between the average pixel values for selected regions of the FTIR images and the degree of yellowing showed a gradual change in the pixel values with increasing temperature. This relationship indicated a clear change in the

nylon polymer as the temperature is increased. However, more experiments are needed to establish a clear trend.

According to the experimental results observed in this work, FTIR microscopy provides a promising approach to allow further investigation of the microscopic behavior of nylon-6,6 polymer samples with varying levels of moisture content and thermal degradation. The spectral preprocessing method based on the SNV transform and PCA provided a workable strategy to display information from the collected spectra.

As stated previously, this work should be considered a very preliminary investigation. Further work is needed to improve both the spectral collection strategies and the methods employed for image generation and interpretation.

The spectral collection strategy could be improved significantly by performing the data acquisition in a closed environment. In the work described here, the nylon piece to be studied was placed on the microscope stage in such a way that it was open to the laboratory environment. Given the approximately 20 minutes required to acquire a single set of imaging data, there can be no guarantee the level of moisture content of any of the nylon pieces was constant with respect to time.

Constructing a controlled chamber for housing the sample would allow spectra to be collected without external influences such as changes in percent relative humidity conditions in the laboratory. It would also allow for the creation of constant atmospheric conditions surrounding the sample. A design for building a controlled chamber is presented in Figure 8-21. Is this design, a Plexiglas tube is used to create a controlled chamber which is sealed at either side (objective and condenser) to allow an enclosed environment. Material used as the sealer needs to have high tensile strengths to allow it to expand/contract as the sample is being focused to obtain a desirable image. The two openings can be used to introduce dry air, moisture, inert gas etc. and measurement probes (e.g. relative humidity probe, etc.). A further enhancement would be the

integration of a temperature module to controllably heat/cool the sample during the spectral acquisition.

Changing the data acquisition from reflectance to transmittance mode would also be potentially advantageous to enhancing spectral reproducibility. This would require either the availability of thinner samples than those employed here or the ability to slice the currently available nylon pieces into thinner samples. Attempts were made in the current work to pursue both of these avenues without success.

Finally, the data analysis efforts employed here were somewhat rudimentary. No thorough study of spectral preprocessing methods was attempted and only block averaging of small sections of the images was performed to explore the possible relationships between spectral intensities and the two property variables (moisture content and yellowing). Further investigations of the data analysis methodology with higher quality data are needed to advance this preliminary work.

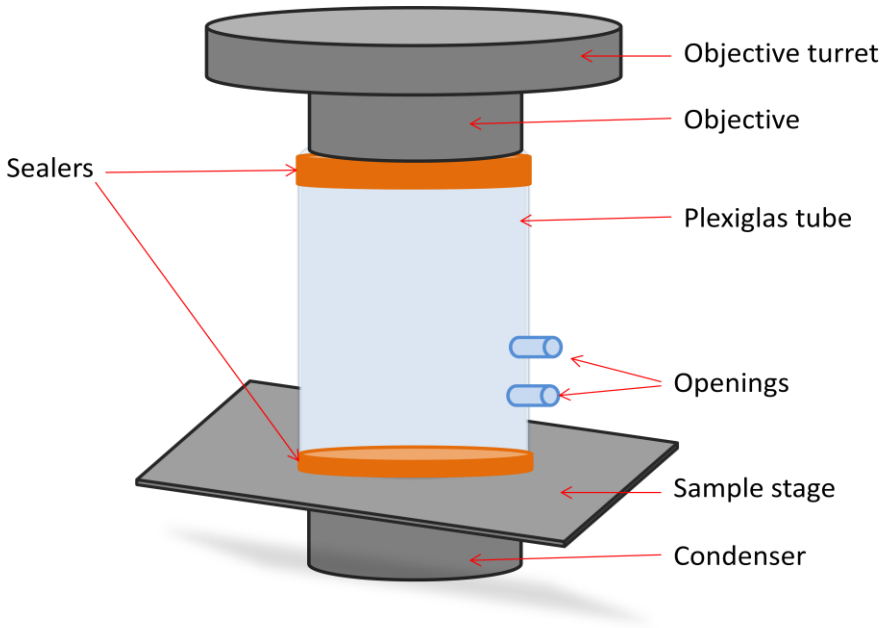

Figure 8-21. Proposed design for constructing a controlled chamber to house the sample in an enclosed environment.

CHAPTER 9
CONCLUSIONS AND FUTURE DIRECTIONS

Near-infrared (NIR) spectroscopy is a very useful technique in applications as diverse as clinical measurements and materials characterization. The research presented in Chapters 4 and 5 of this dissertation describes novel and specific applications of near-infrared (NIR) spectroscopy in measurements in aqueous solutions such as those encountered in clinical chemistry. The research presented in Chapters 6 and 7 provides novel methodology for use in characterizing materials such as polymers. Chapter 8 describes initial investigations of infrared microscopy as a promising polymer characterization technique.

The research discussed in this dissertation also highlights the use of chemometric techniques to aid the extraction of meaningful information from NIR spectra. Use of the discrete wavelet transform (DWT) as a signal preprocessing method was found especially useful in the work described in Chapters 4 through 6, and it was observed that the DWT provided an excellent tool for helping to standardize spectra collected over time. Coupling the DWT with multivariate regression models such as those obtained with partial-least squares (PLS) also proved to be a powerful combination that yielded excellent modeling results.

In Chapter 4, a spectral preprocessing method using the standard normal variate (SNV) transform combined with the DWT, followed by PLS regression was utilized successfully in developing calibration models to determine the temperature of aqueous-based samples directly from their NIR spectra. The spectral preprocessing strategy based on the DWT was successfully utilized to isolate the low-frequency background information which carries the spectral features due to temperature fluctuations in aqueous-based samples. These calibration models were developed from spectra of pH 7.40 phosphate buffer collected over the range of 20.0 to 40.5 °C. With wavelet

preprocessing, these calibration models required only one PLS factor to explain temperature fluctuations and gave robust prediction results (standard error of prediction (SEP) values ranging from 0.19 to 0.36 °C) over a period of one year. By comparison, models based on buffer spectra with no preprocessing gave much higher SEP values (> 2°C) and performed increasingly poorly with time. The prediction performance of the temperature models based on no preprocessing also gave very high SEP values (> 9 °C) when applied to spectra of samples with increased complexity (i.e., samples with constituents other than buffer). Wavelet-preprocessed NIR spectra gave SEP values ranging from 0.33 to 1.01 °C and performed well with the increasing complexity of the sample matrix. Values of SEP obtained for bovine plasma (BVP) samples were the highest regardless of the calibration model used. This could be due to the presence of dissolved proteins (globulins, albumins, etc.) and different ionic species (K^+, Cl^-, Ca^{2+}, etc.) in the plasma samples.

Further investigations were conducted to investigate the ability to model temperature fluctuations in an aqueous-based sample with dissolved proteins, and including pH and molarity variation. For this purpose, calibration models were developed separately based on phosphate buffer solutions with human serum albumin (HSA) and varying pH and molarity values. The best calibration models for both situations were obtained with DWT-preprocessed spectra. It was observed that these calibration models required more latent variables (3 vs. 1) than the models generated using buffer alone. The prediction performance of the calibration models which included dissolved proteins was assessed using both HSA and BVP samples. The SEP values obtained for both prediction sets were 0.29 and 0.18 °C, respectively. The prediction performance of the calibration model which included pH and molarity variations was assessed using two prediction sets. The SEP values obtained for both prediction sets were 0.30 and 0.31 °C, respectively.

This study was extended to consider dynamic systems in order to investigate the ability to model temperature fluctuations in a flowing solution. Calibration models were

developed using a pH 7.40 phosphate buffer solution in a custom made flow-cell system. This flow-cell design demonstrated excellent performance in achieving and equilibrating at a desired temperature. The best calibration models were again obtained with DWT-preprocessed buffer spectra. The prediction performance of these models was assessed using six prediction sets of buffer spectra obtained at three different flow rates. All the calibration models at different flow rates gave SEP values ranging from 0.13 to 0.23 °C, with the model developed from data at 85 mL/min producing the lowest SEP values (average SEP of 0.135 °C). During the assessment of the effect of flow rate fluctuations on the calibration models, reasonably good prediction results were obtained (SEP values ranging from 0.15 to 0.23 °C) for prediction spectra that were collected at a different flow rate than that used in the collection of the calibration spectra. These results indicate that the temperature models are capable of tolerating some degree of fluctuation in flow rates.

Although the temperature range studied in these experiments ranged only from 20.0 to 40.5 °C, these models can be extended towards the entire temperature range in which water behaves as a liquid. This is possible due to the thermal behavior of the hydrogen-bonding network of liquid water being essentially the same regardless of the temperature range studied.

Temperature modeling in an aqueous-based sample directly from the NIR spectrum has promising applications in situations in which it is difficult or inaccurate to use a conventional temperature probe. Such applications could be promising in non-invasive glucose sensing measurements. A useful extension of this research would be to employ the custom-made flow cell system to model temperature variation in other biological fluids such as blood. The same concept of temperature modeling could be employed in environmental analysis, food and agricultural analyses, and process monitoring (e.g., bioreactors). Each of these areas is dominated by the need to analyze aqueous-based samples and there is a continuing interest in moving analyses from the laboratory to the field, chemical plant, etc.

In Chapter 5, a temperature-correction strategy to improve quantitative analyte predictions in aqueous-based samples was successfully developed. This correction strategy is based on the systematic pattern of analyte concentration residuals observed with respect to changes in temperature. The relationship between glucose or lactate residuals and temperature was successfully modeled using a second-order polynomial fit which then led to an additive correction that ultimately resulted in corrected analyte predictions. This methodology was tested in solutions of glucose in buffer and glucose/lactate mixtures in buffer. The basis for this correction strategy is the baseline artifacts introduced by the systematic shift of water absorption peaks with increasing temperature. The correction procedure incorporates temperature information into the calibration model without requiring a full-scale experimental design in which temperature is systematically varied together with analyte concentrations. The correction procedure can be applied with or without an experimental measurement of the sample temperature. If no reference temperature is available, a temperature prediction model of the type developed in Chapter 4 can be used to estimate the sample temperature. Clearly, the effectiveness of the temperature correction strategy in this case is dependent on the prediction performance of the temperature model. As discussed in Chapter 4, however, temperature models for aqueous solutions can give good long-term prediction results and can tolerate some changes in the sample matrix.

Despite the effectiveness of the correction strategy, some deterioration of prediction performance was observed with time. This might be due to the degradation of analyte prediction models with time as the temperature prediction models were observed to be stable with time. Calibration models developed using DWT-preprocessed spectra gave better prediction results than calibration models developed using raw absorbance spectra when combined with the temperature correction procedure. In the case of glucose predictions in laboratory-prepared glucose solutions, the glucose prediction model based on raw absorbance spectra gave an average SEP value of 0.34 mM whereas the model

based on DWT-preprocessed spectra gave an average SEP value of 0.26 mM. Similarly, in the case of glucose predictions in mixture solutions of glucose and lactate, the average SEP values obtained for glucose predictions using raw spectra was 0.27 mM. This value reduced to 0.23 mM when the preprocessed spectra were used. Improvements in prediction performance for the model based on preprocessed spectra were less clear for lactate, however. In this case, the models based on raw and preprocessed spectra performed similarly.

An alternative strategy for overcoming the effects of temperature variation is to build both concentration variation and temperature variation into the calibration model. This approach was also evaluated in conjunction with spectral preprocessing based on both the DWT and digital Fourier filtering. The proposed temperature correction strategy performed favorably when compared to this alternative approach.

Finally, the temperature correction strategy developed in this work is not limited to biomedical applications such as glucose or lactate sensing or to aqueous-based samples. The method is general and can be applied to any sample matrix in which the temperature dependence of the concentration residuals can be modeled. In fact, the relatively simple relationship between concentration residuals and sample temperatures may allow the use of a significantly smaller data set than was employed here for establishing the polynomial correction function.

Temperature modeling methodology developed in Chapters 4 and 5 was successfully extended toward solid samples in the research discussed in Chapter6. In doing so, a signal preprocessing method combining the SNV and DWT methods followed by PLS regression was utilized to develop calibration models to determine temperatures of a given piece of nylon-6,6 polymer directly from the NIR transmission spectrum. Near-infrared spectra at different temperatures show deviations in intensity and peak position which arise due to the changes in hydrogen-bonded amide groups and hydrocarbon chains. The long-term prediction performance of the temperature models

was assessed using 10 prediction sets of nylon-6,6 spectra at different temperatures spanning a time period of seven weeks. The temperature model based on raw absorbance spectra gave very high SEP values (> 6 °C) three weeks after the calibration, whereas the model based on preprocessed spectra provided improved SEP values (0.697 to 2.65 °C) with time. Use of the wavelet functions to extract spectral information significantly improved the performance of the temperature model with time and also improved prediction performance across different sheets of nylon. Principal component analysis (PCA) of the preprocessed and raw absorbance spectra further explained the effect of this preprocessing approach. Temperature models based on preprocessed spectra also gave similar SEP values across the different nylon sheets. However, one nylon piece (nylon piece C) gave high SEP values (average SEP: 2.23 °C) when compared to the other three pieces of nylon (average SEP: 1.19 °C). This might be due to the inhomogeneous nature of different sheets of nylon at a microscopic level.

In principle, these temperature models are not limited to nylon-6,6 polymers, but could be applied to other nylon polymers as well since all the nylon polymers contain the same basic chemical structure. Other potential extensions of this project would be to study the effect of physical properties such as thickness, degree of swelling (moisture content) and chemical properties such as additives, plasticizers, coloring agents, etc. on the thermal behavior of nylon polymers. This represents a potential area for further investigation.

Experimental results obtained in Chapter 7 clearly indicate the reversible nature of moisture uptake of nylon and its dependence on the percentage relative humidity of the environment as explained in previous studies. Experimental results also demonstrate that commercially available nylon-6,6 polymers are capable of absorbing up to an average of 8-10 % of water (relative to their dry weight) upon saturation. The amount of moisture loss during the spectral data collection was explained in terms of an exponential decay correction. This proposed exponential decay correction was able to addresses the

moisture loss during the spectral acquisition effectively, thereby improving the predictive ability of the computed quantitative models for moisture uptake. The combination of spectral preprocessing by the SNV transform and PLS regression was utilized successfully in developing calibration models to determine the moisture content of nylon-6,6 polymers directly from their NIR spectra. Two calculation methods were used to determine the moisture uptake percentage of a given piece of nylon at a given time. Both methods performed equally well, providing cross-validated SEP (CV-SEP) values of 0.841% and 0.874%, respectively. These moisture models were primarily based on the amount of water that was absorbed by the nylon. This was evident from the first principal component (98.01% variance explained) which mainly explained the contribution from water.

The long-term prediction performance of these moisture models was assessed using 10 prediction sets of nylon-6,6 spectra at different moisture levels spanning a time period of six months. The SEP values obtained for these prediction sets ranged from 0.958 % to 2.09 %, with an average ± standard deviation of 1.4 ± 0.3 %. These models were successful in predicting the moisture uptake across different sheets of nylon-6,6 polymers. It was also observed that the performance of both models deteriorated slightly with time, specifically after 18 weeks relative to the calibration data.

When compared to existing experimental techniques such as thermogravimetric analysis, NIR spectroscopy combined with PLS regression provides a reliable, fast, and non-destructive method to determine the moisture content of a given nylon polymer. This methodology could be easily integrated with on-line analyses. In addition, this method can be applied to reasonably thick polymer sheets (e.g., in the mm range) as opposed to methods based on mid-infrared spectroscopy.

The methodology developed in this work is not limited to nylon-6,6 polymers, but could be applied to other nylon polymers as well since all nylon polymers contain the amide linkage which is responsible for absorbing moisture. Other potential extensions of

this method would be to study the effect of aging, thickness, additives, fillers, plasticizers, coloring agents, etc. on moisture uptake of nylon polymers. Furthermore, the methodology could be extended to other condensation polymers such as polyesters since they contain an ester linkage that follows a similar mechanism of moisture uptake as polyamides.

Research work presented in Chapter 8 included some preliminary investigations conducted with infrared microscopy to study the moisture uptake patterns and yellowing of nylon-6,6 polymers at a microscopic level. This work was motivated by the research described in Chapters 6 and 7. According to the observations and experimental results from Chapters 6 and 7, the inhomogeneous nature of nylon-6,6 polymers can influence the moisture uptake pattern and thermal degradation/yellowing of nylon-6,6 at a microscopic level. Furthermore, the moisture uptake and yellowing processes can be understood by investigating the structural and chemical properties of nylon-6,6 polymer at a microscopic level Therefore the goals of the work were to use infrared microscopy to investigate the effect of the inhomogeneous nature of nylon-6,6 on moisture uptake and thermal degradation, the nature of hydrogen bonding between water and nylon-6,6 polymer as a function of moisture content and the microscopic nature of yellowing/thermal degradation of nylon-6,6 polymers.

During this work, a spectral preprocessing method using the SNV transform combined with PCA was used to generate the infrared images for both moisture uptake and yellowing experiments. Furthermore, values of the first principal component score were used and an appropriately scaled color map was employed in generating images. For both moisture uptake and yellowing experiments, the wavenumber range of 2,800 to 3,500 cm^{-1} gave the best images. This indicates that spectral variations in the N-H and C-H stretching frequencies are useful in understanding the microscopic nature of nylon polymers as they uptake moisture as well as degrade due to heat.

Changes in the pixel values (color) in the images were observed as the amount of moisture content was varied on the nylon polymer. Similarly, changes in the pixel values in the images were observed as the degree of yellowing was varied. The relationship between the average pixel values for selected regions of the images and moisture content gave different patterns for each of the four points of interest. These relationships indicated a clear change in the nylon polymer as the moisture content varied, yet no clear trend was established. The relationship between the average pixel values for selected regions of the images and the degree of yellowing gave a gradual change in the pixel values with increasing temperature. This relationship indicated a clear change in the nylon polymer as the temperature is increased. However, more experiments are needed to establish a clear trend.

According to the experimental results observed in Chapter 8, infrared microscopy provides a promising approach to investigate the microscopic behavior of nylon-6,6 polymer with varying moisture content and thermal degradation. The preprocessing method based on the SNV transform combined with PCA provided reasonably good results.

This research could be continued to improve the spectral collection procedures, thereby improving the image generation and interpretation. A key improvement needed is to conduct the spectral collection in a closed environment (Chapter 8, figure 8-21). This approach would allow the spectra to be collected without external influences such as changes in the percent relative humidity conditions in the laboratory. It would also allow the creation of atmospheric conditions surrounding the sample. Some examples would be creating an environment with controlled moisture levels or an inert atmosphere. It would also be possible to integrate a temperature module to heat/cool the sample during the spectral acquisition. Infrared microscopic images could also be generated using spectra collected in the transmittance mode. This could be done with nylon samples which have appropriate thicknesses and could further assist in understanding the structural and

chemical properties of nylon at a microscopic level. Incorporating depth profiling studies is another strategy that could be applied in future work.

Finally, all the work documented in this dissertation has beneficial applications. The temperature modeling and correction strategy described in Chapters 4 and 5 could be integrated with non-invasive blood glucose sensing and other similar clinical and process monitoring applications. The polymer characterization strategies described in Chapters 6, 7 and 8 could be incorporated into analyses directed to improving the properties of polymers and to enhancing quality control in their manufacture.

REFERENCES

1. Skoog, D.A; Holler, F.J.; Crouch, S. R. *Principles of Instrumental Analysis 6th ed,* Brooks/Cole, Cengage Learning: California, USA, 2007.

2. Burns, D. A.; Ciurczak. E. W. *Practical Spectroscopy Series, Volume 13, Handbook of Near-Infrared Analysis,* Marcel Dekker Inc. New York, USA, 1992.

3. Burns, D. A.; Ciurczak, E. W. *Practical Spectroscopy Series, Volume 27, Handbook of Near-Infrared Analysis, 2nd ed, revised and expanded,* Marcel Deckker Inc.: New York, 2001.

4. Stuart, B. *Analytical Techniques in the Science, Infrared Spectroscopy: Fundamentals and Applications,* John Wiley & Sons: West Sussex, UK, 2004.

5. Reichenbacher, M.; Popp, J. *Challenges in Molecular Structure Determination,* Springer-Verlag: Berlin, Germany, 2012.

6. Libnau, F. O.; Kvalheim, O. M.; Christy, A. A.; Toft, J. Spectra of water in the near- and mid-infrared region. *Vibrational Spectroscopy* **1994**, *7*, 243-254.

7. Kauppinen, J.; Partanen, J. *Fourier Transforms in Spectroscopy, 1st ed*, Wiley-VCH: Berlin, Germany, 2001.

8. Saptari, V. *Fourier-Transform Spectroscopy Instrumentation Engineering*, The International Society for optical Engineering: Washington, USA, 2004.

9. Sun, D. *Infrared Spectroscopy for Food Quality Analysis and Control,* Elsevier: Oxford, UK, 2009.

10. Ewing, G. W. *Analytical Instrumentation Handbook, 2nd ed*, Marcel Dekker Inc: New York, USA, 1997.

11. Wartewig, S. *IR and Raman Spectroscopy, Fundamental Processing*, Wiley-VCH, Weinheim, Germany, 2003.

12. Cazes, J. *Ewing's Analytical Instrumentation Handbook, 3rd ed*, Marcel Dekker Inc: New York, USA, 2005.

13. Sawyer, L. C; Grubb, D.T.; Meyers G. F. *Polymer Microscopy, 3rd ed,* Springer: New York, USA, 2008.

14. Otto, M. Chemometrics, *Statistics and Computer Application in Analytical Chemistry, 2nd edition,* Wiley-VCH: Weinheim, Germany, 2007.

15. Chau, F.; Liang, Y.; Gao J.; Shao, X. *Chemometrics From Basics to Wavelet Transform* John Wiley & Sons Inc.: New Jersey, USA, 2004.

16. Kowalski, B. R. *Chemometrics Mathematics and Statistics in Chemistry,* Riedel Publishing Company: Dordrecht, Holland, 1984.

17. Brereton, R.G. *Chemometrics Data Analysis for the Laboratory and Chemical Plant,* John Wiey & Sons Ltd.: West Sussex, England, 2003.

18. Gemperline, P. *Practical Guide to Chemometrics, 2nd ed,* CRC Press.: Florida, USA, 2006.

19. Kramer, R. *Chemometric Techniques for Quantitative Analysis,* Marcel Dekker Inc.: New York, USA, 1998.

20. Misiti, M.; Misiti, Y.; Oppenheim, G.; Michel, J. *Matlab Wavelet Toolbox User's Guide, Version 3,* The Math Works Inc.: Natick, MA, 2004.

21. Addison, P. S. *The Illustrated Wavelet Transform Handbook, Introductory Theory and Applications in Science, Engineering, Medicine and Finance,* IOP publishing Ltd.: London, UK, 2002.

22. The utility of wavelets in the analysis of hyperpectral aerial imagery acquired under sub-optimal conditions. http://www.geos.ed.ac.uk/~s0790136/intro4_wavelets.html (accessed July 2013).

23. Singular Value Decomposition Tutorial by Kirk Baker. http://www.ling.ohiostate.edu/~kbaker/pubs/Singular Value Decomposition Tutorial.pdf (accessed July 2013).

24. Small, G.W. Chemometrics and near-infrared spectroscopy: Avoiding the pitfalls. *Trends in Analytical Chemistry* **2006**, *25*, 1057-1066.

25. Lu, G.; Zhou, X.; Arnold, M. A.; Small, G. W. Multivariate Calibration Models Based on the Direct Analysis of Near-Infrared Single –Beam Spectra. *Applied Spectroscopy* **1997**, *51*, 1330-1339.

26. Lavine, B. Workman, J. Chemometrics. *Analytical Chemistry* **2008**, *80*, 4519-4531.

27. Draper, N. R.; Smith, H. *Applied Regression Analysis, 2nd ed.*, Wiley & Sons: New York, USA, 1981.

28. Mattu, M. J.; Small, G. W.; Arnold, M. A. Application of Multivariate Calibration Techniques to Quantitative Analysis of Bandpass-Filtered Fourier Transform Infrared Interferogram Data. *Applied Spectroscopy* **1997**, *51*, 1369-1376.

29. Macho, S.; Larrechi, M. S. Near-infrared spectroscopy and multivariate calibration for the quantitative determination of certain properties in the petrochemical industry. *Trends in Analytical Chemistry*, **2002**, *21*, 799-806.

30. Hall, J.; Pollard, A. Near-Infrared Spectrophotometry: A New Dimension in Clinical Chemistry. *Clinical Chemistry*, **1992**, *38*, 1623-1631.

31. Tsai, C.; Chen, J.; Wang, W. Near-infrared Absorption Property of Biological Soft Tissue Constituents. *Journal of Medical and Biological Engineering*, **2001**, *21*, 7-13.

32. Arnold, M. A.; Small, G. W. Determination of Physiological Levels of Glucose in an Aqueous Matrix with Digitally Filtered Fourier Transform Near-Infrared Spectra. *Analytical Chemistry* **1990**, *62*, 1457-1464.

33. Amerov, A. K.; Chen, J.; Arnold, M. A. Molar Absorptivities of Glucose and Other Biological Molevules in Aqueous Solutions over the First Overtone and Combination Regions of the Near-Infrared Spectrum. *Applied Spectroscopy* **2004**, *58*, 1195-1204.

34. Chung, H.; Arnold, M. A.; Rhiel, M.; Murhammer, D. W. Simultaneous Measurements of Glucose. Glutamine, Ammonia, Lactate and Glutamate in Aqueous Solutions by Near-Infrared Spectroscopy. *Applied Spectroscopy* **1996**, *50*, 270-276.

35. Woo, Y-A.; Ahn, J-W.; Chun, I-K.; Kim, H-J. Development of a method for the determination of human skin moisture using a portable near-IR system. *Analytical Chemistry* **2001**, *73*, 4964-4971.

36. Navea, S.; de Juan, A.; Tauler, R. Modeling Temperature-Dependent Protein Structural Transitions by Combined Near-IR and Mid-IR Spectroscopies and Multivariate Curve Resolution. *Analytical Chemistry* **2003,** *75,* 5592-5601.

37. Hazen, K.H.; Arnold, M. A.; Small, G. W. Temperature-Insensitive near Infrared Spectroscopic Measurement of Glucose in Aqueous Solutions. *Applied Spectroscopy*, **1994**, *48*, 477-483.

38. Wulfert, F.; Kok, W. Th.; Smilde, A. K. Influence of Temperature on Vibrational Spectra and Consequences for the Predictive Ability of Multivariate Models. *Analytical Chemistry* **1998**, *70*, 1761-1767.

39. Workman Jr, J.; Weiyer, L. *Practical Guide to Interpretive Near-Infrared Spectroscopy,* CRC Press: Florida, 2008.

40. Brown, T. L.; LeMay Jr, H. E.; Bursten, B. E.; Murphy, C. J. *Chemistry The Central Science*, 11th ed.; Pearson: New Jersey, 2009; pp 443-446, 666-737, 1115.

41. Cracolice, M. S.; Peters, E. I. *Introductory Chemistry: An Active Learning Approach, 4th ed.;* Brooks/Cole Cengage Learning: California, 2011; pp 437-440.

42. Arnold, M. A.; Small, G. W. Noninvasive Glucose Sensing. *Analytical Chemistry* **2005**, *77*, 5429-5439.

43. Koolman, J.; Roehm, K. H. *Color Atlas of Biochemistry 3rd ed.;* Georg Thieme Verlag KG: Stuttgart, Germany, 2013.

44. Valverde,J. L. *Blood, Plasma And Plasma Proteins: A Unique Contribution to Modern Healthcare, Pharmaceuticals Policy and Law, Volume 7;* IOS Press: Amsterdam, The Netherlands, 2005-2006.

45. Harris, D. C. *Quantitative Chemical Analysis 7th ed,;* W.H. Freeman and Company: USA, 2007.

46. Langford, V. S.; McKinley, A. J.; Quickenden, T. I. Temperature dependence of the visible-near-infrared absorption spectrum of liquid water. *J. Phys. Chem. A* **2001**, *105*, 8916–8921.

47. Thompson, S. A.; Andrade, F. J.; Inon, F. A. Light emission diode water temperature: a low-cost and noninvasive strategy for monitoring temperature in aqueous solutions. *Applied Spectroscopy* **2004**, *58*, 344–348.

48. Otal, E. H.; Inon, F. A.; Andrade, F. J. Monitoring the temperature of dilute aqueous solutions using near-infrared water absorption. *Applied Spectroscopy* **2003**, *57*, 661–666.

49. Kakuta, N.; Arimoto, H.; Momoki, H.; Li, F.; Yamada, Y. Temperature measurements of turbid aqueous solutions using near-infrared spectroscopy. *Applied Optics* **2008,** *47*, 2227-2233.

50. Workman Jr., J.; Koch, M.; Lavine, B.; Chrisman, R. Process Analytical Chemistry. *Analytical Chemistry* **2009**, 81, 4623-4643.

51. Lin, J.; Brown, C. W. Universal Approach for Determination of Physical and Chemical Properties of Water by Near-IR Spectroscopy. *Applied Spectroscopy* **1993**, *47*, 1720-1727.

52. Reeves III, J. B. Near- versus Mid-Infrared Spectroscopy: Relationships between Spectral Changes Induced by Water and Relative Information Content of the Two Spectral Regions in Regard to High-Moisture Sample. *Applied Spectroscopy* **1995**, *49*, 295-303.

53. Segtnan, V. H; Sasic, S.; Isaksson, T.; Ozaki, Y. Studies on the Structure of Water Using Two-Dimensional Near-Infrared Correlation Spectroscopy and Principal Component Analysis. *Analytical Chemistry* **2001**, *73*, 3153-3161.

54. Hazen, K. H.; Arnold, M. A.; Small, G. W. Measurement of Glucose in Water with First-Overtone Near-Infrared Spectra. *Applied Spectroscopy 1998, 52*, 1597-1605.

55. Jensen, P. S.; Bak, J.; Anderson-Engels, S. Influence of Temperature on Water and Aqueous Glucose Absorption Spectra in the Near- and Mid-Infrared Regions at Physiologically Relevant Temperatures. *Applied Spectroscopy* **2003**, *57*, 28-36.

56. Ding, Q.; Small, G. W.; Arnold, M. A. Evaluation of Data Pretreatment and Model Building Methods for the Determination of Glucose from Near-Infrared Single-Beam Spectra. *Applied Spectroscopy* **1999**, *53*, 402-414.

57. Kramer, K. E.; Small, G. W.; Digital Filtering and Model Updating Methods for Improving the Robustness of Near-Infrared Multivariate Calibrations. *Applied Spectroscopy* **2009**, *63*, 246-254.

58. Ding, Q.; Boyd, B. L.; Small, G. W. Determination of Organic Contaminants in Aqueous Samples by Near-Infrared Spectroscopy. *Applied Spectroscopy* **2000**, *54*, 1047-1053.

59. Chen, Z.; Morris, J.; Martin, E. Correction of Temperature-Induced Spectral variations by Loading Space Standardization. *Analytical Chemistry* **2005**, *77*, 1376-1384.

60. Wulfert, F.; Kok, W. Th.; deNoord, O. E.; Smilde, A. K. Correction of Temperature-Induced Spectral Variation by Continuous Piecewise Direct Standardization. *Analytical Chemistry* **2000**, *72*, 1639-1644.

61. Lin J.; Brown C. Spectroscopic Measurement of NaCl and Seawater Salinity in the Near-IR region of 680-1230 cm^{-1}. *Applied Spectroscopy* **1993**, *47***,** 239-241.

62. Lin J.; Brown C. Near-IR Fiber-Optic Temperature Sensor. *Applied Spectroscopy* **1993**, *47***,** 62-68.

63. Arimoto, H.; Tarumi, M.; Yamada Y. Temperature insensitive measurement of glucose concentration based on near-infrared spectroscopy and partial least squares analysis. *Optical Review* **2003**, *10*, 74-76.

64. Brown, T. L.; LeMay Jr, H. E.; Bursten, B. E.; Murphy, C. J. *Chemistry The Central Science*, 11th ed.; Pearson: New Jersey, 2009; pp 499-503.

65. Pienta, N. J. *General, Organic and Biochemistry-Context and Cases,1st ed*.; McGraw Hill: 2011.

66. Joesten, M.; Hogg, J. L. *CHEM in your world, Instructor's Edition*; Brooks/Cole Cengage Learning: California, 2011; pp 282-285.

67. Braun, E.; Levin, B. C. Nylon: A Review of the Literature on Products of Combustion and Toxicity. *Fire and Materials* **1987**, *11*, 71-88.

68. U.S. Resin Production and Sales 2012 vs. 2011. American Chemistry Council April 2013.http://www.americanchemistry.com/Jobs/EconomicStatistics/Plastics-Statistics/Production-and-Sales-Data-by-Resin.pdf (accessed June 2013).

69. *Handbook of Plastics Joining: A Practical Guide*, Plastics Design Library, William Andrew Inc.: New York, 1997, pp-532.

70. Olabisi, O. *Handbook of thermoplastics*; Marcel Dekker Inc.: New York, 1997.

71. Nylon, San Diego Plastics, Inc. http://www.sdplastics.com/nylon.html (accessed September 2013).

72. More About Performance Plastics McMaster-Carr Supply Company. http://www.anagada.com/files/anagada/pdf/delrin.specifications.pdf (accessed September 2010).

73. Ghosh P. *Polymer Science and Technology: Plastics, Rubbers, Blends and Composites, 2nd ed.;* Tata McGraw-Hill: New Delhi, 2002.

74. Gooch, J. W. *Encyclopedic Dictionary of Polymers, Volume 1*, 2nd *ed.;* Springer: New York, 2011.

75. Mohan, J. *Organic Spectroscopy: Principles and Applications, 2nd ed.;* Alpha Science International Limited: Oxford, U.K., 2002, pp 59-63.

76. Foster, G. N.; Row, S. B.; Griskey, R. G. Infrared Spectrometry of Polymers in the Overtone and Combination Regions. *Journal of Applied Polymer Science* **1964**, *08*, 1357-1361.

77. Charles, J.; Ramkumar, G. R.; Azhagiri, S.; Gunasekaran, S. FTIR and Thermal Studies on Nylon-66 and 30% Glass Fiber Reinforced Nylon-6,6. *E-Journal of Chemistry* **2009**, *6*, 23-33.

78. Dasgupta, S.; Hammond, W. B.; Goddard III, A. Crystal Structures and Properties of Nylon Polymers from Theory. *Journal of American Chemical Society* **1996**, *118*, 12291-12301.

79. Orendroff, C. J.; Huber, D. L.; Bunker, B. C. Effects of Water and Temperature on Conformational Order in Model Nylon Thin Films. *Journal of Physical Chemistry C* **2009**, *113*, 13723-13731.

80. Camacho, W.; Valles-Liuch, A.; Ribes-Greus, A.; Karlsson, S. Determination of Moisture Content in Nylon 6,6 by Near-Infrared Spectroscopy and Chemometrics. *Journal of Applied Polymer Science* **2003**, *87*, 2165-2170.

81. Wu, P.; Yang, Y.; Siesler, H. W. Two-dimensional near-infrared correlation temperature studies of an amorphous polyamide. *Polymer* **2001,** *42*, 10181-10186.

82. Lachenal, G. Dispersive and Fourier transform near-infrared spectroscopy of polymeric material. *Vibrational Spectroscopy* **1995**, *9*, 93-100.

83. Ghebremeskel, Y.; Fields, J.; Garton, A. The Use of Near Infrared (NIR) Spectroscopy to Study Specific Interactions in Polymer Blends. *Journal of Polymer Science, Part B: Polymer Physics* **1994**, *32*, 383-386.

84. Rodgers, J. E.; Lee, S. Structural properties of Nylon 66 Carpet Yarns with Near Infrared Analysis. *Textile Research Journal* **1991**, *61*, 531-536.

85. Thermal properties of plastic materials. Professional Plastics. http://www.professionalplastics.com/professionalplastics/ThermalPropertiesofPlasticMaterials.pdf (accessed June 2013).

86. Thermal Degradation of Polymers, Gallagher, D. A.; CAChe Group, Fujitsu America Inc. http://www.cacheresearch.com/polydeg.pdf (accessed August 2012).

87. Lewin, M. *Handbook of Fiber Chemistry 3rd ed.;* CRC Press: Boca Raton, FL, 2007, pp 118.

88. Dry vs. Conditioned Polyamide Nylon Explained. Howe, B.; UL IDES http://articles.ides.com/dry_conditioned.asp (accessed June 2013).

89. Miller, C. E.; Svendsen, S. A.; Naes, T. Nondestructive Characterization of Polyethylene/Nylon Laminates by Near-Infrared Spectroscopy. *Applied Spectroscopy* **1993**, *47*, 346-356.

90. Roush, P.B. *The Design, Sample Handling, and Applications of Infrared Microscopes*; American Society for Testing and Materials: Michigan, USA, 1987, pp 74-96.

91. Zhang, L.; Small G. W.; Haka, A. S.; Kidder, L. H.; Lewis, E. N. Classification of Fourier Transform Infrared Microscopic Imaging Data of Human Breast Cells by Cluster Analysis and Artificial Neural Networks. *Applied Spectroscopy* **2003**, *57*, pp 14-22.

92. Alexeeva, N. V.; Arnold, M. A. Near-Infrared Microspectroscopic Analysis of Rat Skin Tissue Heterogeneity in Relation to Noninvasive Glucose Sensing. *Journal of Diabetes Science and Technology* **2009**, *3*, pp 219-232.

93. Humecki, H. J. *Practical guide to Infrared Microscopy: Practical Spectroscopy Series, Volume 19,* Marcel Dekker Inc.: New York, USA, 1995.

94. Chalmers, J. M.; Everall, N. J.; Ellison, S. Specular reflectance: A convenient tool for polymer characterization by FTIR-microscopy?. *Micron* **1996**, *27*, pp 315-328.

95. Sahlin, J. J.; Peppas, N. A. Near-field FTIR Imaging: A Technique for Enhancing Spatial Resolution in FTIR Microscopy. *Journal of Applied Polymer Science* **1997**, *63*, pp 103-110.

96. Yang, T. C. –K.; Lin, S. S. –Y.; Chauang, T. –H. Kinetic analysis of the thermal oxidation of metallocene cyclic olefin copolymer composites by FTIR microscopy and thermogravimetry. *Polymer Degradation and Stability* **2002**, *78*, pp 525-532.

97. Mayo, D. W.; Miller F. A.; Hannah R. W. *Course Notes on the Interpretation of Infrared and Raman Spectra*, John Wiley & Sons Inc.: New Jersey, USA, 2003 pp261-281.

98. Sichina, W. J. Characterization of Polymers Using TGA. Thermal Analysis Application note, Perkin Elmer instruments. http://depts.washington.edu/mseuser/Equipment/RefNotes/TGA_Notes.pdf (accessed May 2012).

99. Holland, B. J.; Hat, J. N. Thermal Degradation of Nylon Polymers. Polymer International **2000**, *49*, pp 943-948.

100. Spinu, I.; McKenna, G. B. Physical Aging of Thin Films of Nylon and PET. *Journal of Plastic film and Sheeting* **1997**, *13*, 311-326.